

Unsteady Aerodynamic Forces on NACA 0015 Airfoil in Harmonic Translatory Motion

Gaunaa, Mac; Sørensen, Jens Nørkær; Larsen, Poul Scheel

Publication date:
2002

Document Version
Publisher's PDF, also known as Version of record

[Link back to DTU Orbit](#)

Citation (APA):
Gaunaa, M., Sørensen, J. N., & Larsen, P. S. (2002). Unsteady Aerodynamic Forces on NACA 0015 Airfoil in Harmonic Translatory Motion. (MEK-FM-PHD; No. 2002-02).

DTU Library
Technical Information Center of Denmark

General rights

Copyright and moral rights for the publications made accessible in the public portal are retained by the authors and/or other copyright owners and it is a condition of accessing publications that users recognise and abide by the legal requirements associated with these rights.

- Users may download and print one copy of any publication from the public portal for the purpose of private study or research.
- You may not further distribute the material or use it for any profit-making activity or commercial gain
- You may freely distribute the URL identifying the publication in the public portal

If you believe that this document breaches copyright please contact us providing details, and we will remove access to the work immediately and investigate your claim.

Unsteady Aerodynamic Forces on NACA 0015 Airfoil in Harmonic Translatory Motion

by

Mac Gaunaa

Dissertation submitted to Technical University of Denmark in partial fulfillment of
the requirements for the degree of Doctor of Philosophy in Mechanical Engineering

Fluid Mechanics
Department of Mechanical Engineering
Technical University of Denmark
April, 2002

Fluid Mechanics
Department of Mechanical Engineering
Building 403
Technical University of Denmark
DK-2800 Lyngby, Denmark

Copyright © Mac Gaunaa, 2002

Printed in Denmark by DTU-Tryk, Lyngby

MEK-FM-2002-02 / ISBN 87-7475-258-8

This thesis has been typeset using L^AT_EX2e.

Preface

This dissertation is submitted in partial fulfillment of the requirements for the Ph.D. degree. The dissertation is based on the experimental, theoretical and numerical work carried out during the period from August 1998 to December 2001 at the Fluid Mechanics Section at the Department of Mechanical Engineering, Technical University of Denmark. The work has been carried out under the guidance of Professor Poul Scheel Larsen, to whom I would like to express my deepest gratitude for inspiring supervision.

I also wish to thank Associate Professor Jens Nørkær Sørensen for valuable inputs, and Andreas G Jensen, Danish Maritime Institute, for fruitful discussions on the art of experimental work.

For fruitful discussions and insights Martin O.L. Hansen and Niels Sørensen are thanked.

Finally, I would like to thank Mia for her love and patience with me during the course of my study.

It is acknowledged that the experimental setup was financed by the Danish Technical Research Council, through the Research Frame Program on Computational Hydrodynamics.

Technical University of Denmark
Copenhagen, April 2002

Mac Gaunaa

Abstract

The unsteady two-dimensional aerodynamic forces acting on a NACA 0015 airfoil undergoing harmonic translatory motions have been investigated experimentally and theoretically/numerically.

The focus of the experimental investigations was to determine the factors that influence the aerodynamic damping of harmonic translatory motion. Specifically, measurements of unsteady pressure distributions were undertaken at a range of incidences, movement directions, amplitudes and reduced frequencies matching real life conditions for the flap and lead-lag motion of wind turbine rotors.

From the experimental results it was seen that the maximum negative aerodynamic damping take place at moderate stall at an incidence of about 15° , at a movement direction close to the chordwise direction, and that the aerodynamic damping at 15° and 20° for the stalling cases decreases as the reduced frequency is decreased. The dependance on the amplitude of the motion was weak.

Up to three distinctively different stall modes occurring in both steady and unsteady experiments at incidences $15^\circ \leq \alpha \leq 20^\circ$ was observed. Both the mean and dynamic characteristics was found to differ from mode to mode.

As a part of the theoretical work an unsteady panel code was implemented. This code was used to investigate the differences in the dynamic response of an airfoil undergoing heaving motion and pitching motion.

Another application of the panel code was to compute the effect of the imposition of wind tunnel walls on the dynamic response of the airfoil. From these results dynamic tunnel corrections was derived.

A different part of the theoretical work concerned the development of a new heuristic stall model, which can be considered an ‘interpolation’ between quasi-stationary theory and unsteady potential theory. Comparison with the experimental results shows very good agreement in the attached cases, but the new model fails to reproduce the features of the moderately and deeply stalled flows due to the assumption of similarity between the dynamics in the attached and stalling cases.

Comparison of results obtained with a Navier-Stokes solver showed excellent agreement with the experimental data for incidences up to 8° . Fully turbulent flow was assumed in the Navier-Stokes simulations. The differences between the results for incidences 12° and above were caused by too late predicted onset of stall in the simulations, and that the Navier-Stokes solver predicted a strong effect from vortex shedding at incidence 20° , which was not found in the experiments.

The overall features of the aerodynamic damping was captured correctly for incidences up to 15° . The discrepancies at 20° was caused by the strong vortex dynamics in the predictions.

Synopsis

De instationære to-dimensionelle aerodynamiske kræfter på et NACA 0015 vingeprofil som udfører harmoniske translatoriske bevægelser er blevet undersøgt eksperimentelt og teoretisk/numeriskt.

I de eksperimentelle undersøgelser har fokus været på at bestemme de faktorer som influerer på den aerodynamiske dæmpning af harmoniske translatoriske bevægelser. Målinger af instationære trykfordelinger er blevet udført for en række indfaldsvinkler, bevægelsesretninger, amplituder og reducerede frekvenser for værdier som svarer til typiskt forekommende for en vindmøllerotors flap- og kantvise svingninger.

Fra de eksperimentelle resultater sås, at den maksimale, negative aerodynamiske dæmpning forekommer ved moderat afløst strømning ved cirka 15° indfaldsvinkel, med en bevægelsesretning tæt på den kantvise retning, og at den aerodynamiske dæmpning for de afløste strømninger ved indfaldsviklerne 15° og 20° aftager for aftagende reduceret frekvens. Afhængigheden af amplituden af bevægelsen viste sig at være svag.

Der blev observeret op til tre forskellige afløsningsniveauer for både stationære og instationære eksperimenter for indfaldsvinkler i området $15^\circ \leq \alpha \leq 20^\circ$. Både middel- og dynamiske karakteristika for de aerodynamiske kræfter afviger fra tilsvarende størrelser for de andre afløsningsniveauer.

Som en del af de teoretiske undersøgelser blev der implementeret en instationær panel kode. Denne blev brugt til at undersøge forskellen i den dynamiske respons af et vingeprofil under translatorisk og roterende bevægelse.

I en anden applikation af panel koden, blev den anvendt til at beregne effekten af vindtunnel vægge på det dynamiske respons af vingeprofilet. Disse resultater dannede basis for udledningen af dynamiske vindtunnelkorrektioner.

En anden del af de teoretiske undersøgelser omhandlede udviklingen af en ny heuristisk stall model. Den nye stall model kan opfattes som en ‘interpolation’ mellem kvastationær teori og instationær potential teori. Sammenligning med eksperimentelle resultater viste for de ikke-afløste strømninger en god overensstemmelse, hvorimod modellen ikke kunne reproducere de dynamiske karakteristika for de moderate eller massivt afløste strømninger på grund af antagelsen om lighed mellem strømnings dynamikken i den afløste og den ikke-afløste strømning.

Sammenligninger af resultater beregnet med en Navier-Stokes kode viste meget god overensstemmelse med de eksperimentelle data for indfaldsvinkler op til $\alpha = 8^\circ$. Navier-Stokes beregningerne antog en fuldt turbulent strømning. Forskellen mellem resultaterne for indfaldsvinkler fra 12° og derover skyldes at den beregnede strømning afløser senere end den målte, og at Navier-Stokes beregningerne viste en kraftig effekt fra hvirvelafkastning ved indfaldsvinklen 20° , som ikke forekom i de eksperimentelle resultater.

De overordnede karakteristika for den aerodynamiske dæmpning blev beregnet korrekt for indfaldsvinkler op til 15° . Uoverensstemmelserne ved 20° skyldes den kraftige hvirveldynamik i de beregnede resultater.

Contents

| | | |
|----------|---|-----------|
| 1 | Introduction | 1 |
| 1.1 | Objectives of the present work | 3 |
| 1.2 | Outline of the dissertation | 4 |
| 2 | Experiments | 5 |
| 2.1 | Previous studies | 5 |
| 2.2 | Experimental targets | 6 |
| 2.2.1 | Design considerations | 7 |
| 2.3 | Test rig | 8 |
| 2.4 | Instrumentation | 11 |
| 2.5 | Data processing and analysis | 12 |
| 2.6 | Measurement accuracy | 14 |
| 2.6.1 | Pressure measuring system | 16 |
| 2.6.2 | Angle of attack | 16 |
| 2.6.3 | Acceleration of pressure transducers | 16 |
| 2.6.4 | Wind tunnel corrections | 17 |
| 2.6.5 | Statistical Uncertainty | 18 |
| 2.7 | Multiple stall | 20 |
| 2.8 | Results | 23 |
| 2.8.1 | Determination of distinct stall modes | 23 |
| 2.8.2 | Stationary airfoil | 28 |
| 2.8.3 | 1 DOF translatory oscillatory motion | 32 |
| 3 | Theoretical Models | 43 |
| 3.1 | Background | 43 |
| 3.2 | Analytic Unsteady Potential Theory | 45 |
| 3.2.1 | Normal Force and Moment | 46 |
| 3.2.2 | Tangential Force | 52 |
| 3.2.3 | Lift and Drag Forces | 53 |
| 3.2.4 | Oscillatory Motion | 54 |
| 3.3 | Quasi-steady Theory | 56 |
| 3.4 | New Stall Model | 61 |
| 3.4.1 | Motivation | 61 |
| 3.4.2 | The Model | 62 |
| 3.5 | Panel Code | 68 |
| 3.5.1 | Singularity Elements | 68 |

| | |
|--|------------|
| 3.5.2 Steady Solution | 71 |
| 3.5.3 Unsteady Solution | 72 |
| 3.5.4 Reduction of Computational Cost Linked to Evaluation of the Unsteady Wake | 75 |
| 3.5.5 Tunnel effect modelling | 78 |
| 3.5.6 Separated flows | 79 |
| 3.6 Navier-Stokes Code | 80 |
| 3.6.1 Reynolds Averaged Navier-Stokes Equations | 81 |
| 3.6.2 $k - \omega$ Shear Stress Transport Model | 82 |
| 3.6.3 Numerical code | 83 |
| 3.6.4 Moving grid | 84 |
| 4 Results | 87 |
| 4.1 Wind Tunnel Corrections | 87 |
| 4.1.1 Steady Tunnel Corrections | 87 |
| 4.1.2 Unsteady Tunnel Corrections | 93 |
| 4.2 Pitching versus translatory motion | 114 |
| 4.3 Analytical Models | 116 |
| 4.4 Navier-Stokes Model | 132 |
| 4.4.1 Stationary Airfoil | 133 |
| 4.4.2 Airfoil undergoing one DOF oscillatory translatory motion . . . | 142 |
| 5 Conclusion | 161 |
| Bibliography | 164 |
| Nomenclature | 173 |
| Appendix | 175 |
| A Airfoil section and movement mechanism | 177 |
| B Expressions for Unsteady Potential Forces for Oscillatory Motion | 183 |
| C Numerical Panel Code Validation | 187 |
| C.1 Van de Vooren airfoil | 187 |
| C.2 Joukowski airfoil | 188 |
| C.3 Impulsive Motion, the Wagner function | 189 |
| C.4 Oscillating airfoil | 191 |
| C.5 Tunnel validation | 192 |
| D RANS grid sensitivity study and code validation | 195 |
| D.1 Grid sensitivity study | 195 |
| D.1.1 Grid radius | 195 |
| D.1.2 Grid discretization | 196 |
| D.2 Moving grid validation | 199 |

Chapter 1

Introduction

The task of simulating the flow field around the rotors of a wind turbine is not a simple one. Not only is the flow for a wide range of free stream velocities massively stalled at the inner part of the blades and therefore strongly three dimensional and unsteady, it is also influenced by a combination of complex effects such as rotational effects, turbulence, surface roughness effects, and the effects caused by the highly complex inflow conditions due to operation in yaw and tilt, gusts, tower effects, atmospheric boundary layer and coupled fluid-structure interaction.

Due to this inherent complexity of the flow around a wind turbine, the development in the design of wind turbine rotors has to a large extent relied on empirical correlations, acquired through systematic model testings and simplified theoretical considerations, as well as on the intuition and experience of the designer. Over the years, this has resulted in reliable and efficient aerodynamic and structural designs of wind turbines. However, as the design of a component is gradually changed, new problems or phenomena may arise that has to be understood in order to be taken into consideration in the design phase.

An example of this is stall-induced vibrations, which arose for horizontal axis stall regulated wind turbines in the 1990's [47] [37], as the rotor diameters increased. Possible ways to circumvent these vibrations include modification of the stall characteristics of the rotors, or modification of the structural dynamics of the rotors. It can be shown, that the aerodynamic damping of a wind turbine rotor is highly dependent on the direction of the vibrational motion of the blades [41]. If this dependence can be predicted correctly, then one way of avoiding the unwanted vibrations can be tailoring of the structural dynamics of the turbine such that the direction of the vibrational modes are in the directions which have a sufficiently high aerodynamic damping to assure that the total damping of the combined aerodynamic and structural system is positive.

In many cases, the direction of the vibrations which lead to failure, or a drastic reduction in the life-time of the rotor, is in the chordwise direction. This particular phenomena is referred to as lead-lag instability. Experimental investigations on full scale turbines have shown that the aerodynamic damping of motions in the chordwise direction is less damped than the flapwise counterpart [56].

Besides causing a dramatic reduction in lifetime, chordwise motions are difficult to incorporate into aerodynamic prediction codes.

Several models aimed at describing the fluid forces on wind turbine rotors exist. The standard designing tools among wind turbine manufacturers are methods based on Blade Element Momentum (BEM) theory [21] [64], but a wealth of other methods exist. Among more sophisticated models capable of determining both steady and unsteady forces on rotors undergoing relative motion are potential methods [58], actuator disc models [62] [49], acceleration potential models [8] and Navier-Stokes models, such as Reynolds Averaged Navier Stokes (RANS) models [52] and Detached Eddy Simulation (DES) [48] [24] [25].

The latter of the models mentioned are very computationally expensive.

It is of the utmost importance for the manufacturers to be able to determine whether a certain vibrational mode of a blade is prone to be amplified or damped by interaction with the air-flow, or how time varying inflow conditions affect the forces on the rotor. If the simpler and faster models based on the BEM theory need to describe the response from the fluid forces for unsteady inflow conditions, they have to be extended to deal with phenomena occurring when the rotor is vibrating or experiencing time varying inflow conditions.

Many of the models that describe the unsteady interaction between motion and forces on a blade were developed with helicopter rotors in mind. Specifically, the dynamic stall models of Beddoes and Leishman [29] and Tran and Petot [57] should be mentioned. Dynamic stall is a complex fluid dynamic phenomenon, which refers to the unsteady stall behavior of airfoils moving transiently with respect to the free-stream. This unsteady stall behavior typically involves massive unsteady separation and large scale vortices. The effect of these unsteady phenomena is hysteresis in separation and reattachment, which can cause the forces in the dynamic case to greatly exceed their static counterparts.

Dynamic stall models specifically designed for wind turbine applications exist. A simple, but very practical and in many cases sufficiently accurate, dynamic stall model was proposed by Øye [63], in which the dynamic stall phenomenon is simulated as a time-lag of the separation. This model is widely used in the wind-turbine industry.

Most experimental investigations of unsteady airfoil aerodynamics concern helicopters in forward flight, as for instance Piziali [42] or McCroskey et. al. [31], and focus on airfoils in pure pitching or combined pitching and heaving motions.

One of the main differences in the flow situation between a wind turbine and a helicopter is that the change in relative angle of attack of the airfoil in a rotor-fixed coordinate system is less evident in the wind turbine case. In fact, if the turbine is working under ideal conditions, the relative angle of attack of the airfoil in a rotor-fixed coordinate system is close to constant over the cycle of the rotor.

With the rapid increase in computer performance, computational fluid dynamics (CFD) is possible in three dimensions at reasonably low costs. This can be employed to investigate complex dynamic three-dimensional effects, such as the aerodynamic damping of a full three dimensional wind turbine rotor [5].

However, there is still need to study two-dimensional flows to gain fundamental

knowledge about phenomena such as two dimensional dynamic stall.

Fully coupled fluid-structure problems are still computationally very costly using three-dimensional CFD, but two-dimensional versions of these, as for example the ones by Johansen [23] or Gaunaa [16] [17] exist.

Previous comparative studies with several different fully coupled two-dimensional fluid-structure interaction codes, performing computations on airfoils undergoing both translatory and pitching motion have shown a great scatter of the results [9]. The aeroelastic codes were all based on state of the art 2D Reynolds Averaged Navier Stokes (RANS) solvers coupled to simple models for the motion of the airfoil. The conclusion were that substantial differences in the predicted aerodynamic damping and frequencies were present, indicating big differences in the forces from the RANS solvers. This was evident from both stalling and non stalling simulations, albeit differences were clearly greatest for stalling flows.

These results clearly show the need for validation of the used models, not only with respect to pitching motion, but also with respect to translatory motion.

1.1 Objectives of the present work

The objectives of the present work falls into two categories, namely experimental and theoretical. In the first category the objectives are:

- to provide detailed instantaneous data of the dynamic behavior of the pressure on an airfoil undergoing translatory motion
- to determine the choice of parameters of the 1 Degree Of Freedom (DOF) motion that minimizes the damping forces from the flow on the airfoil
- to investigate the isolated unsteady flow phenomena leading to lead-lag instabilities
- to establish a detailed database that allows the evaluation of numerical techniques and dynamic stall models

In the second category the objectives are:

- to investigate the differences between the dynamic forces from pitching motions and translatory motions
- to propose, develop and evaluate new heuristic model for prediction of dynamic forces from the flow, taking into account the inherent differences in the response from angular and translatory motion
- to investigate the performance of a two-dimensional RANS algorithm against the experimentally obtained data

1.2 Outline of the dissertation

The dissertation is organized into five chapters. Following this introduction is chapter 2, in which the experimental setup, data processing and the main experimental results are shown.

Chapter 3 concerns the description of the five theoretical models for prediction of unsteady forces from two dimensional flow. The first three models are analytical in nature, and the two last, an inviscid panel code and a Navier-Stokes code, are numerical in nature.

Chapter 4 presents the results obtained with the theoretical models. The results include derivation of unsteady tunnel corrections for the experiments, investigation of the difference between pitching translating airfoils, and comparison of the experimental and theoretical results. The main focus in the investigation of the performance of the dynamic features of the theoretical models is the prediction of aerodynamic damping, which is a critical parameter in prediction of fluid-structure stability.

Finally, chapter 5 draws general conclusions and discusses the future perspectives of the study.

Chapter 2

Experiments

This chapter describes the experimental setup and shows the results of the pressure measurements performed on a NACA 0015 airfoil undergoing harmonic one-degree of freedom (DOF) translatory motion. Following a brief survey of previous studies in the field, the experimental objectives are stated and the test rig is presented along with the instrumentation. Subsequently, the data processing and analysis is described, after which the measurement accuracy is assessed. Due to the occurrence of multiple stall in the experiments, the phenomenon is described in section 2.7. Finally, the experimental results are shown.

2.1 Previous studies

Most measurements on airfoils in dynamic oscillatory motion have been performed with helicopter rotors in mind. Therefore, most tests have been performed for pitching motion of the airfoil, as noted in a review by McCroskey [30]. In the majority of the existing tests the airfoil is oscillated sinusoidally in pitch about the quarter chord.

An investigation of the effect of varying Reynolds number, oscillation amplitude, reduced frequency, and leading edge geometry of a NACA 0012 airfoil was undertaken by McCroskey [31]. It was found that oscillation amplitude, reduced frequency and leading edge geometry, including leading edge trip tape, had major influence on dynamic stall. Variation of the Reynolds number from $Re = 1 \cdot 10^6$ to $Re = 3.5 \cdot 10^6$, on the other hand, had only a weak influence on the phenomenon.

Leishman [28] carried out dynamic stall investigations on a NACA 23012 airfoil at $Re = 1.5 \cdot 10^6$. One of the conclusions of this work was that the static stall characteristics are not necessarily useful indicators as to how an airfoil will behave under dynamic stall conditions.

A number of works presents results from extensive pitch oscillating airfoil experiments suitable for evaluating unsteady viscous theories and computational methods. Three specific works should be mentioned.

McCroskey [32] presented the key features of the dynamic stall phenomenon by ten specific test cases for $Re = 4 \cdot 10^6$.

Piziali [42] presented a comprehensive experimental investigation of the pressure

distribution of a wing undergoing pitching motions. In this work data for both 2-D and 3-D cases are shown. The 3-D cases are measurements of dynamic stall characteristics for an airfoil including tip effects.

Galbraith [14] has carried out numerous dynamic stall experiments which are collected in the extensive Glasgow University database on the dynamic loops of 13 different airfoils.

Another type of experiments that has been investigated is constant pitch rate of an airfoil. Walker [59] conducted large amplitude pitch oscillations with constant pitch rates for $Re = 4.5 \cdot 10^4$. The non-dimensional pitch rate, $\alpha^+ = \dot{\alpha}c/V$, show a dramatic effect on flow structure in dynamic stall. As the pitch rate was increased, the large scale vortical structures appeared later, and were of a different form.

Recent development in optical measuring technique has rendered possible the use of Particle Image Velocimetry (PIV) to obtain planar instantaneous velocity measurements. Such data can yield information about flow and vorticity structures. Oshima [39] used this technique for obtaining quantitative information on the evolution of flow structures on the suction side of a NACA 0015 airfoil pitching at constant angular velocity for Reynolds numbers $Re = 5.4 \cdot 10^4$ and $Re = 1.5 \cdot 10^5$.

In the case of wind turbine rotors, the relative pitching motion is less evident than in the helicopter case. Since the torsional stiffness of wind turbine blades are generally very high, the relative pitching motion is caused by turbine misalignment and spatial and temporal changes in wind velocity such as gusts, tower effects and atmospheric boundary layer.

Problems with chordwise vibrations related to negative aerodynamic damping have been observed for wind turbine rotors in recent years [41], which calls for an experimental investigation of the effects of unsteady translatory motion of an airfoil.

2.2 Experimental targets

The target of setting up an experiment that allows accurate measurements of the unsteady pressure acting on an airfoil in motion poses experimental challenges of a higher complexity than in the static case. Issues that require special attention is model stiffness, sensitivity of pressure transducers to fictitious forces, precise measurement of the airfoil motion, to name a few.

In the light of the limited work done in the field of detailed instantaneous pressure measurements on an airfoil in translatory motion, the main objectives of the present study were formulated as follows (as stated already in chapter 1):

- to provide detailed instantaneous data of the dynamic behavior of the pressure on an airfoil undergoing translatory motion
- to determine the choice of parameters of the 1DOF motion that minimizes the damping forces from the flow on the airfoil

- to investigate the isolated unsteady flow phenomena leading to lead-lag instabilities
- to establish a detailed database that allows the evaluation of numerical techniques and dynamic stall models

2.2.1 Design considerations

With the experimental objectives in mind, the test rig for the present experiments was designed to accommodate the following requirements:

- enable high resolution of the pressure measurements in time.
- the experimental setup should allow the direction of the translatory motion to be changed independently of the geometrical angle of attack of the free-stream wind on the airfoil.
- enable the frequency and amplitude of the motion to be varied.

The profile chosen for the airfoil test section was a NACA 0015 airfoil, because that type of airfoil is known to be predicted well using RANS Navier-Stokes codes, as noted by Bertagnolio et. al. [6].

Due to the physical constraints of the wind tunnel and pressure transducers, some considerations had to be made considering the construction of the model.

For the purpose of determining the dimensionless quantities that match real life data for a standard wind turbine, the following standard dimensional case was proposed.

- $r_{\text{rotor}} = 20\text{m}$. Rotor radius.
- $r_{\text{eff}} = 0.75 \cdot r_{\text{rotor}} = 15\text{m}$. Effective lumped radius.
- $\Omega = 3\text{rad/s}$. Angular velocity.
- $V_{\text{wind}} = 15\text{m/s}$. Wind velocity.
- $V_{\text{rel}} = \sqrt{V_{\text{wind}}^2 + (\Omega r_{\text{eff}})^2} = 47.5\text{m/s}$. Relative velocity.
- f_{eig} . $1.805/2.963 \text{ Hz} \sim 2/3\text{Hz}$ Flap/Chordwise eigenfrequency.
- $c_{\text{real}} = 1\text{m}$. Chord length.

The reduced frequencies are comparable to real rotor data in the lead-lag instability case [41]. The dimensional quantities correspond to the following dimensionless velocity and frequency

- $\text{Re} = \frac{V_{\text{rel}} \rho c}{\mu} = 3.2 \cdot 10^6$
- $f_{\text{red}} = \frac{f_{\text{mov}} c}{2V_{\text{rel}}} = 0.02/0.03$ in the flap/chordwise direction.

As a reasonable tradeoff between blockage and Reynolds number effects, the chord length of the model was set to $c = 0.38m$. Since the wind tunnel at Danish Maritime Institute is capable of wind velocities up to $\sim 22m/s$, the maximum Reynolds number for the model was $Re \sim 0.55 \cdot 10^6$.

In order to match the dimensionless frequency for the model, the frequency for the experiments should be set in the range

$$f_{\text{model}} = \frac{f_{\text{red}} 2V}{c} = 2.3/3.4 \text{ Hz.}$$

Unsteady motion of the test airfoil induces fictitious forces which influence the amount of unwanted vibration in the flexible test airfoil. Another aspect of unsteady fictitious forces in this respect is that the pressure transducers interpret fictitious forces as a pressure signal. In order to keep the above effects at a minimum, it was chosen to settle for a maximum frequency of 2.4 Hz and a maximum amplitude of the motion of $A/c = 0.05/0.38 = 0.132$. Reduced frequencies higher than $f_{\text{red}} = 0.02$ were obtained by reducing the free-stream velocity below 22 m/s.

When using pressure transducers in a moving frame of reference, special attention has to be paid to the orientation of these, since the induced signals from the fictitious forces are dependant on the orientation of the transducers. By keeping the same orientation on all pressure transducers, the signal from the fictitious forces were identical for all pressure taps. This causes the effect of the fictitious forces to vanish in computations of integral quantities such as lift, drag and moment coefficients.

Another issue that requires special attention is the stiffness of the airfoil test section. The construction of the airfoil test section should be rigid enough to endure the fictitious forces and the forces from the air. Furthermore, the eigenfrequency of the relatively slender structure should be kept as high as possible to have a big gap between the frequency of the motion of the airfoil and the eigenfrequency of the wing.

2.3 Test rig

The NACA 0015 airfoil model used for the measurements in this work was built in the workshop at Danish Maritime Institute. The construction is based around a rectangular aluminum cylinder/beam providing stiffness to the model. The measuring section, which was manufactured in plexiglass, is located in the mid-span position. A total of 117 pressure taps are distributed over three spanwise positions, as shown in figure 2.1. The spanwise distances from the center measuring cross-section are 8% and 16% of the chord length placed on each side of the center measuring span. The chord-length of the airfoil is 0.38 m, and the span-width of the model is 2.55 m, which is identical to the width of the open-loop wind tunnel at Danish Maritime Institute.

In order to keep the stiffness to mass ratio high, the outer parts of the airfoil were manufactured in a light material, to make the cross-section identical through out the span without adding considerably to the mass of the system. Measurement of the eigenfrequency of the airfoil using accelerometers showed that the lowest eigenfrequency of the airfoil including the pressure transducers was approximately 16 Hz, which is safely above the frequency of the prescribed oscillations, 2.4 Hz.

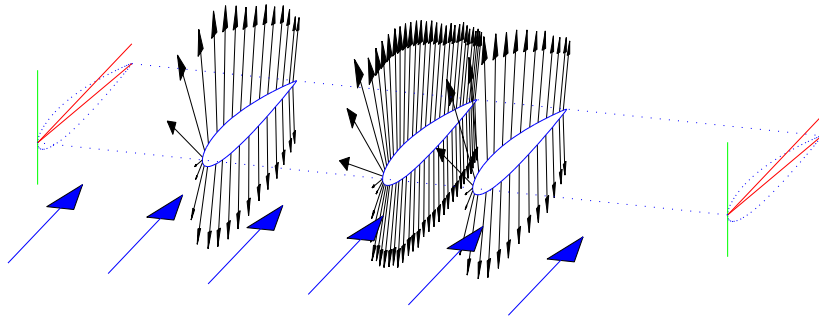


Figure 2.1: *The 117 pressure taps are distributed over three spanwise measuring sections. The placement of the three spanwise measuring sections are not to scale.*

The chordwise distribution of the pressure taps on each measuring section were distributed after the cosine function to ensure refined resolution of the leading and trailing edges of the airfoil. Identical distributions were employed on the upper and lower sides of the airfoil. The 117 pressure taps were distributed on the three measuring sections with 29 taps each on the outer measuring spans and 59 taps on the center measuring span, as shown in figure 2.2.

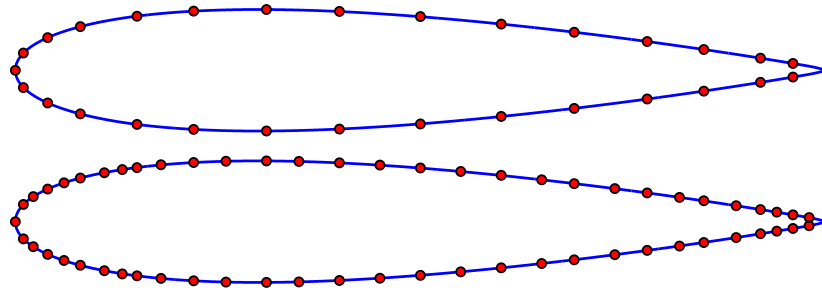


Figure 2.2: *Chordwise distribution of pressure taps. The upper figure shows the coarse distribution for the outer measuring spans, span 1 and span 3. The lower figure shows the distribution of the pressure taps in the middle measuring span.*

All pressure measurements were carried out in the $1.80m \times 2.55m$ open loop wind tunnel at Danish Maritime Institute using the PSI 8400 pressure system. The PSI 8400 pressure system is a set of differential pressure measurement units consisting of arrays of silicon piezoresistive pressure sensors. The pressure sensors were located inside the airfoil to minimize the distance from the pressure measurement units to the pressure taps on the measuring sections, thereby allowing higher resolution of the pressure signal in time. The static pressure measured $3.05 m$ upstream from the airfoil was used as reference pressure. This was measured with a pitot tube that was connected to the pressure sensors inside the airfoil using rubber tubing.

Trip tape was used at the leading edge of the profile to ensure a turbulent boundary layer, as depicted in figure 2.3. The trip tape consisted of 4 mm wide strips of 0.45 mm high self-adhesive sand paper. Investigation of the airfoil test section after the measurements were carried out revealed, that there was a difference in the position of the trip tape on the upper and lower sides of the airfoil. The upper trip tape was located 3.7%

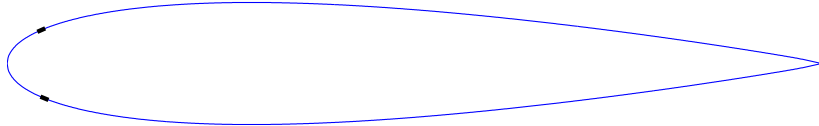


Figure 2.3: *Location of the trip tape on the leading edge of the airfoil. The upper trip tape is located 3.7% chord-lengths from the leading edge , whereas the lower trip tape is located at 4.2% chord-lengths from the leading edge. The difference is approximately 2 mm.*

chord-lengths from the leading edge, whereas the lower trip tape was located at 4.2% chord-lengths from the leading edge. The difference is approximately 2 mm. Despite the efforts to minimize the Reynolds number effects, some sensitivity to the Reynolds number should be expected near maximum lift and in the moderately stalled region. The drag forces are often an order of magnitude lower than their lift counterparts, and therefore harder to obtain accurate measurements for. Especially so in the case of determining the drag forces at low incidences by integration of the surface pressures, where a big part of the drag force is integrated from relatively few pressure taps. Nevertheless, it was chosen to obtain both the lift and drag forces from integration of the surface forces, since the dynamic nature of the experiment would complicate or even render impossible the use of force measurement units and wake rakes.

The motion of the profile was generated by transforming the rotational motion from a servo motor to a harmonic linear motion with a movement mechanism, such that the direction of the motions, β , could be changed independently of the angle of attack, α , of the airfoil. The geometric definitions used throughout this work are defined in

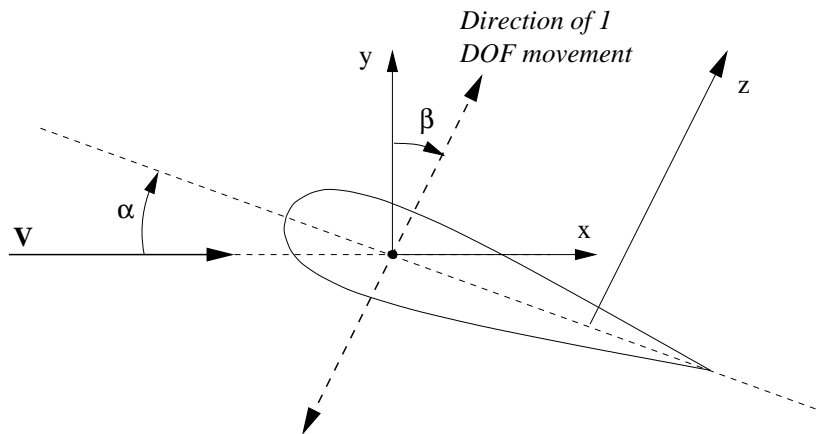


Figure 2.4: *Definitions and positive directions of the angle of attack, α , the angle of movement, β , which are defined with respect to the free stream velocity, V . The z -axis defines the positive direction for the motion of the profile.*

figure 2.4.

The movement mechanism was constructed and built by Mogens Pettersen of IMP Engineering. In appendix A figures showing the details regarding the airfoil test section and the movement mechanism is located.

The position of the 1 DOF motion was measured in each side of the movement mecha-

nism using potentiometers.

Sampling frequencies up to 600 Hz was possible with the pressure measuring system used. A minimum sampling frequency of 250 Hz was employed to ensure more than 100 samples per period while limiting the amount of data to a tolerable level. Pressures and positions were both sampled at this frequency to obtain accurately the phase of the motion.

2.4 Instrumentation

The instrumentation used in the experimental setup is summarized below.

Pressure Transducers The pressure transducers used for measurement of the pressures acting on the airfoil in the experimental setup is the PSI 8400 pressure system, which is a set of differential pressure measurement units consisting of an array of silicon piezoresistive pressure sensors, one for each pressure port. The pressure transducers were located inside the airfoil to minimize the distances from the pressure transducers to the pressure taps on the measuring sections, thereby allowing higher resolution of the pressure signal in time. The static pressure measured 3.05m upstream from the airfoil was used as reference pressure for the differential pressure measurement units.

Calibration of the pressure transducers is automated. When placed in the calibrate position, all sensors are automatically connected to a common calibration pressure port. A series of accurately measured pressures is applied through this port to characterize the sensors, in place, at the condition to which they are subjected. The calibration pressures are supplied by an in-house built reference pressure unit.

Periodic calibration maintains static errors within $\pm 0.05\%$ of the full scale pressure range, which corresponds to worst case errors on the static C_P values of $\Delta C_P = 0.05$.

Angle of attack The angle of attack of the airfoil was measured using an inclinometer attached to an inverse mold, which was manufactured to fit on the airfoil such that the top of the inverse mold, where the inclinometer was attached, is parallel to the chord-line. The inclinometer used was a Wedge Smart Level, with an angular resolution of 0.1° .

Position measurement Consists of one high precision Bourns 65745-001-102 potentiometer in each side of the movement mechanism. The potentiometers are linear $\pm 2.5\%$. The potentiometers were used for determination of the phase of the motion of the airfoil only, since the amplitude was set on the movement mechanism.

Thermometer The test section air temperature was obtained with a Wilhelm Lambrecht thermometer located in the recirculation room of the open loop wind tunnel.

Barometer The atmospheric pressure was obtained with a Wilhelm Lambrecht barometer located in the recirculation room.

Dynamic pressure The test section dynamic pressure was determined from the difference between the static and stagnation pressures measured with a Furness FC-012 micromanometer. The accuracy is $\pm 1\%$ of the reading.

2.5 Data processing and analysis

The experimental setup produces a vast quantity of data that has to be processed to obtain various levels of information about the flow. The sample time for all data series in this work was 60 seconds, leading to $1.8 \cdot 10^6$ real numbers for each of the runs in the experiment.

The pressures are measured by sweeping through all pressure taps one at a time. This means that the pressures have to be corrected in order to obtain data corresponding to the same time for all pressure taps. This is done by the in-house data logging program at DMI before the data is written to the hard disk.

The finest level of information in the flow can be investigated by viewing the raw non-dimensional pressure distribution on which noise from for instance turbulence appears.

From the information on the motion of the airfoil section, it is possible to compute a mean period, such that noise is reduced significantly whilst still showing the mean period flow details. For example; if a vortex is shed at the same time of the movement period, it will appear in the mean period without the noise that appears in the raw pressure distribution. Linear interpolation in time combined with a weighted summation procedure was used to compute the mean period data.

Moving a level up in processing, lift and drag forces were computed by integrating the measured surface pressure using the trapezoidal rule.

It should be noted that the terms lift and drag throughout this work corresponds to the forces perpendicular and parallel to the free-stream direction. Analogously, all lift, drag and moment coefficients are obtained by non-dimensionalizing the forces using the free-stream velocity.

Throughout this work the integral quantities aerodynamic damping and aerodynamic added mass are used to gain insight into the dynamic response of the forces from the flow on the airfoil. It can be shown, that the work carried out by the forces from the flow is closely related to the aerodynamic damping. If the motion of the airfoil is given by

$$z = A \sin(\omega t), \quad (2.1)$$

then the velocity and acceleration can be obtained by differentiation

$$\dot{z} = A\omega \cos(\omega t) \quad (2.2)$$

$$\ddot{z} = -A\omega^2 \sin(\omega t). \quad (2.3)$$

If furthermore the mean period unit-span force in the direction of the movement, $\overline{F_z}(t)$,

is expressed as a fourier-series in time

$$\bar{F}_z = C + \sum_{n=1}^{\infty} (a_n \cos(n\omega t) + b_n \sin(n\omega t)), \quad (2.4)$$

then it seen that the work carried out during one period of the motion for a unit-span is

$$w = \oint \bar{F}_z dz = \int_0^{2\pi/\omega} \bar{F}_z(t) A\omega \cos(\omega t) dt = \pi A a_1. \quad (2.5)$$

Introducing the force related to aerodynamic damping as an ordinary damping term

$$F_{z,da} = D \cdot \dot{z} = DA\omega \cos(\omega t), \quad (2.6)$$

the relation between the aerodynamic damping and a_1 is

$$a_1 = DA\omega. \quad (2.7)$$

Combining equation 2.7 with equation 2.5 yields the relation between the work and the aerodynamic damping

$$w = DA^2\omega\pi. \quad (2.8)$$

From this it is seen that the work associated with aerodynamic forces is proportional to the aerodynamic damping. The damping forces are the component of the forces in phase with the velocity of the airfoil, or 90° out of phase with the displacement of the airfoil.

Analogous arguments lead to the conclusion that the forces in phase with the acceleration of the airfoil,

$$F_{z,ma} = M \cdot \ddot{z}, \quad (2.9)$$

the aerodynamic added mass, arises from the b_1 term in equation 2.4 exclusively.

On the basis of these observations, the aerodynamic damping and added mass is computed from the mean period force, \bar{F}_z , by a least squares fit of D and M to

$$\begin{pmatrix} \vdots & \vdots & \vdots \\ \ddot{z} & \dot{z} & 1 \\ \vdots & \vdots & \vdots \end{pmatrix} \begin{pmatrix} M \\ -D \\ C \end{pmatrix} = \begin{pmatrix} \vdots \\ \bar{F}_z \\ \vdots \end{pmatrix}. \quad (2.10)$$

The negative sign on the damping signifies that the aerodynamic acts as structural damping, meaning that the force from a positive damping acts in the opposite direction of the velocity, thus damping the motion. What is interesting in terms of dynamic stability is the areas with negative aerodynamic damping.

By use of the Buckingham Pi theorem, the non-dimensional groups corresponding to the aerodynamic damping and added mass can be found

$$C_{DA} = \frac{D}{1/2 \rho c V} \quad (2.11)$$

$$C_{MA} = \frac{M}{\pi/4 c^2 \rho}. \quad (2.12)$$

The reason for the factor $1/2$ in the expression for the non-dimensional aerodynamic damping is that the term $1/2 \rho c V$ appears in the quasi-steady model presented in chapter 3. Analogous, the factor $\pi/4$ in the expression for the non-dimensional added mass is chosen because the term $\pi/4 c^2 \rho$ appears in the virtual mass terms of the unsteady potential flow solutions presented in chapter 3. The quantity with which the added mass term is non-dimensionalized is the mass of the fluid of a unit-depth circular cylinder with the same diameter as the chord of the airfoil.

The non-dimensional parameters on which the non-dimensional aerodynamic damping and added mass depend are reduced frequency, f_{red} , Reynolds number, Re , non-dimensional amplitude of the motion, \tilde{A} , and the angle of attack and direction of movement, α and β :

$$f_{red} = \frac{f_{mov} c}{2V} \quad (2.13)$$

$$Re = \frac{\rho V c}{\mu} \quad (2.14)$$

$$\tilde{A} = \frac{A}{c} \quad (2.15)$$

$$\alpha \quad (2.16)$$

$$\beta \quad (2.17)$$

The density used for non-dimensionalization of the quantities was obtained using the ideal gas law

$$\rho = \frac{p}{mRT}, \quad (2.18)$$

with temperature and atmospheric pressure obtained from a thermometer and a barometer located in the wind tunnel room. Due to heating of the tunnel air under tunnel operation, temperature and atmospheric pressure was noted each 10 minutes.

The viscosity of the air was calculated using the empirical Sutherland correlation [12]

$$\mu = \frac{bT^{0.5}}{1 + S/T} \quad (2.19)$$

where the constants b and S are

$$b = 1.458 \cdot 10^{-6} \frac{kg}{m \cdot s \cdot K^{0.5}}$$

$$S = 110.4K$$

for standard air.

2.6 Measurement accuracy

The accuracy of the measured quantities are influenced by numerous factors in an experiment as complex as the present one. A list of factors that determine the accuracy of the experimental results is given below, after which the key elements of the measurement accuracy are assessed.

Model shape The machining tolerance of the airfoil cross section shape was not determined.

Pressure outtake positions The accuracy of the locations of the pressure tap positions was not determined.

Model rigidity The lowest eigenfrequency of the airfoil fully equipped with pressure transducers and tubing was $f_{eig} = 15$ Hz. The eigenfrequency was measured using accelerometers. Since the maximum frequency of the excitations was $f_{mov} = 2.4$ Hz, it was concluded that the model structural response would be negligible.

Inflow conditions The rms¹ value of the velocity in the wind tunnel was determined from pitot measurements to 0.04 m/s, which is negligible compared to the free-stream velocities in the experiments ($\sim 0.2\%$). The uniformity of the wind profile in the wind tunnel was not investigated.

Movement mechanism Error on determination of the position of the model. Mechanical free-play in the movement mechanism. Initial test data indicated that the motion produced by the movement mechanism could be measured with a high precision.

Dynamic Pressure The accuracy of the used differential pressure measurement unit was $\pm 1\%$ of the reading.

Pressure transducers The accuracy of the differential pressure measurement unit is discussed in section 2.6.1 below. The influence of the acceleration of the transducers in the test airfoil are assessed in section 2.6.3.

Dysfunctional pressure tap From investigation of the pressure coefficients it was found that one pressure tap was not working correctly. Linear interpolation in surface distance was employed to assign a value from the neighboring pressure taps upstream and downstream from the defect pressure tap.

Trip tape Errors connected to presence of the trip tape. Errors connected to difference in position of trip tape on upper and lower sides of the airfoil.

Incidence The accuracy in determining the angle of attack is investigated in section 2.6.2 below.

Pressure outtakes The pressure outtakes are located downwind of each other, causing a disturbance in the flow as compared with a cross section without pressure outtakes. Burrs in the pressure tap outtakes can introduce additional errors in the measured pressures.

Pressure tube length The time-lag connected with the length of the tubes from pressure outtake to transducer was estimated to $4 \cdot 10^{-4}$, which is small compared to the time between the samples.

¹Root Mean Square: $\sqrt{\langle \cdot \rangle^2}$.

Data processing errors For instance errors connected with integration of the pressure forces or the discretization of the airfoil surface.

Tunnel effects The imposition of the wind tunnel walls causes the flow around a body to differ from the flow as it would have been in an unlimited stream. The corrections proposed in chapter 4 are summarized in section 2.6.4 below.

Statistical Uncertainty The statistical uncertainty connected to the experimental results is investigated in section 2.6.5.

In the sections below key elements from the factors mentioned above are elaborated.

2.6.1 Pressure measuring system

According to the specifications of the electronic pressure scanners, the static errors are within $\pm 0.05\%$ of the full-scale pressure range, which corresponded to worst-case errors on the static C_P values of $\Delta C_P = 0.05$.

In order to minimize zero drift of the pressure transducers with temperature, calibration of the transducers was performed such that a calibration has been performed within half an hour prior to all measurements.

2.6.2 Angle of attack

One of the crucial quantities in any experimental airfoil setup is the angle of attack. Changing the angle of attack required mechanical adjustment to the airfoil suspension. Determination of the angle of attack was done using an inclinometer attached to an inverse mold. The inverse mold was manufactured to fit on the airfoil such that the top of the inverse mold was parallel to the chord of the airfoil. The inclinometer had an angular resolution of 0.1° .

The consistency of the read-outs from the inclinometer was investigated by measuring the angle of attack before and after running a measurement. The difference in the read-out from the inclinometer before and after the experimental run never exceeded 0.1° .

Based on the above discussion, the uncertainty in the measurement of the angle of attack was estimated to no more than 0.2° .

2.6.3 Acceleration of pressure transducers

The systematic errors from acceleration of the pressure transducers were measured by blocking the pressure holes on the airfoil using tape and measure a variety of directions of motion. The results from these initial tests are shown in figure 2.5, where the signal is non-dimensionalized using the two main wind velocities $22m/s$ and $15m/s$, shown in the right and left figures, respectively. It is seen that the systematic errors on the force coefficients connected to the acceleration of the pressure transducers are below 0.0016 and 0.0036 in the case of $V = 22m/s$ and $V = 15m/s$, respectively. Due to the very low level of these errors, a correction for these were not carried out.

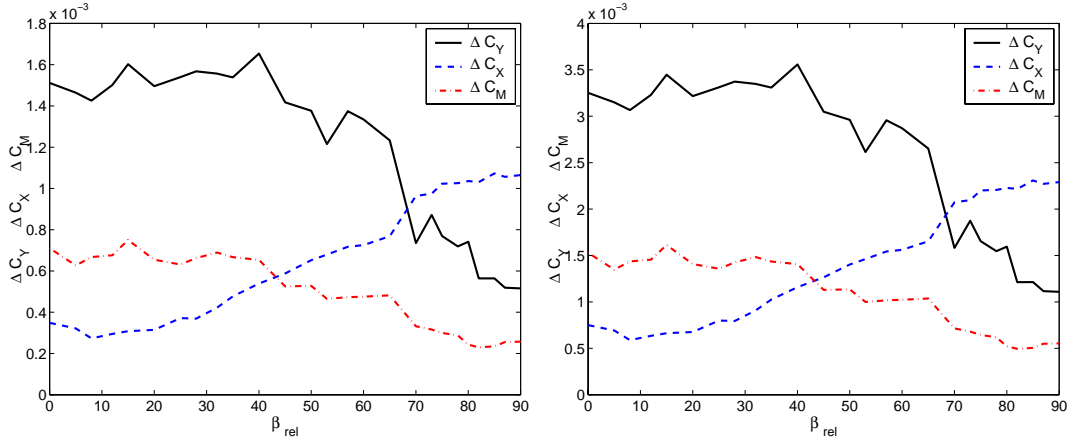


Figure 2.5: Non dimensional force-amplitudes from systematic errors due to acceleration of the pressure transducers. The amplitudes are shown as functions of the direction of motion relative to the airfoil, $\beta_{\text{rel}} = \beta - \alpha$. The signal is non-dimensionalized using the wind velocities 22m/s and 15m/s, shown in the right and left figures, respectively.

2.6.4 Wind tunnel corrections

Another type of errors in wind tunnel testing that may be classified as systematic errors arise due to the presence of the tunnel walls. The imposition of the wind tunnel walls causes the flow around a body to differ from the flow as it would have been in an unlimited stream. The boundary conditions do not match free flow conditions because the velocity component normal to the walls must be zero, and therefore a variety of phenomena occurs.

The effects of wind tunnel blockage can be accounted for with wind tunnel corrections. Wall corrections for steady two dimensional testing can be found in for example Pankhurst and Holder [40], Selig et. al. [46] or Rae and Pope [43].

Due to the unsteady character of the majority of the experiments in the present work, and the lack of wind tunnel corrections for unsteady two dimensional experiments in the literature, unsteady corrections based on results from unsteady panel code calculations are proposed in section 4.1. Summarizing the results for the combined unsteady solid body correction, streamline curvature, and effect of motion, the corrections read

$$C_L^* = \overline{C_{LT}}F_1 + (C_{LT} - \overline{C_{LT}})F_2 \quad (2.20)$$

$$C_M^* = \overline{C_{MT}}F_3 + (C_{MT} - \overline{C_{MT}})F_4, \quad (2.21)$$

where the functions F_1 to F_4 are determined from the potential code simulations. In the general case F_1 and F_3 are functions of the height to chord ratio only, whereas the corrections to the dynamic quantities, F_2 and F_4 depend on the height to chord ratio and reduced frequency. If we restrict ourselves to the experimental set-up of this work, with $h/c = 4.47$, F_1 and F_3 are constants with the values

$$F_1 = \frac{\overline{C_L}}{\overline{C_{LT}}} = 0.9722 \quad (2.22)$$

$$F_3 = \frac{\overline{C_M}}{\overline{C_{MT}}} = 0.8616 \quad (2.23)$$

The dynamic correction terms, F_2 and F_4 , are functions of reduced frequency

$$F_2 = \frac{C_L \text{ Amplitude}}{C_{LT} \text{ Amplitude}} = -3862f_{red}^3 + 346.1f_{red}^2 - 7.400f_{red} + 0.9466 \quad (2.24)$$

$$F_4 = \frac{C_M \text{ Amplitude}}{C_{MT} \text{ Amplitude}} = -4412f_{red}^3 + 340.8f_{red}^2 - 4.508f_{red} + 0.9227. \quad (2.25)$$

The additional correction for the wake blockage is essentially the steady wake blockage correction applied on the corrected unsteady values

$$C_L = C_L^*(1 - 2\epsilon_{wb}) \quad (2.26)$$

$$C_M = C_M^*(1 - 2\epsilon_{wb}). \quad (2.27)$$

The unsteady drag is corrected using the same approach, but including the analytical correction for the solid blocking

$$C_D = C_{DT}(1 - 3\epsilon_{sb} - 2\epsilon_{wb}). \quad (2.28)$$

In equations 2.26 to 2.28, the values of ϵ_{wb} and ϵ_{sb} are given by

$$\epsilon_{wb} = \frac{\Delta V_{wb}}{V_T} = \frac{c/h}{4} C_{DT} \quad (2.29)$$

and

$$\epsilon_{sb} = \frac{\Delta V_{sb}}{V_T} = \frac{K_1 \text{Vol}_{\text{Model}}}{(A_T)^{3/2}}, \quad (2.30)$$

where the mean value of the drag coefficient during the movement cycle is used in equation 2.29 to determine the wake blockage parameter ϵ_{wb} .

2.6.5 Statistical Uncertainty

The uncertainties in an experiment can be classified as random errors or systematic errors. The random errors give rise to uncertainty which can be quantified by statistical methods.

If N discrete measured samples of a quantity, x , is measured

$$x_i, \quad i = 1..N$$

then the mean and variance is given by

$$X = \sum_{i=1}^N \frac{x_i}{N} \quad (2.31)$$

$$\overline{x'^2} = \sum_{i=1}^N \frac{x'_i{}^2}{N} \simeq \sigma^2, \quad (2.32)$$

where the fluctuating part, x'_i , of the quantity is given by

$$x'_i = x_i - X. \quad (2.33)$$

The standard deviation of the mean value is

$$s(X) = \frac{\sigma}{\sqrt{N_{eff}}}. \quad (2.34)$$

In equation 2.34 N_{eff} signifies the effective number of statistically independent samples in the samples. This is given by

$$N_{eff} = \begin{cases} N/(2\tau f_s) & \text{for } 2\tau f_s > 1 \\ N & \text{for } 2\tau f_s \leq 1 \end{cases}. \quad (2.35)$$

In the equation above, f_s and τ signifies the sampling frequency and integral time scale, respectively. Equation 2.35 is based on the assumption that two samples are considered statistically independent if the time between these equals, or is greater than, 2τ . The integral time scale, τ , can be estimated from an autocorrelation as the time to the first zero.

If a gaussian distribution is assumed for x'_i , then the 95% confidence interval is given by $X \pm 2s(X)$.

A worst-case 95% confidence interval was computed for the steady experiments. The computations were based on the most unfavourable combinations of σ and N_{eff} in the steady experiments.

$$\text{Conf}_{95\%}(\overline{C_L}) = \overline{C_L} \pm 0.01 \quad (2.36)$$

$$\text{Conf}_{95\%}(\overline{C_D}) = \overline{C_D} \pm 0.004 \quad (2.37)$$

These result shows that the level of the statistical uncertainty in the steady experiments is very low.

The corresponding statistical confidence level for the force loops in the unsteady experiments was obtained by assuming, that the force level at one instant in the oscillation cycle is statistically independent of the force level the previous oscillation cycle at the same position. This was assumed because $2\tau f_{mov} < 1$ for all computed τ from the steady experiments, leading to $N_{eff} = \Delta T f_{mov} = 144$. Based on these results and the variance of the forces at fixed positions in the oscillation cycle, the statistical worst-case 95% confidence interval for the unsteady experiments is

$$\text{Conf}_{95\%}(\overline{C_{L,mov}}) = \overline{C_{L,mov}} \pm 0.014 \quad (2.38)$$

$$\text{Conf}_{95\%}(\overline{C_{D,mov}}) = \overline{C_{D,mov}} \pm 0.0033 \quad (2.39)$$

These result shows that the level of the statistical uncertainty in the unsteady experiments is of the same order of magnitude as the static results. However, it should be noted that the statistical uncertainty for some specific stall modes which appeared for a small number of oscillation cycles, may be up to four times higher than for the quantities which are computed from oscillation cycles through an entire time-span of the experimental run.

2.7 Multiple stall

As mentioned in the introduction to this chapter, the phenomenon known as multiple stall occurred in the experiments. Multiple stall, also known as double stall, is characterized by at least two different distinct stall modes for identical inflow conditions. According to McCullough et. al. [33], three different types of stall exist

- Trailing-Edge Stall. Typically appearing on thick airfoils. An increase in the angle of attack moves the turbulent separation point towards the leading-edge.
- Leading-Edge Stall. Typically appearing on airfoils of moderate thickness.
- Thin-Airfoil Stall. Appears on sharp-edge airfoils and airfoils with small leading-edge radius, generally airfoils less than 9% thickness.

Figure 2.6 shows a sketch of the lift characteristics of the three stall types. For some

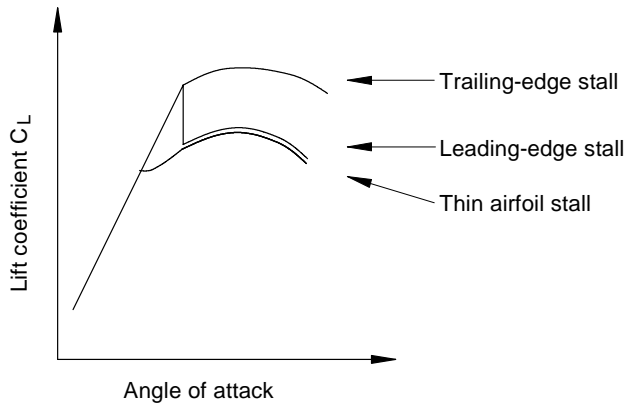


Figure 2.6: *Stall characteristics of the three types of stall. From [4].*

airfoils of intermediate thickness ratios, both leading-edge and trailing-edge stall can occur. This was investigated by Gault [15], who correlated the different types of stall with Reynolds number and a single airfoil ordinate at the leading edge, $y_{0.0125c}$, defined as the upper-surface ordinate at 1.25% chord-length from the leading edge measured in chord-lengths. For the NACA 0015 airfoil, this quantity is $y_{0.0125c} = 0.0237$. The stalling characteristics of NACA airfoil sections are shown in figure 2.7 correlated with Reynolds number and $y_{0.0125c}$.

From the figure it seems likely that a NACA 0015 profile should experience trailing edge stall only. The investigations by Gault, however, were focusing on Reynolds numbers above 10^6 , and therefore did not have any measurements on airfoils in the range of Reynolds numbers below $0.7 \cdot 10^6$. The maximum obtainable Reynolds number for the current experiment is $Re = 0.55 \cdot 10^6$, which falls in the region not investigated by Gault.

In recent years, attention has been given multiple stall again because of the implications it may have on in particular the stall regulated wind turbines. Observations of the power production on a number of stall regulated wind turbines have shown that several distinct power levels can occur for identical inflow conditions. This involves

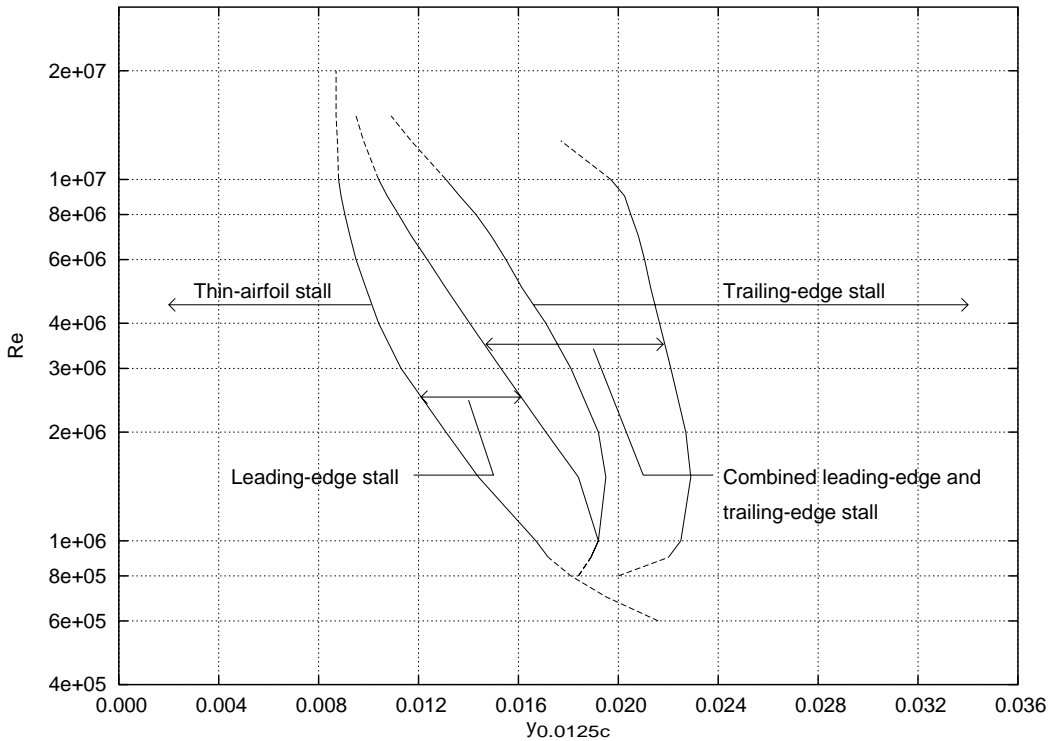


Figure 2.7: *Stalling characteristics of NACA airfoil sections correlated with Re and $y_0.0125c$. From [4].*

significant uncertainty on power production and loads. In some cases, the difference in loads for the different levels can be up to 25% [2].

Bak et al. [4] suggests that the cause for the different levels in the power production on the wind turbine is linked to a laminar separation bubble at the leading edge of the rotors. Figure 2.8 show the laminar separation bubble on a NACA 63₂-215 airfoil at 15° incidence computed using a Navier-Stokes code. According to Bak et. al., three different levels of the lift is possible for identical inflow conditions. The first level is characterized by a very high lift. In this case the flow is fully turbulent and no laminar separation bubble exist. The second level has a moderately high lift, but this time the flow at the leading edge of the airfoil is laminar, and a laminar separation bubble exist near the suction peak of the airfoil. The transition to turbulent flow occurs on top of the separation bubble which ensures that the flow reattaches. The lift of the second mode is slightly lower due to the presence of the laminar separation bubble. According to Bak et. al. bursting of this bubble can appear if the transition point moves downstream of the critical transition point, which is the point where the flow cannot reattach to the surface but separates from the leading edge. For both high lift levels trailing-edge stall is present. The third lift level is significantly lower than the two other levels due to the massive separation starting from the leading edge.

Figure 2.9 shows C_p curves associated with the three different stall modes. The fully turbulent C_p -curve (solid line) in figure 2.9 corresponds to the situation with a fully attached flow, resulting in a high suction peak and high lift. The free transition curve, shown with a dashed line, corresponds to a laminar separation bubble at the leading edge, as shown in figure 2.8. The effect of this laminar separation bubble is the reduc-

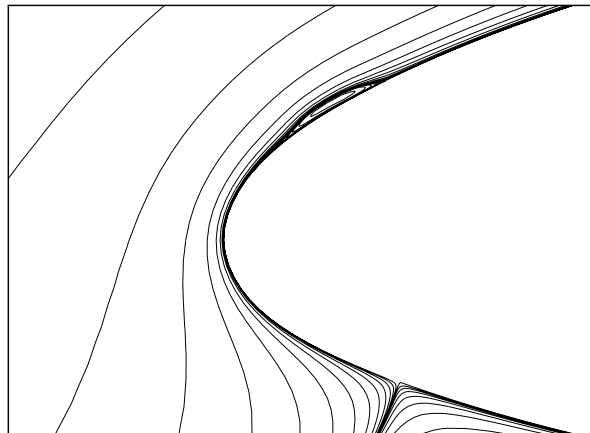


Figure 2.8: Streamlines showing a laminar separation bubble on a NACA 63-215 airfoil. $\alpha = 15^\circ$ and $Re = 1.15 \cdot 10^6$. From [3].

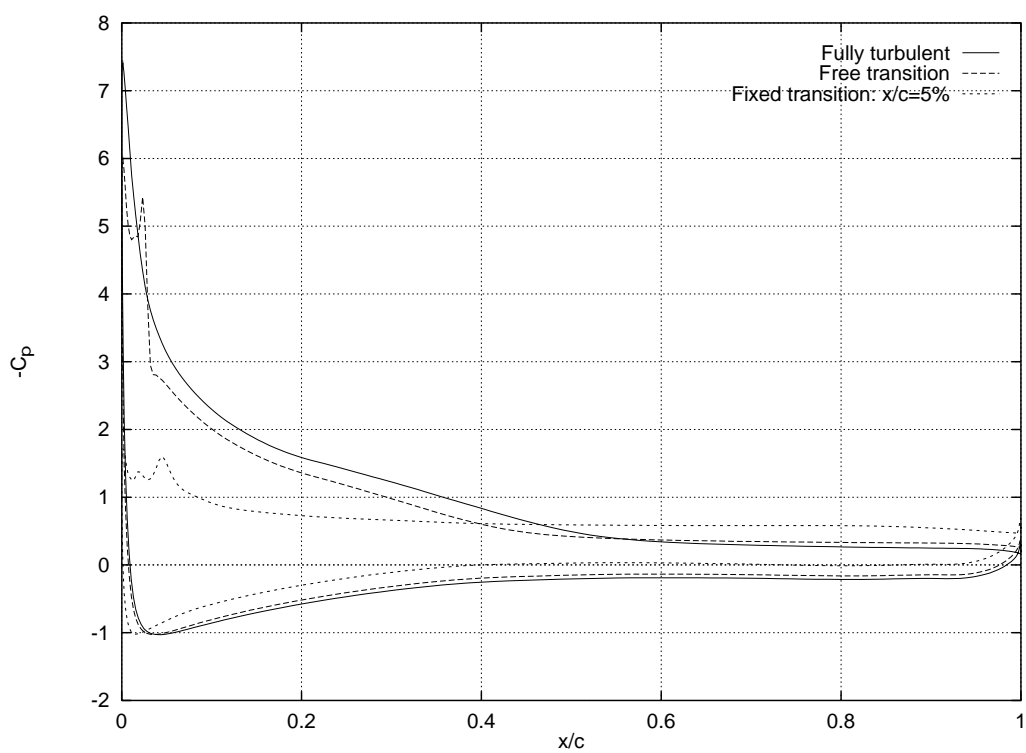


Figure 2.9: C_p -curves for a NACA 63-215 airfoil at $\alpha = 15^\circ$ and $Re = 1.15 \cdot 10^6$. From [4].

tion of the suction peak and the level of the $-C_p$ curve on the suction side, reducing the lift on the airfoil. Finally, the fixed transition curve (dotted line) corresponds to leading edge stall.

Experimental results showing at least three distinct different levels for a stationary airfoil have been reported by Bak and Fuglsang [2].

2.8 Results

In this section the main results from the steady and unsteady experiments are presented. Preliminary results from the experiments have been shown previously in [18] and [19]. The presentation is split up in three parts. The first part concerns determination of the different stall modes. After this the results from the static experiments are presented. Finally, the results from the main part of the experimental work, the unsteady experiments, are shown.

The unsteady experiments consist of three parts:

- Influence of angle of attack and direction of movement on the dynamic loads at $Re = 555000$ and $Re = 383000$.
- Influence of the amplitude of the motion on the dynamic loads for four different combinations of reduced frequency and angle of attack.
- Influence of the reduced frequency on the dynamic loads for four different combinations of angle of attack and direction of movement.

As mentioned above, only the main experimental results are shown in this section. More detailed experimental results are shown in chapter 4, in the comparison of results obtained with theoretical models with the experimentally obtained results.

2.8.1 Determination of distinct stall modes

As mentioned previously, the phenomenon known as multiple stall occurred in some of the experiments where the incidence of the airfoil was between $\alpha = 15^\circ$ and $\alpha = 20^\circ$. The upper graphs in figure 2.10 show the time-series of the non-dimensional forces perpendicular to the chord, C_Y , and in the chordwise direction, C_X , as well as the velocity in the tunnel. Note that the positive direction for C_X is towards the trailing edge. It is seen that (at least) three distinctly different levels, or modes, are present in the forces. Three periods where different levels occur are outlined in the figure with the letters A, B and C.

Figure 2.10 shows that the flow velocity during the experiment was fairly constant, slightly above 22 m/s. It is clear that the drastic jump in the forces is not caused by changes in the free-stream velocity.

The lower graph in figure 2.10 show the non-dimensional pressure coefficients corresponding to the stall modes labelled A, B and C in the upper part of the figure.

Stall mode A is characterized by a low C_Y -value and a clearly positive C_X -value. The C_P curve shows a constant value on the suction side of the airfoil. This indicates massive stalling from the leading edge, so-called leading edge stall.

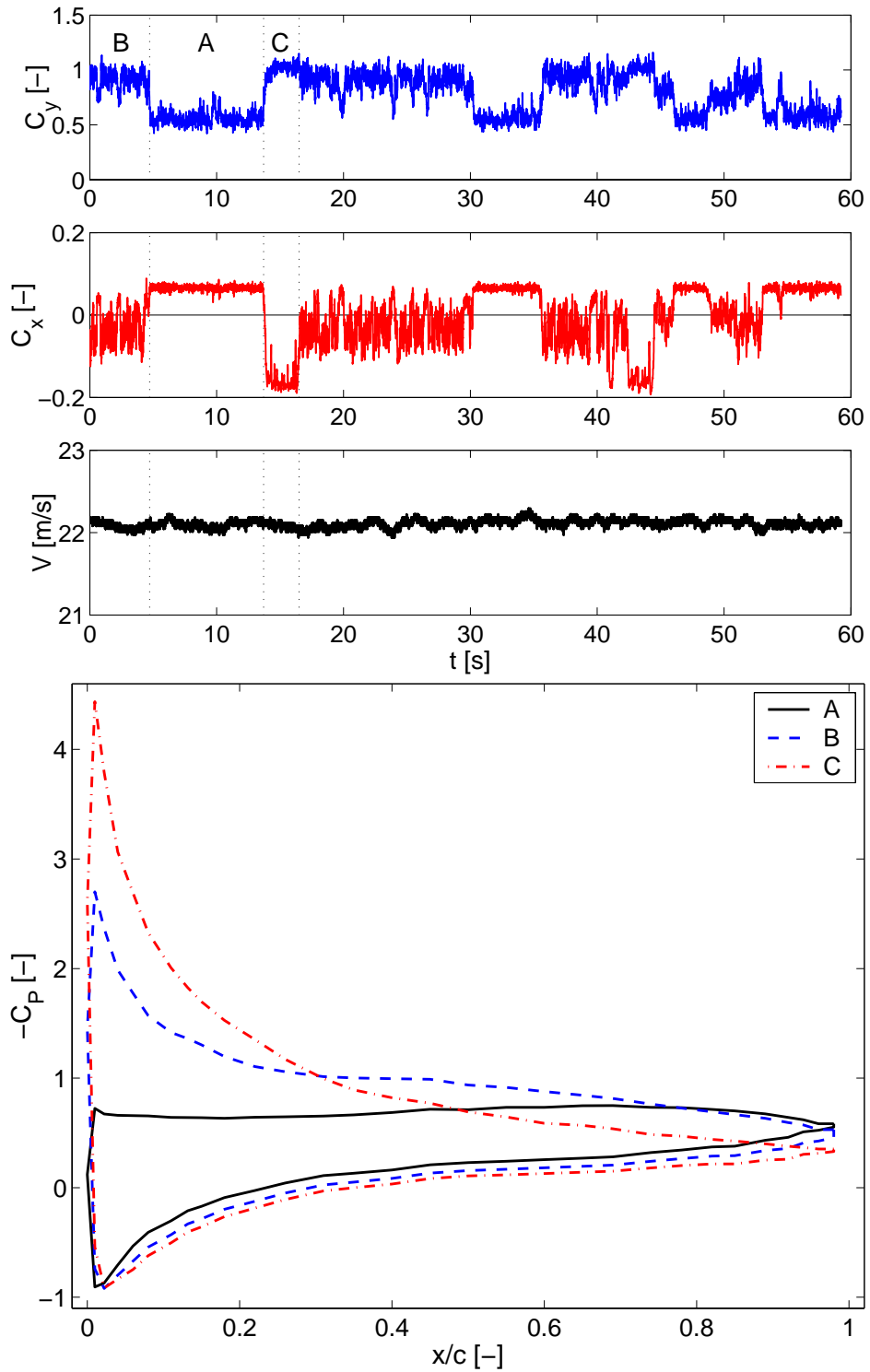


Figure 2.10: *Multiple stall on a stationary NACA 0015 airfoil at $\alpha = -15^\circ$ and $Re = 555000$. The upper graphs show the measured non-dimensional forces perpendicular to, and in the chordwise direction, as well as the velocity in the tunnel. The lower figure shows the pressure coefficients corresponding to the three distinct levels.*

The pressure coefficient for the next stall mode, labelled B in the figure, has a suction peak approximately 1% from the leading edge which dramatically increases the forces perpendicular to the chord, C_Y , and reduces the forces in the direction of the chord, C_X , compared to stall mode A. The mean value of C_X in this case is close to zero, and the fluctuations of C_X are much greater than for the other two stall modes.

The last stall mode, level C, has an even stronger suction peak than stall mode B, which further increase the level of C_Y and decrease the level of C_X to strictly negative values.

On the basis of these results it is clear that (at least) three distinct different stall modes are present for identical inflow conditions. This corresponds well to the explanation of the phenomenon given in section 2.7.

When computing the lift for the three different stall modes, it was seen that stall mode A corresponds to a fairly low lift, whereas stall modes B and C corresponds to a high and a very high lift level, respectively. The lift levels of the three different stall modes are used to name the modes. With this nomenclature, stall modes A, B and C are referred to as the low, high and very high stall mode in the remainder of this work.

A comparison of the dynamic behavior of the forces for the three different stall modes show that the fluctuation in the forces are greatest for the high stall mode. According to the findings of Bak et. al. [3], this level corresponds to the case with a separation bubble at the leading edge of the airfoil. It seems likely that the location of such a separation bubble might influence the forces on the airfoil a great deal, such that the greater oscillations of the forces in this case could be explained by movement of this bubble due to interaction with the trailing edge stall or imperfections in the inflow.

The characteristics of C_X and C_Y for the different stall modes explained above were used to classify the stall modes occurring in all steady and unsteady experiments for incidences in the interval between $\alpha = 15^\circ$ and $\alpha = 20^\circ$.

Figure 2.11 show an example where multiple stall occur for unsteady 1 DOF translatory motion of the airfoil. In the upper graphs, where C_L , C_D and C_M are shown as functions of time, three distinct levels are recognized. It is seen that the disturbance from the motion of the airfoil does not cause the stall modes to shift with the frequency of the motion. This indicate that the stall modes are fairly insensitive to perturbations in the sense that it is not easy to force the flow from one stall mode to another by disturbing the flow.

What triggers the shift from one stall mode to another is unknown to the author. From the figure it is seen that the low stall mode can be found for instance from $t = 33$ s to $t = 37$ s, the high stall mode from $t = 40$ s to $t = 50$ s, and the very high stall mode from $t = 4$ s to $t = 12$ s. The level of the lift for the different stall modes are in agreement with the names of the stall modes, whereas the mean drag levels are in opposite order, i.e. the drag of the very high stall mode is lowest, and the drag level of the low stall mode is highest. It is noted that the mean moment coefficients for the low and high stall modes are almost identical, close to $C_M = -0.05$, whereas the mean moment coefficient for the very high stall mode is positive, $C_M = 0.02$. This is caused by the difference in the distribution of the forces on the airfoil.

Analogous to the non-moving case, the oscillations of the high stall mode forces are

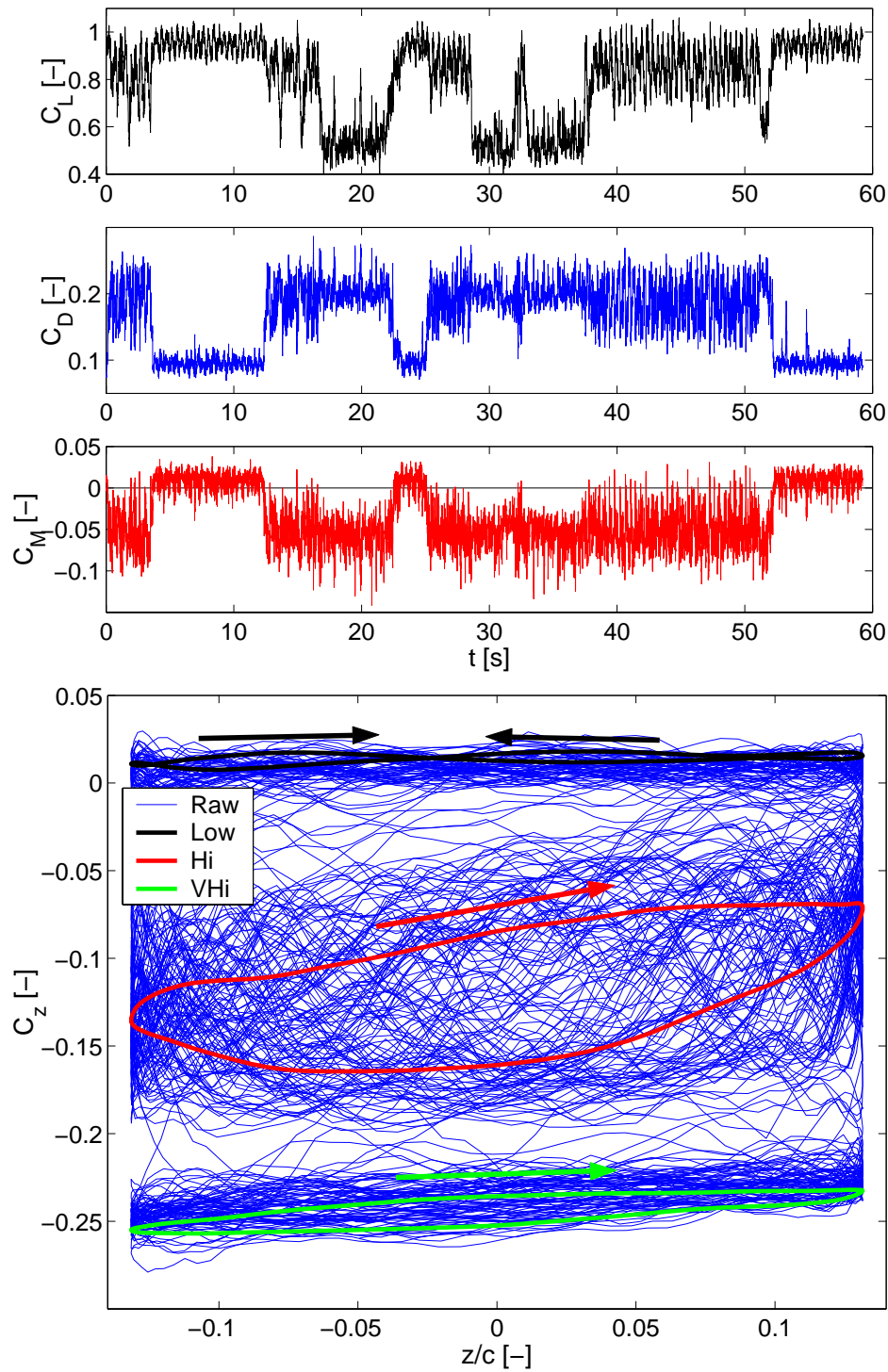


Figure 2.11: *Multiple stall occurring in a unsteady experiment. Upper graphs show histories of lift, drag and moment coefficients in time. The lower graph show the non-dimensional force component in the direction of the motion versus non-dimensional displacement. $\alpha = 15^\circ$, $\beta = 110^\circ$, $f_{red} = 0.02$ and $Re = 555000$.*

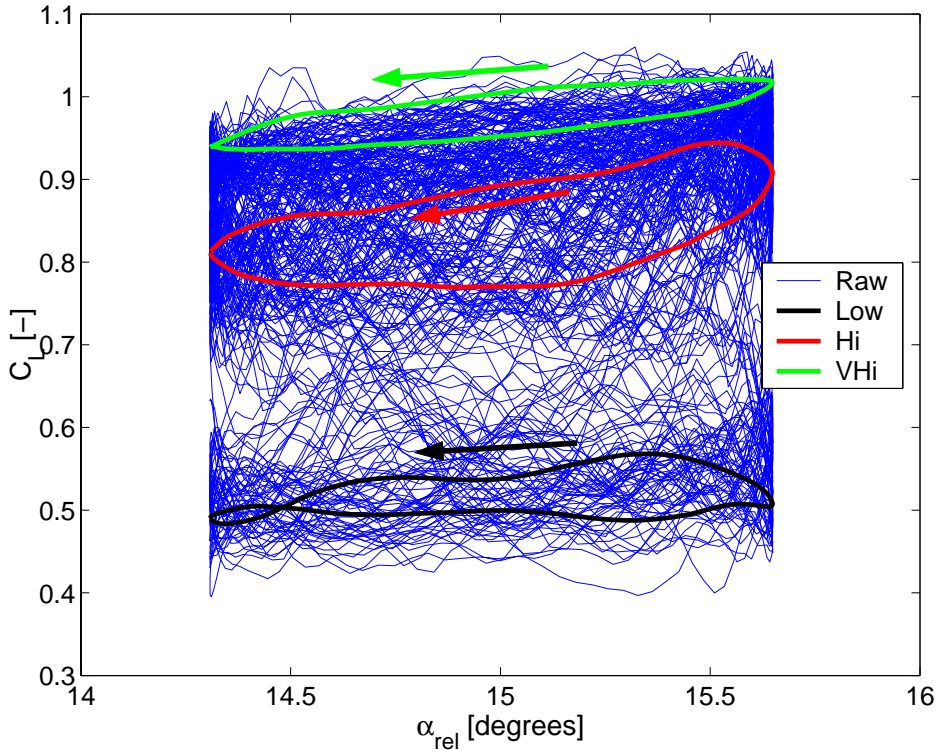


Figure 2.12: *Lift coefficient versus relative angle of attack for the results shown in figure 2.11.*

greater than the oscillations of the forces in the other stall modes.

In the lowest graph of figure 2.11, the time-series are shown as the force coefficient in the direction of the motion, C_Z , versus the non-dimensional displacement of the airfoil. The thin curve corresponds to the instantaneous non-dimensional force component, whereas the thicker curves correspond to the mean non-dimensional force loops for the different stall modes. Since the direction of the force-component and the direction of the motion are identical, the direction and openness of the hysteresis loops show the sign and magnitude of the work carried out during one oscillation cycle. As shown previously, the work carried out during one oscillation cycle is proportional to the aerodynamic damping. The clockwise direction of the hysteresis loops indicate that energy is pumped into the airfoil system by the fluid. From this it is seen that the aerodynamic damping of the three different stall modes differ significantly in this case. The aerodynamic damping of the low stall mode is close to zero, whereas the damping of the high and very high stall modes is negative. The most negative aerodynamic damping is obtained for the high stall mode.

The lift coefficient for the same case is shown in figure 2.12 as function of the relative incidence, α_{rel} . Here it is seen that the mean slopes of these curves are all different.

The conclusions that can be drawn from the investigations is that both mean and dynamic characteristics differ from one stall mode to another in spite of the identical boundary conditions.

2.8.2 Stationary airfoil

Even though this work focuses on the behavior of the flow about a translatory moving airfoil, measurements on a stationary airfoil was carried out as well to obtain information on the steady characteristics of the NACA 0015 airfoil with the current experimental setup.

Non-dimensional pressure coefficients for the NACA 0015 airfoil at incidences $\alpha = 3^\circ, 5^\circ, 8^\circ, 10^\circ, 12^\circ, 15^\circ, 20^\circ$ and 25° are shown in figure 2.13 for $Re = 555000$. It is seen that a bump is located on the suction side of the airfoil for incidences up to $\alpha = 12^\circ$. The location of the bump corresponds to the position of the trip-tape, and is probably caused by the local disturbance in the flow by the trip-tape. Likewise, there is a bump on the pressure side of the C_P curves for $\alpha = 20^\circ$ and $\alpha = 25^\circ$, which could also be explained by the disturbing effect of the trip-tape.

Multiple stall modes were observed in the $\alpha = 15^\circ$ and $\alpha = 20^\circ$ cases. In the $\alpha = 25^\circ$ case, only one stall mode exist. This is a massively separated leading edge stall, corresponding to the low stall mode found in both the $\alpha = 15^\circ$ and $\alpha = 20^\circ$ cases. The pressure coefficient profiles of the high stall modes at these incidences does not look similar, but the characteristics of the C_X and C_Y values in these cases were similar. The characteristics of the C_X and C_Y values for incidences below $\alpha = 12^\circ$ corresponds to the very high stall mode.

The mean pressure coefficient curves shown in the cases where multiple stall occur are connected with a very high degree of uncertainty. The sampling time for all the experiments carried out were 60 seconds. As shown in the previous section, this is not long compared to the time one specific stall mode exist in the measurements. This implies that the total sampling time needed in determining the mean C_P values with a higher level of accuracy would be somewhat longer than 60 seconds.

Figure 2.14 show the lift, drag and moment coefficients for incidences ranging from $\alpha = 0^\circ$ to $\alpha = 30^\circ$.

In the figure, the force and moment coefficients corresponding to the different stall modes are shown. The blue, red and black curves corresponds to the low, high and very high stall modes, whereas the green curve corresponds to the mean level of the entire measured run, $\Delta t = 60$ s. The curves shown to the left are at Reynolds number $Re = 383000$, whereas the right curves are at $Re = 555000$.

The slope of the lift curves in the linear region is 75% ($Re = 383000$) and 81% ($Re = 555000$) of $\pi^2/90$, as predicted by potential flow theory. This is attributed to the relatively low Reynolds number. Similar effects are observed in other experiments at similar Reynolds numbers, for example Selig et. al. [46].

Multiple stall modes occurred at $\alpha = 15^\circ$ for the case with $Re = 383000$. This effect was more pronounced in the $Re = 555000$ case, where multiple stall modes occurred between $\alpha = 15^\circ$ and $\alpha = 20^\circ$.

The mean lift reaches a local minimum at $\alpha = 20^\circ$ at both investigated Reynolds numbers, and in both cases the maximum lift was obtained at $\alpha = 15^\circ$, with the actual maximum value of the lift coefficient being slightly higher for $Re = 555000$ than for $Re = 383000$.

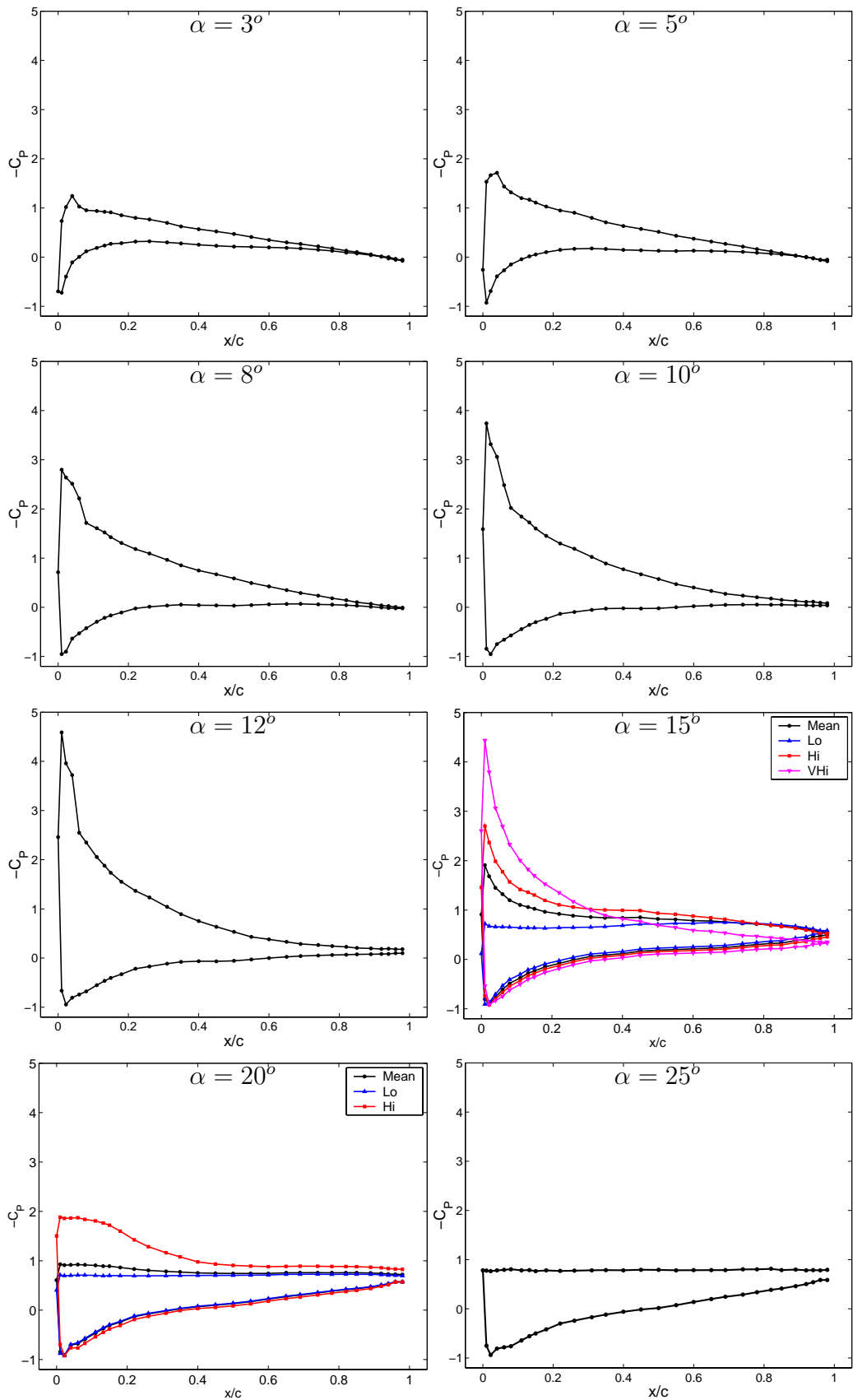


Figure 2.13: Mean $-C_P$ curves for a stationary NACA 0015 airfoil at various incidences, α . $Re = 555000$.

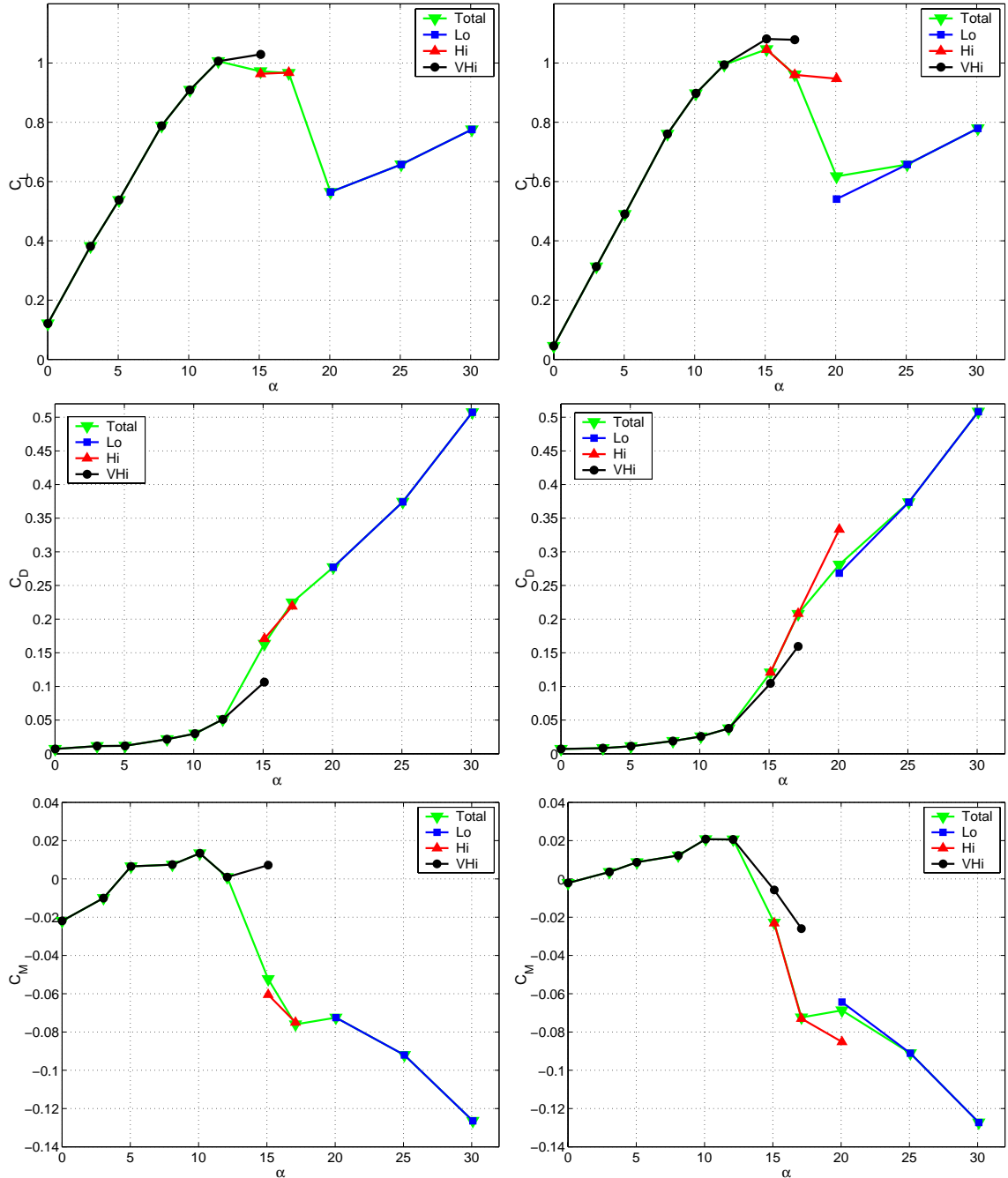


Figure 2.14: Steady C_L (upper), C_D (middle) and C_M (lower) curves for $Re = 383000$ (left) and $Re = 555000$ (right). The green curves corresponds to the mean measured level, whereas the blue, red and black curves corresponds to the low, high and very high stall modes, respectively.

The measured lift coefficient at zero incidence, $\alpha = 0^\circ$, was $C_L = 0.12$ for $Re = 383000$ and $C_L = 0.04$ for $Re = 555000$. Since the NACA 0015 airfoil is symmetric, the lift coefficient should be zero at zero incidence. The deviation from this, which in the $Re = 383000$ case is quite substantial, could be attributed to a number of the factors listed in the section on measurement accuracy. Since the forces on the airfoil are non-dimensionalized using the squared wind velocity, any error due to drift of the zero level of the transducers give rise to errors $22^2/15^2 = 2.15$ times greater in the $Re = 383000$ (15 m/s) case than in the $Re = 555000$ (22 m/s) case. This indicate that a substantial part of the error in the measured forces are due to drift of the zero of the pressure transducers.

Another error that could cause an apparent offset in the lift curves would be inaccurate measurement of the angle of attack, α . The offset corresponding to the errors in the $Re = 383000$ and $Re = 555000$ cases would be 1.06° and 0.36° , which on an airfoil is not detectable by eye. According to the inclinometer used in the experiments, the angle of attack did not change more than 0.1° during any of the runs in the experiment including the unsteady ones. This is an indication that the measured values of the angle of attack were consistent. However, this does not guarantee that there was no systematic errors biasing the values to one side throughout the measurements.

The last of the three circumstances which the author believes to be the main causes of the offset of the lift curve at $\alpha = 0^\circ$ is the difference in positions of the trip-tape. The disturbances from the trip tape may be very different on different sides of the airfoil on the pressure taps near the tape due to the difference in the position of it. It is not known whether this effect increases or decreases with the Reynolds number.

When the drag curves for the two different Reynolds numbers are compared, it is seen that the level of the drag coefficients are quite similar for both Reynolds numbers in the attached region, from $\alpha = 0^\circ$ to $\alpha = 10^\circ$, and in the deeply stalling region, from $\alpha = 25^\circ$. Comparison of the results between these regions show that the increase in the mean drag coefficient occur earlier in at the lower Reynolds number. The increase in the drag corresponds to the onset of stall, indicating that the onset of stall is reached slightly earlier at the lower Reynolds number than at the higher one.

From the cases where multiple stall modes occur, it is seen that the drag of the high stall mode is higher than the drag of the low and very high stall modes.

Since the forces obtained from these measurements are the pressure forces only, it should be noted that the true drag is slightly higher than the shown values at small incidences due to viscous forces. The effect of this is investigated in section 4.4.1 using a Navier-Stokes code.

The moment curves, shown in the lower graphs in figure 2.14, show an offset at $\alpha = 0^\circ$ in the case where $Re = 383000$. The explanation to this could be two of the three circumstances believed to be the main causes of the offset of the lift curves at $\alpha = 0^\circ$, namely drifting of the pressure levels from the pressure transducers and errors connected to the difference in position of the trip tape.

In general, the moment curve for the $Re = 383000$ case seems more noisy than for the $Re = 555000$ case. This is attributed to the drifting problem as well.

The offset in the moment curve at $\alpha = 0^\circ$ for the $Re = 555000$ case is very close to zero.

A comparison of the moments connected with the different stall modes show that the moment of the high stall mode is lower (more negative) than for the low and very high stall modes.

It should be stressed that the force levels of the different stall modes are not determined with as high certainty as in the cases where multiple stall did not occur. This is especially true for the mean values in these cases.

2.8.3 1 DOF translatory oscillatory motion

The detailed information from the pressure distribution in time yields valuable insight into the physics of the flow, but due to the vast amounts of data in the raw signals, they have to be processed to extract information about the dynamic features of the flow.

In order to give an impression of the force loops in the attached case, figure 2.15 and 2.16 show the time histories and force loops at $\alpha = 5^\circ$, $\beta = 0^\circ$, $Re = 555000$ and $f_{red} = 0.02$. The figures show the same quantities as the figures showing the time series and force coefficient loops for the case with double stall, figures 2.11 and 2.12. From figures 2.15 and 2.16 it is seen that the fluctuations of the forces around the mean period force on the airfoil in the attached case are quite small. Furthermore, it is observed that the aerodynamic damping in this case is positive because the direction of the loop shown in the lowest graph of figure 2.15 is counter-clockwise. This means that the fluid in this case is transferring energy from the motion of the airfoil into the flow, corresponding to a positive aerodynamic damping. The integral of the curve is proportional to the amount of work produced by the fluid on the wing per oscillation, which is proportional to the aerodynamic damping.

Figure 2.16 shows the non-dimensional force component in the direction of the motion versus the relative angle of attack. The non-dimensional force component is in this case is identical to the lift coefficient since the motion of the airfoil is perpendicular to the free-stream. It is seen that the value of the lift coefficient is lagging the relative angle of attack. This hysteresis effect is caused by the unsteady wake shed from the trailing edge of the airfoil. This effect is investigated later in this thesis, and comparison of various hysteresis loops with theoretical models are undertaken in chapter 4.

Despite the relatively big uncertainties on the mean quantities in the steady case, it is seen that the scatter of the dynamic values are quite low. On the basis of this, it is suspected that the dynamics of the flow can be captured quite well using the present experimental setup.

One of the main objectives of the experimental investigation concerns localization of the minimum aerodynamic damping for parameters of the motion similar to the ones encountered by real wind turbines.

An investigation of the influence of the angle of attack and direction of movement on the aerodynamic damping and added mass was undertaken by carrying out the experiments in the test matrix shown graphically in figure 2.17. All experiments in this test matrix was carried out for reduced frequencies $f_{red} = 0.02$ and $f_{red} = 0.03$, corre-

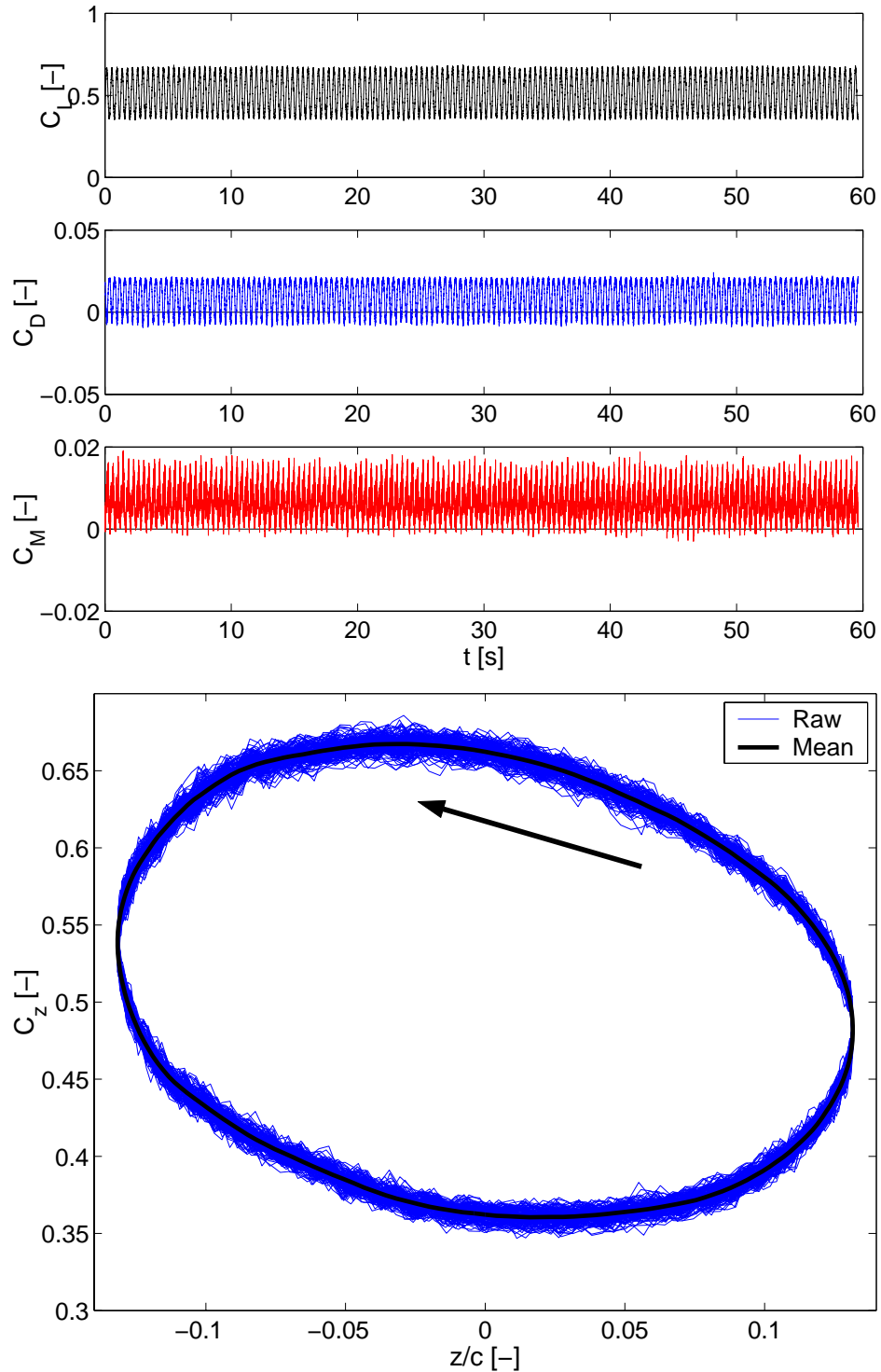


Figure 2.15: *Unsteady experiment, attached flow. The upper graphs show histories of lift, drag and moment coefficients in time. The lower graph show the non-dimensional force component in the direction of the motion versus non-dimensional displacement. $\alpha = 5^\circ$, $\beta = 0^\circ$, $f_{red} = 0.02$ and $Re = 555000$.*

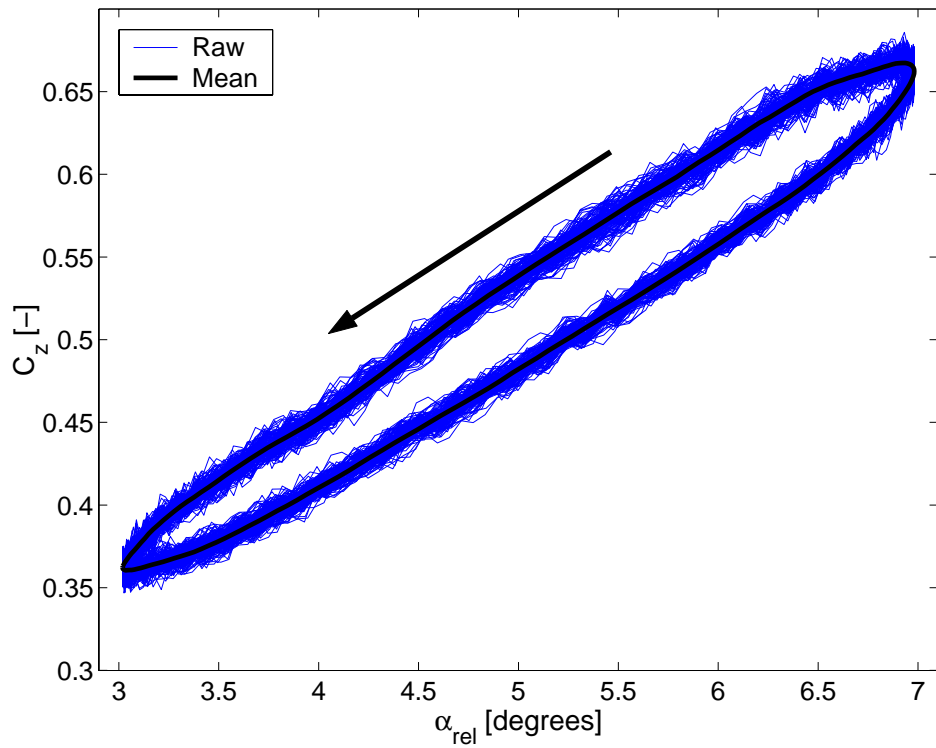


Figure 2.16: Force coefficient in the direction of the motion versus relative angle of attack for the results shown in figure 2.15. Note that in this case, where $\beta = 0^\circ$, this is identical to the lift coefficient.

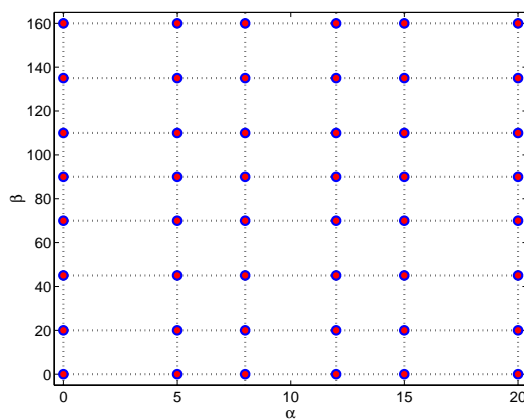


Figure 2.17: Test matrix for investigation of the influence of movement direction, β , and angle of attack, α , on the aerodynamic characteristics.

sponding to Reynolds numbers $Re = 555000$ and $Re = 383000$. The non-dimensional amplitude of the motion was set to $A/c = 0.1316$. An overview of the dynamic characteristics of the flow is shown in figure 2.18. The non-dimensional aerodynamic

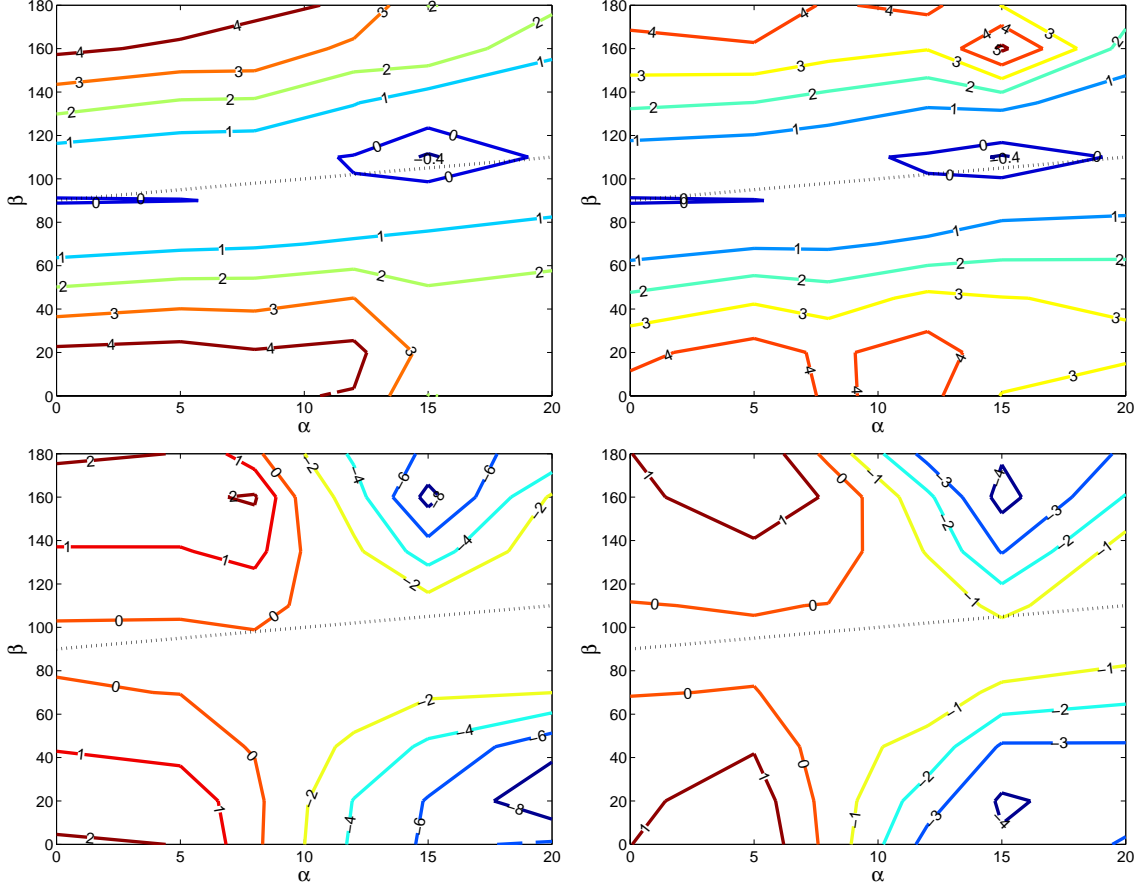


Figure 2.18: Non-dimensional aerodynamic damping (upper) and non-dimensional added-mass (lower) as functions of α and β . The left graphs are at reduced frequency $f_{red} = 0.02$, corresponding to Reynolds number $Re = 555000$. The right graphs are at $f_{red} = 0.03$ corresponding to Reynolds number $Re = 383000$. The shown coefficients for $\alpha \geq 15^\circ$ are based on the mean period forces of the flow. The chordwise direction is inferred by the dashed line.

damping, C_{DA} , and the non-dimensional added-mass, C_{MA} , are shown as functions of α and β at reduced frequencies $f_{red} = 0.02$ and $f_{red} = 0.03$.

It should be noted, that the coefficients for $\alpha \geq 15^\circ$ are based on the mean period forces of the flow in the measured time-span, and does not account for effects of the multiple stall modes encountered in several of the data-points. The effect of this is investigated later.

Inspection of the features of the non-dimensional aerodynamic damping reveals that the minimum in the aerodynamic damping at both reduced frequencies occurs close to the chordwise direction just after stall at 15° incidence, in agreement with full scale observations on real wind turbines [41].

The aerodynamic damping is positive for incidences below $\alpha = 10^\circ$ at both reduced

frequencies, with the maximum value of the damping in the direction perpendicular to the free-stream.

Except for the positive peak at $\alpha = 15^\circ$ and $\beta = 160^\circ$ for $f_{red} = 0.03$, the general shape of the non-dimensional aerodynamic damping is quite similar at the two different reduced frequencies, with the values generally slightly lower in the case of $f_{red} = 0.03$. The details regarding the peak value in the aerodynamic damping is linked to the multiple stall modes, which is investigated later.

The non-dimensional added mass is shown in the lower graphs of figure 2.18. It is seen that positive values are found at low incidences, and negative values at the high angles of attack, where the flow is stalling. Generally, the absolute value of the added mass increases with the component of the motion perpendicular to the free-stream. The absolute value of the non-dimensional added mass is higher at $f_{red} = 0.02$ than it is at $f_{red} = 0.03$.

Analog to the non-dimensional aerodynamic damping, the general shape of the non-dimensional added mass is similar for the two reduced frequencies except for the location of the lower negative peak at the high angles of attack.

It was shown previously that the dynamics of the multiple stall modes can differ considerably for the different stall modes even though the geometric angle of attack is identical. Therefore non-dimensional dynamic coefficients of the flow for $\alpha \geq 15^\circ$ are shown in figures 2.19 and 2.20.

From figure 2.19 which shows the non-dimensional aerodynamic damping as a function of direction of the motion for $\alpha = 15^\circ$ (upper) and $\alpha = 20^\circ$ (lower), it is seen that the damping characteristics of the different stall modes are practically identical at $\alpha = 20^\circ$. However, there is a dependence on the stall modes at $\alpha = 15^\circ$. In the $f_{red} = 0.02$ case, the aerodynamic damping of the high stall mode is significantly lower than the aerodynamic damping of the other stall modes, which are comparable in magnitudes. Since this particular stall mode only appeared in two data-points, it is not possible to determine if this is a general feature of this stall mode at this incidence. As seen in the previous figure, the minimum aerodynamic damping occurs at $\alpha = 15^\circ$ and $\beta = 110^\circ$ at both reduced frequencies. The most negatively damped stall mode is the high stall mode.

In the case of $\alpha = 15^\circ$ and $f_{red} = 0.03$ it is seen that the maximum non-dimensional aerodynamic damping occur at $\beta = 160^\circ$, caused by the high stall mode.

The data-set is too limited to determine whether the direction of the motion determines which stall modes are present.

By viewing the pressure profile histories for the cases with negative aerodynamic damping it was observed that the negative aerodynamic damping was not caused by large-scale vortices being shed from the leading edge at some fixed time in the period of the oscillation cycle. It was observed that the negative aerodynamic damping was not caused by shifting from stall mode to stall mode at up/down-stroke either.

Figure 2.20 shows the non-dimensional added mass corresponding to the non-dimensional aerodynamic damping shown in the previous figure. It is seen, that except

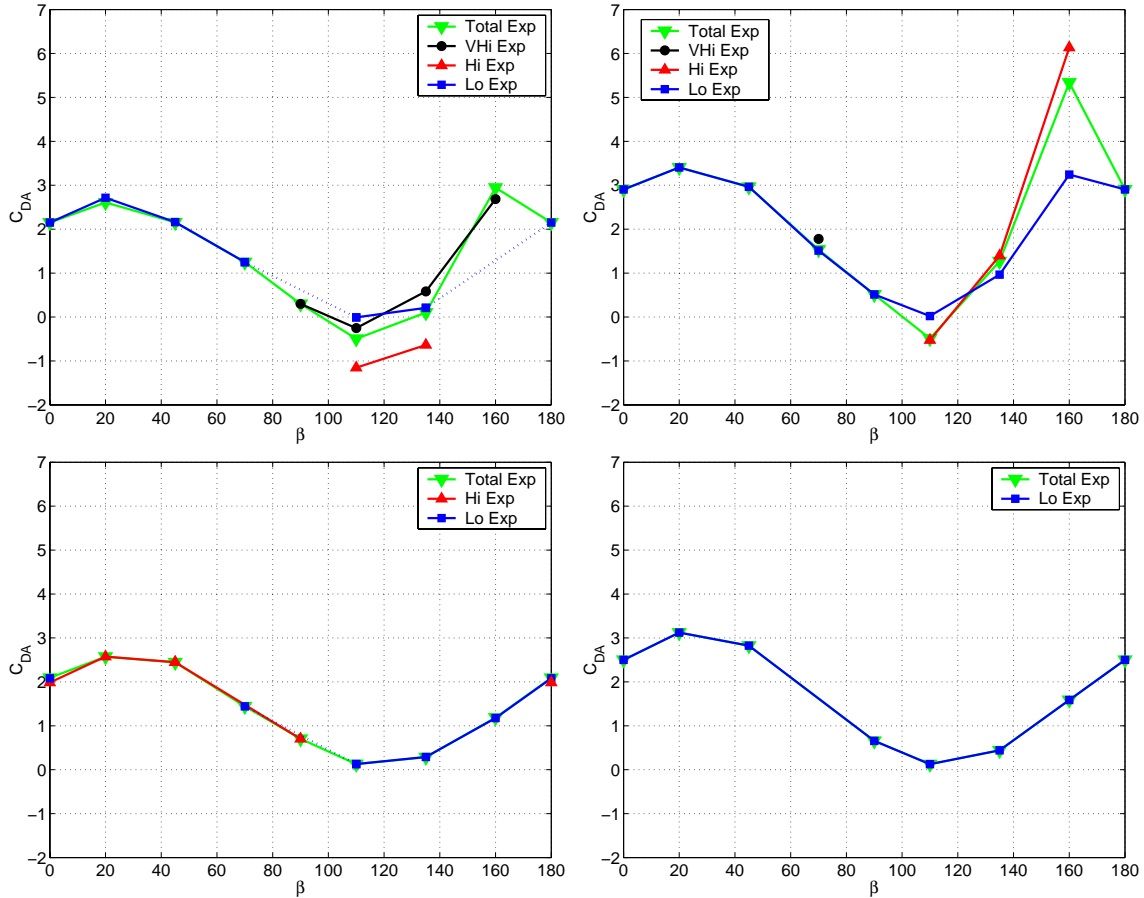


Figure 2.19: Non-dimensional aerodynamic damping, C_{AD} , at $\alpha = 15^\circ$ (upper) and $\alpha = 20^\circ$ (lower). The damping is shown as function of the movement direction, β . The reduced frequencies are $f_{red} = 0.02$ (left) and $f_{red} = 0.03$ (right). The green curves show the damping of the entire measured time-span, whereas the black, red and blue curves show the non dimensional aerodynamic damping from the low, high and very high lift stall modes.

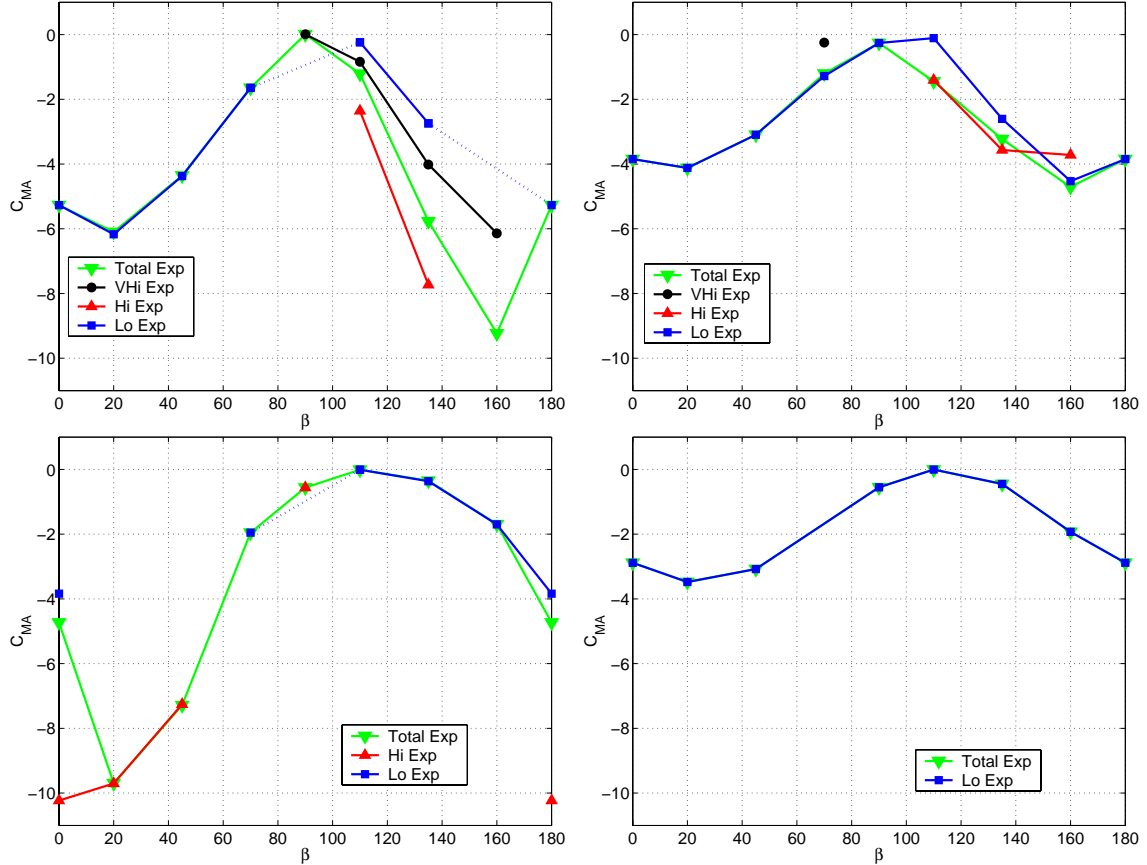


Figure 2.20: Non-dimensional aerodynamic added mass, C_{AM} , at $\alpha = 15^\circ$ (upper) and $\alpha = 20^\circ$ (lower). The added mass is shown as function of the movement direction, β . The reduced frequencies are $f_{red} = 0.02$ (left) and $f_{red} = 0.03$ (right). The green curves show the added mass of the entire measured time-span, whereas the black, red and blue curves show the non dimensional aerodynamic added mass from the low, high and very high lift stall modes.

for $\beta = 0^\circ$, the values are independent on stall mode at $\alpha = 20^\circ$. Analogous to the damping, the added mass shows a big influence of the stall mode, especially in the $f_{red} = 0.02$ case.

In order to determine the influence of the amplitude of the motion on the aerodynamic damping and added mass, experiments were carried out at four different combinations of incidence, α , and reduced frequency, f_{red}

- $\alpha = 5^\circ$ and $f_{red} = 0.02$
- $\alpha = 5^\circ$ and $f_{red} = 0.03$
- $\alpha = 15^\circ$ and $f_{red} = 0.02$
- $\alpha = 15^\circ$ and $f_{red} = 0.03$

for three different amplitudes each

- $A/c = 0.0526$
- $A/c = 0.1053$
- $A/c = 0.1316$.

The direction of the movement was in all these cases perpendicular to the free-stream flow, $\beta = 0^\circ$. The outcome of these investigations is shown in figure 2.21. The

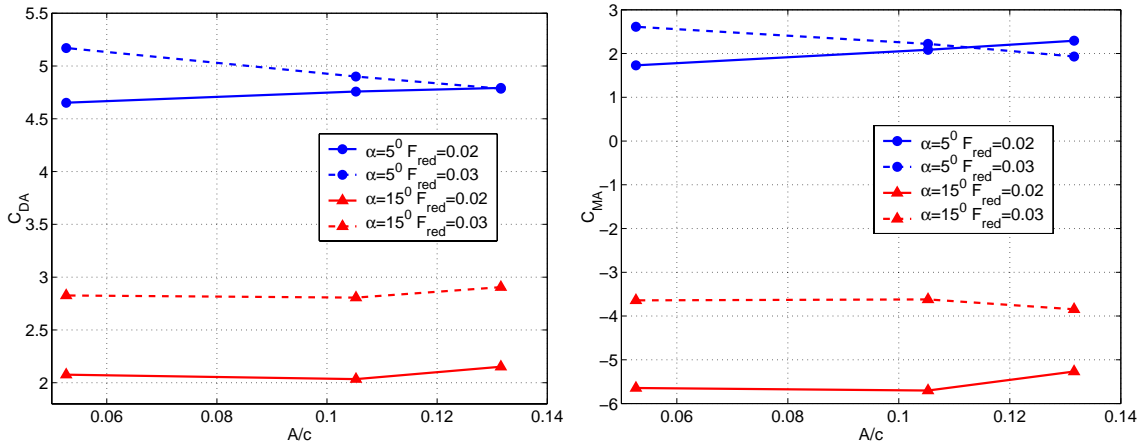


Figure 2.21: Non dimensional aerodynamic damping (left) and added mass (right) versus the non dimensional amplitude of the motion, A/c , at $\beta = 0^\circ$.

results indicate that the non-dimensional aerodynamic damping and added mass are practically independent of the amplitude of the motion.

The results indicate that the measured phenomenon is in essence linear for these relatively small oscillations. This would probably not have been the case if the oscillations, measured in relative angle of attack, had been more violent.

In order to investigate the effect of the reduced frequency on the non-dimensional aerodynamic damping, four different measuring series were undertaken at different angles of attack and angles of movement. In each of these measuring series, the reduced frequency was varied. The angles of attack and angles of movement for the four measuring series was

- $\alpha = 5^\circ$ and $\beta = 0^\circ$
- $\alpha = 8^\circ$ and $\beta = 160^\circ$
- $\alpha = 15^\circ$ and $\beta = 135^\circ$
- $\alpha = 20^\circ$ and $\beta = 0^\circ$.

The reduced amplitude for all experiments was $A/c = 0.1316$.

As explained earlier, the construction of the airfoil and the pressure transducers limited the frequency of the motion to values up to $f_{mov} = 2.4\text{Hz}$. Therefore, increase in reduced frequency above $f_{red} = 0.02$ was achieved through a decrease in free-stream velocity, and thereby Reynolds number.

In order to investigate a wider spectrum of reduced frequencies, some of the measuring points were taken at quite low Reynolds numbers, as shown in the table below, where the Reynolds-numbers corresponding to the reduced frequencies are given.

| | | | | | |
|-----------|----------|---------|---------|---------|---------|
| f_{red} | < 0.0225 | 0.024 | 0.031 | 0.035 | 0.041 |
| Re | 555.000 | 470.000 | 383.000 | 330.000 | 270.000 |

Deviation in the characteristics of the flow from the $Re = 555000$ data points may be evident in the low Reynolds number data points for the stalling cases. This is further investigated in chapter 4 in the comparison with theoretical models.

Figure 2.22 shows non-dimensional aerodynamic damping and non-dimensional added mass as function of reduced frequency for these series.

The non-dimensional aerodynamic damping is shown to obtain more extreme values as the reduced frequency is lowered. Especially so for the motion close to the chordwise direction at $\alpha = 15^\circ$, where the aerodynamic damping has its minimum. The results show that slower oscillations are more prone to negative aerodynamic damping for all stall modes.

Furthermore it is seen that there is quite big difference in the aerodynamic damping associated with the different stall modes. It is seen that in the regions most dangerous in terms of negative aerodynamic damping, the high stall mode has considerably lower damping than the other two modes. However, it is seen that the high stall mode is more damped when the reduced frequency is increased above $f_{red} = 0.03$, but this may be attributed to Reynolds number effects.

Generally, the high stall mode shows considerably more sensitivity to the reduced frequency in terms of aerodynamic damping than any of the other stall modes.

The lower graph in figure 2.22 shows the non-dimensional added mass as function of the reduced frequency. In this case, the same trend is observed as in the aerodynamic damping. The non-dimensional added mass is shown to obtain more extreme values

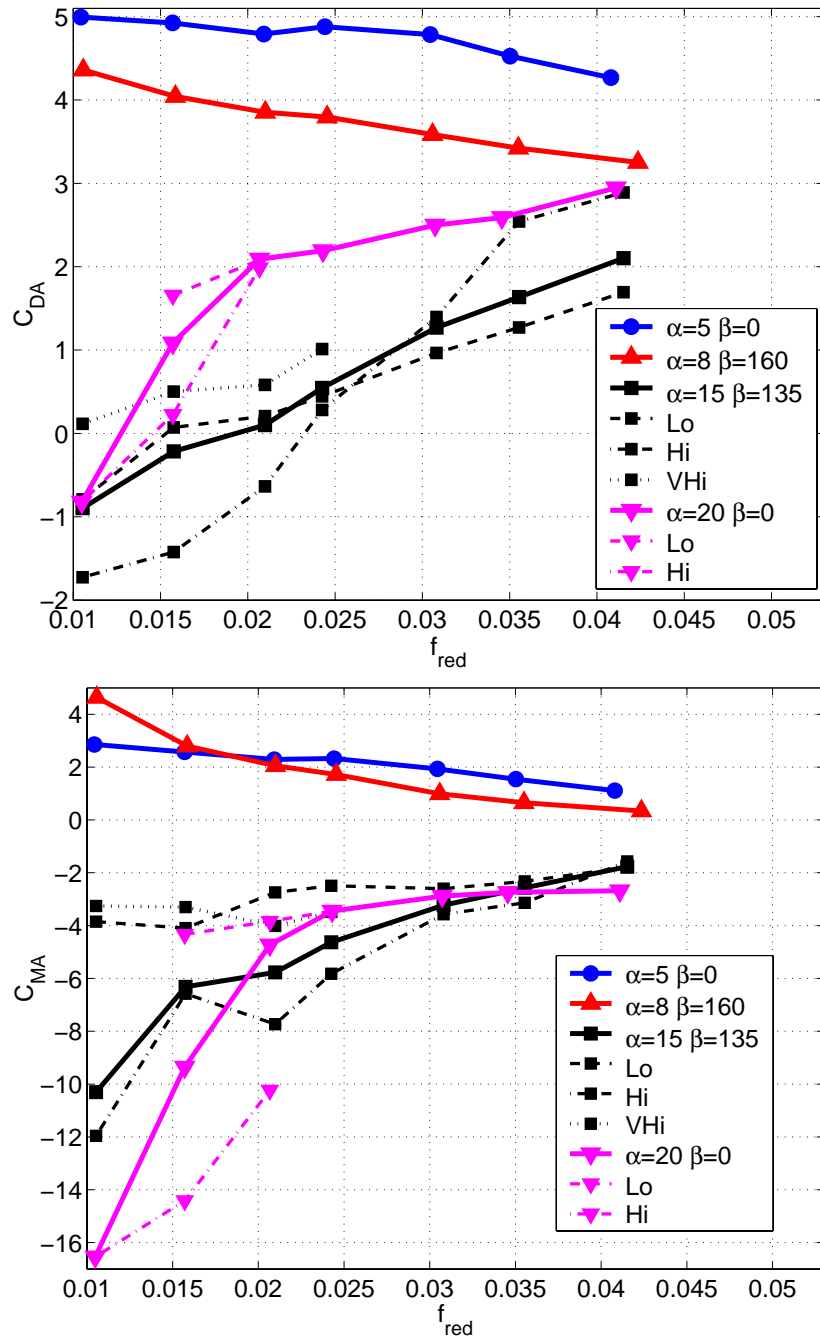


Figure 2.22: Non dimensional aerodynamic damping (upper) and added mass (lower) versus reduced frequency at four different configurations of incidence and movement direction. The full lines show the mean damping over the whole measured time-span, whereas the dashed, dash-dotted and dotted curves correspond to the low, high and very high stall modes in the multiple stall cases. $A/c = 0.1316$.

as the reduced frequency is lowered, and the non-dimensional added mass obtains the highest absolute values for the high stall mode in the cases where multiple stall modes occur.

From dimensional analysis it was shown that the Reynolds number was one of the non-dimensional parameters influencing the non dimensional aerodynamic damping and added mass. Note that the Reynolds number is not kept constant in the data shown in figure 2.22, which could have an effect on the non-dimensional added mass. This is investigated in chapter 4, where the present data is compared to results obtained with a Navier-Stokes solver.

Chapter 3

Theoretical Models

Despite the fact that the flow-fields around wind turbine rotors are highly three-dimensional, and that complex three dimensional effects of rotation are present, most practical models describing the forces on a wind turbine rotor use two dimensional theory as a basis for the analysis.

The objective of this chapter is to present the five different theoretical models used for prediction of the unsteady forces from two dimensional flow in the present work. The first three models presented are analytical models, of which the first two, Analytic Unsteady Potential Theory and Quasi-Stationary Theory, build the basis for the new heuristic analytical stall model presented in section 3.4.

The last two theoretical models presented, the panel code, which is an incompressible inviscid code, and the RANS¹ code, are numerical in nature.

The chapter starts out with a overview of the basic theory which is a foundation for the theoretical models to follow.

3.1 Background

The general continuity and momentum equations for a newtonian fluid can be expressed in differential form [27] as

$$\frac{\partial \rho}{\partial t} + \nabla \cdot \rho \mathbf{U} = 0 \quad (3.1)$$

$$\rho \left(\frac{\partial U_i}{\partial t} + \mathbf{U} \cdot \nabla U_i \right) = \rho f_i - \frac{\partial}{\partial x_i} (p + \frac{2}{3} \mu \nabla \cdot \mathbf{U}) + \frac{\partial}{\partial x_j} \mu \left(\frac{\partial U_i}{\partial x_j} + \frac{\partial U_j}{\partial x_i} \right) \quad (3.2)$$

The boundary condition for these equations on a solid surface is the no-slip condition, implying that the relative velocity of the fluid reduces to zero on the solid surface.

From dimensional analysis it can be shown [27], that density changes caused by pressure changes are negligible if the Mach, Froude and Reynolds numbers obey

$$M \ll 1 \quad \frac{M^2}{F^2} \ll 1 \quad \frac{M^2}{Re} \ll 1, \quad (3.3)$$

¹Reynolds Averaged Navier-Stokes

where the Mach number, M , is given by the ratio of the free-stream velocity, V , to the speed of sound, a :

$$M = \frac{V}{a}.$$

The ratio of inertial force to gravitational force, known as the Froude number, F , is given by:

$$F = \frac{V}{\sqrt{cg}},$$

where c and g denote the airfoil chord and gravitational constant, respectively. The last non dimensional number in the requirements for negligibly density changes due to pressure changes is the well known Reynolds number, which expresses the ratio between the inertial and viscous forces

$$Re = \frac{\rho V c}{\mu},$$

where density and viscosity is denoted by ρ and μ , respectively. If the requirements of equation 3.3 are met, the fluid can be assumed incompressible. If, furthermore, the fluid is isothermal, the fluid elements cannot experience volume change, implying that the fluid elements must have constant density. Therefore the continuity and momentum equations reduce to

$$\nabla \cdot \mathbf{U} = 0 \quad (3.4)$$

$$\rho \left(\frac{\partial \mathbf{U}}{\partial t} + (\mathbf{U} \cdot \nabla) \mathbf{U} \right) = \rho \mathbf{f} - \nabla p + \mu \nabla^2 \mathbf{U} \quad (3.5)$$

The boundary conditions on solid surfaces for the governing fluid equations, 3.4 and 3.5, is the no-slip condition, meaning that the velocity relative to any solid surface should drop to zero at the surface.

Dimensional analysis of the general momentum equation, equation 3.2, shows that for high Reynolds number flows, $Re \gg 1$, the viscous terms outside the boundary layer of the airfoil and wake are negligible. Under the assumption of incompressible, inviscid and irrotational flow with negligible body forces, the momentum equation reduce to what is known as the Euler equation

$$\frac{\partial \mathbf{U}}{\partial t} + (\mathbf{U} \cdot \nabla) \mathbf{U} + \frac{\nabla p}{\rho} = 0. \quad (3.6)$$

The Euler equation is valid throughout the fluid under the given assumptions. Since the flow described by the Euler equation is inviscid, there is no physical reason for the tangential velocity component to be zero on a solid surface. What remains of the no-slip boundary condition is that the relative normal component of the flow should be equal to zero.

When using solutions of the inviscid equations, it is important to be aware of the limitations of the method. Since viscous effects are disregarded, phenomena driven by viscous effects, such as stall and separation, cannot be modelled using these equations

without modification. Therefore the applicability of basic inviscid solutions to airfoil flow is limited to low angles of attack, at below approximately 8° , depending on the characteristics of the airfoil profile.

In the boundary layer on the airfoil, the viscous momentum equation, equation 3.2, can be reduced to the classical boundary layer equations [60]. An important feature of the boundary layer theory is that the pressure does not vary in the direction normal to the surface. Solving the inviscid airfoil flow without taking into account the boundary layer introduces some errors. Firstly, the boundary layer, with the no slip condition on the tangential velocity, introduces a displacement thickness that should be accounted for in the inviscid part of a coupled computation. Secondly, the friction forces from the shear stress distribution computed from the viscous boundary layer is disregarded.

For high Reynolds number flows, however, the thickness of the boundary layer is negligible when viewed on the scale of the airfoil [27]. This implies that quite reasonable results can be obtained by solving only the incompressible, inviscid flow equations for attached airfoil flows, since the forces from the pressure distribution is an order of magnitude greater than the friction forces that could be provided from solution of the boundary layer equations.

The means by which pressure forces are computed in potential theory is the Bernoulli equation, which is derived from the momentum (Euler) equation 3.6, by integration along a path

$$\frac{\partial}{\partial t} \left(\int_1^2 U_s ds \right) + \left(\frac{p_2}{\rho} + \frac{U_2^2}{2} \right) - \left(\frac{p_1}{\rho} + \frac{U_1^2}{2} \right) = 0 \quad (3.7)$$

Note that U_s is the velocity component along the integration path s . The Bernoulli equation is valid throughout the fluid, and is not confined to integration along streamlines. It links the velocities to the pressures, providing a tool for evaluating the pressure, and thus the forces, from the fluid on the airfoil.

A theorem used extensively in unsteady potential theory is Kelvin's Theorem, after the British scientist Lord Kelvin, which states that '*the time rate of change of circulation around a closed curve containing the same fluid elements is zero.*' [27]

Kelvin's theorem is used to determine the strength of the unsteady wake shed after an airfoil.

3.2 Analytic Unsteady Potential Theory

In this section the two dimensional unsteady potential theory solution for a thin wing will be summarized. Theodore Theodorsen [55] solved this problem analytically in 1935, and his solution of the problem is aiming at determining flutter stability for aircraft airfoils, and does not concern motion of, or forces on the airfoil in the direction of the free-stream.

This section will be following the lines of Øye [65], which in addition to the pitching and cross-flow motion investigated in Theodorsen's formulation, incorporates motion and forces in the along-wind direction.

As mentioned previously, the viscous nature of separated flows does not allow for modelling by inviscid theory, limiting the range of applicability for the analytic unsteady

potential theory to fairly low incidences, below approximately 8° , depending on the characteristics of the airfoil profile.

At the heart of the analytical potential theory solutions are singularity elements which in this case are lines of concentrated vorticity. These singularities are solutions to the incompressible, inviscid Navier-Stokes equations. In the general solution of the potential problem superposition is used because the disturbance from the singularity elements are linear in nature.

The solution of the unsteady two dimensional potential flow problem is based on three basic ‘building blocks’ :

- **Kelvin’s Theorem.** Kelvin’s theorem states that the time rate of change of circulation around a closed curve consisting of the same fluid elements is zero [27]. From this follows that if a certain amount of vorticity is generated, an equal amount of the opposite sign must be created at the same time.
- **Kutta-Joukowski Condition.** Boundary-layer theory shows that the fluid outside the boundary layer of a thin airfoil at a small angle of attack may be regarded as inviscid. The Kutta-Joukowski condition is a phenomenological rule stating that the velocity must remain finite and tangent to the airfoil at the sharp trailing edge due to the effect of viscosity in the boundary layer [13].
- **Neumann Boundary Condition.** The Neumann boundary condition states that there can be no flow through a solid surface, which in the general unsteady case is moving.

Kelvins theorem in combination with the Kutta-Joukowski condition implies that the change in vorticity on a body will be reflected in the wake of the body, which is shed from the trailing edge. Since free vortices in incompressible, inviscid fluid remain constant in circulation and are always composed of the same fluid particles [7], the strength of the wake vortices are constant in time once they are shed.

The singularity solution used in this case is a vortex line. The general effect of a vortex line on the velocity field is expressed by Biot-Savart’s law, which in the two dimensional version reads [27]

$$\vec{U} = \int \frac{\gamma}{2\pi r^2} \hat{\vec{r}} ds \quad (3.8)$$

It is noted that a two dimensional point vortex only induces tangential velocities as seen from the location of the vortex. The magnitude of the induced velocity is proportional to the vortex strength and inversely proportional to the distance from the vortex.

In order to compute the forces on the airfoil the Bernoulli equation formulated in a moving frame of reference is used [7]

$$p + \frac{\rho}{2} U^2 + \rho \frac{\partial \phi}{\partial t} = \rho F(t) \quad (3.9)$$

3.2.1 Normal Force and Moment

In addition to the standard potential theory assumptions, it is assumed that the airfoil cross-section is a straight line of infinitesimal thickness. This is known to give surprisingly good results for fully attached flows around thin uncambered airfoils at high

Reynolds numbers [65]. The definitions and positive directions used in the present derivation are shown in figure 3.1. The coordinates are non-dimensionalized by the

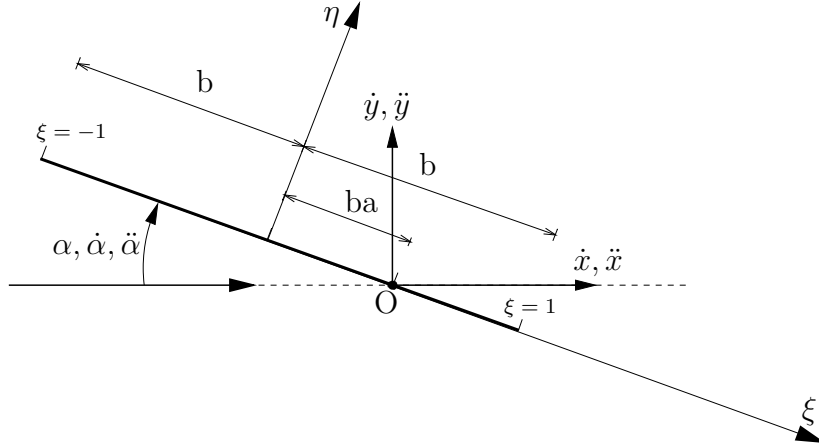


Figure 3.1: Definitions and positive directions used in the derivations of the unsteady potential theory. b is the half-chord of the profile, with which the length parameter ξ is normalized. $\xi = 0$ in the half-chord point, such that the leading and trailing edge corresponds to $\xi = -1$ and $\xi = 1$, respectively. The direction perpendicular to the profile is denoted by η . The angle of attack, α , and its derivatives are determined with respect to the free stream velocity V , and is positive ‘nose up’. The translatory motion of the profile is given by x , y , and the derivatives of these, which defines the translatory motion of the hinge-point O , defined by the non dimensional parameter, a , for which the positive direction is towards the trailing edge.

profile half-chord b such that the leading and trailing edge of the profile is given by $\xi = -1$ and $\xi = 1$ respectively. The position, motion and acceleration of the profile is fully described by α , x , y , and the derivatives of these. Note that ξ is a length parameter, following the chord and extending into the wake as depicted in figure 3.1.

According to Glauert the bound continuous vorticity on the profile is given by [1]

$$\gamma(\xi, t) = A_0(t) \tan \frac{\Theta}{2} + \sum_{n=1}^{\infty} A_n(t) \sin n\Theta \quad (3.10)$$

$$\xi = \cos \Theta \quad (3.11)$$

Figure 3.2 shows the basis functions of the fourier coefficients in equation 3.10. This expression automatically obeys the Kutta-Joukowski condition that the induced velocity at the trailing edge should be finite.

The induced flow velocity perpendicular to the profile, v_η , from the bound vortex strength is found from the two dimensional version of Biot-Savart’s law 3.8.

$$v_\eta(\xi, t) = - \int_{-1}^1 \frac{\gamma(\xi_1)}{2\pi(\xi - \xi_1)} d\xi_1 = -1/2A_0(t) - \sum_{n=1}^{\infty} 1/2A_n(t) \cos n\Theta \quad (3.12)$$

The bound vortex strength changes in time due to the motion of the profile. To fulfill Kelvin’s theorem, that the universal vorticity should be zero, the change in bound

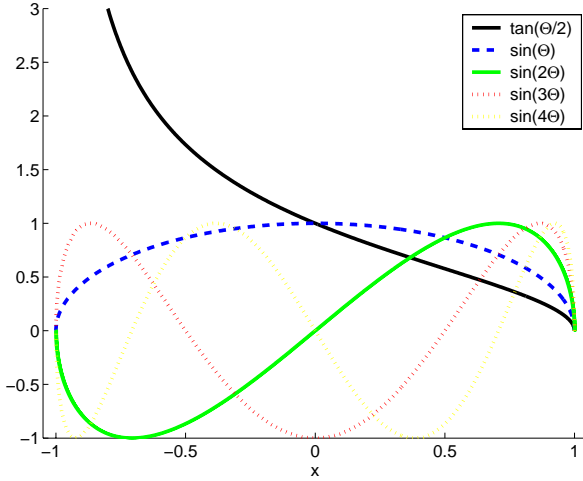


Figure 3.2: The five first basis functions in Glauert's Fourier series of the bound vortex strength, equation 3.10, as function of length parameter, ξ .

vorticity on the airfoil, $d\gamma$, is reflected in the wake vorticity. Due to the change in the bound vorticity, an amount of vorticity with the opposite sign, $-d\gamma$, is shed at the trailing edge. The wake vortices are convected downstream with the free-stream velocity V .

The wake vortices induce a flow velocity, $w_\eta(\xi)$, perpendicular to the profile, that under the assumption of small angles of attack is given by

$$w_\eta(\xi, t) = \int_1^\infty \frac{\gamma(\xi_1)}{2\pi(\xi_1 - \xi)} d\xi_1 \quad (3.13)$$

The ‘memory’, in the time dependant sense, of this model is manifested through the shed vortices in wake, which feed back to the solution.

The component of the free stream and the relative motion of the profile in the direction perpendicular to the profile is, still under the assumption of small angles of attack,

$$u_\eta(\xi, t) = -\dot{y} + (V - \dot{x})\alpha + b(\xi - a)\dot{\alpha} \quad (3.14)$$

The Neumann boundary condition dictates that there be no flow through the solid surface, such that

$$v_\eta(\xi, t) + w_\eta(\xi, t) + u_\eta(\xi, t) = 0 \quad (3.15)$$

Inserting equations 3.12-3.14 into the Neumann boundary condition, 3.15, yields

$$\begin{aligned} -1/2A_0 - \sum_{n=1}^{\infty} 1/2A_n \cos n\Theta + \int_{-1}^1 \frac{\gamma(\xi_1)}{2\pi(\xi_1 - \xi)} d\xi_1 \\ -\dot{y} + (V - \dot{x})\alpha + b(\xi - a)\dot{\alpha} = 0 \end{aligned} \quad (3.16)$$

According to Øye [65], the time dependant coefficients $A_n(t)$ are determined from equation 3.16

$$A_0 = 2\{(V - \dot{x})\alpha - \dot{y} - ba\dot{\alpha}\} + \frac{1}{\pi} \int_1^\infty \frac{\gamma(\xi)}{\sqrt{\xi^2 - 1}} d\xi \quad (3.17)$$

$$A_1 = 2b\dot{\alpha} + \frac{2}{\pi} \int_1^\infty \left(\frac{\gamma(\xi)}{\sqrt{\xi^2 - 1}} - 1 \right) \gamma(\xi) d\xi \quad (3.18)$$

$$A_n = \frac{2}{\pi} \int_1^\infty \frac{(\xi - \sqrt{\xi^2 - 1})^n}{\sqrt{\xi^2 - 1}} \gamma(\xi) d\xi \quad (3.19)$$

The forces are integrated from the pressure on the profile, which is given by Bernoulli's equation in the moving frame of reference, equation 3.9.

Since the profile representation is infinitely thin, the induced velocity in the chordwise direction, ξ , on the profile line due to the bound vorticity reduces to

$$w_\xi(x) = \pm 1/2\gamma(\xi). \quad (3.20)$$

The plus and minus sign refers to the upper and lower side of the profile, respectively. If, apart from the assumption of small angles of attack w_ξ is assumed small in comparison with the free stream velocity, the total tangential velocity relative to the profile can be expressed as

$$V_T^2 = (V - \dot{x} + w_\xi)^2 \simeq (V - \dot{x})^2 + 2(V - \dot{x})w_\xi \quad (3.21)$$

The potential from the bound vorticity is [65]

$$\phi(\xi) = \pm 1/2b \int_{-1}^\xi \gamma(\xi) d\xi \quad (3.22)$$

Again, the plus and minus sign refers to the upper and lower side of the profile. Inserting equations 3.21-3.22 into the Bernoulli equation 3.9, and subtracting the pressures on the upper side of the airfoil from the pressures on the lower side of the airfoil, an expression for the pressure difference over the profile is obtained

$$\Delta p = p_l - p_u = \rho(V - \dot{x})\gamma + \rho b \frac{\partial}{\partial t} \int_{-1}^\xi \gamma d\xi. \quad (3.23)$$

From this, the normal force and moment is obtained by integration over the airfoil

$$N = b \int_{-1}^1 \Delta p dx = \rho b \int_{-1}^1 \left\{ (V - \dot{x})\gamma + b \frac{\partial}{\partial t} \int_{-1}^\xi \gamma d\xi \right\} d\xi \quad (3.24)$$

$$\begin{aligned} M &= b^2 \int_{-1}^1 (a - \xi) \Delta p d\xi \\ &= \rho b^2 \int_{-1}^1 (a - \xi) \left((V - \dot{x})\gamma + b \frac{\partial}{\partial t} \int_{-1}^\xi \gamma d\xi \right) d\xi \end{aligned} \quad (3.25)$$

Inserting γ from equation 3.10 and the A_n coefficients from equations 3.17-3.19 yields after considerable reduction [65]

$$\begin{aligned} N &= 2\pi\rho b(V - \dot{x}) [(V - \dot{x})\alpha - \dot{y} - b(a - 0.5)\dot{\alpha}] \\ &\quad + \rho b(V - \dot{x}) \int_1^\infty \frac{\gamma}{\sqrt{\xi^2 - 1}} d\xi + \pi\rho b^2 [(V - \dot{x})\dot{\alpha} - \ddot{x}\alpha - \ddot{y} - ab\ddot{\alpha}] \end{aligned} \quad (3.26)$$

$$\begin{aligned} M &= (a + 0.5)b \{ 2\pi\rho b(V - \dot{x}) [(V - \dot{x})\alpha - \dot{y} - b(a - 0.5)\dot{\alpha}] \\ &\quad + \rho b(V - \dot{x}) \int_1^\infty \frac{\gamma}{\sqrt{\xi^2 - 1}} d\xi \} - 0.5\pi\rho b^3(V - \dot{x})\dot{\alpha} \\ &\quad + \pi\rho b^3 a [(V - \dot{x})\dot{\alpha} - \ddot{x}\alpha - \ddot{y} - ab\ddot{\alpha}] - 1/8\pi\rho b^4\ddot{\alpha} \end{aligned} \quad (3.27)$$

After labelling the terms in equations 3.26 and 3.27 the equations read

$$N = N_{QS} + N_W + N_{VM} \quad (3.28)$$

$$\begin{aligned} M &= (a + 0.5)b \{ N_{QS} + N_W \} + M_{QS} \\ &\quad + abN_{VM} + M_{VM} \end{aligned} \quad (3.29)$$

The terms are given by

$$N_{QS} = 2\pi\rho b(V - \dot{x}) [(V - \dot{x})\alpha - \dot{y} - b(a - 0.5)\dot{\alpha}] \quad (3.30)$$

$$N_W = \rho b(V - \dot{x}) \int_1^\infty \frac{\gamma}{\sqrt{\xi^2 - 1}} d\xi \quad (3.31)$$

$$N_{VM} = \pi\rho b^2 [(V - \dot{x})\dot{\alpha} - \ddot{x}\alpha - \ddot{y} - ab\ddot{\alpha}] \quad (3.32)$$

$$M_{QS} = -0.5\pi\rho b^3(V - \dot{x})\dot{\alpha} \quad (3.33)$$

$$M_{VM} = -1/8\pi\rho b^4\ddot{\alpha} \quad (3.34)$$

The normal force, equation 3.28, consists of three parts. The first part, N_{QS} , is the quasi-steady potential normal force. The second term, N_W , is the normal force induced by the unsteady wake. Apart from these terms an additional virtual mass term, N_{VM} , is present. The virtual mass term can be interpreted as the force from the acceleration of a virtual mass of air, $\pi\rho b^2$.

By comparing equations 3.28 and 3.29 it is seen that the quasi-steady normal forces, N_{QS} , and the normal forces induced by the unsteady wake, N_W , act on the quarter-chord of the profile line, whereas the virtual mass normal force, N_{VM} , acts on the half-chord point.

Apart from the contributions to the moment from the three terms in the normal force, there exist two additional terms. One of these is the quasi-steady moment, M_{QS} , which arises due to the angular velocity of the profile. The physical interpretation of this term is given in Øye [65] as the analogy to a linear profile in a rotating flow, which in its turn is analog to a cambered profile in a linear flow. The last additional term in the moment equation is a virtual mass term, M_{VM} , due to the angular acceleration of the profile.

It is seen from the equations, that the relative motion of the 3/4 chord point, $b(a - 0.5)$ in the equations, that determines the forces on the airfoil from the bound vorticity.

In order to arrive at the final expressions for the normal force and moment, further manipulation is required.

As a consequence of Kelvin's theorem, the circulation on the profile must be matched by the opposite amount of circulation in the flow

$$\Gamma = b \int_{-1}^1 \gamma \, d\xi = -b \int_1^\infty \gamma \, d\xi. \quad (3.35)$$

From integration of the bound vorticity, equation 3.10, we get

$$\Gamma = b \int_{-1}^1 \gamma \, d\xi = b\pi(A_0 + 0.5A_1) \quad (3.36)$$

Inserting A_0 and A_1 from equations 3.17 and 3.18, and using the result from Kelvin's Theorem, equation 3.35, the following relation is obtained

$$2\pi b [(V - \dot{x})\alpha - \dot{y} - b(a - 0.5)\dot{\alpha}] = -b \int_1^\infty \frac{\xi + 1}{\sqrt{\xi^2 - 1}} \gamma \, d\xi \quad (3.37)$$

Rewriting the expression for the quasi-steady normal force, equation 3.30, with the above expression

$$N_{QS} = -\rho b(V - \dot{x}) \int_1^\infty \frac{\xi + 1}{\sqrt{\xi^2 - 1}} \gamma \, d\xi, \quad (3.38)$$

results in the possibility of rewriting the expressions for the quasi-steady and wake normal forces as

$$\begin{aligned} N_{QS} + N_W &= -\rho b(V - \dot{x}) \int_1^\infty \frac{\xi + 1}{\sqrt{\xi^2 - 1}} \gamma \, d\xi + \rho b(V - \dot{x}) \int_1^\infty \frac{\gamma}{\sqrt{\xi^2 - 1}} \, d\xi \\ &= N_{QS} \cdot \mathbf{C}, \end{aligned} \quad (3.39)$$

where

$$\mathbf{C} = 1 - \frac{\int_1^\infty \frac{\gamma}{\sqrt{\xi^2 - 1}} \, d\xi}{\int_1^\infty \frac{\xi + 1}{\sqrt{\xi^2 - 1}} \gamma \, d\xi} = \frac{\int_1^\infty \frac{\xi}{\sqrt{\xi^2 - 1}} \gamma \, d\xi}{\int_1^\infty \frac{\xi + 1}{\sqrt{\xi^2 - 1}} \gamma \, d\xi}. \quad (3.40)$$

The introduction of \mathbf{C} is an alternative way of expressing the forces from the unsteady wake on the profile, like a re-normalization factor from quasi-steady to unsteady flow including effects from the wake. This formulation will show its usefulness later.

The final expressions for the normal force and the moment acting on the profile is obtained using equation 3.39 to rewrite equations 3.28-3.34.

$$\begin{aligned} N &= 2\pi\rho b(V - \dot{x}) [(V - \dot{x})\alpha - \dot{y} - b(a - 0.5)\dot{\alpha}] \cdot \mathbf{C} \\ &\quad + \pi\rho b^2 [(V - \dot{x})\dot{\alpha} - \ddot{x}\alpha - \ddot{y} - ab\ddot{\alpha}] \end{aligned} \quad (3.41)$$

$$\begin{aligned} M &= (a + 0.5)2\pi\rho b^2(V - \dot{x}) [(V - \dot{x})\alpha - \dot{y} - b(a - 0.5)\dot{\alpha}] \cdot \mathbf{C} \\ &\quad - 0.5\pi\rho b^3(V - \dot{x})\dot{\alpha} + \pi\rho b^3 a [(V - \dot{x})\dot{\alpha} - \ddot{x}\alpha - \ddot{y} - ab\ddot{\alpha}] \\ &\quad - 1/8\pi\rho b^4\ddot{\alpha} \end{aligned} \quad (3.42)$$

or in other terms

$$N = N_{QS} \cdot \mathbf{C} + N_{VM} \quad (3.43)$$

$$M = (a + 0.5)bN_{QS} \cdot \mathbf{C} + M_{QS} + abN_{VM} + M_{VM} \quad (3.44)$$

By inspection of the expression for the vorticity of the profile, equation 3.10, it is seen that a singularity exist at the leading edge, where the vorticity approaches infinity. The non-physical state of having an infinite vorticity on the leading edge of the airfoil is the penalty for using the simplification of an infinitely thin airfoil. However, the singularity at the leading edge of the infinitely thin airfoil may be regarded as the limiting form for the airfoil leading edge radius approaching zero. The analytical results compare very favorably with the chordwise distribution of measured pressure difference at small angles of attack [65]. The only significant discrepancies come from within a few percent chord lengths of the singularity.

3.2.2 Tangential Force

According to Øye [65], the leading edge suction force, which is equal to the negative tangential force can be determined by

$$-T = \pi\rho S^2 \quad (3.45)$$

where S is given by

$$S = \lim_{\xi \rightarrow -1} \left(\frac{\sqrt{b}}{2} \gamma \sqrt{\xi + 1} \right) \quad (3.46)$$

Integration of equation 3.10 yields

$$S = \sqrt{\frac{b}{2}} A_0 \quad (3.47)$$

By combining equations 3.17, 3.30, 3.31 and 3.39 it is possible to express A_0 in terms of

$$A_0 = \frac{N_{QS} \cdot \mathbf{C}}{\pi\rho b(V - \dot{x})^2} - b\dot{\alpha}. \quad (3.48)$$

This can be used to rewrite the tangential force as

$$\begin{aligned} T &= -\frac{\pi\rho b}{2} \left(\frac{N_{QS} + N_W}{\pi\rho b(V - \dot{x})^2} - b\dot{\alpha} \right)^2 \\ &= -\frac{\pi\rho b}{2} \left(\frac{N_{QS} \cdot \mathbf{C}}{\pi\rho b(V - \dot{x})^2} - b\dot{\alpha} \right)^2, \end{aligned} \quad (3.49)$$

or fully written out,

$$\begin{aligned} T &= 2\pi\rho b [(V - \dot{x})\alpha\dot{y} + b(a - 1/2)\dot{\alpha}]^2 \mathbf{C}^2 \\ &\quad - 2\pi\rho b^2 [(V - \dot{x})\alpha\dot{y} + b(a - 1/2)\dot{\alpha}] \mathbf{C}\dot{\alpha} - 1/2\pi\rho b^3\dot{\alpha}^2. \end{aligned} \quad (3.50)$$

The tangential force does not contribute to the moment because the forces are tangential to the infinitely thin airfoil.

3.2.3 Lift and Drag Forces

The lift and drag forces are obtained from a projection of the normal and tangential forces.

$$L = N \cos \alpha - T \sin \alpha \quad (3.51)$$

$$D = N \sin \alpha + T \cos \alpha \quad (3.52)$$

which, assuming small angles of attack and $N \gg T$

$$L = N \quad (3.53)$$

$$D = N\alpha + T \quad (3.54)$$

From this the general analytical results can be stated

$$\begin{aligned} L &= 2\pi\rho b(V - \dot{x}) [(V - \dot{x})\alpha - \dot{y} - b(a - 0.5)\dot{\alpha}] \cdot \mathbf{C} \\ &\quad + \pi\rho b^2 [(V - \dot{x})\dot{\alpha} - \ddot{x}\alpha - \ddot{y} - ab\ddot{\alpha}] \end{aligned} \quad (3.55)$$

$$\begin{aligned} D &= 2\pi\rho b [(V - \dot{x})\alpha - \dot{y} - b(a - 0.5)\dot{\alpha}] \cdot \mathbf{C} \\ &\quad \cdot \{[\dot{y} + b(a + 0.5)\dot{\alpha}] + [(V - \dot{x})\alpha - \dot{y} - b(a - 0.5)\dot{\alpha}] (1 - \mathbf{C})\} \\ &\quad - \frac{1}{2}\pi\rho b^3 \dot{\alpha}^2 + \pi\rho b^2 [(V - \dot{x})\dot{\alpha} - \ddot{x}\alpha - \ddot{y} - ab\ddot{\alpha}] \alpha \end{aligned} \quad (3.56)$$

$$\begin{aligned} M &= (a + 0.5)2\pi\rho b^2(V - \dot{x}) [(V - \dot{x})\alpha - \dot{y} - b(a - 0.5)\dot{\alpha}] \cdot \mathbf{C} \\ &\quad - 0.5\pi\rho b^3(V - \dot{x})\dot{\alpha} + \pi\rho b^3 a [(V - \dot{x})\dot{\alpha} - \ddot{x}\alpha - \ddot{y} - ab\ddot{\alpha}] - 1/8\pi\rho b^4 \ddot{\alpha} \end{aligned} \quad (3.57)$$

In the static case, where all derivatives with respect to time is zero and $C = 1$, the above expressions reduces to

$$\begin{aligned} L_{\text{static}} &= 2\pi\rho bV^2\alpha \\ D_{\text{static}} &= 0 \\ M_{\text{static}} &= (a + 1/2)2\pi\rho b^2V^2\alpha \end{aligned}$$

which is the well known results from steady potential theory, as found in for example Fung [13].

For later use, the drag forces will be interpreted below.

The quasi-steady drag, where positions, velocities and accelerations generally are not zero, and $C = 1$, is seen to consist of three parts. The first part is recognized as the quasi-static result, equal to the lift multiplied with the effective change in angle of attack in the quarter chord point due to the motion parallel to the free stream. The two other terms of the quasi-steady drag are of virtual mass type.

In the general instationary case, where $\mathbf{C} \neq 1$, an additional term arise. From equation 3.51 and 3.39

$$L_W = N_W = -N_{QS}(1 - \mathbf{C})$$

In quasi-stationary terminology, this reduction in the lift corresponds to a reduction of effective angle of attack.

$$\Delta\alpha = \frac{-L_W}{2\pi\rho b(V - \dot{x})^2} = \frac{1}{V - \dot{x}} [(V - \dot{x})\alpha - \dot{y} - b(a - 0.5)\dot{\alpha}] (1 - \mathbf{C})$$

Since $\Delta\alpha$ is a change in the effective angle of attack, the direction of the lift is changed the angle $\Delta\alpha$ as well. This induces a component in the direction of the static drag direction

$$\Delta D = L_{QS}\mathbf{C}\Delta\alpha = 2\pi\rho b [(V - \dot{x})\alpha - \dot{y} - b(a - 0.5)\dot{\alpha}]^2 \mathbf{C}(1 - \mathbf{C}) \quad (3.58)$$

It is noted that ΔD is exactly the part of the drag that vanishes in the quasi-steady case.

The physics of the unsteady potential drag can thus be stated:

The unsteady drag in an unsteady potential flow is a sum of three parts. The first part is the quasi-stationary term, equal to the lift multiplied with the change in effective angle of attack in the three-quarter chord point due to the motion of the airfoil. The second part of the unsteady drag forces is a virtual mass term, and the last part comes from the change in relative angle of attack due to the unsteady wake. This addition to the drag can be computed by assuming that the lift from the bound vorticity and the wake acts perpendicular to the relative direction of the flow in the quarter-chord point angled $\Delta\alpha$, where $\Delta\alpha$ expresses the angular change corresponding to the lift due to the unsteady wake influence.

3.2.4 Oscillatory Motion

An important subcase of the general unsteady motion of the airfoil is oscillation of the profile with angular frequency ω . Introducing complex notation the motion of the airfoil can be expressed as

$$\begin{aligned} x &= x_1 e^{i\omega t} \\ y &= y_1 e^{i\omega t} \\ \alpha &= \alpha_0 + \alpha_1 \\ \alpha_1 &= \alpha'_1 e^{i\omega t} \end{aligned}$$

The amplitude and phase of the motion is given by the modulus and argument of the complex amplitudes, x_1 , y_1 and α'_1 . The physical position of the airfoil is given by the real part of the complex quantities.

The derivation of the expressions for lift, drag, moment and Theodorsen's function, $\mathbf{C}(k)$, in the oscillatory case, is located in appendix B, where it is shown, that the forces due to the oscillatory motion of the airfoil is expressed as

$$\begin{aligned} L &= 2\pi\rho b(V - \dot{x})\{V\alpha_0 + [V\alpha_1 - \dot{x}\alpha_0 - \dot{y} - b(a - 0.5)\dot{\alpha}] \cdot \mathbf{C}(k)\} \\ &\quad + \pi\rho b^2 [(V - \dot{x})\dot{\alpha} - \ddot{x}\alpha - \ddot{y} - ab\ddot{\alpha}] \end{aligned} \quad (3.59)$$

$$\begin{aligned} D &= 2\pi\rho b\{V\alpha_0 + (V\alpha_1 - \dot{x}\alpha_0 - \dot{y} - b(a - 0.5)\dot{\alpha}) \cdot \mathbf{C}(k)\} \\ &\quad \cdot \{[\dot{y} + b(a + 1/2)\dot{\alpha}] + [V\alpha_1 - \dot{x}\alpha_0 - \dot{y} - b(a - 0.5)\dot{\alpha}] (1 - \mathbf{C}(k))\} \\ &\quad - 0.5\pi\rho b^3\dot{\alpha}^2 + \pi\rho b^2 [(V - \dot{x})\dot{\alpha} - \ddot{x}\alpha - \ddot{y} - ab\ddot{\alpha}] \alpha \end{aligned} \quad (3.60)$$

$$\begin{aligned} M &= (a + 0.5)2\pi\rho b^2(V - \dot{x})\{V\alpha_0 + (V\alpha_1 - \dot{x}\alpha_0 - \dot{y} - b(a - 0.5)\dot{\alpha}) \cdot \mathbf{C}(k)\} \\ &\quad - 0.5\pi\rho b^3(V - \dot{x})\dot{\alpha} + \pi\rho b^3a [(V - \dot{x})\dot{\alpha} - \ddot{x}\alpha - \ddot{y} - ab\ddot{\alpha}] - 1/8\pi\rho b^4\ddot{\alpha}, \end{aligned} \quad (3.61)$$

and the complex $\mathbf{C}(k)$, which is a function of k , or reduced frequency, f_{red} , is given by

$$\mathbf{C}(k) = \frac{\int_1^\infty \frac{\xi}{\sqrt{\xi^2-1}} e^{-ik\xi} d\xi}{\int_1^\infty \sqrt{\frac{\xi+1}{\xi-1}} e^{-ik\xi} d\xi}. \quad (3.62)$$

The non-dimensional wavenumber, k , is defined as

$$k = \frac{\omega b}{V} = 2\pi f_{red}. \quad (3.63)$$

According to [13], $\mathbf{C}(k)$ can be expressed using Bessel functions of the first and second kind

$$\mathbf{C}(k) = \frac{H_1^{(2)}(k)}{H_1^{(2)}(k) + i \cdot H_0^{(2)}(k)} \quad (3.64)$$

$$H_n^{(2)}(k) = J_n(k) - i \cdot Y_n(k) \quad (3.65)$$

From the equation for the oscillatory lift, equation 3.59, it is noted that the complex $\mathbf{C}(k)$ acts like a renormalization factor acting on the quasi-stationary lift, taking into account the effect of the wake. Looking more closely into the values from equation (3.64) yields valuable insight into the effects of the unsteadiness of the flow.

The basic geometric representation of a complex multiplication is that the product of two complex numbers is the complex number that has a length equal to the product of the lengths of the two complex numbers, and an argument equal to the sum of the arguments of those numbers.

The effect of the complex multiplication with $\mathbf{C}(k)$ can be visualized by plotting the length and the argument of $\mathbf{C}(k)$ as function of f_{red} , as shown in figure 3.3. It is seen

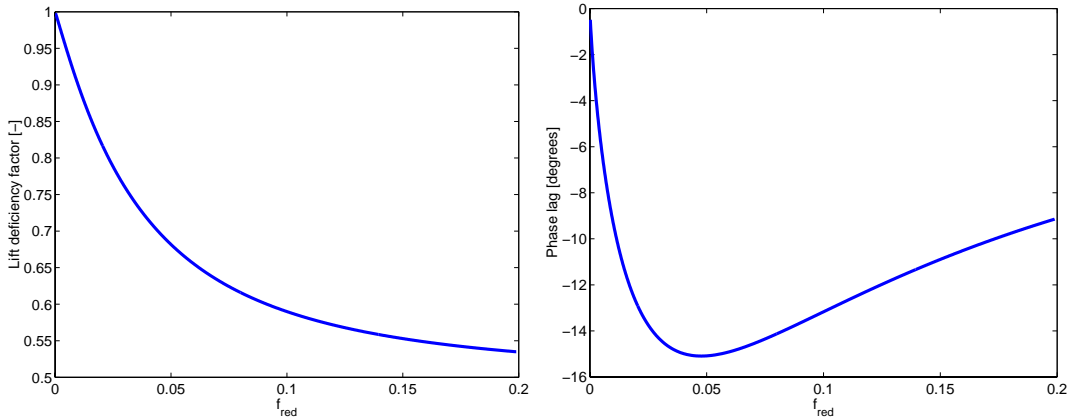


Figure 3.3: Length (left) and argument (right) of the complex $C(k)$ as function of $f_{red} = f_{mov}c/(2V) = k/(2\pi)$.

that the effect of the unsteady wake on the lift, is a reduction of the lift amplitude as well as a phase-shift, or, since the shift is negative, a phase-lag, of the lift forces. The functions depicted in figure 3.3 are known as Theodorsen's lift deficiency and phase-lag functions, respectively.

Since potential flow theory is only valid in the fully attached region, the above expressions are only expected to perform well for angles of attack below approximately 8° . Figure 3.4 shows an example of non-dimensional force loops for $\alpha = 5^\circ$ and $\beta = 0^\circ$.

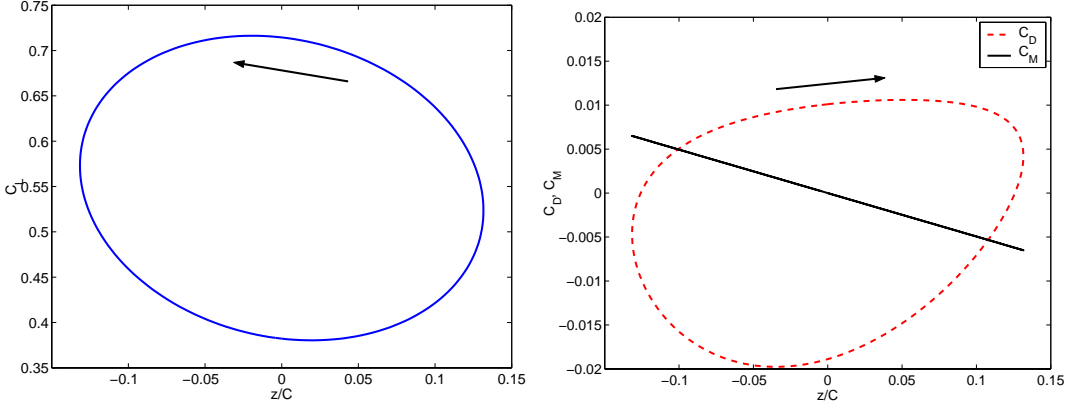


Figure 3.4: *Analytic unsteady potential flow force coefficient loops. The angle of attack is $\alpha = 5^\circ$. The other parameters for this example is $A/c = 0.1316$, $f_{red} = 0.02$ and $\beta = 0^\circ$.*

The direction of the lift loop is counter-clockwise, indicating a positive aerodynamic damping. Note, that the extremum values for the lift is lagging the extremum values for the relative angle of attack, which is at $z/c = 0$. The drag loop, shown in the right hand side, shows a similar lagging effect. The only contribution to the quarter chord moment coefficient comes from the virtual mass terms, making the moment a function of z because $z \propto \ddot{z}$.

3.3 Quasi-steady Theory

In this section the relationships between static force coefficients and linear quasi-stationary lift, drag and aerodynamic damping will be derived. The results from the quasi-steady theory is valid not only in the attached region as the unsteady potential theory presented in the previous section, but remains valid at any angle of attack, assuming the validity of the assumption of quasi-stationarity.

The lift and drag forces from the flow on a two dimensional body can be characterized by the lift and drag coefficients

$$C_L = \frac{F_L}{0.5\rho c V^2} \quad (3.66)$$

$$C_D = \frac{F_D}{0.5\rho c V^2} \quad (3.67)$$

In equations (3.66) and (3.67) ρ is the density of the fluid, c is the chord of the airfoil, V is the magnitude of the free-stream velocity. Notice that the forces F_L and F_D are in direction perpendicular and parallel to the free-stream flow direction.

Assuming quasi-stationarity, the lift- and drag coefficients in a relative, or moving,

coordinate system, $C_{L\text{rel}}$ and $C_{D\text{rel}}$ are functions of the relative angle of attack

$$C_{L\text{rel}} = f_1(\alpha_{\text{rel}}) \quad (3.68)$$

$$C_{D\text{rel}} = f_2(\alpha_{\text{rel}}) \quad (3.69)$$

and the forces corresponding to these coefficients are perpendicular and parallel to the relative free-stream flow direction.

Consider general translation of an airfoil in the 2D plane as shown in figure 3.5. The

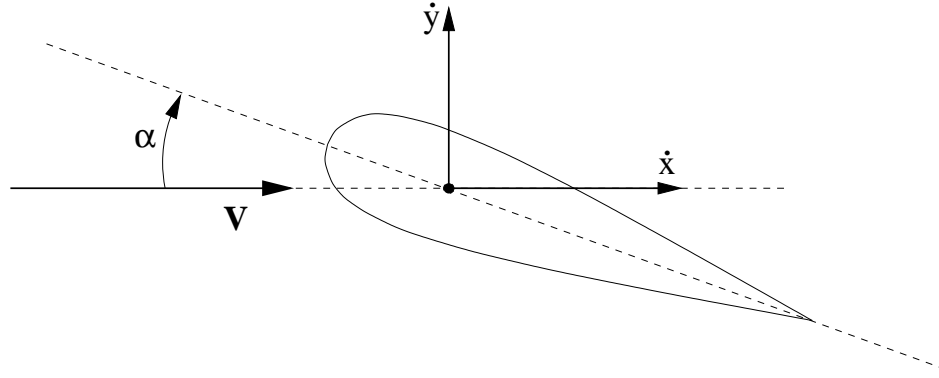


Figure 3.5: Definitions and positive directions of the angle of attack, α , and the x and y directions. All quantities are defined with respect to the free stream velocity V .

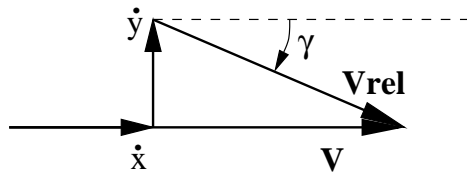


Figure 3.6: Velocity triangle for the general 2D translating case. V_{rel} is the relative velocity as seen from the moving airfoil. V_{rel} is changed the angle γ clockwise from the free stream velocity V .

vectorial expression for the relative velocity is

$$\vec{V}_{\text{rel}} = (V - \dot{x}, -\dot{y}), \quad (3.70)$$

The magnitude of the relative velocity V_{rel} can be expressed as

$$\begin{aligned} |V_{\text{rel}}| &= \sqrt{(V - \dot{x})^2 + (\dot{y})^2} \\ &= \sqrt{V^2 + \dot{x}^2 - 2V\dot{x} + \dot{y}^2}. \end{aligned} \quad (3.71)$$

Simple geometric considerations from the velocity triangle, figure 3.6, yield the relative angle of attack

$$\alpha_{\text{rel}} = \alpha - \gamma, \quad (3.72)$$

where

$$\gamma = \arctan \frac{\dot{y}}{V - \dot{x}}. \quad (3.73)$$

Considering only small oscillations in \dot{x} and \dot{y} , local linearity of $C_{L\text{rel}}$ and $C_{D\text{rel}}$ with respect to α_{rel} can be assumed

$$C_{L\text{rel}} = C_{L\alpha} - \gamma C'_{L\alpha} \quad (3.74)$$

$$C_{D\text{rel}} = C_{D\alpha} - \gamma C'_{D\alpha} \quad (3.75)$$

$C_{L\alpha}$ and $C_{D\alpha}$ refers to static lift and drag coefficients at the angle of attack α , whereas $C'_{L\alpha}$ and $C'_{D\alpha}$ denotes the derivative of these with respect to the angle of attack.

Projecting the forces in the relative system onto the directions of the global lift and drag yields for the global lift and drag coefficients

$$C_L = \frac{V_{\text{rel}}^2}{V^2} \{C_{L\text{rel}} \cos \gamma - C_{D\text{rel}} \sin \gamma\} \quad (3.76)$$

$$C_D = \frac{V_{\text{rel}}^2}{V^2} \{C_{L\text{rel}} \sin \gamma + C_{D\text{rel}} \cos \gamma\} \quad (3.77)$$

Inserting equations 3.71, 3.73, 3.74 and 3.75 into 3.76 and 3.77 the general expressions for the force coefficients are obtained after a first order Taylor expansion in \dot{x} and \dot{y} .

$$C_L = (1 - 2 \frac{\dot{x}}{V}) \{C_{L\alpha} - \frac{\dot{y}}{V} (C_{D\alpha} + C'_{L\alpha})\} \quad (3.78)$$

$$C_D = (1 - 2 \frac{\dot{x}}{V}) \{C_{D\alpha} - \frac{\dot{y}}{V} (-C_{L\alpha} + C'_{D\alpha})\} \quad (3.79)$$

Now consider the subcase of the general translatory case described above, the one degree translatory motion of an airfoil as outlined in figure 3.7. For this motion the

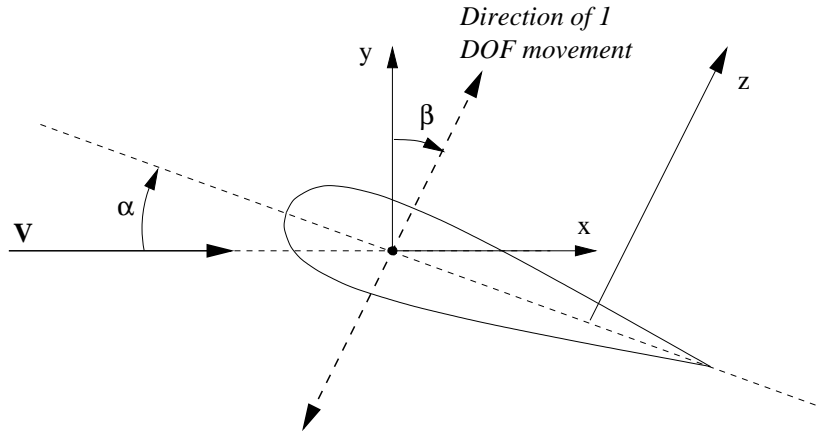


Figure 3.7: Definitions and positive directions of the angle of attack, α , the angle of movement, β , and the x and y axes. All quantities are defined with respect to the free stream velocity, V . The z -axis defines the positive direction for the motion of the profile.

expressions for the relative velocity is

$$\vec{V}_{\text{rel}} = (V - \dot{z} \sin \beta, -\dot{z} \cos \beta) \quad (3.80)$$

$$|V_{\text{rel}}|^2 = V^2 + \dot{z}^2 - 2V\dot{z} \sin \beta. \quad (3.81)$$

In this case \dot{x} and \dot{y} are given by

$$\dot{x} = \dot{z} \sin \beta \quad \text{and} \quad (3.82)$$

$$\dot{y} = \dot{z} \cos \beta. \quad (3.83)$$

Inserting equations 3.81 to 3.83 into the general expressions for the lift and drag coefficients, equations 3.78 and 3.79

$$C_L = C_{L\alpha} + \dot{z} \left\{ -\frac{2 \sin \beta}{V} C_{L\alpha} - \frac{\cos \beta}{V} (C'_{L\alpha} + C_{D\alpha}) \right\} \quad (3.84)$$

$$C_D = C_{D\alpha} + \dot{z} \left\{ -\frac{\cos \beta}{V} (C'_{D\alpha} - C_{L\alpha}) - 2 \frac{\sin \beta}{V} C_{D\alpha} \right\} \quad (3.85)$$

Projection of the forces in the z -direction yields for the force coefficient in the z -direction

$$C_z = C_{L\alpha} \cos \beta + C_{D\alpha} \sin \beta - \frac{\dot{z}}{V} \left\{ \sin \beta \cos \beta (C_{L\alpha} + C'_{D\alpha}) + \cos^2 \beta C'_{L\alpha} + (1 + \sin^2 \beta) C_{D\alpha} \right\} \quad (3.86)$$

If the positive sign for the aerodynamic damping is chosen such that a positive damping is damping the motion, corresponding to general structural damping of the airfoil, the final expression for the quasi-static aerodynamic damping is

$$D_A = 0.5 \rho c V \{ \sin \beta \cos \beta (C_{L\alpha} + C'_{D\alpha}) + \cos^2 \beta C'_{L\alpha} + (1 + \sin^2 \beta) C_{D\alpha} \} \quad (3.87)$$

Note that in equation (3.87), the terms $C_{L\alpha}$, $C_{D\alpha}$ and their derivatives with respect to α denote the values for the geometrical, static incidence α . This allows for evaluation of the aerodynamic damping from static measurements of the lift and drag coefficients. For $D_A > 0$ energy is taken out of the moving system and for $D_A < 0$ energy is put into the system, leading to increasing oscillations if the aerodynamic damping exceeds the structural damping of the rotor in the aeroelastic case.

It is possible to get an indication of how good the quasi-steady assumption is by evaluating the phase lag and the lift deficiency function introduced in section 3.2. The phase lag and lift deficiency function are derived from unsteady potential flow theory, and therefore only valid in the attached region. However, the values give an indication as to how well the quasi-stationary assumption should work.

Figure 3.8 shows an example of non-dimensional force loops for C_L and C_D for two cases having the same stationary lift, $C_{L\alpha} = 0.6$. One case, low- α , in attached flow, and the other case, high- α , in stalling flow. The direction in which the airfoil oscillates is perpendicular to the airfoil, $\beta = 0^\circ$.

Notice in the left graph, that the direction of the lift loop in the low- α case is counter-clockwise, indicating a positive aerodynamic damping, whereas the high- α lift loop is clockwise, indicating a negative aerodynamic damping. The mechanism determining the direction of the loops is evident from equation 3.78. It is seen that the sign of $C_{D\alpha} + C'_{L\alpha}$ determines the direction of the lift loop in the purely heaving case, $\beta = 0^\circ$. The right graph shows the non dimensional drag loops. As before, the direction in which the loops revolve are different in the two cases. The low- α drag coefficient loop is clockwise, whereas the high- α drag coefficient loop is counter-clockwise.

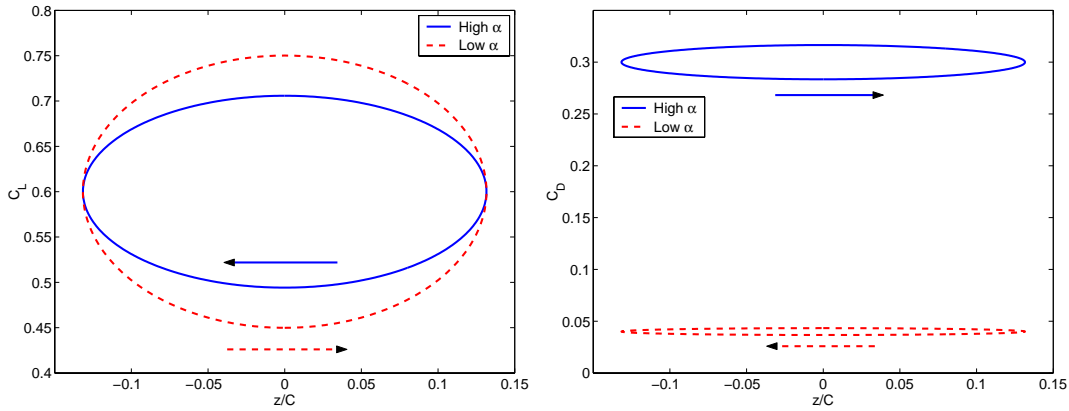


Figure 3.8: *Quasi-stationary force coefficient loops. The high- α curves are computed from $C_{L\alpha} = 0.6$, $C'_{L\alpha} = -3.5$, $C_{D\alpha} = 0.3$ and $C'_{D\alpha} = 1.1$, corresponding to a stalling airfoil at approximately $\alpha = 20^\circ$. The low- α curves are computed from $C_{L\alpha} = 0.6$, $C'_{L\alpha} = 4.5$, $C_{D\alpha} = 0.04$ and $C'_{D\alpha} = 0.5$, corresponding to an airfoil at approximately $\alpha = 7^\circ$. The other parameters for this example were $A/c = 0.1316$, $f_{red} = 0.02$ and $\beta = 0^\circ$.*

All curves have horizontal symmetry axis, in contrast to the analytical unsteady potential results shown in figure 3.4. This follows from the geometrical basis on which the quasi stationary theory is founded. In other words this difference underlines the fact that quasi-stationary theory has no memory.

It is evident from equation 3.79, that the effect of the stationary lift, $C_{L\alpha}$, and the effect of the slope of the stationary drag, $C'_{D\alpha}$, acts in opposite directions. It is the difference between these two terms that determines the direction of the drag loops in the pure heave case, $\beta = 0^\circ$.

Investigation of equation 3.87, yields important information into the driving mechanisms behind quasi-stationary aerodynamic damping for one dimensional translatory motion of an airfoil. The drag term, $C_{D\alpha}$, is always positive, as is $1 + \sin^2 \beta$. This implies that the drag in a quasi-stationary computation is increasing the aerodynamic damping. The term related to the slope of the lift curve involves a $\cos^2 \beta$, which is positive or zero for all values of β . This implies that the effect of this term is greatest in the direction perpendicular to the free stream, $\beta = 0^\circ$, and that the sign of the aerodynamic damping is given by the slope of the lift curve, $C'_{L\alpha}$. The last term involves the sum of the lift coefficient, and the slope of the drag coefficient, which are both positive for α between 0° and 180° . This implies that the sign of the damping from these is dictated by $\sin \beta \cos \beta = 0.5 \sin 2\beta$, which is negative from $\alpha = 90^\circ$ to $\alpha = 180^\circ$, and has minimum for $\alpha = 135^\circ$.

It should be stressed that the results from this analysis is valid only if the assumption of quasi-stationarity is obeyed. However, the results from this analysis give an indication as to how the different terms affect the loops and the aerodynamic damping.

3.4 New Stall Model

In this section a heuristic dynamic model for prediction of the dynamic loads on an two dimensional airfoil undergoing oscillatory motion is proposed. The foundation on which the model is based is the theory presented in the previous two sections.

The new stall model could be considered an ‘interpolation’ between Quasi-Stationary and Unsteady Potential theory. The model is identical to Unsteady Potential Theory when airfoil characteristics from steady potential theory is used as input to the model, and except from the terms arising from acceleration of a virtual mass, the new model is identical to Quasi-Stationary theory as $f_{red} \rightarrow 0$.

Since the validation of the model will be against translatory experimental data only, focus will be on the translatory sub-case. The only inputs to the model are the oscillation frequency and the steady lift and drag coefficients, and their derivatives with respect to angle of attack, which is available for practically all airfoils. The fact that no other model constants are needed means that no tuning of the model is required or possible.

3.4.1 Motivation

The motivation for this model is the obvious similarity between the expressions for the lift coefficients in the general translatory quasi-stationary case, as derived in section 3.3,

$$C_L = (1 - 2\frac{\dot{x}}{V}) \left(C_{L\alpha} - \frac{\dot{y}}{V}(C_{D\alpha} + C'_{L\alpha}) \right) \quad (3.88)$$

and the lift coefficients from unsteady potential flow theory in the case of no angular motion, $\dot{\alpha} = \ddot{\alpha} = 0$,

$$C_L = 2\pi \left[(1 - \frac{\dot{x}}{V})^2 \alpha - \frac{\dot{y}(V - \dot{x})}{V^2} \right] \mathbf{C}(k) - \frac{\pi b}{V^2} (\ddot{x}\alpha + \dot{y}). \quad (3.89)$$

The similarity between the expressions become more evident after a linearization of the potential theory expressions

$$C_L = \left[(1 - 2\frac{\dot{x}}{V}) 2\pi \alpha - \frac{\dot{y}}{V} 2\pi \right] \mathbf{C}(k) - \frac{\pi b}{V^2} (\ddot{x}\alpha + \dot{y}). \quad (3.90)$$

If the general steady state potential flow theory results for the force coefficients on an infinitely thin airfoil

$$C_{L\text{ pot}} = 2\pi\alpha \quad (3.91)$$

$$C_{D\text{ pot}} = 0 \quad (3.92)$$

are inserted in the quasi-steady expression, equation 3.88, it is noted that the result after a linearization

$$C_L = (1 - 2\frac{\dot{x}}{V}) C_{L\alpha} - \frac{\dot{y}}{V} C'_{L\alpha}, \quad (3.93)$$

is identical to the quasi-steady term in the unsteady potential flow theory expression. The additional term in the unsteady potential flow theory is the virtual mass term, which does not appear in the quasi-stationary expressions because the derivation of the quasi-steady theory is based on velocity triangles only, and therefore does not include accelerations.

3.4.2 The Model

The main assumption behind the model to be proposed is that the flow can be described by a model similar to the unsteady potential flow case for both attached and stalling flows. Potential flow theory describes fully attached flows, and is thus only valid at small angles of attack. The new model is similar to the unsteady potential flow theory in the sense that the quasi-steady forces arising from the steady lift, and the corresponding wake effect are assumed to act in the quarter chord point and to be governed by the same variables. Moreover, the virtual mass effect is assumed to have the same form as in the unsteady potential flow theory, and act in the same point on the chord, namely the half-chord. As in the case of the analytic unsteady potential flow solution in section 3.2, it is assumed that the airfoil is undergoing small oscillations in translation and pitch, x , y and α , with the restriction that the frequency of the three motions are identical.

The drag from a steady potential flow solution is zero, a fact which is known as d'Alembert's Paradox. Therefore, the drag in an unsteady potential flow computation basically consists of two parts. The first part is induced from the effect of the lift forces in combination with the change in relative angle of attack from the unsteady wake and the motion of the airfoil, as elaborated in section 3.2. The second part is a contribution from the acceleration of a virtual mass, which can be thought of as the mass of the fluid surrounding the airfoil.

In order to model the characteristics of a real viscous flow-field around an airfoil, additional terms describing the effects of the non-zero steady drag coefficients are required. At high angles of attack, when the airfoil is stalling, the drag forces are of the same order of magnitude as the lift forces, and therefore important to model. In this work the drag forces will be treated analogous to the lift forces in the sense that the force from the experimentally obtained static drag coefficients are modified using the same renormalization coefficient, $C(k)$, as will be used in the lift expression, and that these terms induce forces in the lift direction, analogous to the induced drag term in unsteady potential theory.

The forces in the present model can be split up into three categories

- Force terms related to static C_L values and derivatives
- Force terms related to acceleration of virtual mass
- Force terms related to static C_D values and derivatives

The contribution to the forces from the separate effects are shown below, after which the complete model is stated and discussed.

Force Terms Related to Static C_L

If the force expressions from unsteady potential theory are interpreted along the lines suggested in section 3.4.1, meaning that $2\pi\alpha$ terms are interpreted as $C_{L\alpha}$, and 2π terms are interpreted as $C'_{L\alpha}$, the following force terms related to the static C_L curve arise

$$C_L^L = (1 - \frac{\dot{x}}{V}) \{ C_{L\alpha} - \left[\frac{\dot{y}}{V} C'_{L\alpha} + \frac{\dot{x}}{V} C_{L\alpha} + \frac{b(a-0.5)}{V} \dot{\alpha} C'_{L\alpha} - \alpha_1 C'_{L\alpha} \right] \mathbf{C}(k) \} \quad (3.94)$$

$$C_D^L = \left[\frac{\dot{y}}{V - \dot{x}} + \frac{C_L^{L,QS} - C_L^L}{\text{sign}(C'_{L\alpha}) \max(\text{abs}(C'_{L\alpha}), \pi/8)} \right] C_L^L \quad (3.95)$$

$$C_M^L = 0.5C_L^L(a+0.5)\cos\alpha + 0.5C_D^L(a+0.5)\sin\alpha \quad (3.96)$$

where the quasi-static lift coefficient, $C_L^{L,QS}$, is given by

$$C_L^{L,QS} = (1 - \frac{\dot{x}}{V}) \{ C_{L\alpha} - \left[\frac{\dot{y}}{V} C'_{L\alpha} + \frac{\dot{x}}{V} C_{L\alpha} + \frac{b(a-0.5)}{V} \dot{\alpha} C'_{L\alpha} - \alpha_1 C'_{L\alpha} \right] \} \quad (3.97)$$

The subscripts refer to the direction of the force terms, whereas the superscripts refer to the source of the terms.

Note in the above formulation for the drag coefficient, equation 3.95, that an indirect formulation of C_D^L based on the interpretation of the unsteady potential drag given in section 3.2 is used. The drag in an unsteady potential flow is induced from the lift due to the change in relative angle of attack from the motion of the profile and the induced velocities from the wake. The manipulation with the last term in the bracketed expression in equation 3.95 is effectively a limiter to the size of the term if $C'_{L\alpha}$ is close to zero. This avoids the problems that may occur if the local slope of the lift coefficient is zero.

The forces arising from the static lift forces are assumed to act in the quarter chord point, as in unsteady potential theory, for all angles of attack. The validity of this assumption is questionable for separated flows, since the separated regions loses its lift, hence moving the point in which the forces act towards the leading edge. This, however, only affects the moment coefficient.

Force Terms Related to Acceleration of Virtual Mass

The force terms arising from acceleration of the mass of air surrounding the airfoil are a generalized version of the virtual mass terms from unsteady potential theory, taking into account that the angles of attack are not necessarily small. This results in the following contributions from the acceleration of the virtual mass

$$C_L^{VM} = -\frac{\pi c}{2V^2} (\ddot{x}\sin\alpha + \ddot{y}\cos\alpha + ab\ddot{\alpha} - (V - \dot{x})\dot{\alpha})\cos\alpha \quad (3.98)$$

$$C_D^{VM} = C_L^{VM} \tan\alpha - \frac{\pi c^2}{2V^2} \dot{\alpha}^2 \quad (3.99)$$

$$C_M^{VM} = 0.5aC_L^{VM}\cos\alpha + 0.5aC_D^{VM}\sin\alpha - \frac{\pi c(V - \dot{x})}{8V^2}\dot{\alpha} - \frac{\pi c^2}{64V^2}\ddot{\alpha} \quad (3.100)$$

Force Terms Related to Static C_D

Since real viscous flows separates and stalls, the model should include that a considerable part of the total forces can be in the stream-wise direction in both stationary and moving airfoils. Therefore additional assumptions have to be made regarding the modelling of the forces related to the non-zero stationary drag coefficients and their unsteady counterpart. The basic assumption of the drag related forces, is that the drag and lift are behaving the same way. The instantaneous forces arising from the steady drag is given by the quasi steady drag modified analogous to the quasi-stationary lift in equation 3.94, through the constant \mathbf{C} , taking into account phase lag and magnitude deficiency effects due to wake interaction. Also the drag induced lift, the drag analog to equation 3.95, is included in the model. It is assumed that the drag related forces act in the half-chord point. This is used for calculating the moment from the flow. The forces arising from the steady drag coefficient are given below

$$C_L^D = -C_{D\alpha} \frac{\dot{y}}{V - \dot{x}} \mathbf{C}(k) \quad (3.101)$$

$$C_D^D = C_{D\alpha} - \frac{\dot{y}}{V - \dot{x}} C'_{D\alpha} \mathbf{C}(k) \quad (3.102)$$

$$C_M^D = 0.5aC_L^D \cos \alpha + 0.5aC_D^D \sin \alpha \quad (3.103)$$

Note that the assumption that the drag forces act in the half-chord point at all incidences are based on sheer guessing, rendering the moment expression very uncertain at high incidences.

The Complete Model

Adding the contributions from the lift, virtual mass and drag, equations 3.94 to 3.103, yields the full form of the new dynamic model for the lift, drag and moment coefficients

$$C_L = C_L^L + C_L^{VM} + C_L^D \quad (3.104)$$

$$C_D = C_D^L + C_D^{VM} + C_D^D \quad (3.105)$$

$$C_M = C_M^L + C_M^{VM} + C_M^D \quad (3.106)$$

Since the model will be validated using translatory data, the simpler translatory sub-case, where $\dot{\alpha} = \ddot{\alpha} = 0$, is given below :

$$C_{LT}^L = (1 - \frac{\dot{x}}{V}) \{ C_{L\alpha} - \left[\frac{\dot{y}}{V} C'_{L\alpha} + \frac{\dot{x}}{V} C_{L\alpha} \right] \mathbf{C}(k) \} \quad (3.107)$$

$$C_{LT}^{L,QS} = (1 - \frac{\dot{x}}{V}) \{ C_{L\alpha} - \left[\frac{\dot{y}}{V} C'_{L\alpha} + \frac{\dot{x}}{V} C_{L\alpha} \right] \} \quad (3.108)$$

$$C_{LT}^{VM} = -\frac{\pi c}{2V^2} (\ddot{x} \sin \alpha + \ddot{y} \cos \alpha) \cos \alpha \quad (3.109)$$

$$C_{LT}^D = -C_{D\alpha} \frac{\dot{y}}{V - \dot{x}} \mathbf{C}(k) \quad (3.110)$$

$$C_{LT} = C_{LT}^L + C_{LT}^{VM} + C_{LT}^D \quad (3.111)$$

$$C_{DT}^L = C_{LT}^L \frac{\dot{y}}{V - \dot{x}} + \frac{C_{LT}^{L,QS} - C_{LT}^L}{\text{sign}(C'_{L\alpha}) \max(\text{abs}(C'_{L\alpha}), \pi/8)} C_{LT}^L \quad (3.112)$$

$$C_{DT}^{VM} = C_{LT}^{VM} \tan \alpha \quad (3.113)$$

$$C_{DT}^D = C_{D\alpha} - \frac{\dot{y}}{V - \dot{x}} C'_{D\alpha} \mathbf{C}(k) \quad (3.114)$$

$$C_{DT} = C_{DT}^L + C_{DT}^{VM} + C_{DT}^D \quad (3.115)$$

$$C_{MT}^L = 0.5 C_{LT}^L (a + 0.5) \cos \alpha + 0.5 C_{DT}^L (a + 0.5) \sin \alpha \quad (3.116)$$

$$C_{MT}^{VM} = 0.5a C_{LT}^{VM} \cos \alpha + 0.5a C_{DT}^{VM} \sin \alpha \quad (3.117)$$

$$C_{MT}^D = 0.5a C_{LT}^D \cos \alpha + 0.5a C_{DT}^D \sin \alpha \quad (3.118)$$

$$C_{MT} = C_{MT}^L + C_{MT}^{VM} + C_{MT}^D \quad (3.119)$$

The T in the subscripts of equations 3.107 to 3.119 refer to the translatory motion. As mentioned earlier, the model can be considered an extension of the quasi-steady theory to take into account the unsteady interaction as explained by unsteady potential theory. In the limit of $f_{red} \rightarrow 0$, the proposed model is equal to the quasi-stationary theory with the addition of the virtual mass terms from the unsteady potential flow theory. If, on the other hand, lift and drag coefficients from steady potential theory,

$$C_{Lpot} = 2\pi\alpha \quad (3.120)$$

$$C_{Dpot} = 0, \quad (3.121)$$

are used as input to the new model, the model is identical to the expressions from the unsteady potential theory for small angles of attack.

In order to give an impression of the relative importance of the different terms in the model, figure 3.9 shows the non dimensional force terms as function of position coordinate, z , for translatory motion of an stalling airfoil oscillating in the direction perpendicular to the free-stream. The values of the lift, drag and reduced frequency corresponds to values in the experimental measurements described in chapter 2. The left figures show the non dimensional terms related to the lift forces. On the upper figure the phase shifting effect of the unsteady wake is observed when comparing the quasi-steady lift term, $C_{LT}^{L,QS}$, with the term including the effect from the unsteady wake, C_{LT}^L . The direction of all three loops in the upper left figure is clockwise, indicating a negative aerodynamic damping. It is seen that the aerodynamic damping

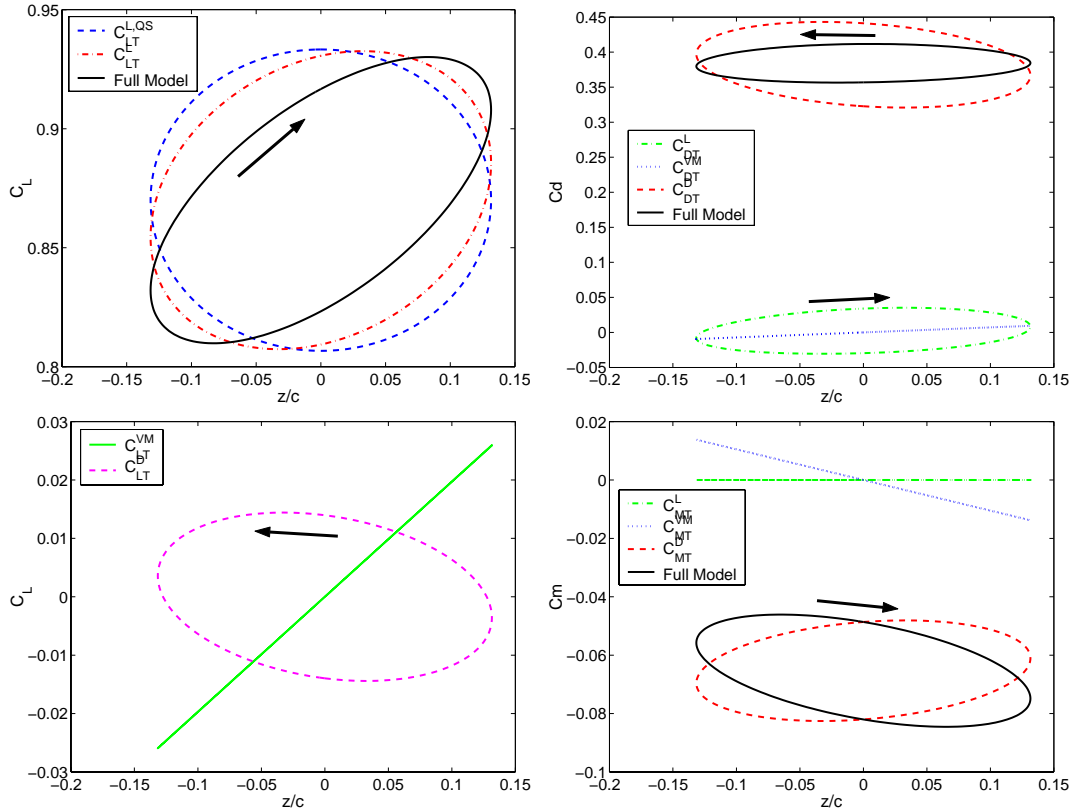


Figure 3.9: Force terms for translatory motion in stall. Non-dimensional force terms versus z/c . The data shown are based on $\alpha = 20^\circ$, $\beta = 0^\circ$, $f_{red} = 0.03$, $A/c = 0.1316$, $C_{L\alpha} = 0.87$, $C'_{L\alpha} = -1.67$, $C_{D\alpha} = 0.38$ and $C'_{D\alpha} = 1.62$. Upper left : Lift coefficient terms C_{LT}^{LQS} , C_{LT}^L and C_{LT} . Lower left : Lift coefficient terms C_{LT}^{VM} and C_{LT}^D . Upper right : Drag coefficient terms C_{DT}^L , C_{DT}^{VM} , C_{DT}^D and C_{DT} . Lower right : Quarter chord moment coefficient terms C_{MT}^L , C_{MT}^{VM} , C_{MT}^D and C_{MT} .

from the full model lift forces is less than for the terms from the unsteady lift forces, C_{LT}^L . The difference in damping comes from the forces induced from the damping, C_{LT}^D , shown in the lower left figure together with the contribution from the virtual mass, C_{LT}^{VM} . It is seen that the contribution to the aerodynamic damping from the forces induced by the drag, C_{LT}^D , are positive, acting in the opposite direction of the damping from the lift contribution, C_{LT}^L . The phase shifting effect is evident from this term as well, as a pure quasi-steady induced drag would have maximum at $z/c = 0$. The aerodynamic damping of the virtual mass lift terms, C_{LT}^{VM} , is zero, as suspected. The upper right figure show the non dimensional drag terms. These forces do not contribute to aerodynamic damping because the direction of the motion is perpendicular to these forces in this case. The hysteresis loops of the drag terms from the lift, C_{DT}^L , and the drag, C_{DT}^D , are in opposite directions as for the lift. The direction of the hysteresis loops for the full model is the same as for the terms from the drag, C_{DT}^D , which is counter-clockwise. Again, the virtual mass loop, C_{DT}^{VM} , is a line with positive slope, in agreement with the nature of the virtual mass terms.

The contributions to the dimensionless quarter-chord moment loop are shown in the lower right figure. There is no contribution from the lift, C_{MT}^L , since these forces act in the quarter chord point. The slope of the virtual mass force-line in this case is negative due to the fact that the forces from acceleration of the virtual mass act in the half-chord point. The major contribution to the moment, C_{MT}^D , comes from the drag which act in the half-chord point. The direction of the full model hysteresis loop is clockwise.

As a side note it should be mentioned that the term mainly responsible for the negative aerodynamic damping is the term involving the slope of the static lift, $C'_{L\alpha}$, analogous to quasi-steady theory. Unsteady potential theory always predicts a positive aerodynamic damping because the flow is always attached, corresponding to a positive lift slope. The effect of the terms from the drag are an added aerodynamic damping in the lift direction, whereas the effect of the drag terms on the aerodynamic damping in the drag direction depends on the direction of the motion, β , analogous to the quasi-steady case.

The present formulation of the model concerns oscillatory motion only. It is, however, possible to rewrite equations 3.107 to 3.119 to include arbitrary motion of the airfoil. The method is outlined for a standard unsteady potential theory solution in section 5-7 of Bisplinghoff [7], but is applicable to the present model with minor modifications only.

The questionable issues and simplifications regarding this model are summarized below.

- The assumptions on which the expression for the moment is based on are very crude. The mean value as well as the amplitude of the moment coefficient will most likely not be correct at high incidences.
- It is dubious that the complex dynamics of the flow at deep stall are captured accurately due to the assumption of similarity with the unsteady potential flow solution.
- The model cannot deal with big oscillations due to the fact that it is based on a linearization around a single angle of attack.

The effect of the assumptions made is studied in the comparison with experimental data in chapter 4.

3.5 Panel Code

Solution of the unsteady inviscid, incompressible flow equations by means of analytical approaches are only possible in very few cases, mostly by use of coarse simplifications and crude assumptions. The use of numerical modelling allows treatment of more realistic geometries, such as specific airfoils, flaps, or, as it will be shown in this section, a complete system of an airfoil in a wind tunnel.

The solution of incompressible, inviscid flows can be obtained by distributing elementary solutions of the continuity equation

$$\nabla \cdot \mathbf{U} = 0, \quad (3.122)$$

on the problem boundaries, such that the Neumann condition is fulfilled on the solid surfaces. The additional condition in the formulation of the general potential problem is automatically fulfilled when using elementary solutions. This additional requirement is that the difference between the undisturbed flow velocity and the actual flow velocity should decay far from the body [27].

Since each elementary solution affects the whole fluid field, the general solution of the potential flow problem requires integration over all the elementary solutions. The velocity components of the elementary solutions are incremental, and can be added up according to the principle of superposition. The problem is then reduced to finding the singularity element distribution satisfying the Neumann boundary condition.

For a given set of boundary conditions, the solution of the problem using superposition of singular elements is not unique. This means that some freedom is allowed, as will become evident later in this section.

The panel method used in the present work was proposed by Hess [22]. Hess' method uses constant strength source and vortex distributions, and overcomes the problems with pressure coefficient fluctuations at the thin trailing edge associated with solutions using constant strengths doublets, see figure 3.10.

Validation of the implemented panel code are found in appendix C, along with discretization independence studies.

3.5.1 Singularity Elements

The singularity elements used in this work are two dimensional point vortices, constant strength source distributions, and constant strength vortex distributions. The distributed elements are used on the solid bodies, whereas the point vortices are used in the unsteady wake.

The velocity induced at (x, y) from a point vortex located in (x_0, y_0) with circulation

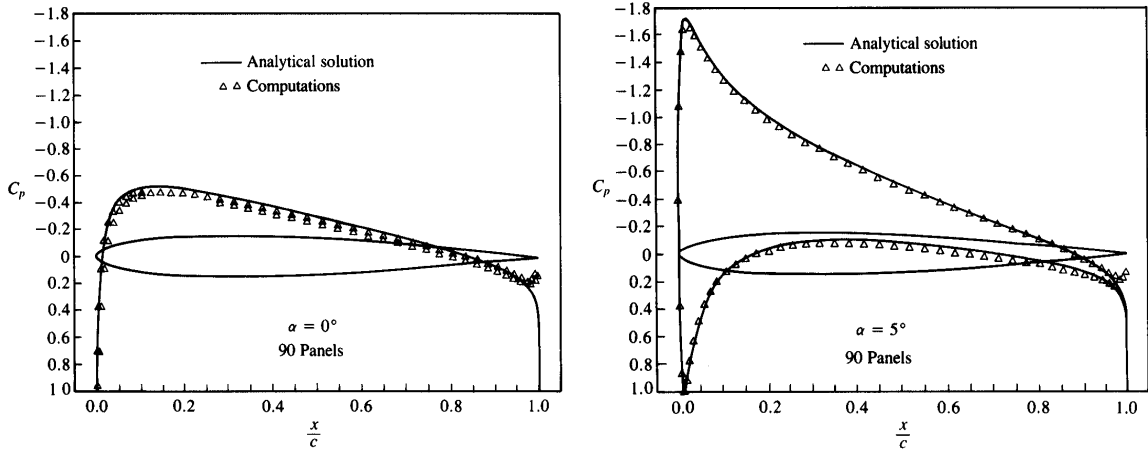


Figure 3.10: *Chordwise pressure distribution computed by a constant-strength doublet method. Symmetric airfoil at $\alpha = 0^\circ$ (left) and $\alpha = 5^\circ$ (right). From Katz et. al. [27].*

Γ is given by [27]

$$U = \frac{\Gamma}{2\pi} \frac{y - y_0}{(x - x_0)^2 + (y - y_0)^2} \quad (3.123)$$

$$V = \frac{-\Gamma}{2\pi} \frac{x - x_0}{(x - x_0)^2 + (y - y_0)^2}. \quad (3.124)$$

The most straightforward way to use the two dimensional constant strength singularity elements is in a panel attached coordinate system as shown in figure 3.11. In this local

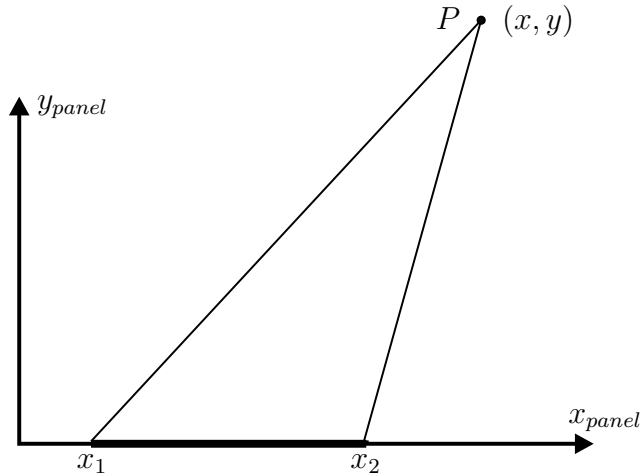


Figure 3.11: *Panel-attached coordinate system.*

system, the velocities induced at point P from the panel of constant source strength per length is

$$U_{panel} = \frac{\sigma}{2\pi} \int_{x_1}^{x_2} \frac{x - x_0}{(x - x_0)^2 + y^2} dx_0 \quad (3.125)$$

$$V_{panel} = \frac{\sigma}{2\pi} \int_{x_1}^{x_2} \frac{y}{(x - x_0)^2 + z^2} dx_0. \quad (3.126)$$

It can be shown [27], that this is equal to

$$U_{panel} = \frac{\sigma}{4\pi} \ln \frac{(x - x_1)^2 - y^2}{(x - x_2)^2 - y^2} \quad (3.127)$$

$$V_{panel} = \frac{\sigma}{2\pi} \left(\arctan \frac{y}{x - x_2} - \arctan \frac{y}{x - x_1} \right). \quad (3.128)$$

When P is on the center of the panel the velocities are

$$U_{panel} = 0 \quad (3.129)$$

$$V_{panel} = \pm \frac{\sigma}{2}, \quad (3.130)$$

where the \pm refer to the upper and the lower side of the panel, respectively.

Since the velocities and coordinates in equations 3.125-3.130 are given in panel coordinates, the coordinates for P have to be transformed from global coordinates to panel coordinates

$$x_{panel} = (x - x_0) \cos \alpha_i - (y - y_0) \sin \alpha_i \quad (3.131)$$

$$y_{panel} = (x - x_0) \sin \alpha_i + (y - y_0) \cos \alpha_i, \quad (3.132)$$

where α_i is the angle the panel system is rotated with respect to the global system, positive clockwise. The velocities from equation 3.127-3.130 has to be transformed from panel coordinates to global coordinates

$$U = U_{panel} \cos \alpha_i + V_{panel} \sin \alpha_i \quad (3.133)$$

$$V = -U_{panel} \sin \alpha_i + V_{panel} \cos \alpha_i. \quad (3.134)$$

Since the induced velocities from a point vortex and a point source are identical, except that the velocity induced from the point vortex is rotated 90° clockwise with respect to the velocity induced by the point source, it follows from the principle of superposition, that the same feature is evident for the two dimensional constant strength singularity elements. Therefore it follows from equations 3.127 and 3.128, that the induced velocities from a constant-strength vortex distribution is

$$U_{panel} = \frac{\gamma}{2\pi} \left(\arctan \frac{y}{x - x_2} - \arctan \frac{y}{x - x_1} \right), \quad (3.135)$$

$$V_{panel} = -\frac{\gamma}{4\pi} \ln \frac{(x - x_1)^2 - y^2}{(x - x_2)^2 - y^2} \quad (3.136)$$

in panel coordinates. Analogous to equations 3.129 and 3.130, the local velocities at the center of the panel are

$$U_{panel} = \pm \frac{\gamma}{2} \quad (3.137)$$

$$V_{panel} = 0. \quad (3.138)$$

As previously, the \pm refer to the upper and the lower side of the panel.

3.5.2 Steady Solution

As explained in the beginning of this section, the principle of superposition is used for computation of the total velocities from the singularity elements. Since the velocity increments depend linearly on the strength of the elements, a linear system of equations has to be solved to determine the panel code solution.

The panel code method used in the present work was proposed by Hess [22], and uses distributed source and vorticity on the airfoil. If the airfoil is discretized using N panels, then N collocation points are defined on the mid-panel points, on the side of the panel facing outward. The Neumann condition is enforced in these points. However, one additional constraint on the solution is needed.

The trailing edge condition known as the Kutta-Joukowski condition is a consequence of viscosity. The effect of the thin viscous dominated boundary layer on an airfoil in attached flow, is that the velocity must remain finite and tangent to the airfoil at the sharp trailing edge. This implies that the total tangential velocity on the upper and lower side of the airfoil should be identical in steady flows.

The total sum of constraints is $N + 1$, but there are $2N$ independently adjustable source and vortex strengths. Hess [22] used this freedom to specify that all vortex panels should keep the same strength relative to each other, such that the strength of all vortex elements is controlled by one parameter. The strength of the vortex panels is a parabolic function of surface length, zero on the trailing edge, and maximum at the leading edge of the airfoil,

$$\gamma_u(s) = C_1 \left(\frac{s}{s_{max}} - \left(\frac{s}{s_{max}} \right)^2 \right). \quad (3.139)$$

In the above equation, the surface length parameter is denoted by s . The value of the 'unit-level' vorticity, γ_u , is scaled using the constant C_1 , such that the total circulation of the airfoil is one.

$$C_1 = \frac{6}{s_{max}} \quad (3.140)$$

In the numerical code, the continuous γ_u is approximated with the constant strength vorticity panels. Linking all vortex strengths together reduces the number of variables to $N + 1$, and the linear system for the steady case can thus be stated

$$\begin{pmatrix} a_{1,1} & a_{1,2} & \dots & \dots & a_{1,N} & b_1 \\ a_{2,1} & a_{2,2} & \dots & \dots & a_{2,N} & b_2 \\ \vdots & \vdots & \ddots & & \vdots & \vdots \\ \vdots & \vdots & & \ddots & \vdots & \vdots \\ a_{N,1} & a_{N,2} & \dots & \dots & a_{N,N} & b_N \\ c_1 & c_2 & \dots & \dots & c_N & c_T \end{pmatrix} \begin{pmatrix} \sigma_1 \\ \sigma_2 \\ \vdots \\ \vdots \\ \sigma_N \\ \Gamma \end{pmatrix} = \begin{pmatrix} \text{RHS}_1 \\ \text{RHS}_2 \\ \vdots \\ \vdots \\ \text{RHS}_N \\ \text{RHS}_{\Delta T} \end{pmatrix}. \quad (3.141)$$

The first N equations in the linear system above is the enforcement of the Neumann boundary condition, meaning that the total normal component of the velocity relative to the solid surface should be zero. The last equation expresses the Kutta-Joukowski

condition. The σ_i 's are the source strengths of the panels, and Γ is the total circulation on the airfoil from the vortex panels. The influence coefficient, a_{ij} , expresses the normal velocity induced on collocation point i from source strength 1 on panel j . b_i is the normal velocity induced on collocation point i , induced by a strength of the vortex panels with total circulation $\Gamma = 1$. c_i expresses the addition to the difference in tangential velocity at the upper and lower trailing edge panels from source panel i . The term c_Γ expresses the difference in tangential velocity induced by a strength of the vortex panels with total circulation $\Gamma = 1$. The right hand side terms, RHS_i , is the negative normal component of the free stream on panel i at the given incidence of the airfoil. The last term, $\text{RHS}_{\Delta T}$, is the negative difference in tangential components at the trailing edge from the free stream velocity.

Once this linear system is set up, it is straightforward to solve for the source and vortex strengths, after which the velocity distribution can be evaluated. From these the forces can be found using Bernoulli's equation, 3.7, noting that the time dependant terms vanish in this case.

It should be pointed out that the steady solution is not in conflict with the Kelvin theorem. It is assumed that the unsteady starting vortex corresponding to the steady lift is convected very far downstream, such that the influence of it is negligible. Since there is no change in the bound vorticity, no wake is shed.

3.5.3 Unsteady Solution

The incompressible continuity equation does not directly include time-dependant terms. The time dependency in unsteady panel codes is introduced through the boundary conditions. It could be stated that the 'memory' of panel methods lies in the unsteady wake.

The strength of the unsteady wake is determined from Kelvin's theorem, which states that the total vorticity of in a closed amount of fluid cannot change in time. This implies that any change in bound vorticity on the airfoil is reflected in the wake of the airfoil. From Kelvin's theorem it follows that, for time-step i , the circulation of the shed vorticity, Γ_{w1} , is

$$\Gamma_{w1} = \Gamma_{i-1} - \Gamma_i. \quad (3.142)$$

From the Kutta-Joukowski condition, it follows that the vortex-sheet, which in the present work is discretized using point vortices, is shed from the trailing edge of the airfoil. Since there is a jump in the velocity over the vortex-sheet, the unsteady version of the Kutta-Joukowski condition implies that this velocity-difference should be equal to the difference in the tangential velocities at the upper and lower trailing edge panels. The velocity jump over the part of the wake-sheet closest to the airfoil can be determined by considering a vortex panel with the same circulation as the first wake vortex, with a length equal to the distance a fluid particle would travel in one time-step,

$$l = V_{\text{Kutta}} \Delta t. \quad (3.143)$$

The velocity difference over such a vortex panel is equal to

$$\Delta V = \gamma = \frac{\Gamma_{w1}}{l} \quad (3.144)$$

at mid-panel.

The direction of the first vortex sheet is in the trailing-edge half-angle-direction, which for symmetric airfoils equals the centerline of the airfoil. This direction will be referred to as the kutta-direction. The magnitude of the velocity at the trailing edge, V_{Kutta} , is determined as

$$V_{\text{Kutta}} = \left(\frac{1}{2} (\vec{V}_{TE,u} + \vec{V}_{TE,l}) + \vec{V}_{\text{mov}} + \vec{V}_{\text{freestr}} + \vec{V}_{\text{wake}} \right) \cdot \vec{n}_{\text{Kutta}}, \quad (3.145)$$

where 'TE,u' and 'TE,l' refer to the upper and lower trailing edge panels, 'mov' refer to relative motion at the trailing edge, 'freestr' to free-stream flow and 'wake' to induced velocities from the wake. \vec{n}_{Kutta} is a unit vector in the kutta-direction.

The first wake vortex is positioned the distance $C_{WV} V_{\text{Kutta}} \Delta t$ from the trailing edge in the kutta-direction, where the value of C_{WV} in the present work was set to 0.25. According to Katz et. al. [27], values of the wake constant, C_{WV} , should be set in the range $C_{WV} = 0.2$ to $C_{WV} = 0.3$. This is done because the lumped vortex approach with $C_{WV} = 0.5$ underestimates the induced velocities close to the trailing edge compared to a continuous constant strength vortex sheet with the same circulation.

The unsteady wake is integrated in time in the global coordinate-system, with the local flow velocities obtained from vectorial summation of free-stream velocity, induced velocity from solid body source panels, induced velocity from solid body vortex panels and induced velocity from the unsteady wake. Euler integration was employed in the present work, since the evaluation of the wake velocity is among the more time consuming steps in an unsteady panel code.

Below, the linear system of equations in the unsteady case is given

$$\begin{pmatrix} a_{1,1} & a_{1,2} & \dots & \dots & a_{1,N} & b_1 & d_1 \\ a_{2,1} & a_{2,2} & \dots & \dots & a_{2,N} & b_2 & d_2 \\ \vdots & \vdots & \ddots & & \vdots & \vdots & \vdots \\ \vdots & \vdots & & \ddots & \vdots & \vdots & \vdots \\ a_{N,1} & a_{N,2} & \dots & \dots & a_{N,N} & b_N & d_N \\ c_1 & c_2 & \dots & \dots & c_N & c_\Gamma & c_{\Gamma w1} \\ 0 & 0 & \dots & \dots & 0 & 1 & 1 \end{pmatrix} \begin{pmatrix} \sigma_1 \\ \sigma_2 \\ \vdots \\ \vdots \\ \sigma_N \\ \Gamma_i \\ \Gamma_{w1} \end{pmatrix} = \begin{pmatrix} \text{RHS}_1 \\ \text{RHS}_2 \\ \vdots \\ \vdots \\ \text{RHS}_N \\ \text{RHS}_{\Delta T} \\ \Gamma_{i-1} \end{pmatrix}. \quad (3.146)$$

The meaning of the terms in the above equation are identical to the steady case, but some additional terms exist. First, the added equation, the last row in the equations, expresses Kelvin's theorem directly from equation 3.142. The terms d_1 to d_N is the influence coefficients for the nearest wake vortex on the normal velocities on the panels. These are equal to the induced normal velocity on the panels from the nearest wake vortex with unit strength. The last influence coefficient, $c_{\Gamma w1}$, consist of two parts. The fist part is the induced tangential velocity difference on the upper and lower trailing edge collocation points, the other part arise because the strength of the first wake vortex determines the difference in tangential velocity at the trailing edge, shown in equation 3.144. In a more mathematical formulation this corresponds to

$$c_{\Gamma w1} = \vec{V}_{TE,u} \cdot \vec{T}_{TE,u} - \vec{V}_{TE,l} \cdot \vec{T}_{TE,l} + \frac{1}{V_{\text{Kutta}} \Delta t}. \quad (3.147)$$

$\vec{T}_{\text{TE},u}$ and $\vec{T}_{\text{TE},l}$ denotes unit vectors in the airfoil-fixed relative system, positive in the attached flow direction, in the tangential direction on the upper and lower panels at the trailing edge. Note that in the above expression, the result from equation 3.143 and 3.144 is used to link the first wake vortex strength to the difference in tangential velocity on the trailing edge upper and lower sides.

Note that the linear system of equations is formulated in the relative, airfoil-fixed, coordinate-system. Since the position of the first wake-vortex is not constant in the relative frame of reference, d_1 to d_N , and $c_{\Gamma w1}$ has to be re-computed each time-step. This is true also for all right-hand side terms, since these terms reflect the influence of free-stream, relative motion and unsteady wake on the airfoil system. The relative velocity due to the motion of the airfoil is determined from simple geometric vectorial expressions, and the induced velocities from the unsteady wake is integrated from the wake vortices, not including the first one, Γ_{w1} , which is included in the computations.

Once the linear system is solved for a time-step, the forces can be derived from the velocities on the profile by use of the unsteady Bernoulli equation, equation 3.7.

$$\frac{\partial}{\partial t} \left(\int_1^2 U_s ds \right) + \left(\frac{p_2}{\rho} + \frac{U_2^2}{2} \right) - \left(\frac{p_1}{\rho} + \frac{U_1^2}{2} \right) = 0 \quad (3.7)$$

The unsteady term is discretized in the numerical code as

$$\frac{\partial}{\partial t} \left(\int_1^2 U_s ds \right) \simeq \frac{\left(\int_1^2 U_s ds \right)_t - \left(\int_1^2 U_s ds \right)_{t-\Delta t}}{\Delta t}, \quad (3.148)$$

where the indexes 1 and 2 refer to points on the surface of the airfoil. In this way the information about the velocities at the present and previous time-step, and the value of the time-step, are used to compute the unsteady term in the Bernoulli equation. Thereby the unsteady pressure distribution, and the integral forces can be found.

The schematic flow chart for one step of the numerical solution of the unsteady airfoil problem is

- **Assign positions and derivatives.** The position of the airfoil is assigned, as is the derivative of the positions.
- **Calculation of influence coefficients.** The main part of the influence coefficients does not change in time, and are computed before the time loop is started. In the time loop only d_1 to d_N , and $c_{\Gamma w1}$ have to be updated each time-step.
- **Calculate RHS vector.** The RHS vector is a function of momentary position and velocity, free-stream velocity, and induced velocities from the wake. All terms are updated each time-step.
- **Solution of linear system.** In the present work the resulting linear system was solved using the standard solver for linear equations in Matlab.
- **Calculate loads.** The velocities on the airfoil are calculated. From these the pressures are calculated using the Bernoulli equation. The pressures are used to compute the integral forces.

- **Wake roll-up.** The position of the wake vortices are updated in the global frame of reference using the total velocities, which are vectorial sums of the free-stream velocity, the induced velocities from the solid body panels, and the induced velocity from the wake itself.

The panel code was implemented using Matlab.

3.5.4 Reduction of Computational Cost Linked to Evaluation of the Unsteady Wake

Since the computational cost of evaluating the flow velocities from the wake on the airfoil and the wake itself grows rapidly with the number of wake vortices, approximately proportional to $N(N - 1)$ for big N , measures were taken to reduce the amount of computations linked to evaluation of the unsteady wake.

One way of reducing the computational cost is to reduce the number of vortices. In order to reduce the number of actual vortices in the wake, the wake vortices are split up in zones, as shown in figure 3.12. The general idea behind the zonal concept is that

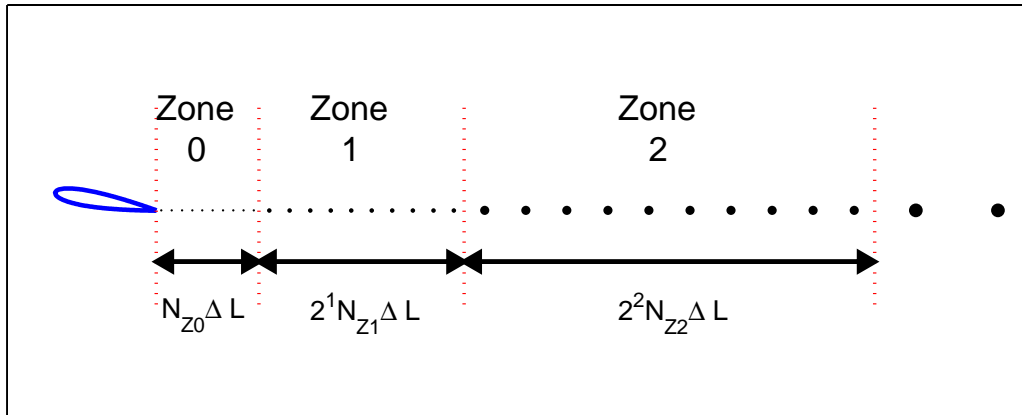


Figure 3.12: *Zonal concept for reducing the number of wake vortices. Zone i has a maximum of N_{Zi} vortices. If a new vortex enters the zone, the two last vortices in the zone are merged, and put into the next zone. The shown example has $N_{Zi} = 10$.*

each zone has a maximum number of allowed vortices, N_{Zi} . If the actual number of vortices at any time is greater than this number, then the two last vortices of the zone are merged together and put into the next zone. The zonal concept is based on the index of the vortices and not on length parameters.

In order to fulfill Kelvin's Theorem at all times, the circulation of the new vortex by merging of the two wake vortices, indexed 1 and 2, has to fulfill

$$\Gamma_{new} = \Gamma_1 + \Gamma_2. \quad (3.149)$$

The position of the new vortex is computed such that the induced velocity from the new vortex is identical to the induced velocity from wake vortices 1 and 2 at a specified

point, $(x, y)_{\text{ind}}$:

$$r_i^2 = (x_{\text{ind}} - x_i)^2 + (y_{\text{ind}} - y_i)^2 \quad (3.150)$$

$$U_{\text{new}} = \frac{\Gamma_1}{2\pi} \frac{y_{\text{ind}} - y_1}{r_1^2} + \frac{\Gamma_2}{2\pi} \frac{y_{\text{ind}} - y_2}{r_2^2} \quad (3.151)$$

$$V_{\text{new}} = -\frac{\Gamma_1}{2\pi} \frac{x_{\text{ind}} - x_1}{r_1^2} - \frac{\Gamma_2}{2\pi} \frac{x_{\text{ind}} - x_2}{r_2^2} \quad (3.152)$$

$$x_{\text{new}} = \frac{\Gamma_{\text{new}}}{2\pi} \frac{V_{\text{new}}}{U_{\text{new}}^2 + V_{\text{new}}^2} + x_{\text{ind}} \quad (3.153)$$

$$y_{\text{new}} = -\frac{\Gamma_{\text{new}}}{2\pi} \frac{U_{\text{new}}}{U_{\text{new}}^2 + V_{\text{new}}^2} + y_{\text{ind}}. \quad (3.154)$$

$(x, y)_{\text{ind}}$ is set to the three quarter chord point in all computations because it was shown in section 3.2 that the response of the airfoil in the analytical expression is determined by the state of this point.

The effect on the total number of vortices from this approach is shown in the left of figure 3.13. The right graph shows N^2/N_V^2 versus N , where N and N_V is the number of time-steps and wake vortices, respectively. This quantity is an approximate measure of the relative speed-up of the wake computations by use of the zonal approach for large numbers of N . Further speed up of the unsteady calculations were achieved by

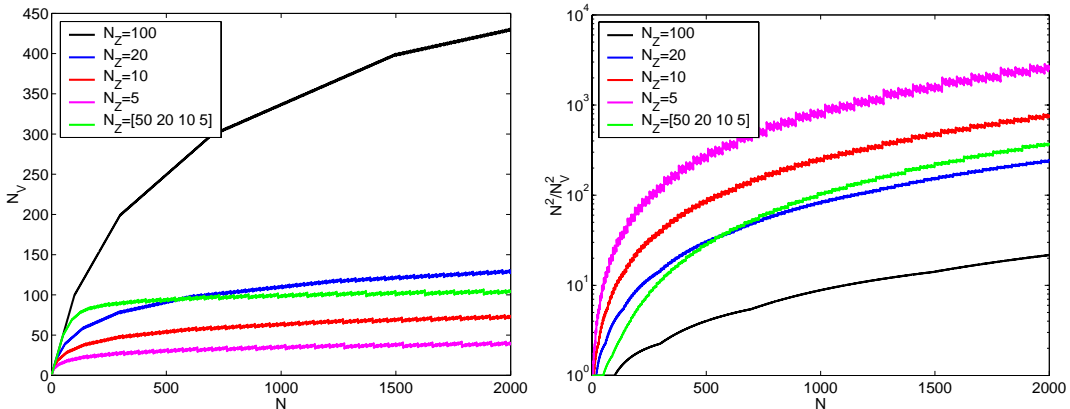


Figure 3.13: *Effect of the reduction of wake vortices from the zonal concept. Left : Number of vortices, N_V , as function of number of time-steps, N , for different N_Z . Right : N^2/N_V^2 versus N . This quantity is a measure of the relative speed-up of the wake computations by use of the zonal approach for large N .*

introducing a vortex-limit, N_{WWI} , after which the full wake-wake interaction is abandoned in favor of a frozen wake approach. This means that the nearest N_{WWI} wake vortices are updated with the full velocity field from all panels and wake vortices. The frozen wake approach for the convection of the rest of the wake means that the wake vortices in this part of the wake are moved only with the free-stream velocity, $\Delta L = \Delta t \cdot V$.

The final moderation for speed-up of the computationally heavy wake is an x -limit, x_{PV} , after which the effect of the airfoil is reduced to a point vortex located in the quarter chord point. The circulation of the equivalent point vortex is equal to the sum

of all vortex panels on the airfoil.

The influence from all wake vortices on all collocation points are always computed. This is done to maximize the accuracy of the flow prediction on the airfoil.

The effect of the modifications for reduction of the computational time are shown in figure 3.14. Lift, drag and quarter-chord moment coefficients, computed with and without the wake modifications, are shown as a function of time.

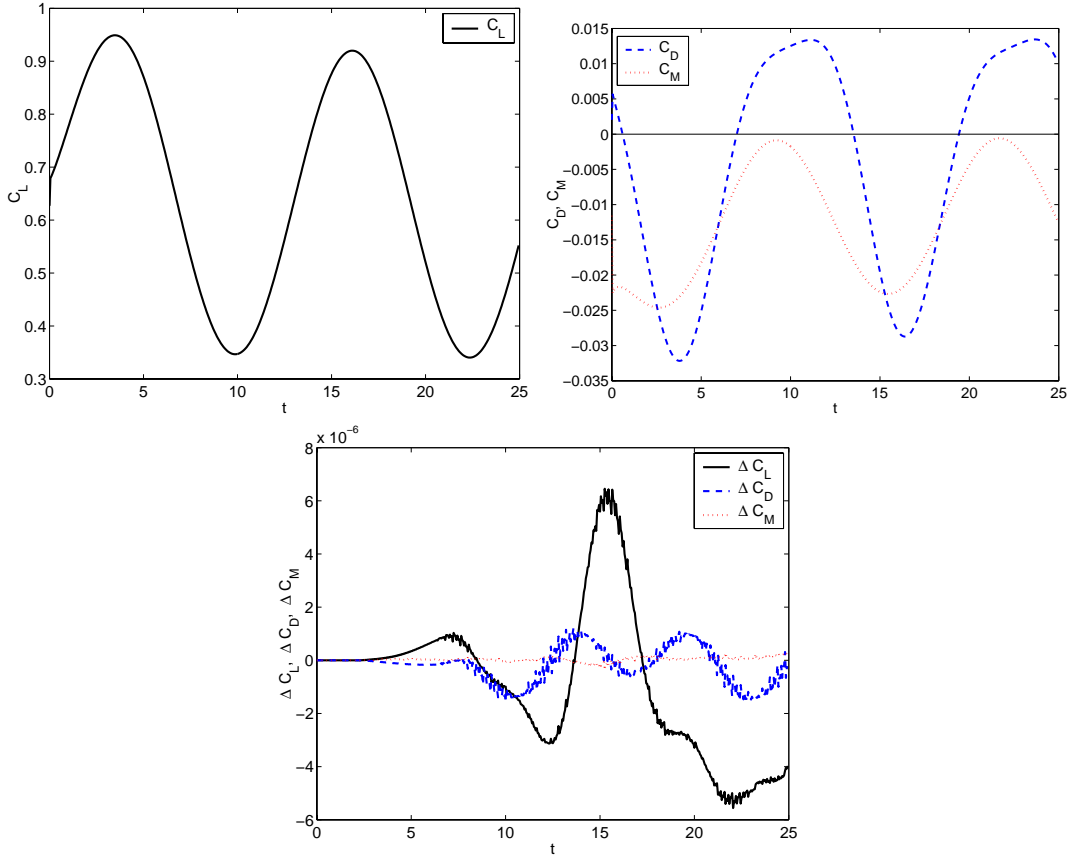


Figure 3.14: Comparison of lift (left), drag and moment-histories (right) computed with the wake modifications for reduction of computational time. The lower graph shows the difference between the computations with and without the wake modifications. The NACA 0015 airfoil was discretized using 100 panels. Harmonically oscillating motion in the heave direction, $\beta = 0^\circ$, at $\alpha = 5^\circ$. $f_{red} = 0.04$, $\Delta\tilde{t} = 0.05$. The speed-up of the wake computations were obtained by employing the following parameters : $N_Z = [40 \ 20 \ 10 \ 5]$, $N_{WWI} = 70$ and $x_{PV}/c = 6$. The total speed-up ratio of the computation for 500 time-steps was $t_{Full}/t_{SpeedUp} = 4.91$.

It is evident from the figure, that the error introduced by the speed-up of the wake computations is very small. The total speed-up ratio of the computation for 500 time-steps was $t_{Full}/t_{SpeedUp} = 4.91$, which is somewhat lower than the mean value of the corresponding speed-up factor up to $N = 500$ in the right graph of figure 3.13. The discrepancy is attributed to the relatively few wake vortices. Thereby, the relative cost of evaluating the induced velocities on, and from the solid surfaces are not negligible, as assumed in the approximate expression for the speed-up, N^2/N_V^2 . The set-up of the

unsteady wake speed-up parameters used for the computations in figure 3.14 were used for all unsteady panel computations in this work.

In the applications of the code in this work it was found that the predicted forces were very close to periodic after four oscillations if the steady solution was used as the initial state. Therefore four oscillation cycles were simulated prior to the oscillation cycle for which the periodic force loops were saved.

3.5.5 Tunnel effect modelling

One of the apparent forces of panel codes is the fact that no discretization of the fluid domain is required, making computations in complex and time dependant geometries much simpler than in the case of methods where fluid domain discretization is required. In the present case, simulation of tunnel walls around the moving airfoil was implemented using flat, constant strength source panels on the tunnel walls to enforce the Neumann boundary condition on the tunnel walls. Figure 3.15 shows the airfoil and

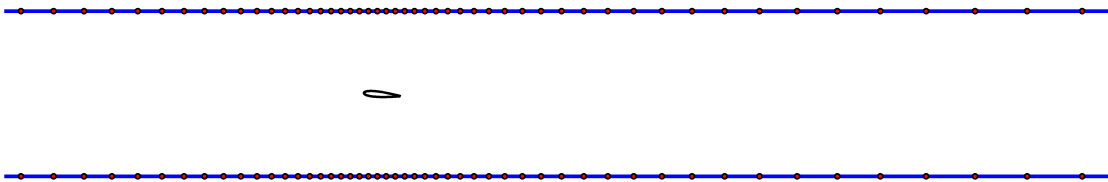


Figure 3.15: *Discretization of the tunnel walls using 2×50 constant strength source panels.*

tunnel panels used in the present computations.

The modification of the solution procedure to take into account tunnel walls is fairly straightforward. The linear system of equations for the combined airfoil/tunnel system is

$$\begin{pmatrix} \mathbf{A1}_{N \times N} & \mathbf{A2}_{N \times M} & b_1 & d_1 \\ & & \vdots & \vdots \\ & & b_N & d_N \\ & & b_{T1} & d_{T1} \\ \mathbf{A3}_{M \times N} & \mathbf{A2}_{M \times M} & \vdots & \vdots \\ & & b_{TM} & d_{TM} \\ c_1 & \dots & c_N & c_{T1} & \dots & c_{TM} & c_\Gamma & c_{\Gamma w1} \\ 0 & \dots & 0 & 0 & \dots & 0 & 1 & 1 \end{pmatrix} \begin{pmatrix} \sigma_1 \\ \vdots \\ \sigma_N \\ \sigma_{T1} \\ \vdots \\ \sigma_{TM} \\ \Gamma_i \\ \Gamma_{w1} \end{pmatrix} = \begin{pmatrix} \text{RHS}_1 \\ \vdots \\ \text{RHS}_N \\ \text{RHS}_{T1} \\ \vdots \\ \text{RHS}_{TM} \\ \text{RHS}_{\Delta T} \\ \Gamma_{i-1} \end{pmatrix}. \quad (3.155)$$

Analog to the unsteady set of equations for the airfoil without tunnel walls, equation 3.146, the first N linear equations is the Neumann boundary condition for the airfoil panels. The next M equations are the Neumann boundary condition for the tunnel walls. As in the free-flow airfoil system, the last two equations are the Kutta-Joukowski and Kelvin conditions, respectively.

Due to the relative motion of the airfoil with respect to the tunnel walls, several influence coefficients must be updated each time-step : $\mathbf{A2}_{N \times M}$, $\mathbf{A3}_{M \times N}$, b_{T1} to b_{TM} , d_1 to d_N , d_{T1} to d_{TM} , c_{Tw1} and c_{T1} to c_{TM} . The fact that a relatively big part of the influence matrix has to be updated each time-step in combination with the general added number of panels makes the solution of the tunnel-airfoil problem computationally more demanding than the free-flow airfoil case. However, since panel-methods in general are not computationally heavy compared to for instance Navier-Stokes solvers, solution of the airfoil-tunnel system using this method is still many times faster than solving a free-flow airfoil flow using a RANS code.

The effect of the tunnel on the airfoil flow is a fairly complex process even in the stationary case. On one hand, the blocking of the airfoil in the tunnel augments the local velocity around the airfoil. On the other hand the walls influence the curvature of the streamlines, and thereby the pressure on the airfoil. These effects are evident also from the coupling effect of the wall panels with the tunnel walls. The disturbance velocities from the airfoil panels is balanced by the source strengths on the tunnel walls, which again effects the strengths on the airfoil (and opposite tunnel wall), so the implications of adding tunnel walls are not simple even when the airfoil is not moving.

In the case of a moving airfoil, the disturbance velocities normal to the wind tunnel walls vary due to the motion of the profile, and due to the unsteady wake. These add even more to the already complex airfoil-tunnel feedback system.

Another effect of the tunnel walls in the unsteady case is the change of geometry of the wake. The influence from the tunnel wall boundary conditions affects the strength and geometry of the wake, which in its turn modifies the dynamic characteristics of the airfoil.

In the case of attached flows, $|\alpha| \leq 8^\circ$, the developed code can be used directly to investigate the effect of the tunnel walls. For all experimental runs in the range $|\alpha| \leq 8^\circ$, corresponding panel code results were computed with and without tunnel to investigate the differences, in steady as well as oscillating cases.

For all unsteady computations carried out in this work, the number of panels on the airfoil was 100, and the tunnel walls were discretized using 50 panels on each wall, extending 10 chord-lengths upstream and 20 chord-lengths downstream of the test section. Grid independence studies for the airfoil, tunnel walls and time step are found in appendix C.

3.5.6 Separated flows

As the angle of attack is increased into the stalling region, the panel code does not give results with any physical meaning, since viscous effects are not modelled. The model assumes fully attached flow, and results in a steady lift coefficient as shown in figure 3.16, as well as zero drag (d'Alembert's paradox), which is clearly far from the physically occurring situation. A potential code will not be able to give any sensible airfoil data at high incidences, but certain tunnel effects can be investigated using the method if it is modified.

The idea is to compare the tunnel wall source strengths for two situations where the lift is identical, but where the tunnel blockage is different.

Producing a flow that at a given angle of attack has a given lift can be obtained by

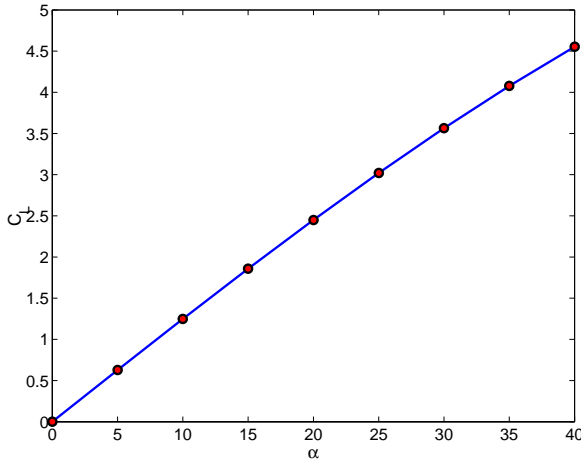


Figure 3.16: C_L values at high incidences from standard potential code computations.

violating the Kutta condition. Specifically, the element in the influence matrix which expresses the influence of the total airfoil circulation on the difference in the tangential velocity at the trailing edge, is multiplied by a constant. This violates the Kutta condition, resulting in a flow field as shown in figure 3.17. As mentioned previously,

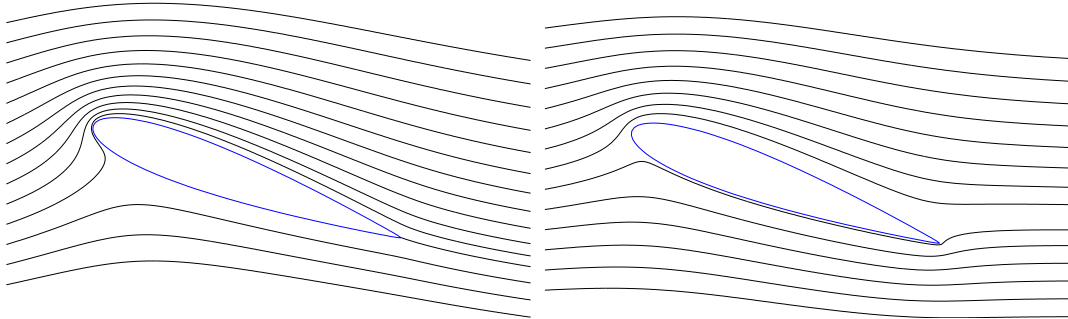


Figure 3.17: Streamlines around a NACA 0015 airfoil at $\alpha = 20^\circ$. Computed by Euler integration in the velocity field from the potential code. Left : Standard panel code. $C_L = 2.5$. Right : Kutta condition violated. $C_L = 0.8$

this will not produce any airfoil data which is physically meaningful, but the effect of a stationary airfoil at a specific angle of attack with a specified lift, on the tunnel walls can be investigated to investigate corrections for tunnel blockage effects at high incidences.

The results of the tunnel correction investigations are shown in section 4.1.

3.6 Navier-Stokes Code

Solving the Navier-Stokes equations, equations 3.1 and 3.2, directly is not even with the use of supercomputers possible for standard airfoil flows. This is due to the very big difference in the smallest and largest spatial and temporal features of the flow that has to be resolved. The extremely small structures in turbulent flows would require

a computational grid that was very fine in order to resolve the finest scales of the flow. Furthermore, the grid should be big enough for the airfoil not to feel the outer boundaries.

These facts renders direct numerical simulation of the Navier-Stokes equations for airfoil flows impossible.

3.6.1 Reynolds Averaged Navier-Stokes Equations

In this work the approach to predicting turbulence is based on statistical methods, namely the one point closure, where the equations of motion for the mean flow are solved rather than the equations of motion for the instantaneous flow.

Following the Reynolds time averaging procedure, all variables are separated into a mean part and a fluctuating part, where the time averaging period is large compared to the turbulent time scale. The mean part of the variables are allowed to vary with time, but much more slowly than the time averaging period.

For incompressible flow, the averaged equations of continuity and momentum, known as the Reynolds Averaged Navier-Stokes (RANS) equations, are given by

$$\frac{\partial \rho}{\partial t} + \frac{\partial \rho U_i}{\partial x_i} = 0 \quad (3.156)$$

$$\frac{\partial \rho U_i}{\partial t} + \frac{\partial(\rho U_j U_i)}{\partial x_j} = -\frac{\partial P}{\partial x_i} + \frac{\partial}{\partial x_j} \left(\mu \left(\frac{\partial U_i}{\partial x_j} + \frac{\partial U_j}{\partial x_i} \right) - \rho \bar{u}_i \bar{u}_j \right) + \rho g_i + S_{v,i} \quad (3.157)$$

The term, S_v , in the momentum equation is a general part for inclusion of volume forces.

The additional term appearing from the time averaging procedure, $-\rho \bar{u}_i \bar{u}_j$, is known as the Reynolds stress tensor, τ_{ij} . The closure problem of turbulence consists of modelling the Reynolds stress tensor.

The effect of the turbulence in linear eddy viscosity models is modelled through the eddy viscosity concept, which is based on the assumption that the turbulent eddies represents an extra viscosity, the turbulent viscosity μ_t , which is modelled analog to the viscous stresses in laminar flow. The turbulent viscosity is related to characteristic scales of turbulent motion and depends on the local turbulence of the flow.

Common for all linear eddy viscosity models is that the Reynolds stresses are modelled by applying the Boussinesq approximation [38],

$$\tau_{ij} = \mu_t \left(\frac{\partial U_i}{\partial x_j} + \frac{\partial U_j}{\partial x_i} \right) - \frac{2}{3} \rho k \delta_{ij},$$

to relate the Reynolds stresses to mean flow gradients. If furthermore the flow is incompressible, the continuity and momentum equations, 3.156 and 3.157, can be rewritten as

$$\frac{\partial \rho U_i}{\partial x_i} = 0 \quad (3.158)$$

$$\frac{\partial \rho U_i}{\partial t} + \frac{\partial(\rho U_j U_i)}{\partial x_j} = -\frac{\partial P}{\partial x_i} + \frac{\partial}{\partial x_j} \left((\mu + \mu_t) \left(\frac{\partial U_i}{\partial x_j} + \frac{\partial U_j}{\partial x_i} \right) \right) + S_{v,i}. \quad (3.159)$$

Note that the pressure, P , in the momentum equation denotes pressure fluctuations around the hydrostatic pressure.

3.6.2 $k - \omega$ Shear Stress Transport Model

Turbulence occurs in flows at high Reynolds numbers after a complex transition process from laminar flow at low Reynolds numbers. In the present work the transitional stages are not considered since trip tape was used to trigger a turbulent boundary layer in the experimental part.

In wind turbine aerodynamics, where the prediction in the stalled region is of interest, the demand on the turbulence model is very high. The turbulent stress model employed in the present work is the $k - \omega$ Shear Stress Transport (SST) model proposed by Menter [34], which is a two equation linear turbulent eddy viscosity model designed to improve the sensitivity to adverse pressure gradients compared to standard $k - \omega$ models. The $k - \omega$ SST model has shown good prediction of airfoil flows in the attached and moderately/lightly stalled cases [20] [11]. However, an overestimation of $C_{L\max}$ due to overestimation of the onset of stall is still evident, even though not as outspoken as for the standard turbulence models.

The $k - \omega$ SST turbulence model is based on the $k - \omega$ baseline model also by Menter [34], which combines the $k - \omega$ model by Wilcox [61] in the inner region of the boundary layer, and the standard $k - \epsilon$ model, in a $k - \omega$ formulation, in the outer region and the free stream. The transport equations for the turbulent quantities in the SST model reads

$$\frac{Dk}{Dt} = \frac{\tau_{ij}}{\rho} \frac{\partial U_i}{\partial x_j} + \frac{\partial}{\partial x_j} \left[(\nu + \sigma_k \nu_t) \frac{\partial k}{\partial x_j} \right] - \beta^* \omega k \quad (3.160)$$

$$\frac{D\omega}{Dt} = \frac{\gamma}{\rho \nu_t} \tau_{ij} \frac{\partial U_i}{\partial x_j} + \frac{\partial}{\partial x_j} \left[(\nu + \sigma_\omega \nu_t) \frac{\partial \omega}{\partial x_j} \right] + 2(1 - F_1) \sigma_\omega^2 \frac{1}{\omega} \frac{\partial k}{\partial x_j} \frac{\partial \omega}{\partial x_j} \quad (3.161)$$

Equation 3.160 is a transport equation for the turbulent kinetic energy, defined as the kinetic energy per unit mass of the flow, $k = 0.5 u_i \bar{u}_i$. The transport equation for the specific dissipation rate of turbulent kinetic energy ω , is equation 3.161.

The blending function, F_1 , is zero at the solid walls and zero away from surfaces, and is used to determine the value of the model constants, generally denoted θ :

$$\theta = F_1 \theta_1 + (1 - F_1) \theta_2 \quad (3.162)$$

The blending function is given by

$$F_1 = \tanh(\arg_1^4), \quad (3.163)$$

where

$$\arg_1 = \min \left[\max \left(\frac{\sqrt{k}}{0.09 \omega y}; \frac{500 \nu}{y^2 \omega} \right); \frac{4 \sigma_\omega^2 k}{CD_{k\omega} y^2} \right]. \quad (3.164)$$

The distance to the wall is y , and

$$CD_{k\omega} = \max \left(2 \sigma_\omega^2 \frac{1}{\omega} \frac{\partial k}{\partial x_j} \frac{\partial \omega}{\partial x_j}; 10^{-20} \right). \quad (3.165)$$

Constants for the inner (1) and outer (2) model is

$$\begin{aligned}\sigma_{k1} &= 0.85, \quad \sigma_{\omega 1} = 0.5, \quad \beta_1 = 0.0750, \quad \gamma_1 = \frac{\beta_1}{\beta^*} - \sigma_{\omega 1} \frac{\kappa^2}{\sqrt{\beta^*}} \\ \sigma_{k2} &= 1.00, \quad \sigma_{\omega 2} = 0.856, \quad \beta_2 = 0.0828, \quad \gamma_2 = \frac{\beta_2}{\beta^*} - \sigma_{\omega 2} \frac{\kappa^2}{\sqrt{\beta^*}}\end{aligned}\quad (3.166)$$

Both the inner and outer models use $\kappa = 0.41$ and $\beta^* = 0.09$. The solid wall boundary conditions for the transport equations 3.160 and 3.161 are

$$k_w = 0 \quad \text{and} \quad \omega_w = \frac{60\nu}{\beta_1(\Delta y)^2}. \quad (3.167)$$

The eddy viscosity is

$$\mu_t = \rho \frac{a_1 k}{\max(a_1 \omega; \Omega F_2)}, \quad (3.168)$$

where

$$F_2 = \tanh(\arg_2^2), \quad (3.169)$$

and

$$\arg_2 = \max \left(2 \frac{\sqrt{k}}{0.09\omega y}; \frac{500\nu}{y^2\omega} \right). \quad (3.170)$$

Since $F_2 = k/\omega$ far from the walls, the $k - \omega$ SST model is identical to the BSL model far from the walls.

This definition of the turbulent viscosity secures that the production of turbulent kinetic energy is larger than its dissipation for adverse pressure gradient boundary layer flows, leading to earlier separation than for standard $k - \omega$ or $f - \epsilon$ models.

Apart from its good behavior in flows with adverse pressure gradients, the $k - \omega$ SST model is insensitive to the inlet free stream turbulent quantities [34]. All computations in the present work were computed using this turbulence model.

It is shown in for example [11] or [23] that transition modelling can have a great impact on the outcome of a RANS simulation of an airfoil flow. Transition modelling is, however, not included in the present work because trip tape was used to trigger turbulence in the experimental counterpart of the work.

3.6.3 Numerical code

The computations shown in this work were carried out using the *EllipSys2D* code, developed by Michelsen [35], [36] and Sørensen [51] [54]. The isothermal incompressible Reynolds averaged Navier-Stokes equations are solved for the simple variables U , V and P , using a block structured, cell centered, non-staggered, finite volume method in general curvilinear coordinates. The solution process is built on a predictor-corrector method with two corrector steps, the PISO algorithm. The discretization scheme employed for the convective terms is the Second Order Upwind Scheme (SUDS), while the pressure decoupling is avoided using the Rhie-Chow interpolation technique [44].

3.6.4 Moving grid

Considering the case of a computational grid undergoing unsteady motion with respect to an inertial system, corrections have to be made to the standard solution process for the non moving grid in order to model the change in relative boundary conditions and fictitious forces.

Since the computational grid is moving with respect to an inertial system, the boundary conditions for the inlet velocity has to be transformed into the corresponding velocities in the relative frame of reference. The fictitious forces arising from the unsteady motion of the computational grid are modelled through the additional source terms, $S_{v,i}$, in the momentum equations of the RANS equation 3.159. In this work these source terms are treated explicitly.

The vectorial relations that connects positions, velocities and accelerations in inertial and non-inertial systems can be found in elementary solid mechanics books, such as [10]. The relations are given by

$$\vec{r} = \vec{r}_0 + \vec{r}' \quad (3.171)$$

$$\vec{V} = \vec{V}_0 + \vec{V}' + \vec{\omega} \times \vec{r}' \quad (3.172)$$

$$\vec{a} = \vec{a}_0 + \vec{a}' + 2\vec{\omega} \times \vec{V}' + \frac{d\vec{\omega}}{dt} \times \vec{r}' + \vec{\omega} \times (\vec{\omega} \times \vec{r}') \quad (3.173)$$

Since there is no angular motion involved in the case considered in the present work, $\vec{\omega} = 0$, the general transformation equations for the velocity and the acceleration, equations 3.172 and 3.173 reduce to

$$\vec{V} = \vec{V}_0 + \vec{V}' \quad (3.174)$$

and

$$\vec{a} = \vec{a}_0 + \vec{a}'. \quad (3.175)$$

The primed quantities, $(\cdot)'$, refer to vectors in the relative system, the subscript, O , refer to the origio of the relative system.

The inlet velocities in the moving grid are generally computed from equation 3.172, or in the sub-case of no angular motion, equation 3.174, by isolation of the velocity in the moving system, \vec{V}' .

In order to relate the transformation equation for the acceleration to source terms in the momentum equation, Newton's second law is considered

$$\begin{aligned} m \cdot \vec{a} &= \sum \vec{F}_{ext} \\ &\Downarrow \\ m \cdot \vec{a}' &= \sum \vec{F}_{ext} + m \cdot \vec{a}_{fict}. \end{aligned} \quad (3.176)$$

The fictitious forces are obtained from equation 3.173,

$$\vec{a}_{fict} = -\vec{a}_0 - 2\vec{\omega} \times \vec{V}' - \frac{d\vec{\omega}}{dt} \times \vec{r}' - \vec{\omega} \times (\vec{\omega} \times \vec{r}'), \quad (3.177)$$

which in this specific sub-case is reduced to

$$\vec{a}_{\text{fic}} = -\vec{a}_0. \quad (3.178)$$

Equation 3.176 shows, that the fictitious forces can be considered external forces in Newton's second law, and hence, in the RANS momentum equations, 3.159.

Before arriving at the final expression for the source terms, we consider the fictitious force that a 'fluid-particle', P , in the non-inertial system is experiencing

$$\begin{aligned} \vec{F}_{\text{fic},P} &= \vec{a}_{\text{fic},P} m_P \\ &= \vec{a}_{\text{fic},P} \mathcal{V} \rho \end{aligned}$$

Since the dimension of the source term, $S_{v,i}$, in equation 3.159, is force per volume, we get that

$$\vec{S}_V = \vec{a}_{\text{fic}} \cdot \rho. \quad (3.179)$$

Validation of the moving-grid implementations are found in appendix D.2.

Chapter 4

Results

In this chapter results from the theoretical models will be presented and discussed. Apart from the first two sections, this chapter deals with comparison of results from theoretical models with the experimental data described in chapter 2.

The first section concerns unsteady wind tunnel corrections for the experiments. The corrections presented are based on results obtained with the numerical potential code, which is described in section 3.5. Following a short section on the difference in the aerodynamic response of airfoils undergoing translatory or pitching motion is a comparison of the results from the analytical models with the experimental results, focussing on the performance of the new heuristic dynamic stall model proposed in section 3.4. Finally, the results obtained with the Navier-Stokes code are compared with the experimental results.

4.1 Wind Tunnel Corrections

The imposition of the wind tunnel walls causes the flow around a body to differ from the flow as it would have been in an unlimited stream. Therefore the quantities measured in the wind tunnel has to be corrected for a number of phenomena to match the corresponding free flow quantities.

4.1.1 Steady Tunnel Corrections

In steady wind tunnel testing the effects of wind tunnel blockage are usually accounted for using wind tunnel corrections as found in for example Pankhurst and Holder [40], Selig et. al. [46] or Rae and Pope [43].

Generally four different effects occurs in steady two-dimensional wind tunnel testing with solid wall boundaries :

- Buoyancy: Additional drag force resulting from a decrease in static pressure along the test section due to the growth of the boundary layer on the walls.
- Solid Blockage: The physical presence of a model within a test section produces a decrease in the effective area. This increases the local flow velocity at the test section, augmenting the aerodynamic forces.

- Streamline Curvature: Due to the boundary conditions imposed by the tunnel walls, the streamline curvature, and hence lift force, is altered, increasing the effective camber of the profile, and thereby the lift and aerodynamic pitching moment.
- Wake Blockage: The lower velocity within the airfoil wake compared to the free stream velocity increases the velocity outside the wake, affecting the quantities at the model. The effect of the wake blockage depends on wake size, and thus to the measured drag force.

Below each of the steady tunnel effects and the corrections are commented with respect to the present experimental setup.

Buoyancy

In order to estimate the effect of the buoyancy for the experiments carried out in the present work, the displacement thickness from the turbulent one seventh power law [60]

$$\frac{\delta^*}{x} \sim \frac{0.16}{Re_x^{1/7}},$$

is combined with the Bernoulli equation to obtain

$$\Delta C_{DBuoyancy} \sim 0.0016.$$

Dimensions and standard operational conditions for the wind tunnel have been used to arrive at the result above. Since this value is lower than the uncertainty of the obtained results, that correction will not be employed in this work.

Solid Blockage

The decrease in effective area in the wind tunnel test section causes an increase of the flow velocity around the model compared to the free flow case. This affects all forces on the profile. A correction for the solid-blockage effect have been given by Thom [43]

$$\epsilon_{sb} = \frac{\Delta V_{sb}}{V_{Tunnel}} = \frac{K_1 \text{Vol}_{\text{Model}}}{(A_{\text{Tunnel}})^{3/2}}, \quad (4.1)$$

where $K_1 = 0.74$ for a wing spanning the entire tunnel width. The volume of the model can be approximated by $\text{Vol}_{\text{Model}} = 0.7 \times \text{model thickness} \times \text{model chord} \times \text{model span}$. The tunnel test section area is denoted by A_{Tunnel} .

It is noted that the expression for the solid-blockage effect only involves the dimensions of the model and not the incidence. At high angles of attack, where the airfoil is in deep stall, it could be argued that the blockage of the airfoil should depend on the incidence as well, but this is not been done presently.

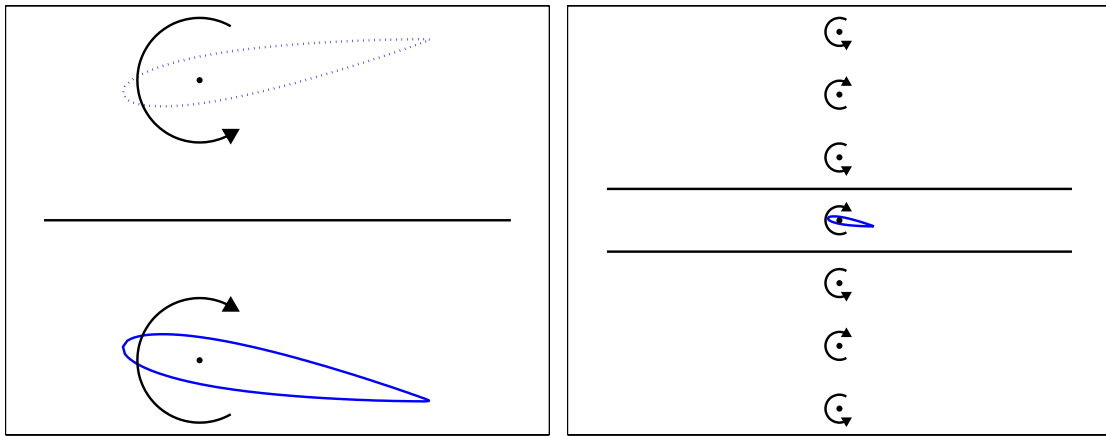


Figure 4.1: *Modelling of streamline curvature through image vortices. Left : modelling of one wall using a mirror image. Right : modelling of two parallel walls using an infinite line of vortices of alternating sign.*

Streamline Curvature

The presence of the tunnel walls alters the curvature of the streamlines compared to that of the free flow case. Two dimensional streamline curvature corrections for closed test sections are based on simple vortex theory, where solid walls are modelled by image vortices as shown in figure 4.1. The streamline curvature effect of a single wall can be modelled by introducing a mirror vortex of opposite strength at a position corresponding to the mirror point of the quarter chord point. This ensures that there is no flow through the wall.

If an airfoil is confined between two parallel walls, two semi-infinite rows of mirror vortices with shifting signs are needed. One above and one below the real vortex. This is shown in the right hand side of figure 4.1.

The effect of these mirror vortices on the velocity in the tunnel is a upwash angle that varies almost linearly on the chord of the airfoil and is zero at the quarter chord point. This situation is equivalent to a circular stream curvature, which in turn is equivalent to an airfoil with an added camber in an unbounded straight flow.

According to Rae and Pope [43], this effect is properly corrected for by corrections to both the measured lift and moment coefficients $C_{LTunnel}$, $C_{MTunnel}$, and to the angle of attack α as well. The corrections to the lift and moment coefficients are

$$\Delta C_{Lsc} = -\sigma C_{LTunnel} \quad (4.2)$$

$$\Delta C_{Msc} = -\frac{\sigma}{4} \Delta C_{Lsc}, \quad (4.3)$$

where

$$\sigma = \frac{\pi^2 c^2}{48 h^2}. \quad (4.4)$$

Note that C_M in these equations refer to the moment coefficient with respect to the quarter chord.

If it is assumed that the airfoil can be approximated by a single vortex at the quarter

chord, the correction to the angle of attack is [43]

$$\Delta\alpha_{sc} = \frac{\sigma}{2\pi} C_L. \quad (4.5)$$

A more correct expression is obtained if the vorticity is spread out along the airfoil. In this case the correction for the lift and moment coefficients remain unaltered, but the angle of attack correction is changed to [43]

$$\Delta\alpha_{sc} = \frac{\sigma}{2\pi} (C_L + 4C_M). \quad (4.6)$$

Since the above expressions are derived from potential theory, the validity of the stream-line curvature corrections will be discussed briefly for separated flows.

The lift correction may be plausible for both attached and separated flows because the correction of the lift is proportional to the measured lift, which in turn is proportional to the circulation leading to the correction. Since the simple correction to the angle of attack, equation 4.5, and the moment correction, equation 4.3, have the same form as the lift correction, these corrections may be considered valid for all types of flows as well, even though the measured moment itself is not close to the potential value for separated flows.

The last correction, equation 4.6, the more complex correction of the angle of attack, involves the measured moment, and is therefore not applicable for stalling flows.

Wake Blockage

Due to the viscosity of the fluid, a boundary layer develops on the airfoil. This region of lower velocity extends downstream and forms the wake of the airfoil. Due to the lowered velocity in the boundary layer and in the resulting wake, the velocity outside the wake in a tunnel must be higher than that of the free stream. From Bernoulli's equation higher velocity in the free stream corresponds to lower pressure. Therefore, the airfoil is in a pressure gradient. Rae and Pope [43] suggests the following correction for wake blockage

$$\epsilon_{wb} = \frac{\Delta V_{wb}}{V_{Tunnel}} = \frac{c/h}{4} C_{DTunnel}. \quad (4.7)$$

The drag on an airfoil in a wind tunnel can be computed from the velocity profiles upstream and downstream of the profile, using the momentum equation regardless of how the velocity fields are generated, be it attached or stalling flow. Therefore it is assumed that the drag correction is valid for both attached and stalling flows.

Full Corrections

Summarizing the results of the steady tunnel blocking effects, we have the following corrections to Reynolds number, force coefficients and angle of attack [43]:

$$Re = Re_{\text{Tunnel}}(1 + \epsilon) \quad (4.8)$$

$$C_L = C_{L\text{Tunnel}}(1 - \sigma - 2\epsilon) \quad (4.9)$$

$$C_M = C_{M\text{Tunnel}}(1 - 2\epsilon) + \frac{\sigma C_L}{4} \quad (4.10)$$

$$C_D = C_{D\text{Tunnel}}(1 - 3\epsilon_{sb} - 2\epsilon_{wb}) \quad (4.11)$$

$$\alpha = \alpha_{\text{Tunnel}} + \frac{\sigma}{2\pi}(C_L + 4C_M) \quad (4.12)$$

$$\alpha = \alpha_{\text{Tunnel}} + \Delta\alpha \quad (4.13)$$

$$\Delta\alpha = \frac{\sigma}{2\pi}C_L \quad (4.14)$$

where the solid and wake blocking coefficients are combined to one blocking coefficient

$$\epsilon = \epsilon_{sb} + \epsilon_{wb}. \quad (4.15)$$

Note that the first of the two corrections to the incidence, equation 4.12, is only applicable in cases where the flow is attached.

Panel Code Corrections

According to the author, specific corrections for unsteady 2D experiments applying to the present set-up are not documented in the literature up to now. Therefore the validity of corrections obtained with the panel code described in section 3.5 was examined for the steady case in order to determine if unsteady corrections based on results from the unsteady version of the panel code could be plausible.

The effects for which a potential code can be used to compute corrections are the solid blocking and the streamline curvature effects. The panel code was used to compute lift and moment coefficients for a NACA 0015 airfoil in both unbounded flow and flow bounded by tunnel walls. Computations were made at identical geometrical angles in the free flow and the tunnel computations. The airfoil was discretized using 100 panels, and the tunnel walls were discretized using 50 panels on each tunnel wall, summing up to 200 panels describing the airfoil/tunnel system in total. Appendix C describes grid refinement studies for the airfoil and tunnel walls.

Since the tunnel and free flow force coefficients related by equations 4.9-4.10 are not at the same geometrical angle¹, the difference in angle has to be accounted for when comparing the results from the potential code with the corrections.

The lift coefficient for the airfoil in free flow and in the tunnel is to a good approximation expressed as

$$C_L = K_1\alpha \quad (4.16)$$

$$C_{L\text{Tunnel}} = K_2\alpha_{\text{Tunnel}}, \quad (4.17)$$

¹The tunnel quantities are linked to the incidence α_{Tunnel} whereas the corresponding corrected values corresponds to the incidence α , given by equation 4.13.

where both K_1 and K_2 are close to 2π .

Using equations 4.9, 4.13 and 4.14, the free-flow-to-tunnel-flow ratio of the lift coefficients can be expressed.

$$\begin{aligned} \frac{C_L(\alpha_{\text{Tunnel}})}{C_{\text{LTunnel}}(\alpha_{\text{Tunnel}})} &= \frac{C_L(\alpha)}{C_{\text{LTunnel}}(\alpha_{\text{Tunnel}})} - \frac{C_L(\Delta\alpha)}{C_{\text{LTunnel}}(\alpha_{\text{Tunnel}})} \\ &= (1 - \sigma - 2\epsilon) - \frac{C_L(\frac{\sigma}{2\pi} C_L(\alpha_{\text{Tunnel}}))}{C_{\text{LTunnel}}(\alpha_{\text{Tunnel}})} \\ &= (1 - \sigma - 2\epsilon) - \frac{K_1^2}{2\pi K_2} \sigma \end{aligned} \quad (4.18)$$

which, since $K_1 \sim 2\pi$ and $K_2 \sim 2\pi$

$$\frac{C_L(\alpha_{\text{Tunnel}})}{C_{\text{LTunnel}}(\alpha_{\text{Tunnel}})} \simeq (1 - 2\sigma - 2\epsilon) \quad (4.19)$$

Since there is no wake blockage for a steady panel code computation, the analytic lift

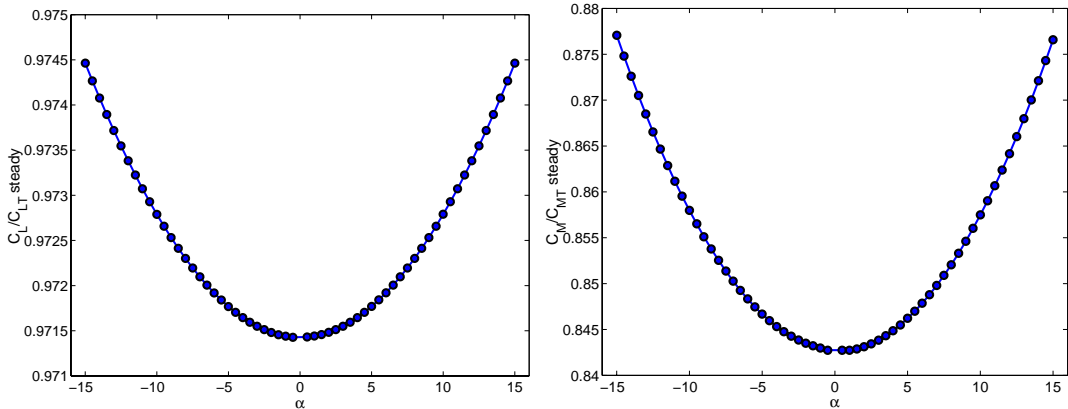


Figure 4.2: *Solid blocking and streamline curvature effects. Steady free-flow-to-tunnel-flow ratios. Left : Lift ratios. Right : Moment ratios. Both the lift and drag ratios are nearly constant. The tunnel height to chord ratio is $h/c = 4.47$ for the presented results.*

correction for solid blocking and stream line curvature, equation 4.19, turns out to be a function of model and tunnel dimensions only. The results from the potential code (figure 4.2) show that the lift ratio vary between 0.9715 and 0.9727 (0.12%), and the drag ratio varies between 0.842 and 0.857 (1.75%) for $\alpha < 10^\circ$ and $h/c = 4.47$, which is essentially constant. This is in agreement with the analytic lift correction. The fact that the moment ratios are fairly constant implies, from equation 4.9 and 4.10, that the lift to moment ratio in the tunnel should be constant as well. This was seen from the potential results to hold true.

The ratio between the forces for an airfoil in free air and the forces for an airfoil situated in the wind tunnel will be referred to as free-flow-to-tunnel-flow ratios from this point on.

The left graph of figure 4.3 compares the free-flow-to-tunnel-flow ratio of the lift force from equation 4.19 with the results obtained from the potential code. As seen, the

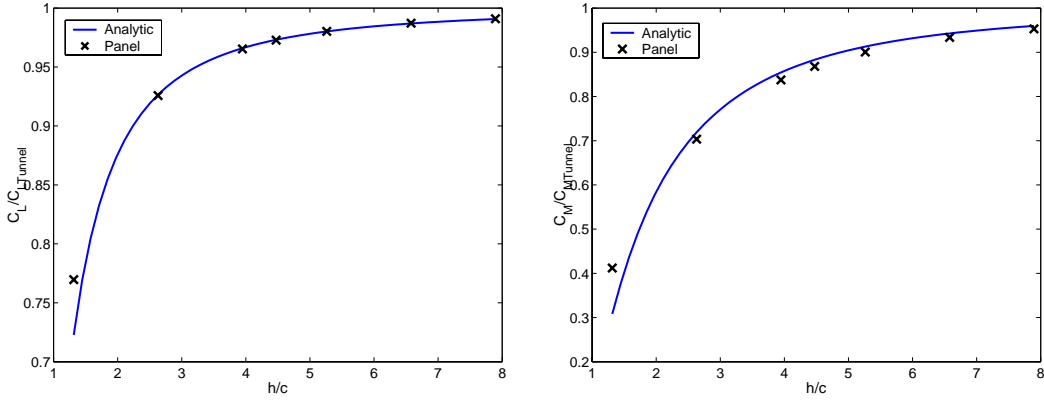


Figure 4.3: *Solid blocking and streamline curvature effects. Comparison between analytic and panel code steady tunnel corrections. Left : lift correction. Right : moment correction.*

potential code results are in excellent agreement with the analytical result in for h/c above 2.5. As expected, the analytical results become inaccurate at low h/c ratios due to the heavy simplifications under which the analytical expressions were derived. The height to chord ratio for the experiments in this work is $h/c = 4.47$, for which the agreement between analytic and numerical results is excellent.

The curve to the right in figure 4.3 shows comparison of the free-flow-to-tunnel-flow ratios of the moment coefficient. The analytical expression in this case is

$$\frac{C_M}{C_{MTunnel}} = 1 + 2\epsilon + \frac{\sigma(1 - \sigma - 2\epsilon)}{4} \frac{C_{LTunnel}}{C_{MTunnel}} \quad (4.20)$$

In lack of analytic expressions for the quarter chord moment, the ratios obtained from the potential computations were used. As mentioned previously, the ratios were not dependant of the angle of attack, but only on h/c . In the right hand side of figure 4.3, it is seen that the agreement is still good even though the panel code values are generally slightly lower than the analytical ones. Notice that the tunnel effect is stronger on the moment than on the lift.

The good agreement between the analytic and potential code results indicate that potential code results can be used for solid blocking and streamline corrections.

4.1.2 Unsteady Tunnel Corrections

The unsteady nature of the experiment carried out introduces dynamic errors. To the knowledge of the author, dynamic corrections suitable for correction of the experimental data presented in this work are not documented in the literature so far. Some additional systematic periodic tunnel effects arise when the airfoil is subject to oscillatory motion. Due to the variation in bound circulation, which is a key element in the determination of the unsteady forces, the presence of the walls becomes evident through the restriction of the dynamic wake. The ‘memory’ of an unsteady potential solution lies in the dynamic wake. This is altered by the presence of the tunnel walls. An other effect is that the motion of the profile in the general case has a component normal to the tunnel walls, thus augmenting the source strength needed to enforce the

Neumann condition. Taking the strengths of the sources as an indication of the tunnel effect, it is seen that motion of the airfoil causes extra tunnel effects.

Even though it can be argued that the most correct correction in the steady case is a combination of corrections on the angle of attack and of the forces, this method might not be feasible in the unsteady case. The unsteadiness of the forces, and hence, the bound and wake circulation renders a steady correction of the angle of attack impossible. Therefore it was chosen to correct the forces only, letting the effect of the angular correction be embedded in these.

The magnitude of the buoyancy is assumed to be independent of the motion, and therefore disregarded in the unsteady experiments as it was in the steady experiments.

Since the potential code was able to reproduce the steady corrections for solid blocking and streamline curvature very well, it most likely will be able to produce corrections for the change in the dynamic wake interaction and the imposed velocity normal to the wind tunnel walls as well. In the following, results from the potential code will be shown. The movement period was discretized using a minimum of 400 time steps, which corresponds to a dimensionless time-step of maximum 0.06 based on the airfoil chord. A study of the influence of the time step on the panel code solution is given in appendix C, where the solution obtained with the panel code is compared to the analytical unsteady potential theory solutions of an oscillating airfoil from section 3.2, and to Wagner's solution to the impulsively started flow, described in [13]. From this investigation it was seen that the current temporal discretization is adequate.

Since the effect of the unsteady wake in potential computations is a reduction in the amplitude of the oscillating forces and a shift in the phase² as compared to quasi-steady results. Due to the changed wake, it could be suspected that the tunnel walls might change the phase of the forces as well the amplitude of the forces.

In order to investigate the effect of movement direction, β , and angle of attack, α , on various tunnel effects, free flow and tunnel computations were carried out at reduced frequencies $f_{red} = 0.02$ and $f_{red} = 0.03$ for $\alpha = 0^\circ, 5^\circ, 8^\circ$ and $\beta = 0^\circ, 20^\circ, 45^\circ, 70^\circ, 90^\circ, 110^\circ, 135^\circ, 160^\circ$. For all simulations with $f_{red} = 0.02$ a simulation period of 2.75 movement periods was employed. In the $f_{red} = 0.03$ cases a simulation period of 3.75 movement periods was employed. This corresponds to dimensionless times

$$\tilde{t} = 2.75 \frac{VT}{c} = \frac{2.75}{2f_{red}} = 68.75 \quad (4.21)$$

$$\tilde{t} = 3.75 \frac{VT}{c} = \frac{3.75}{2f_{red}} = 62.50. \quad (4.22)$$

Since the time is non-dimensionalized with the chord length, the starting vortex is convected \tilde{t} chord lengths downstream in this time. The results for the last period, for example from $\tilde{t} = 2.75$ to $\tilde{t} = 3.75$ were used for the computations of mean values, amplitudes and phase-shifts. As a measure for the periodicity could be noted that Wagners function³ at beginning of the last period, has a value of 0.997 and 0.9975 in the $f_{red} = 0.02$ and $f_{red} = 0.03$ cases, respectively, indicating that the results are quite close to being periodic.

²the so called phase-lag described in section 3.2.

³described in appendix C.3

Figure 4.4 shows an example of computed lift, quarter-chord moment, and drag coefficient loops in free flow and tunnel. $\alpha = 5^\circ$ and $\beta = 20^\circ$. It is seen that the mean

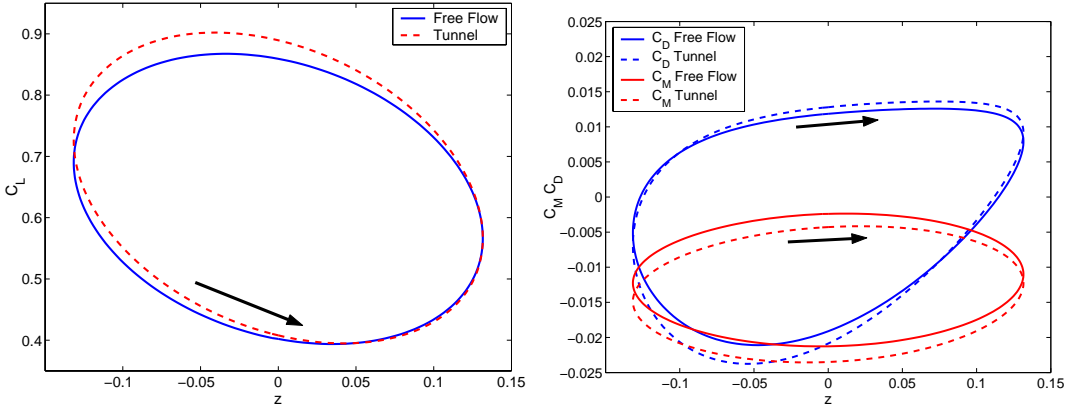


Figure 4.4: Lift coefficient (left), quarter-chord moment and drag coefficients (right) versus position in free flow and tunnel. $\alpha = 5^\circ$, $\beta = 20^\circ$, $f_{red} = 0.03$, $c/A = 13.16$ and $h/c = 4.47$.

value as well as the amplitude of the lift is augmented due to the restriction of the tunnel. Furthermore a slight phase shift is noted. The tunnel adds a phase lag to the lift. Similar trends are observed on the magnitude of the quarter-chord moment coefficient, where the mean value is moved further away from zero, and the amplitude is increased as well. On the drag loop a small augmentation of the amplitude is noticed.

In order to understand the unsteady tunnel effect better, computed unsteady free flow results are shown next.

From figure 4.5, it is evident that the mean lift and moment is independent of movement direction and reduced frequency, whereas the mean drag decreases with reduced frequency and component of motion perpendicular to the free stream. This effect is known as the Knoller-Betz effect [26], which produces a net force in the opposite direction of the flow by translating an oscillatory airfoil in a stream. The fact that the mean drag is affected by the angle of attack is attributed to discretization errors, which increase with the angle of attack due to the relatively more localized pressure peak on the suction side of the airfoil. Figure 4.6 shows the influence of α , β and f_{red} on the unsteady free flow force coefficient amplitudes. As expected, all force amplitudes increase with reduced frequency. Moreover they follow the general trend of maximum values for a movement direction perpendicular to the free stream, and minimum when the motion is in the stream-wise direction.

In the following, comparison between computed unsteady free flow and tunnel solutions will be shown. These form the basis for the formulation of the unsteady tunnel corrections.

Figure 4.7 shows the effect of movement direction, β , and angle of attack, α , on the tunnel effect on the lift at reduced frequencies $f_{red} = 0.02$ (left figures) and $f_{red} = 0.03$ (right figures). The upper figures show the ratios of the mean lift in the unsteady cases compared to the steady ratios. It is observed that the values, are very close ($<0.1\%$) to

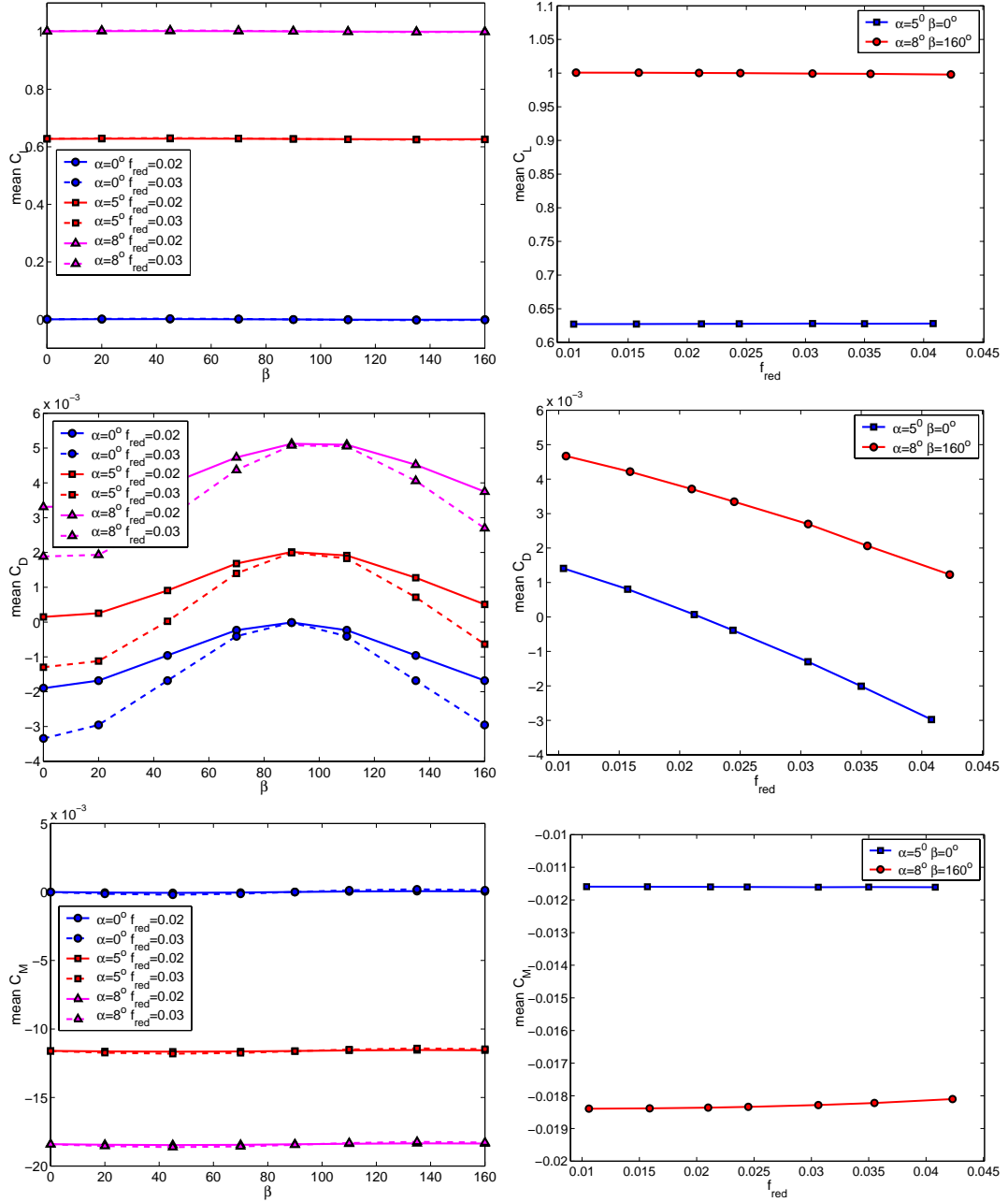


Figure 4.5: Mean forces and moments for free flow. Influence of movement direction, β , and angle of attack, α (left figures). Influence of reduced frequency f_{red} (right figures). $A/c = 13.16$ and $h/c = 4.47$.

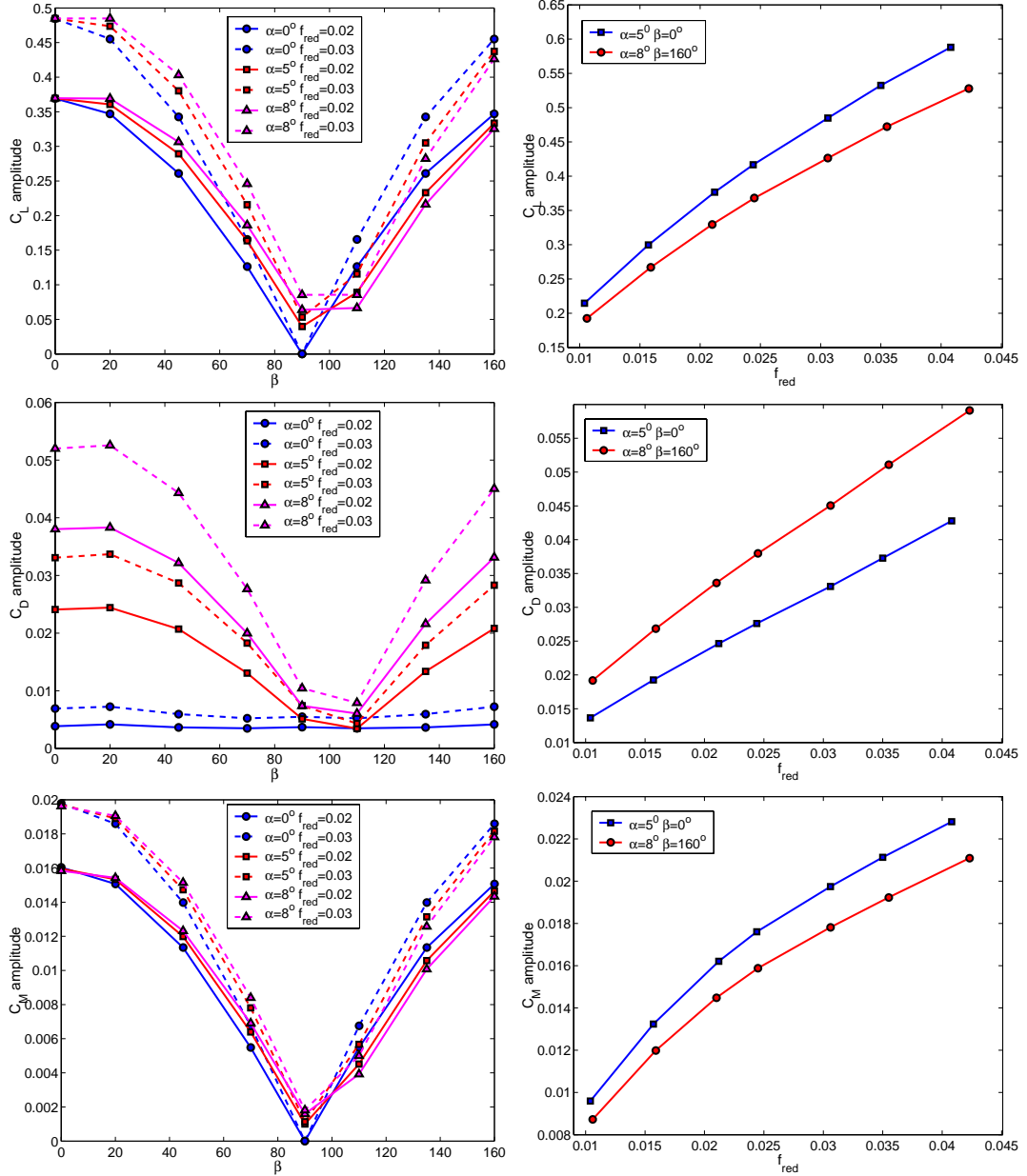


Figure 4.6: Amplitudes of forces and moments for free flow. Influence of movement direction, β , and angle of attack, α (left figures). Influence of reduced frequency f_{red} (right figures). $A/c = 0.1316$ and $h/c = 4.47$.

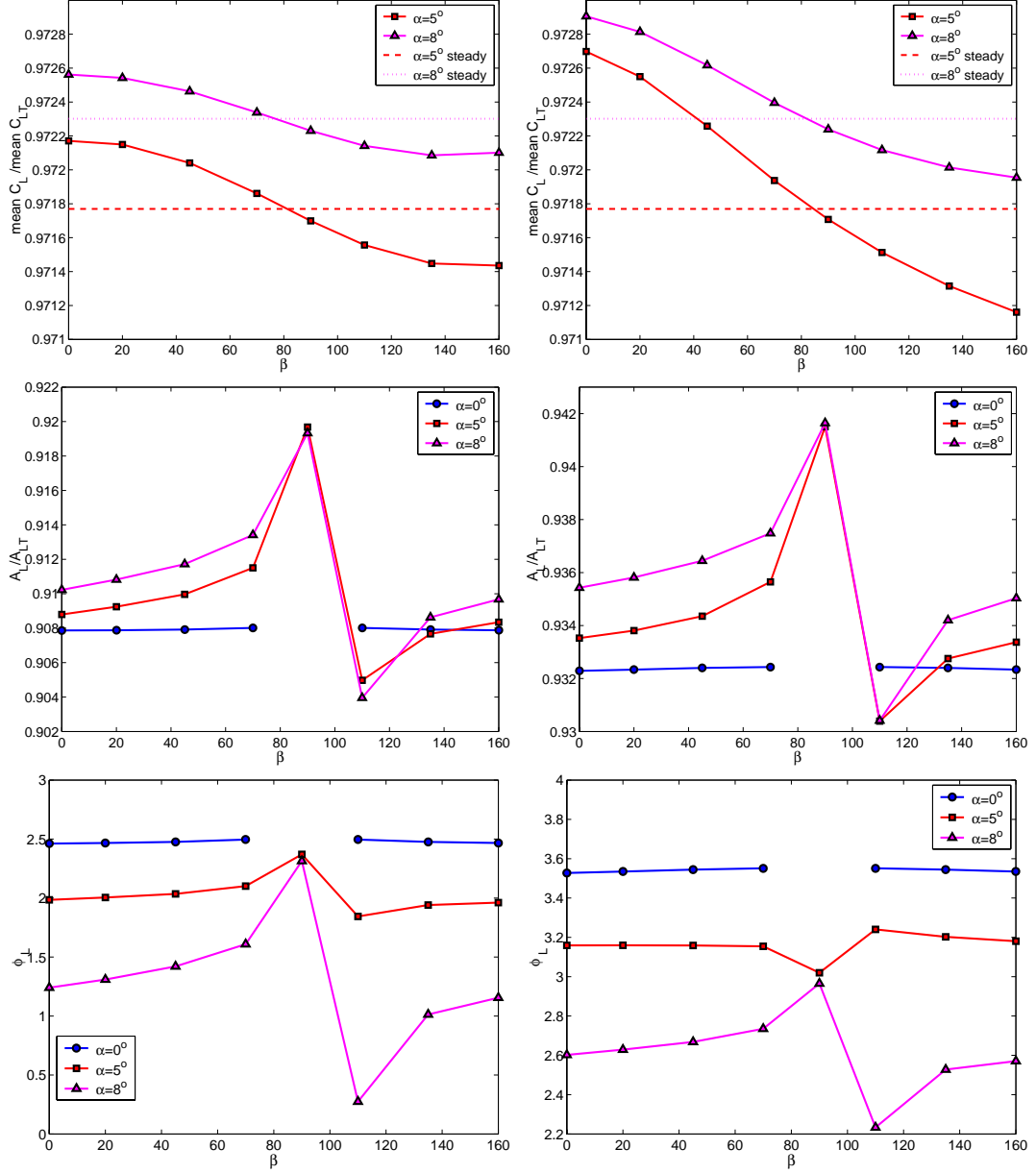


Figure 4.7: Influence of movement direction, β , and angle of attack, α , on the free-flow-to-tunnel-flow ratios of the mean lift (upper figures), lift amplitudes (middle figures) and lift phase shift in degrees (lower figures). The phase shift is defined positive when the maximum tunnel signal is after that of the free flow (lags the free flow signal). The reduced frequencies are $f_{red} = 0.02$ (left figures) and $f_{red} = 0.03$ (right figures). $A/c = 13.16$ and $h/c = 4.47$.

the steady ones, independent on the variation in α and β . This is not surprising, since the potential theory is linear in nature. The slight difference between the unsteady and steady ratios is attributed to the fact that the fully periodic behavior is approached exponentially, due to the starting vortex in the unsteady calculations, analogous to Wagners function. The strength of this starting vortex is dictated by the local conditions, the velocity of the flow and profile and tunnel walls, at the starting time of the flow. This effect would be interpreted as what is observed in the upper figures of figure 4.7. If the flow was in fact fully periodic a periodicity of 180° in β would be present.

Moving on to the free-flow-to-tunnel-flow ratios for amplitudes of the lift, which are shown in the middle figures of figure 4.7, it is noted that these values are constant within 1% at a given reduced frequency. The level of the amplitude ratios increases with reduced frequency, indicating that the augmentation of the lift amplitude by the presence of the tunnel walls is decreasing with relative frequency. This is an unexpected effect which will be discussed more in depth later in this section. It is seen that the mean lift amplitude ratios increase slightly with α . Furthermore it is noticed that the deviation from the mean amplitude of the lift ratios is greatest when β is near 90° , corresponding to the smallest variations in the unsteady lift. The reason for this is unknown to the author, but discretization errors may play a role, as may the fact that truly periodic results are not fully obtained.

The free-flow-to-tunnel-flow phase shift of the lift signal is shown in the lower figures in 4.7. The phase shift is defined positive when the tunnel quantity is behind the free flow quantity, meaning that the tunnel quantity reaches the extremum later than the free flow case. The phase shift is determined from the extrema of the lift signals. The accuracy in determining the extremum of the signal was refined by calculating the exact extremum of the second order polynomium going through the extremum point and its two neighbor points.

The phase shift of the lift is positive in all cases considered. This implies that the effect of the tunnel works is in the same direction as the phase lag effect from the unsteady wake. The general level of the phase shift increases when the reduced frequency is increased from 0.02 to 0.03, and the mean values of the phase shift decreases with the angle of attack. At a given angle of attack and reduced frequency, the phase shift is fairly constant, with the biggest variations, up to 1° , near $\beta = 90^\circ$. The reason for the greater variation near this movement direction is attributed to the greater uncertainty due to the nearly constant lift signal in this region.

Figure 4.8 shows free-flow-to-tunnel-flow quantities for the quarter-chord moment, corresponding to the one in figure 4.7. The free-flow-to-tunnel-flow ratios of the mean moments are shown in the upper figures of figure 4.8. In this case an upward shift of the ratios as compared to the steady results is noted. This corresponds to a decrease in the enhancing effect of the tunnel. The shift in mean value, however, differs only $\sim 1.5\%$ from the steady values, which is still fairly low. As was the case with the lift, the moment amplitudes show little dependence (a few percent) on the direction of the motion. An interesting thing to note, is that the amplitudes of the moment are not

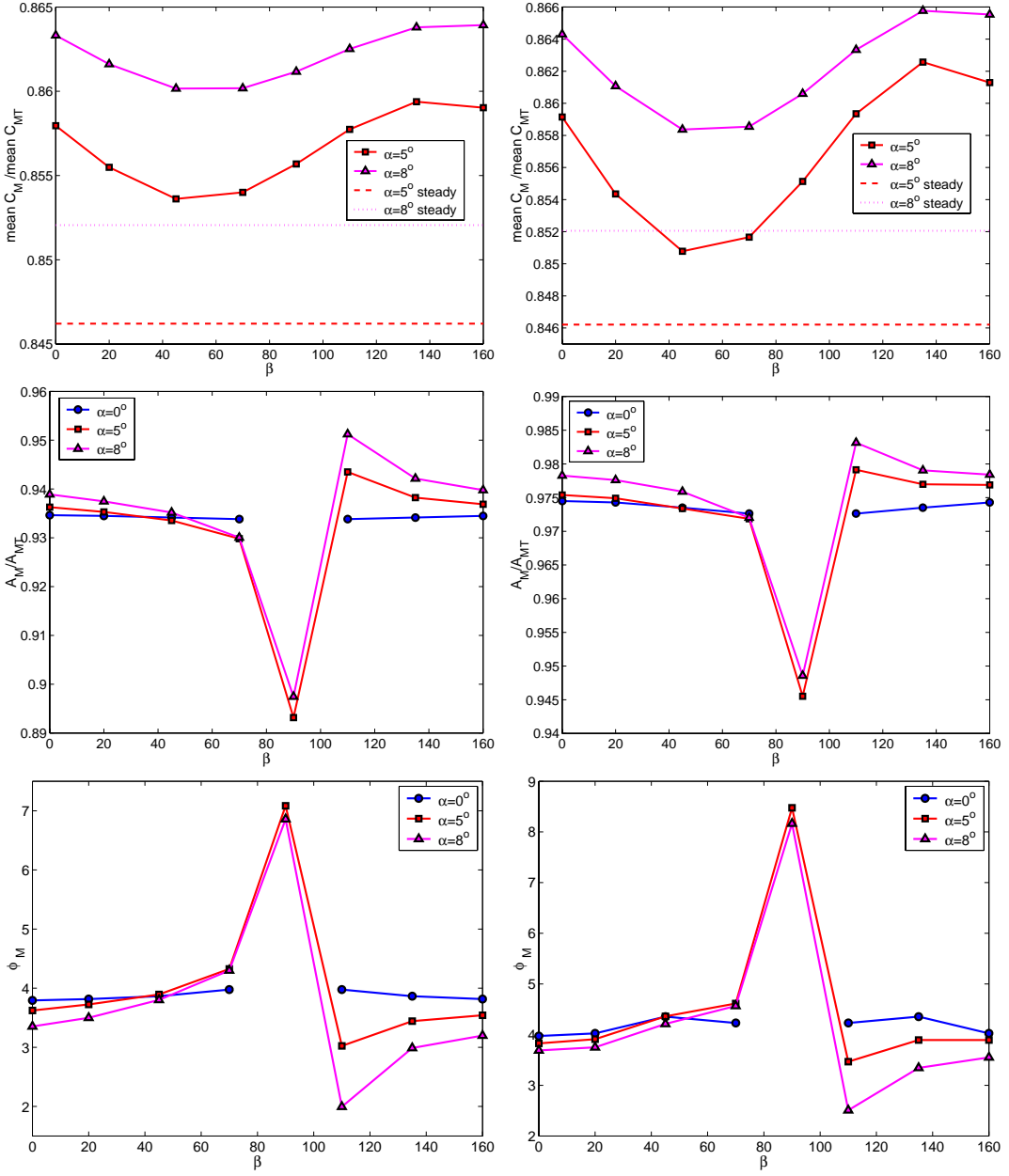


Figure 4.8: Influence of movement direction, β , and angle of attack, α , on the free-flow-to-tunnel-flow ratios of the mean quarter chord moment (upper figures), moment amplitudes (middle figures) and moment phase shift in degrees (lower figures). The phase shift is positive when the tunnel signal lags the free flow signal. The reduced frequencies are $f_{red} = 0.02$ (left figures) and $f_{red} = 0.03$ (right figures). $A/c = 13.16$ and $h/c = 4.47$.

affected as much as the mean level by the tunnel. This is a big difference compared to the lift results. Again, at the $\beta = 90^\circ$ point, where the amplitude of the moments are small, the ratios differ somewhat from the general trend. The ratio of amplitudes of the moment is increased, analogous to the lift, with the reduced frequency. As in the previous figure, the lower graphs in figure 4.8 shows the phase lag of the moment added by the tunnel effect. This is higher than for the lift, around 4° , and shows no big difference in level between $f_{red} = 0.02$ and $f_{red} = 0.03$, and only a slight variation in α . Again the $\beta = 90^\circ$ point shows a peak value, which is attributed to the low amplitudes of the moment.

In order to investigate more thoroughly the influence of the reduced frequency on the unsteady tunnel effects, calculations were performed with and without tunnel for two cases of angle of attack and movement direction : $\alpha = 5^\circ$, $\beta = 0^\circ$ and $\alpha = 8^\circ$, $\beta = 160^\circ$. The results of these simulations are shown in figure 4.9. In the upper figures, the tunnel effect on the ratio of the mean lift (left) and mean quarter-chord moment (right), is shown. In agreement with the earlier results, the lift ratios are very close to the static ones, within 0.1%, whereas the moments lie above the static ratios, at a maximum of 1.7%, increasing with reduced frequency. As stated previously, the reason for the difference is unknown.

The middle graphs of figure 4.9 depicts the lift amplitude and moment amplitude ratios, left and right respectively. In accordance with the results shown earlier, the lift and moment amplitude ratios are fairly independent of incidence and movement direction, but shows a dependance on the reduced frequency. The lift amplitude ratios has a minimum at $f_{red} \simeq 0.015$, and lies in the range from $f_{red} = 0.01$ to $f_{red} = 0.045$. The amplitude of the moment is increasing in the whole interval. Notice that the values of the lift amplitude ratios differ from the moment amplitude ratios.

The lowest two graphs in figure 4.9 shows the phase shift between the free flow and tunnel forces. The phase shift of the lift (left figure) increases up to $f_{red} \simeq 0.032$, after which the phase shift values remain fairly constant. The levels as well as the form of the quarter chord moment, shown in the bottom right graph of figure 4.9 differs from the lift phase values, increasing from $0.3^\circ - 0.7^\circ$ up to $3.5^\circ - 4.0^\circ$ at $f_{red} \simeq 0.025$, after which they decrease to $1.5^\circ - 2.5^\circ$ at $f_{red} \simeq 0.041$.

The drag from a steady potential flow solution is zero. This implies that the drag component in the unsteady potential computations is of an induced nature. In figure 4.5 and 4.6, the mean levels and force amplitudes was shown for the unsteady free flow panel code solutions, showing for example that the drag amplitude at $\alpha = 5^\circ$, $\beta = 0^\circ$ and $f_{red} = 0.03$ is 0.032, which is in the same order of magnitude as the total true drag observed from static measurements [46]. In order to gain insight into how the lift-induced drag is changed in the tunnel, the ratios of the drag amplitudes and the phase shifts are shown in figure 4.10. Notice however, that these figures can not be used as a basis for tunnel corrections, since effects from viscosity such as separation and viscous drag, which is the major contributor to the total drag in a big part of the experimental cases, are not modelled in these data. The results may, however, show the parameters on which the tunnel effect on the induced type of drag depends. The results shown in figure 4.10 indicate that the amplitude ratio of the induced drag depends strongly on the angle of attack and movement direction, and somewhat less

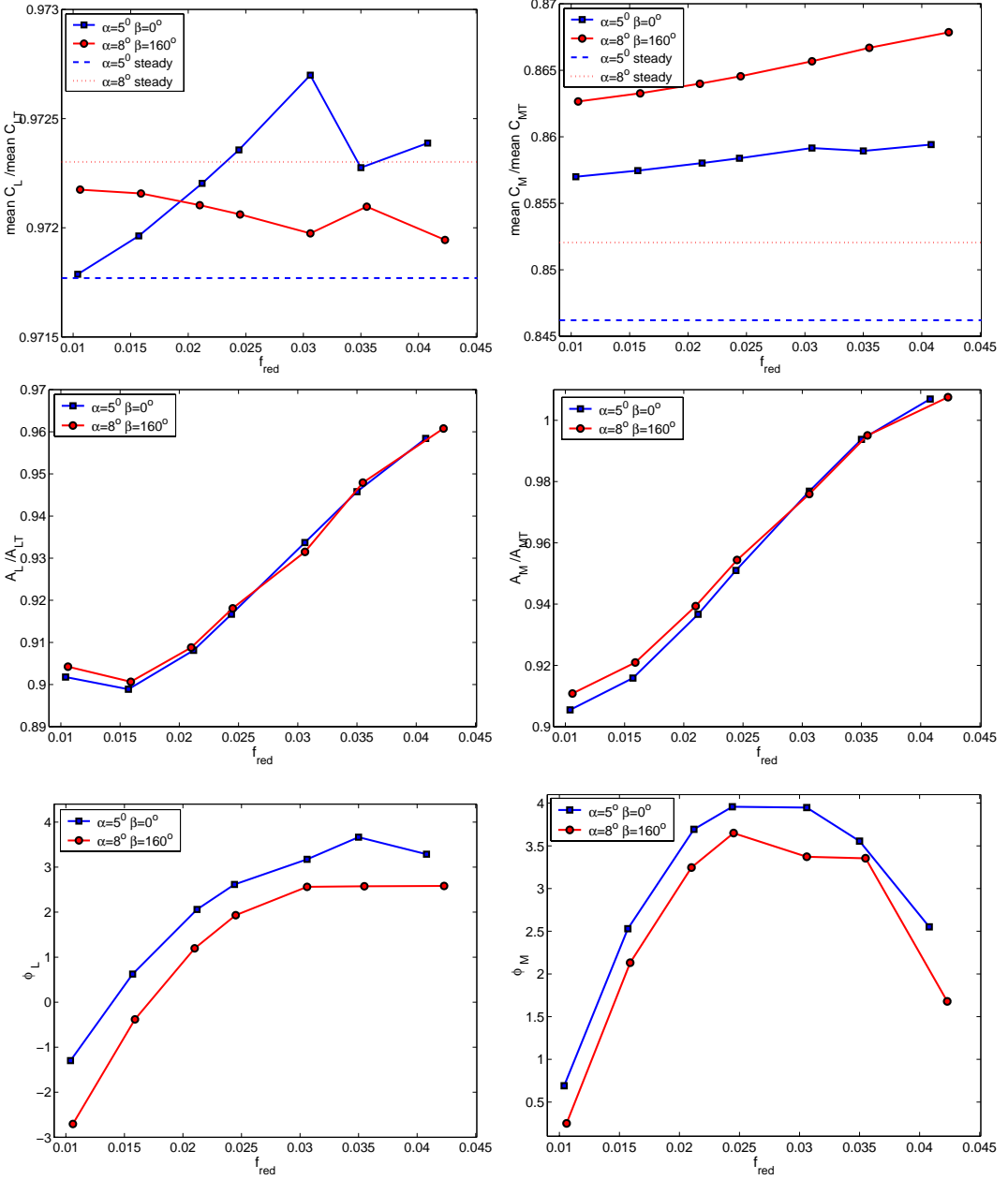


Figure 4.9: Influence of reduced frequency on the free-flow-to-tunnel-flow ratios of the lift characteristics (left figures) and moment (right figures) for two different configurations of α and β , $(\alpha, \beta)_1 = (5^\circ, 0^\circ)$ and $(\alpha, \beta)_2 = (8^\circ, 160^\circ)$. The ratios of the mean quantities are shown in the upper figures, the ratios of the amplitudes are shown in the middle figures, and the phase shift, in degrees, is shown in the lower figures. The phase shift is positive when the tunnel signal lags the free flow signal. $A/c = 13.16$ and $h/c = 4.47$.

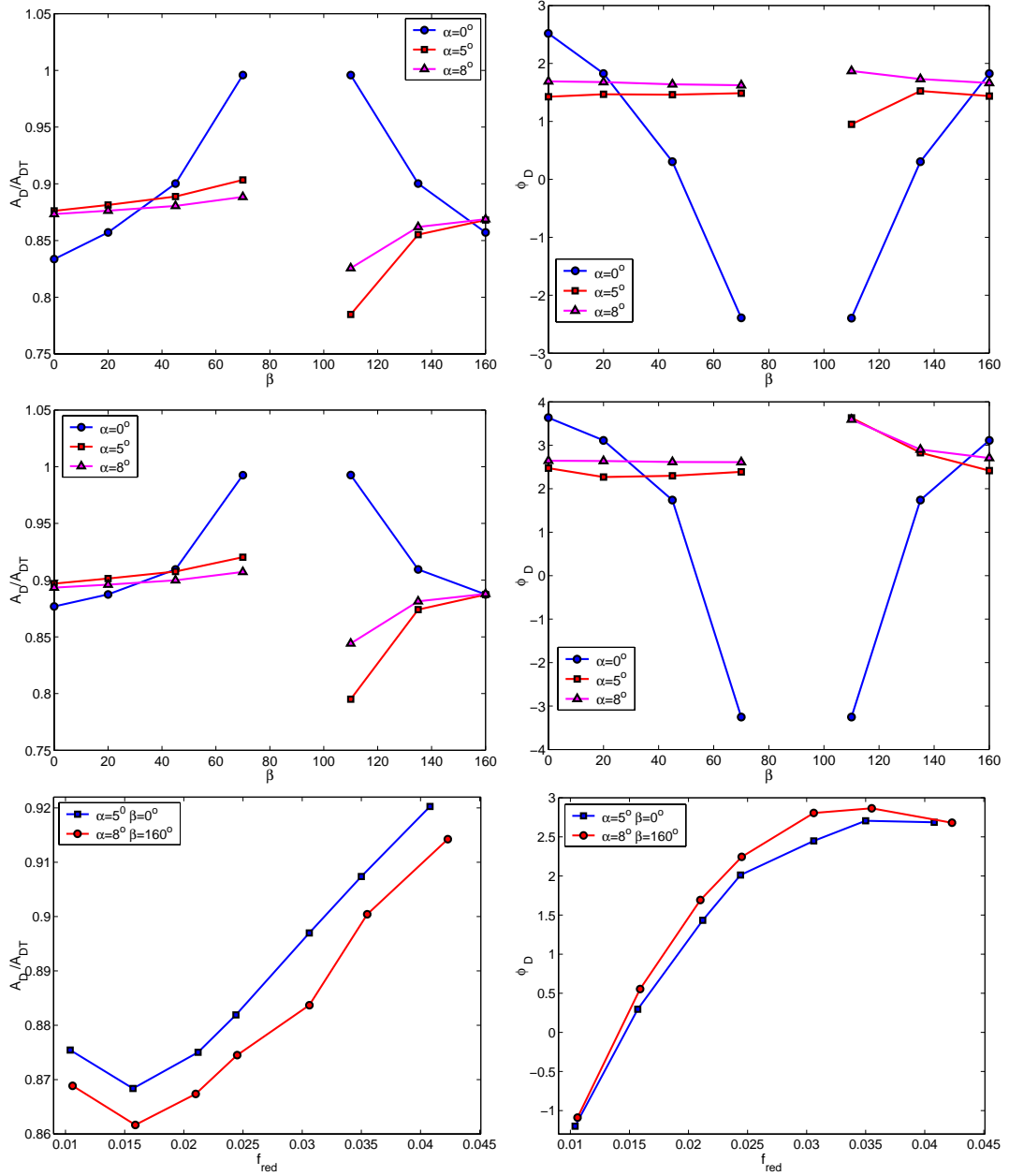


Figure 4.10: Dependence of drag quantities on change in movement direction and angle of attack (upper figures: $f_{red} = 0.02$, middle figures $f_{red} = 0.03$). The dependence of drag quantities on change in reduced frequencies are shown in the lower figures. The left figures show the drag ratios, and the right figures show the drag phase shifts. In the lower two figures, the same configuration for α and β was used as in figures 4.9. $A/c = 13.16$ and $h/c = 4.47$.

drastically on reduced frequency. The strong dependance on the drag quantities of the angle of attack and movement direction clearly reflects the fact that the drag in these computations is induced by the lift. The added phase lag from the tunnel effect is again strongly dependant on the angle of attack, direction of motion, and in this case on the reduced frequency as well. Note that the overall shape and magnitude of the two lower graphs match the corresponding graphs for the lift, again underlining the fact that the unsteady drag in a potential solution is induced from the lift.

Even though it may be plausible to perform unsteady drag corrections based on the panel code results for the lift induced drag forces in the fully attached case, this is not done. The reason for this is that the corrections can only be used when the flow is fully attached, which only holds true for a part of the experiments, leaving part of the experiments uncorrected. Therefore another strategy was employed for the drag forces, as will become evident later.

The results of an investigation of the influence of the amplitude of the motion is shown in figure 4.11. It is seen that the ratio of the mean forces in free flow and tunnel

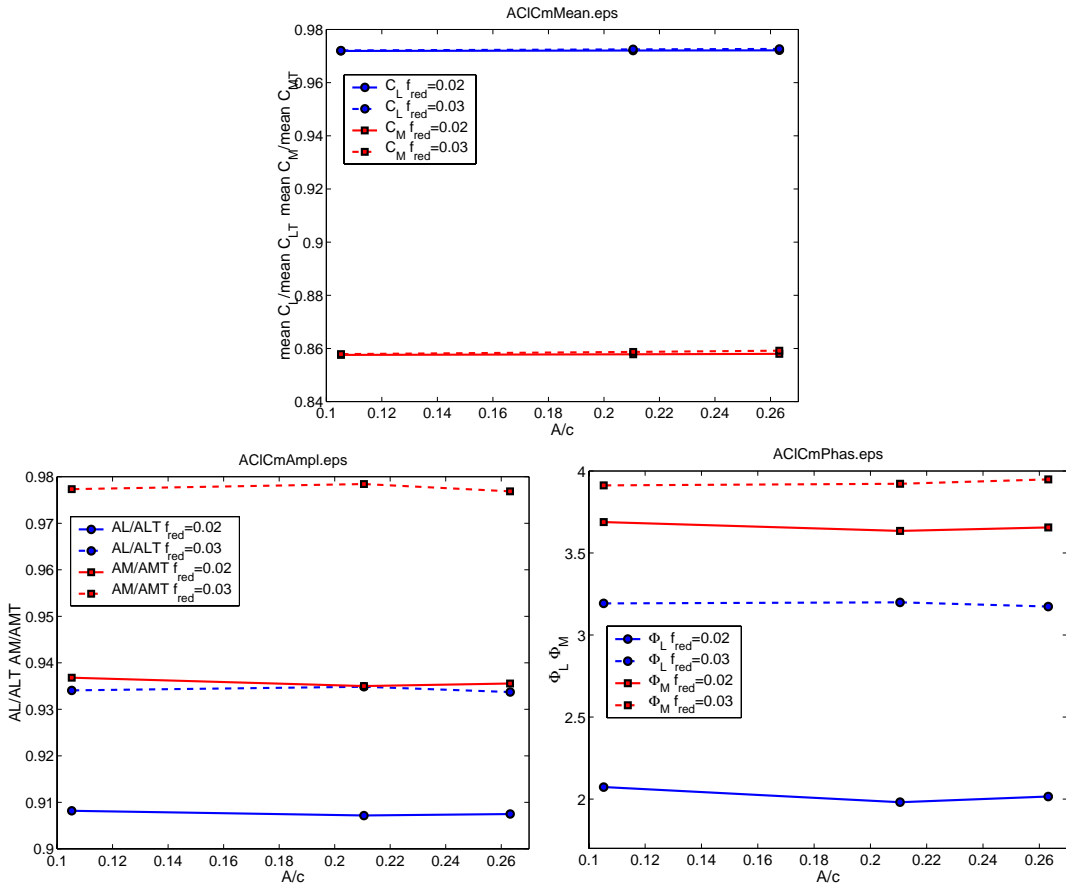


Figure 4.11: *Influence of movement amplitude on tunnel effect. The upper graph shows the ratios of the mean quantities, the lower left graph shows the amplitude ratios of the forces, and the lower right figure shows the phase change of the forces. $\alpha = 5^\circ$ and $\beta = 0^\circ$.*

flow is constant, as in all previous figures. Moreover, it is evident that there is no

influence of the movement amplitude on neither the amplitude ratios or the phase shifts.

It has been observed that the amplitude ratios of all forces increase with reduced frequency, signifying that the augmenting effect of the tunnel is decreasing as the frequency, and hence amplitude of the velocity with which the airfoil moves, is increased. It would be expected that an increase in the movement velocity should have greater influence at the boundary, thus enhancing the tunnel effects on the airfoil. This would lower the amplitude ratio, which is seen from the panel code results not to be the case. In order to investigate the isolated effect of the tunnel walls on the induced velocities on the airfoil from the wake, a simple model of the wake was considered. The unsteady wake of the airfoil was modelled by a straight line expanding in the free flow direction from the trailing edge of the airfoil, as shown in the right hand side of figure 4.12, which shows the phenomenological relation between position, velocity, relative angle of attack, lift, bound circulation and rate of vorticity shed in the wake. The position,

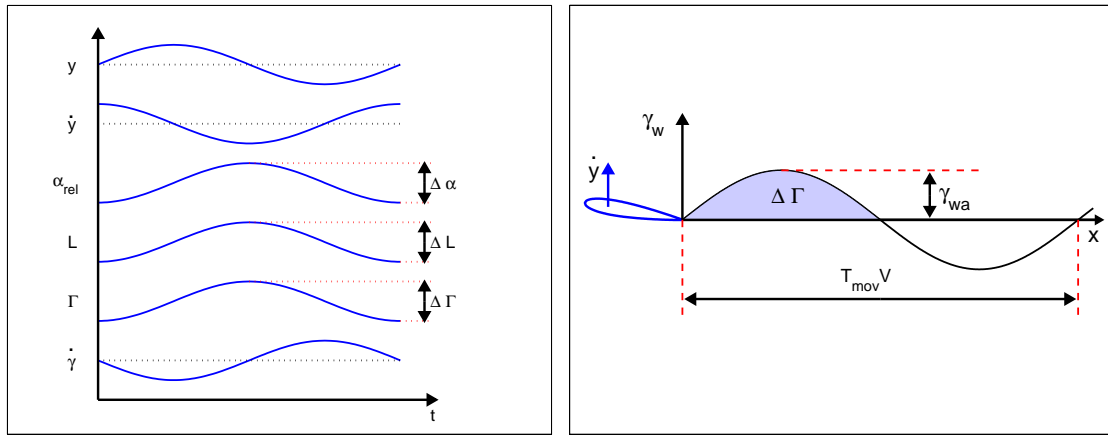


Figure 4.12: *Simple model of the unsteady wake of an airfoil undergoing translatory oscillations parallel to the incoming flow, $\beta = 0^\circ$. Left : phenomenological relation between position, velocity, relative angle of attack, lift, bound circulation and rate of vorticity shed in the wake. Right : Spatial distribution of wake vorticity at $t = nT_{mov}$.*

velocity and relative angle of attack of the airfoil are related through

$$\begin{aligned} y &= A \sin(2\pi f_{mov} t) \\ \dot{y} &= 2\pi f_{mov} A \cos(2\pi f_{mov} t) \\ \alpha_{rel} &= \alpha - \arctan \frac{\dot{y}}{V}. \end{aligned}$$

From this, the expression for $\Delta\alpha_{rel}$ is

$$\Delta\alpha_{rel} = \arctan \frac{4\pi f_{mov} A}{V} \simeq \frac{4\pi f_{mov} A}{V}.$$

In order to relate the motion of the airfoil to the lift, and hence circulation, the following relations are used

$$L = 2\pi\alpha_{rel} \quad (4.23)$$

$$L = \rho V \Gamma, \quad (4.24)$$

thus obtaining

$$\begin{aligned}\Delta L &= 8\pi^2 \frac{f_{mov} A}{V} \quad \text{and} \\ \Delta \Gamma &= 8\pi^2 \frac{f_{mov} A}{\rho V^2}.\end{aligned}$$

The use of the lift and relation between lift and circulation from the potential solution of the steady flow over an infinitely thin airfoil is not strictly correct, but will suffice in this phenomenological investigation. The main effect of the instationarity would be the introduction of a phase lag of the wake with respect to the airfoil motion. However, this effect is of no interest in the current derivation, as will become evident later. From Kelvins theorem we get the shape of rate of vorticity shed in the wake, as shown in the lower left of figure 4.12. From this the spatial variation of the wake vorticity is as shown in the right hand side of the figure. The spatial period of the wake is given from the period of the motion and the free flow velocity as

$$\Delta X_w = T_{mov} V = \frac{V}{f_{mov}} = \frac{c}{2f_{red}}.$$

Employing Kelvins theorem once more, we get that $\Delta \Gamma$ is the amount of vorticity shed in the wake between $x = 0$ and $x = T_{mov} V / 2$, as illustrated in figure 4.12. From this the amplitude of the wake vorticity is determined as

$$\gamma_{wa} = 8\pi^3 \frac{f_{mov}^2 A}{\rho V^2} = 32\pi^3 \frac{f_{red}^2 A}{\rho c^2}. \quad (4.25)$$

Based on the previous result, the final expression of the wake at time t is

$$\gamma(x) = 32\pi^2 \frac{A f_{red}^2}{\rho c^2} \sin\left(\frac{4\pi f_{red} x}{c} - 4\pi \frac{V f_{red} t}{c}\right) \quad 0 < x. \quad (4.26)$$

The induced velocity at the origio of a system in which two vortices with strengths Γ located in (x_v, h) and $(x_v, -h)$, as shown in the left hand side of figure 4.13, is

$$w = \frac{\Gamma}{\pi h} f_{ind}(x_v/h) \quad (4.27)$$

$$f_{ind}(x_v/h) = \frac{x_v/h}{1 + (x_v/h)^2}. \quad (4.28)$$

From this expression it is seen that f_{ind} determines the geometrical influence of the x -coordinate of the vortices. It is noted that f_{ind} is a function of x_v/h only. The right graph in figure 4.13 shows f_{ind} versus x_v/h . It is noted that the maximum value of f_{ind} is at $x_v/h = 1$. This implies for the tunnel mirror wakes that the most important part of the wake with respect to the induced velocities from the nearest mirror-wakes lies one tunnel height downstream of the airfoil. The wake and the two nearest mirror wakes are shown for three different reduced frequencies in figure 4.14. It is noted that the phase of the mirror vortex sheets in the most sensitive area, around $x \sim h$, is shifted with respect to the motion of the airfoil as the reduced frequency of the motion is changed.

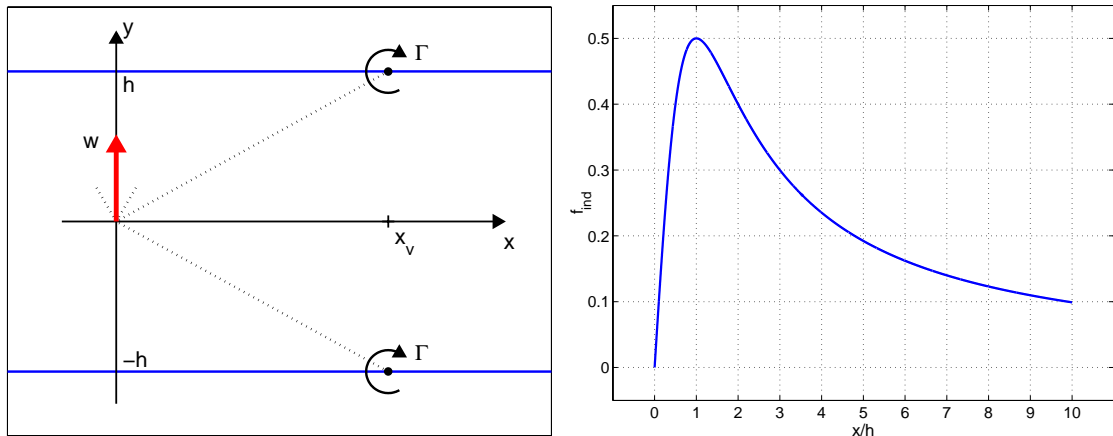


Figure 4.13: *Left : induced velocity from two vortices with strengths Γ located in (x_v, h) and $(x_v, -h)$. Right : $f_{ind}(x_v/h)$ from equation 4.28.*

In order to investigate the full effect of the tunnel on the induced velocities, the induced velocity from the wake was computed numerically from equation 4.26 and 4.27 using 30 mirror images of shifting sign above and below the actual wake vortex, a total of 60 mirror wakes. Each wake was discretized using 200 equidistantly located concentrated vortices per period of the wake. Two spatial periods of the wake was considered. Figure 4.15 shows the effect of tunnel walls on the induced velocity from the wake at the quarter-chord point. On the upper graph, which shows an example of the induced velocity from the wake in free flow and in a tunnel, it is seen that the effect of the wake is substantially modified by the addition of the tunnel walls. In the lower right graph, the phase change introduced by the addition of the tunnel wall is shown as a function of reduced frequency. The values of the phase change ranges from -25.7° to -23° , indicating a strong tunnel effect on the phase of the induced velocity from the wake. Another manifestation of the strong tunnel effect on the induced velocities from the wake is evident in the lower left figure, where the amplitude ratios of the free-flow-to-tunnel-flow values for the induced velocity is shown as a function of reduced frequency. This value is decreasing towards unity as the reduced frequency is increased. This may give an explanation to the surprising behavior of the force amplitude ratios versus reduced frequency depicted in the middle graphs of figure 4.9.

The general effect of the unsteady wake in oscillating potential flow is a reduction of the amplitudes of the forces compared to quasi-steady results, as well as a shift in the phase, the so-called phase lag⁴. The fact that the amplitude ratios decrease towards one with increasing reduced frequency, indicates that the reduction of the induced velocities by the presence of the tunnel walls decrease. If this is interpreted as a general increase of the wake effect on the forces, then this is a possible explanation of the increase in the force amplitude ratios with reduced frequency.

The instationary effect on the forces, and hence circulation, is a reduction of the amplitudes, as well as a phase lag. This effect is reflected in the wake of an unsteady flow, but the phase change and amplitude ratio change of the induced velocities due to the presence of the tunnel walls remains unaltered. Therefore the present results apply in

⁴this is explained in chapter 3.2

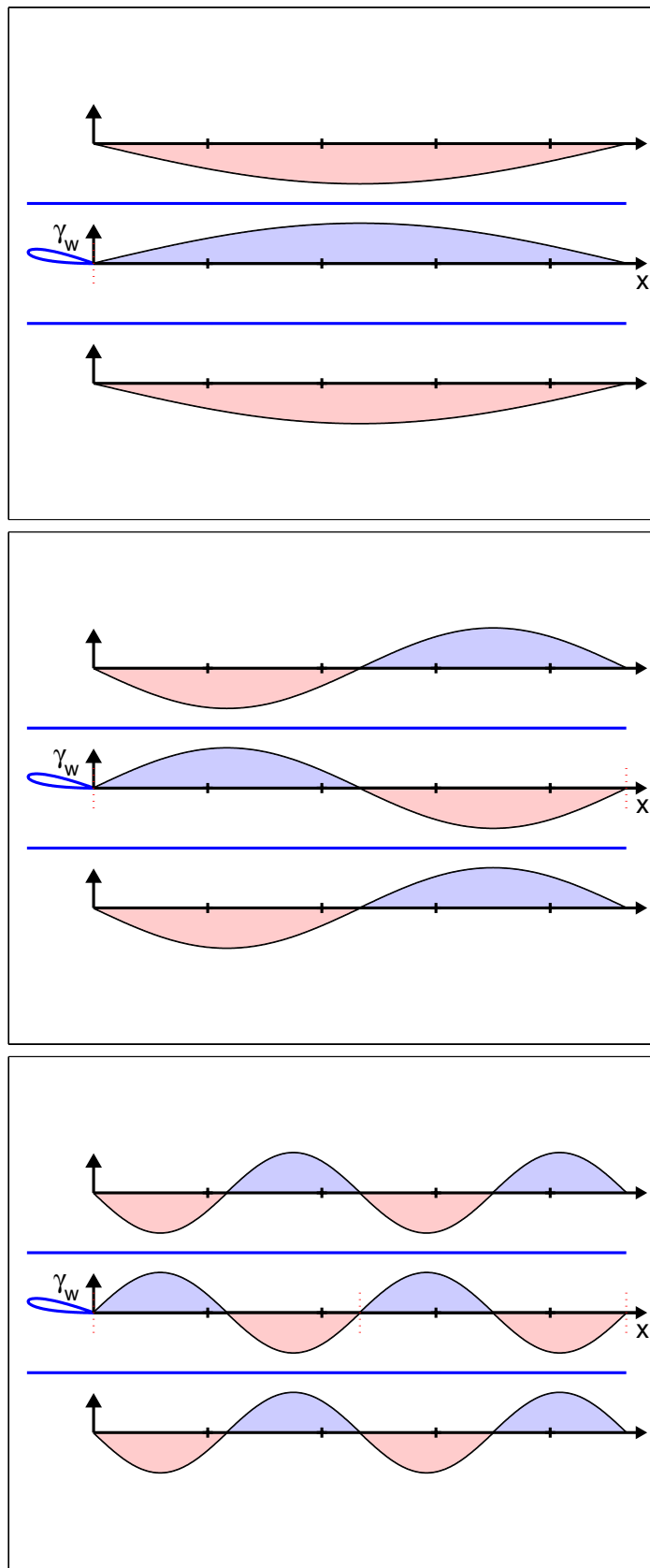


Figure 4.14: Wake and first mirror wakes at three different reduced frequencies.

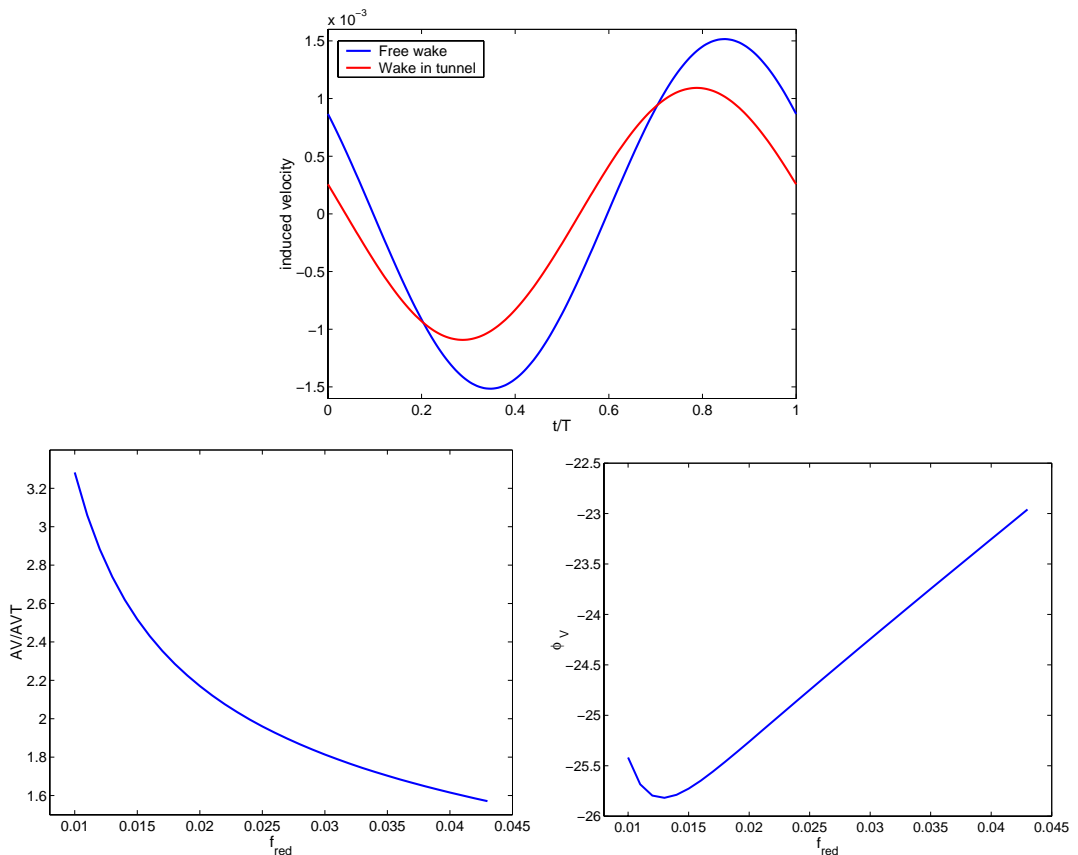


Figure 4.15: *Influence of tunnel walls on induced velocity from the wake at the quarter chord point. The upper graph shows an example of the induced velocity from the wake in free flow and in a tunnel. The lower graphs show the amplitude ratio (left) and phase difference (right) as functions of reduced frequency. $h/c = 4.47$.*

the unsteady case as well.

The simple analysis of the tunnel wake effect is essentially based on the geometric proportions of the wake-tunnel system, meaning that the relative effect of the tunnel, the phase shift and velocity amplitude ratios of the induced velocities, are independent of the actual wake strength. Therefore, the key parameter on the effect is the wake wavelength to tunnel height ratio

$$\frac{V}{f_{\text{mov}} h},$$

or, in terms of non dimensional quantities

$$\frac{c/h}{2f_{\text{red}}}.$$

The fact that the dynamic behavior of the airfoil-tunnel system is independent of the amplitude of the airfoil motion, and hence, the amplitude of the velocity with which the airfoil moves, suggests that the explanation to the relative decrease in force augmentation by the tunnel walls is not related to the amplitude. This is another indication that the alteration of the wake effect by the presence of tunnel walls is responsible for the decreasing tunnel effect with increasing reduced frequency.

The very simplified analysis of the tunnel effect on the induced velocity by the wake gives a hint at the explanation to the observed effect, but it is the author's belief that the full explanation to this effect lie hidden in the complex feedback effect of the wing-wake-wall system.

In order to investigate the correctness of the corrections obtained with the panel code for stalling airfoils, modifications were made to the steady code, allowing the airfoil to be at a high incidence while limiting the lift/circulation to a specified level, emulating the characteristics of a stalling airfoil. The modified solution still obeys the Neumann condition on the surface of the airfoil, but violates the Kutta condition, as explained in section 3.5.6. This modification creates a singular point at the sharp trailing edge of the profile. Since the conditions for the airfoil are not directly physically meaningful, an indirect comparison of the tunnel effect was undertaken by comparing the tunnel source strengths for the two cases, since the tunnel wall source strength obtained from the solution is an indirect measure of the tunnel effect.

Figure 4.16 shows the comparison between the tunnel wall source strength for an attached flow around an airfoil at 8° incidence, and an airfoil at 20° incidence, with identical circulation (left) and lift (right), where it is noted that the tunnel source distributions for attached and stalling cases are almost identical. From this it was concluded that the extra physical blockage associated with a stalling profile compared to a profile with attached flow having the same lift, is of minor importance.

Correction of the dynamic signal based on panel code results are basically based on a positive slope of the steady lift curve, meaning that more or less the same relation between the wake strength and profile motion exist. The wake is locked into a certain phase shift range with respect to the motion due to the limitations of the panel code. This could have implications on the correctness of the obtained corrections in the stalling case because in this case the slope of the lift curve can be negative due to

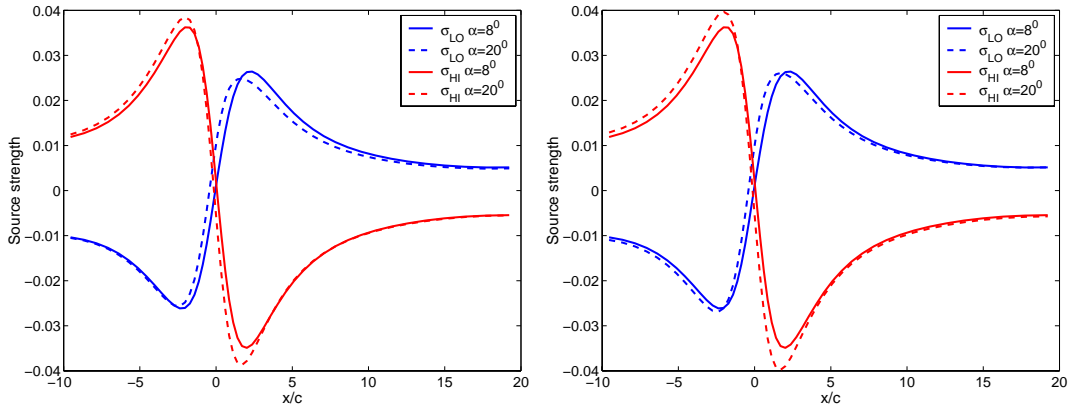


Figure 4.16: *Comparison between tunnel wall sources for attached and stalled flow with identical circulation (left) and identical lift (right). The incidences of the airfoils are $\alpha = 8^\circ$ and $\alpha = 20^\circ$ for the attached and stalled cases, respectively. $h/c = 4.47$.*

the complex nature of separation and stall, shifting the phase of the wake strength drastically in relation to the airfoil motion.

In spite of this, the unsteady corrections obtained with the panel code were used to obtain corrections for both attached and stalling experiments for blocking, streamline curvature, and unsteady effects.

The effect of the tunnel walls on the highly non-linear dynamic effects, such as the onset of stall and separation, are not modelled in the present corrections due to the inherent limitations of the potential code. Standard steady corrections do not take into account these effects either, and are still being used widely in lack of better tools. However, the tunnel effect of stall and separation can be indirectly corrected for by use of the wake blockage correction. As this is computed from the mean drag in the unsteady case, the Knoller-Betz effect is actually influencing the magnitude of the correction. As shown previously, this effect is very weak in the cases considered, and will therefore not add considerably to any under-correction of the data.

Corrections to the phase are not applied in this work, since the behavior of the measured system may differ considerably from the panel code results due to turbulence and viscous effects such as stall and separation. The above investigation, however, sheds some light on the magnitude of the tunnel phase shift effect, and on the parameters on which it depends.

From the potential code results it was seen that the effect of the tunnel walls in most cases was a phase lag of the forces, effectively enhancing the effect of the unsteady wake. In most cases the tunnel phase lag for the lift forces ranged from 1° to 3° , and slightly higher for the quarter chord moments.

The effect of a 3° phase shift of the signal may not have a significant effect on the damping coefficient, since the phase shift between the velocity and the forces are not big, always below 15° according to Theodorsens phase-lag function⁵. Due to the same argument, it could be argued that a small change in the phase shift could have a relatively big influence on the mass coefficient, since the part of the aerodynamic forces contributing to that is 90° out of phase with the velocity.

⁵see section 3.2.

Final Form of the Unsteady Corrections

Based on the previous observations and discussions, the following tunnel corrections are proposed.

Summarizing the results for the combined unsteady solid body correction, streamline curvature, and effect of motion, the corrections read :

$$C_L^* = \overline{C_{LT}}F_1 + (C_{LT} - \overline{C_{LT}})F_2 \quad (4.29)$$

$$C_M^* = \overline{C_{MT}}F_3 + (C_{MT} - \overline{C_{MT}})F_4, \quad (4.30)$$

where the functions F_1 to F_4 are determined from the potential code simulations. In the general case F_1 and F_3 are functions of the height to chord ratio only, whereas the corrections to the dynamic quantities, F_2 and F_4 depend on the height to chord ratio and reduced frequency. If we restrict ourselves to the experimental set-up of this work, with $h/c = 4.47$, F_1 and F_3 are constants with the values

$$F_1 = \frac{\overline{C_L}}{\overline{C_{LT}}} = 0.9722 \quad (4.31)$$

$$F_3 = \frac{\overline{C_M}}{\overline{C_{MT}}} = 0.8616 \quad (4.32)$$

Analytical expressions for F_2 and F_4 were determined by the least squares fits of third order polynomials to the amplitude ratio data shown in figure 4.9. Figure 4.17 shows

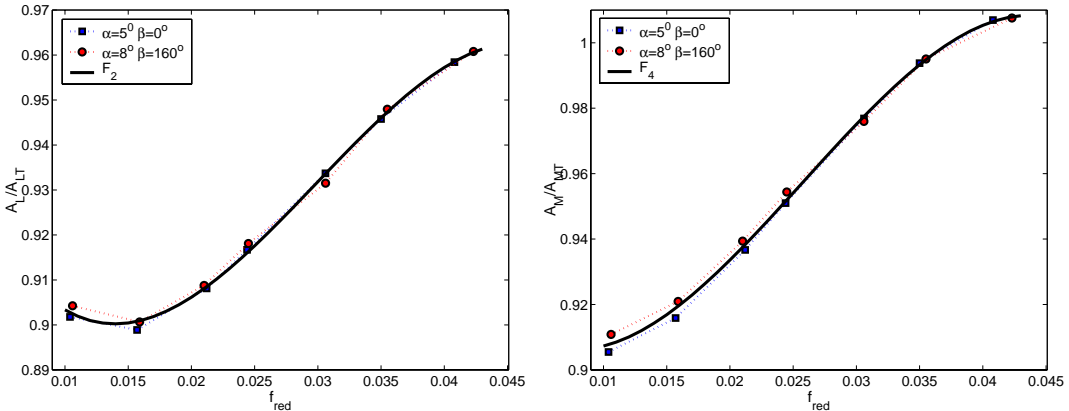


Figure 4.17: Analytical fit for the lift ratio, F_2 , (left) and quarter chord moment amplitude ratio, F_4 , (right), as functions of reduced frequency. $A/c = 13.16$ and $h/c = 4.47$.

the obtained analytical fits for the experimental geometrical setup, which read

$$F_2 = \frac{C_L \text{ Amplitude}}{C_{LT} \text{ Amplitude}} = -3862f_{red}^3 + 346.1f_{red}^2 - 7.400f_{red} + 0.9466 \quad (4.33)$$

$$F_4 = \frac{C_M \text{ Amplitude}}{C_{MT} \text{ Amplitude}} = -4412f_{red}^3 + 340.8f_{red}^2 - 4.508f_{red} + 0.9227. \quad (4.34)$$

The additional correction for the wake blockage is essentially the steady wake blockage correction applied to the corrected unsteady values

$$C_L = C_L^*(1 - 2\epsilon_{wb}) \quad (4.35)$$

$$C_M = C_M^*(1 - 2\epsilon_{wb}). \quad (4.36)$$

The unsteady drag is corrected using the same approach, but including the analytical correction for the solid blocking

$$C_D = C_{DT}(1 - 3\epsilon_{sb} - 2\epsilon_{wb}). \quad (4.37)$$

In equations 4.35 to 4.37, the values of ϵ_{wb} and ϵ_{sb} are given by equations 4.7 and 4.1, respectively, where the mean value of the drag coefficient is used in equation 4.7 to determine the wake blockage parameter ϵ_{wb} .

An example of the effect of the corrections

In order to show the effect of the derived unsteady tunnel corrections, figure 4.18 shows the non-dimensional aerodynamic damping and added mass as function of reduced frequency for uncorrected experimental results, corrected experimental results, and Navier-Stokes simulations. The incidence in the shown case is $\alpha = 8^\circ$, and the

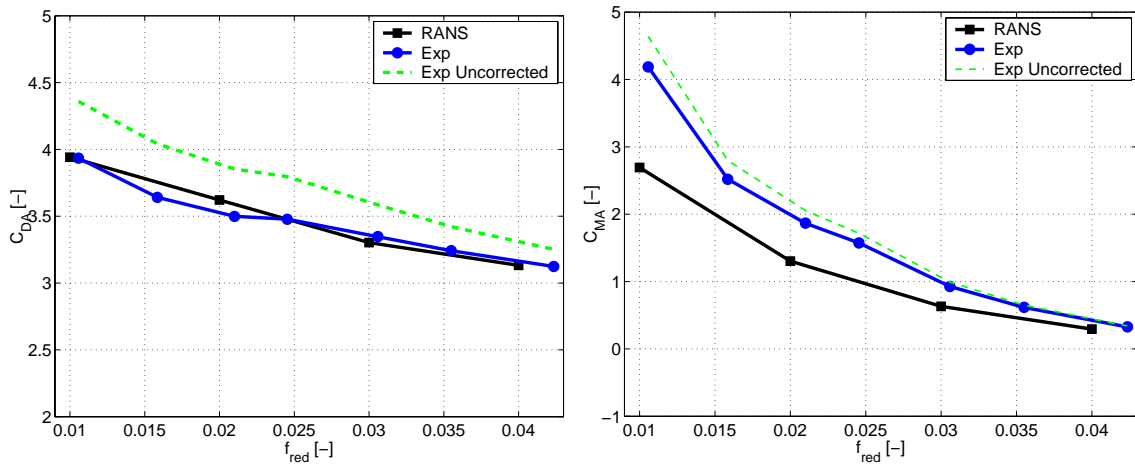


Figure 4.18: *Effect of the unsteady tunnel correction at $\alpha = 8^\circ$, $\beta = 160^\circ$. Non-dimensional aerodynamic damping (left) and non-dimensional aerodynamic added mass (right) as function of reduced frequency. The dashed curve corresponds to the damping and added mass from the uncorrected forces.*

direction of the movement is $\beta = 160^\circ$. In this case the Navier-Stokes computations should be able to predict the dynamics of the flow accurately because of the attached flow at that particular incidence.

It is seen in the left figure, that the aerodynamic damping of the corrected experimental data agrees very well with the aerodynamic damping predicted with the Navier-Stokes code. The results for the added mass, shown in the right figure, is not quite as encouraging as in the damping case. However, the correction drags the experimental values in the direction of the Navier-Stokes results.

It was shown previously that one of the effects of a wind tunnel is a slight phase-lag of the dynamic forces in the tunnel with respect to corresponding free-flow forces. This may have implications on the uncertainty of the aerodynamic damping, and in particular on the aerodynamic added mass.

Consider the following arguments. The source of the aerodynamic damping is found

in both quasi-stationary forces and phase-lag/lift deficiency effects. The source of the aerodynamic added mass are phase-lag/lift deficiency effects exclusively. Therefore, added mass effects are more sensitive to any phase errors introduced by the presence of tunnel walls. This leads to the conclusion that the uncertainty in the prediction of the added mass is higher than the uncertainty of the aerodynamic damping due to the changes in the phase of the dynamic forces caused by tunnel effects.

The general effect of the unsteady wake in fully attached flows can be described by the phase-lag and lift deficiency effects, as described in section 3.2. The phase-lag effects correspond to a positive added mass, as seen in the right figure. Since the effect of the tunnel is an additional phase-lag, the added mass extracted from tunnel experiments would be higher than the corresponding free-flow experiments, even after a correction using the unsteady corrections proposed in this work.

It is the authors belief, that this explanation in combination with the uncertainty of the experiments in general explains the difference between the added mass extracted from the experiments and the ones predicted using the Navier-Stokes code.

Based on the previous discussion, it is seen that figure 4.18 indicates that the proposed unsteady tunnel corrections work fairly well in the shown example.

4.2 Pitching versus translatory motion

Many engineering models describing the aerodynamic forces on wind turbine rotors treat translatory and pitching motion identical. Identical in this sense means that the aerodynamic forces of a translatory motion is evaluated as the forces from the pitching motion with an angular variation corresponding to the relative flow velocity in the translatory case.

As an example of this can be mentioned the dynamic stall model proposed by Stig Øye [63], which is widely used in the wind turbine industry in the program FLEX4/FLEX5 [64]. In many cases, this procedure gives good results. However, sometimes the shortcomings of such models can make simulation of certain phenomena impossible.

The following example outlines the difference between the dynamic response of the forces from motion of an airfoil giving identical relative angles of attack in the case of attached flow.

Figure 4.19 shows a comparison of lift, drag and moment coefficient histories for a NACA 0015 airfoil undergoing heaving motion, $\beta = 0^\circ$,

$$\frac{y}{c} = 0.13 \sin(\omega t), \quad (4.38)$$

and pitching motion corresponding to the relative angle of attack in the heaving case,

$$\begin{aligned} \alpha &= 5^\circ + 4\pi 0.13 f_{red} \cos(\omega t) \frac{180}{\pi} \\ &= 5^\circ + 2.8^\circ \cos(\omega t). \end{aligned} \quad (4.39)$$

The five different pitching curves corresponds to pitching around the leading edge, pitching around the 25%, 50% and 75% chord points and pitching around the trailing edge. The results are computed using the numerical panel code described in section

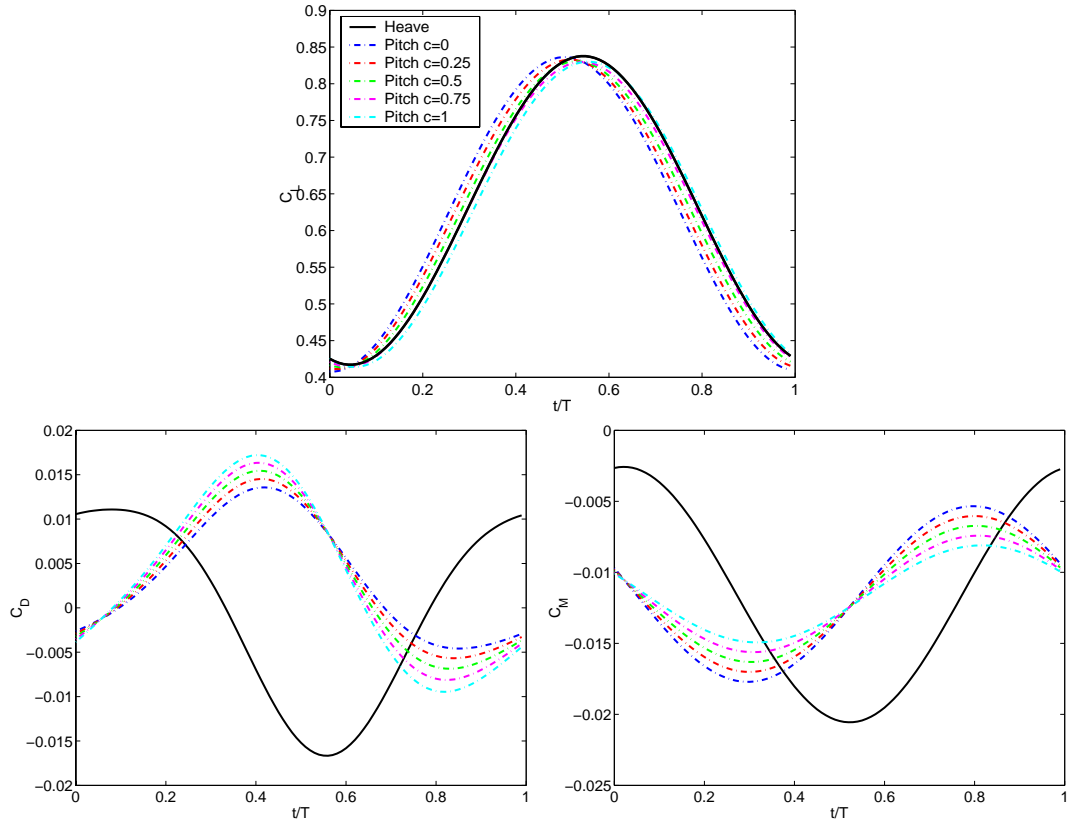


Figure 4.19: Illustration of the difference between the forces in heaving and pitching motion with identical relative angle of attack. The incidence in the heaving case is $\alpha = 5^\circ$ and the reduced frequency is $f_{red} = 0.03$. All results are computed using the unsteady panel code. The upper, lower left and lower right curves show the lift, drag and quarter-chord moment coefficients, respectively. The five different pitching curves corresponds to pitching around the leading edge, pitching around the 25%, 50% and 75% chord points and pitching around the trailing edge.

3.5.

The upper figure clearly shows that the lift coefficient of the heaving case is matched very well for pitching motion around the 75% chord point. This agrees with what is predicted by the unsteady potential theory, where the motion at the 75% chord point determines the forces on the profile, excluding the virtual mass terms.

Even though the lift of a heaving airfoil is matched very precisely by the corresponding pitching motion around the 75% point, the drag and moment are very far from being matched, as seen in the lower left and right figures of figure 4.19. The magnitude, and especially the phase of the drag and moment forces, are far from the corresponding heaving case.

The difference between the drag curves in the two cases can be understood by recalling from section 3.2, that the drag in a potential flow has three terms. A quasi-steady term which arises because the forces from the flow acts perpendicular to the relative flow velocity, a virtual mass term, and a term from the change in relative angle of attack due to the unsteady wake. Clearly, both the quasi-steady term and the virtual mass term are inherently different in the translating and pitching cases despite any efforts to match the relative angle of attack.

The differences between the quarter-chord moment curves in the two cases can be understood similarly. Since both the quasi-steady forces and the forces from the unsteady wake acts in the quarter-chord point, they do not contribute to the quarter-chord moment. The quarter-chord moment in a unsteady potential flow therefore consist of virtual mass terms and a quasi-steady moment term due to the angular velocity of the airfoil. Clearly both of these terms are different in nature for the translating and pitching cases.

If the direction of the motion is different from the heaving direction, it is possible that other effects, such as for instance the variation in bound circulation on the airfoil due to the variation of the relative velocity, might introduce even more effects that render the use of a corresponding pitching motion inappropriate.

The investigation above is valid only for attached flows. However, since the mechanisms for attached flows, which are much lower in complexity than for stalling flows, shows that both drag and moment loops are predicted very different in the cases with identical relative angles of attack, it seems most likely that the response of the aerodynamic forces from airfoils in stall could be substantially different in the two cases as well.

4.3 Analytical Models

In this section results from the analytical models are compared to the experimental data. Focus in the comparison is on the performance of the new heuristic dynamic stall model. Results from analytic unsteady potential theory and quasi-steady theory are shown to highlight the differences between the models.

The comparison between the experimental results and the results of the analytical models begins with a comparison of the non-dimensional aerodynamic damping and added mass, and works its way up in detail level, ending with a comparison of selected force loops.

In order to show the overall features of the analytical models, figure 4.20 shows the non-dimensional aerodynamic damping as function of incidence, α , and direction of motion, β , for the analytical models and the experiments. The left and right figures show the non-dimensional aerodynamic damping at reduced frequencies $f_{red} = 0.02$ and $f_{red} = 0.03$, respectively. The results for the quasi-steady and the new dynamic stall models are based on the mean steady experimental lift and drag coefficients at $Re = 555.000$, and does not include any specific information about the different stall modes. These circumstances will be given attention later in this section.

The upper graphs of figure 4.20 shows the aerodynamic damping computed using analytical potential theory. Potential theory assumes fully attached flow, which means that the results are only physically meaningful at low incidences, $\alpha < 8^\circ$. In this region the agreement with the experimental results, shown in the lower graphs, is good. However, as the incidence is increased into the stalling region the agreement is bad owing to the assumption of attached flow. A region of negative aerodynamic damping exist in the potential analytical results in the region near $\beta = 90^\circ$ for incidences above $\alpha = 10^\circ$. As mentioned, this is beyond the range of validity for a potential model, rendering the results at these incidences meaningless for any potential model. The non-dimensional aerodynamic damping is slightly lower at reduced frequency $f_{red} = 0.03$ compared to the $f_{red} = 0.02$ case. This is attributed to the effect of Theodorsen's function, $\mathbf{C}(k)$, as shown in figure 3.3 in section 3.2. Both the phase lag and lift deficiency effects causes a reduction in the oscillatory forces in phase with the velocity. This leads to a decrease of the non-dimensional damping.

The upper middle figures of figure 4.20 shows the non-dimensional aerodynamic damping from the quasi-steady theory. As mentioned before, these results are based on the steady profile coefficients, and their derivatives with respect to the incidence, and does not take into account the effect multiple stall modes. The non-dimensional aerodynamic damping is independent of the reduced frequency for the quasi-steady theory. This follows from the non-dimensionalisation. The non-dimensional quasi-steady coefficient of aerodynamic damping is obtained from equation 3.87 by division with $0.5\rho cV$

$$C_{DA,QS} = \sin \beta \cos \beta (C_{L\alpha} + C'_{D\alpha}) + \cos^2 \beta C'_{L\alpha} + (1 + \sin^2 \beta) C_{D\alpha}. \quad (4.40)$$

This expression only depends on the aerodynamic coefficients and the direction of the motion.

Comparison of the quasi-steady results with the experimental results show that the quasi-steady model predicts the general aerodynamic damping at the low incidences fairly well. The agreement between quasi-steady and experimental data at the high incidences is not very good. The general level of the aerodynamic damping is somewhat lower for the quasi-steady results than for the experiments, and the model fails to predict the location and magnitude of the minimum aerodynamic damping. Quasi-steady theory predicts that the minimum aerodynamic damping should be located close to the flap-wise direction at $\alpha = 20^\circ$. Clearly, this is not the case in the experiments, where the minimum aerodynamic damping was found to be close to the chordwise direction. The explanation to this effect may lie in the existence of the multiple stall modes, which will be given attention later in this section.

The results from the new stall model is shown in the lower middle figures. The

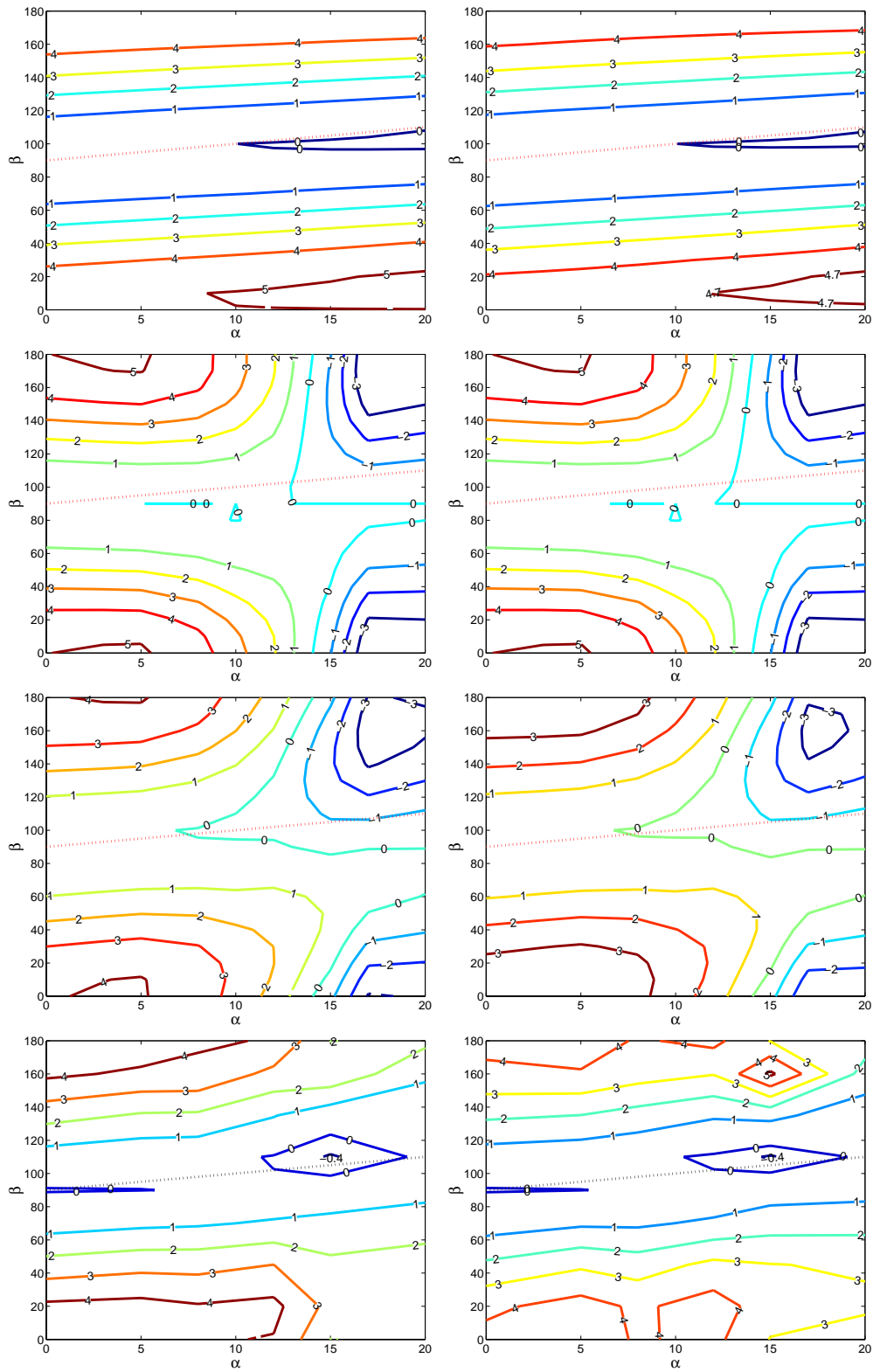


Figure 4.20: Non-dimensional aerodynamic damping versus β and α . Left: $f_{red} = 0.02$, Right: $f_{red} = 0.03$. Upper: Analytical potential theory. Upper middle: Quasi-stationary theory. Lower middle: New stall model. Lower: Experimental results.

absolute value of the non-dimensional damping is slightly lower for the case with $f_{red} = 0.03$ (left) than it is for the case with $f_{red} = 0.02$ (right). The reason for this is the same as for the potential theory results, dictated by Theodorsen's function, $\mathbf{C}(k)$. Comparison of the non-dimensional aerodynamic damping from the new stall model with the quasi stationary results show that the general form of the damping is quite similar for the two models. However, the absolute value of the damping is generally slightly lower for the new model, except for the chordwise direction at incidences below $\alpha = 8^\circ$, where the new model is slightly more negatively damped than the quasi-steady model. As was the case for the quasi-steady model, the new stall model predicts the general aerodynamic damping at the low incidences fairly well, but fails to predict the location and magnitude of the minimum aerodynamic damping. Again, the effect of the multiple stall modes on the performance of the new dynamic stall model will be given attention later in this section.

The aerodynamic damping is an integral quantity expressing the part of the force in phase with the velocity in the direction of the motion. The integral quantity expressing the force in phase with the acceleration is the aerodynamic added mass, which can be non-dimensionalized with the mass of a unit depth circular cross-sectional cylinder of air with half-chord radius, $\pi 0.25c^2\rho$.

Figure 4.21 shows the non-dimensional added mass as function of α and β for the analytical models and the experiments at reduced frequencies $f_{red} = 0.02$ (left) and $f_{red} = 0.03$ (right). Note that forces predicted using quasi-steady theory is in phase with the velocity of the motion because the aerodynamics is based on velocity triangles. Therefore the aerodynamic added mass (upper middle figures) in a quasi-steady computation is zero.

The upper graphs of figure 4.21 shows the non-dimensional added mass computed using analytical potential theory. The shape of the non-dimensional added mass is similar for the two different reduced frequencies, but the absolute level of the surfaces decreases as the reduced frequency is increased. The general agreement with the experimental results is not as good as in the aerodynamic damping case. Again the potential results are only physically meaningful at low incidences, but it seems that high limit on the incidence in this case is maximum $\alpha = 5^\circ$. This shows that the aerodynamic added mass is a more sensitive quantity with regards to the effects of stall.

The lower middle figures show the non-dimensional added mass from the new dynamic stall model. Analogous to the analytical potential results, the general shape of the non-dimensional added mass is similar for the two different reduced frequencies, with the absolute values of the non-dimensional added mass somewhat lower in the case of $f_{red} = 0.03$ than in the case of $f_{red} = 0.02$. A comparison of the non-dimensional added mass computed using the new stall model generally shows the same trends as the experimental results, but the absolute level of the experimental added mass is slightly higher than the results computed using the new stall model. Analogous to the comparison of the non-dimensional aerodynamic damping, the location and level of the minimum non-dimensional added mass is not predicted accurately. In this case the absolute level of the experimental values are significantly larger than the ones predicted by the new stall model. This could indicate that the phase-shifting effect

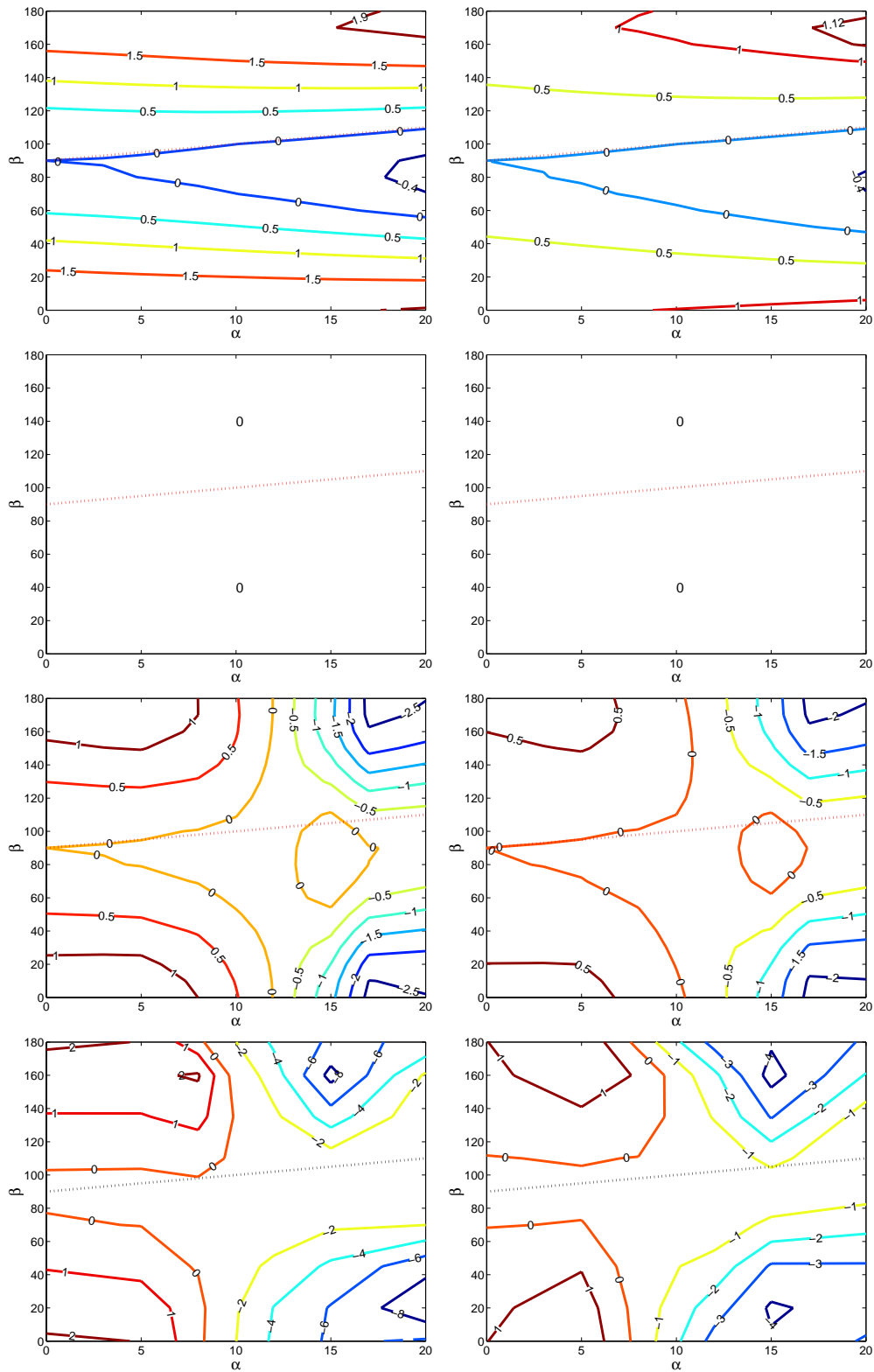


Figure 4.21: Non-dimensional aerodynamic added mass versus β and α . Left: $f_{red} = 0.02$, Right: $f_{red} = 0.03$. Upper: Analytical potential theory. Higher middle : Quasi-steady theory. Lower middle: New stall model. Lower: Experimental results.

increases as the angle of attack is increased into the stalling region. However, since the double stall phenomenon adds a considerable amount of uncertainty to the actual levels of both mean steady and unsteady data, conclusions of this kind should be stated very carefully in this case.

The fact that the general shape of the added mass is correct supports the assumption that the dynamics of the flow can be described by a model similar to a unsteady potential theory model, which is one of the basic assumptions behind the new stall model. However, the present results indicate (as stated previously) that the phase-shifting effect is not modelled correctly in the stalling region.

The presence of the multiple stall modes in the experiments renders the validity of using only one set of characteristic constants for each angle of attack dubious with the present set of data. If the mean data should be extracted with a reasonable accuracy, the time-series would have to be sufficiently long to get enough information on the statistics of each stall mode. This means that the likelihood of having one specific stall mode should be determined with a high degree of certainty. However, since the present experimental measurements consist of only 60 second sampling periods, the uncertainty on the stall-level statistics, and hence the levels of the mean lift, drag and moments, are connected with a very big uncertainty in the region where multiple stall modes occur, for $15^\circ < \alpha < 20^\circ$.

In order to investigate if the aerodynamic damping of the specific stall modes for a moving airfoil can be predicted using steady force coefficients for the corresponding stall modes, figure 4.22 shows a comparison of the non-dimensional aerodynamic damping (left) and added mass (right) from the analytical models and the experiments at angles of attack $\alpha = 15^\circ$ and $\alpha = 20^\circ$. Because not all three stall modes were present in the steady part of the experiments, only force coefficients and derivatives for the two stall modes present at each angle of attack can be found. The force coefficients and derivatives used in the simulations are given in the table below.

| | Mean $\alpha = 15^\circ$ | Hi $\alpha = 15^\circ$ | Vhi $\alpha = 15^\circ$ | Mean $\alpha = 20^\circ$ | Lo $\alpha = 20^\circ$ | Hi $\alpha = 20^\circ$ |
|--|--------------------------|------------------------|-------------------------|--------------------------|------------------------|------------------------|
| C_L | 1.05 | 1.05 | 1.07 | 0.62 | 0.55 | 0.95 |
| C_D | 0.12 | 0.12 | 0.11 | 0.28 | 0.28 | 0.33 |
| $\frac{\partial C_L}{\partial \alpha}$ | -1.07 | -1.07 | 0.01 | -3.93 | 1.38 | -0.26 |
| $\frac{\partial C_L}{\partial \alpha}$ | 2.13 | 2.13 | 1.40 | 1.28 | 1.27 | 2.41 |

As evident from the table, the low stall mode was not present in the steady $\alpha = 15^\circ$ experiment, as was the very high stall mode at $\alpha = 20^\circ$. Furthermore it is seen that the mean and the high stall modes are identical for the $\alpha = 15^\circ$ case. The derivatives of the force coefficients in the low and high stall modes for $\alpha = 20^\circ$ is computed from the steady experimental data shown in figure 2.14 using forward and backward differences, which introduces some uncertainty in the results.

It is seen from figure 4.22, that the specification of separate coefficients for each stall mode generally improves the prediction of the non-dimensional aerodynamic damping; greatly so in the $\alpha = 20^\circ$ case. Note that the mean and high stall mode curves

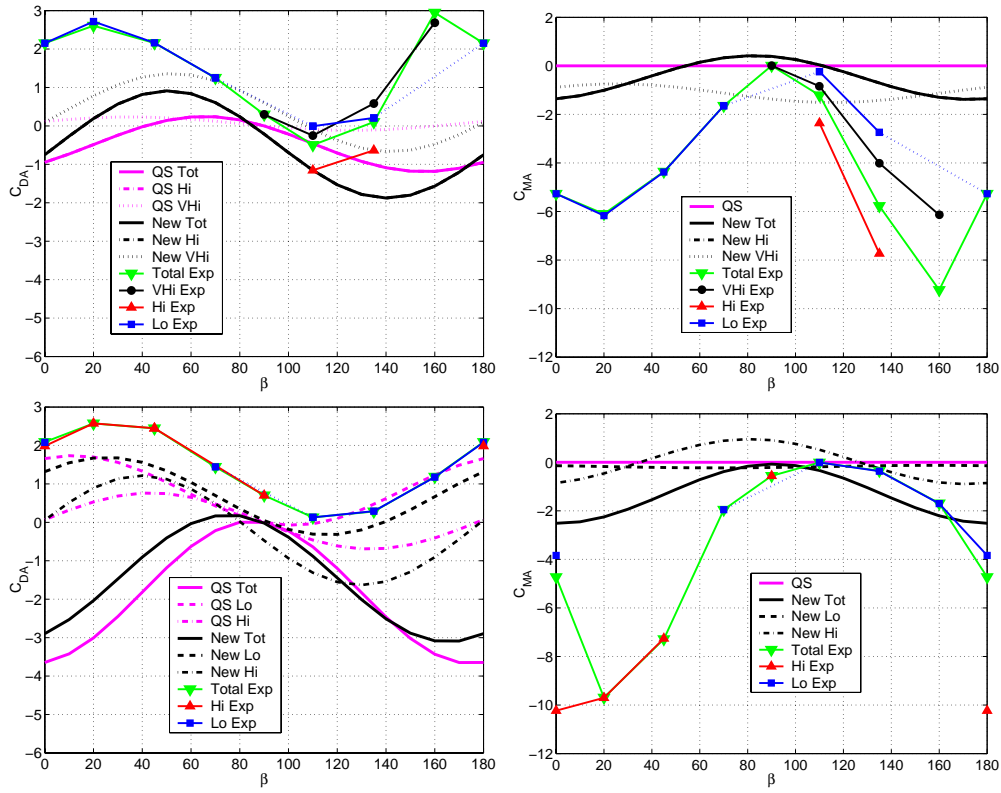


Figure 4.22: Comparison of analytical models and experimental results at incidences where multiple stall occurs. Non-dimensional aerodynamic damping (Left) and non-dimensional added mass (Right) versus movement direction, β . The reduced frequency is $f_{red} = 0.02$. Upper: $\alpha = 15^\circ$. Lower: $\alpha = 20^\circ$.

predicted with the analytical models in the $\alpha = 15^\circ$ case are identical due to the identical force coefficients.

The results from the new stall model is in all cases closer to the experimental results than the quasi-steady results.

Even though the specification of the separate force coefficients for each stall mode improves the prediction, there is still noteworthy discrepancies. Generally the predicted aerodynamic damping is lower than the experimental values. Another difference is the location of the minimum aerodynamic damping in the $\alpha = 15^\circ$ case. The new model predicts the minimum to be located at $\beta = 140^\circ$, which is 30° from the experimental minimum at $\beta = 110^\circ$.

Proceeding to the non-dimensional added mass, shown in the right hand figures of figure 4.22, it is seen that no improvement in the prediction of the added mass was evident when using the data from the specific stall modes as input to the analytical models. This tells us that none of the analytical models are able to predict the exact dynamics of the complex stalling flows.

The experimental aerodynamic damping is fairly independent of the stall mode for all data-points. This could mean that a general mechanism, independent of the stall mode, in the dynamics of a stalling flow determines the aerodynamic damping.

None of the analytical models were able to reproduce this mechanism.

In order to evaluate the performance of the analytical models on a wider spectrum of reduced frequencies, figure 4.23 shows the non-dimensional aerodynamic damping (left) and added mass (right) as function of the reduced frequency of the motion for the experiments and the analytical models. The non-dimensional aerodynamic damping and added mass is shown for four different configurations of incidence, α , and direction of motion, β .

The upper figures are at the incidence $\alpha = 5^\circ$ and direction of motion $\beta = 0^\circ$. The upper left figure shows the non-dimensional aerodynamic damping for the experimental results and all analytical models. The reduced frequency was varied in the range from approximately $f_{red} = 0.01$ to $f_{red} = 0.04$. As shown previously, the quasi-steady results are independent of the reduced frequency, whereas the potential results decrease as the reduced frequency is increased. It is seen that the dynamics of the new model is similar to the dynamics described by potential theory. The level of the aerodynamic damping is lower for the new model than it is for the potential theory results. This is mainly due to the difference between 2π and the slope of the C_L curve. The present slope is $\partial C_L / \partial \alpha = 5.11 = 0.81 \cdot 2\pi$. Both the new model and the potential theory results compare well with the experimental values of the non-dimensional aerodynamic damping. The fairly good agreement between the experimental results and the potential theory is due to the flow being fully attached.

Due to the restrictions of the movement mechanism, the Reynolds-numbers of the dynamic experimental runs had to be reduced in order to increase the reduced frequencies. The Reynolds-numbers corresponding to the reduced frequencies are given in the table below.

| | | | | | |
|-----------|----------|---------|---------|---------|---------|
| f_{red} | < 0.0225 | 0.024 | 0.031 | 0.035 | 0.041 |
| Re | 555.000 | 470.000 | 383.000 | 330.000 | 270.000 |

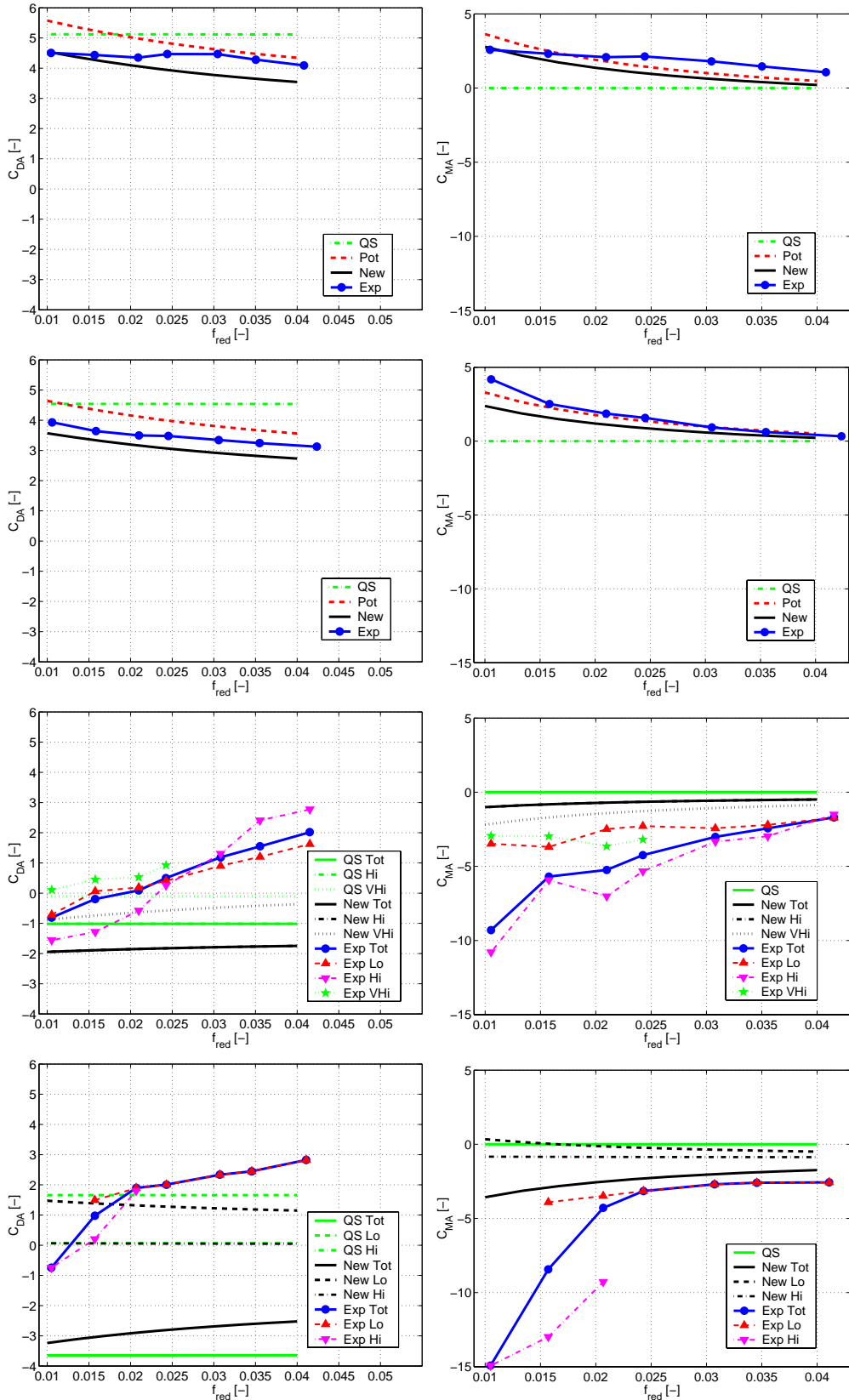


Figure 4.23: Comparison of analytical models and experimental results. Non-dimensional aerodynamic damping (Left) and non-dimensional added mass (Right) versus reduced frequency, f_{red} . Upper: $\alpha = 5^\circ$ and $\beta = 0^\circ$. Upper middle: $\alpha = 8^\circ$ and $\beta = 160^\circ$. Lower middle: $\alpha = 15^\circ$ and $\beta = 135^\circ$. Lower: $\alpha = 20^\circ$ and $\beta = 0^\circ$.

Reynolds-number effects and general increased uncertainty in the experiments at lower Reynolds-numbers may explain the difference between the experimental and the new model aerodynamic damping.

The upper right figure shows the non-dimensional added mass for the same configuration of α and β . Generally, the results of the potential theory and the new model agree well due to the attached flow. The agreement with the experimental data is fairly good, even though the experimental results are at a somewhat higher level for $f_{red} > 0.0225$. The reason for this may lie in uncertainties in the experiments.

The upper middle figures show the non-dimensional aerodynamic damping and added mass at $\alpha = 8^\circ$ and $\beta = 160^\circ$. In general the tendencies are the same as in the upper figures, but the agreement between the new stall model and the experimental results are better in this case, especially for the non-dimensional added mass. This adds to the suspicion about the experimental uncertainty in the $\alpha = 5^\circ$ case stated above.

The lower middle figures are at $\alpha = 15^\circ$ and $\beta = 135^\circ$, for which multiple stall modes exist in both the static and moving experiments. The steady force coefficients and derivatives for the high stall mode and the mean are identical. This leads to identical aerodynamic damping and added mass for the high stall mode and the mean when using the new stall model.

The left lower middle figure shows the non-dimensional aerodynamic added mass. In agreement with the earlier comparisons between the analytical models and the experimental data in the stalling region, the analytical models are not able to predict the correct aerodynamic damping. The predicted damping is lower than the experimentally obtained values at all reduced frequencies. In agreement with the experimental results, the aerodynamic damping of the very high stall mode is higher than the other levels. The new stall model does not show the same dramatic effect of the reduced frequency as the experimental results. A part of this effect may be attributed to Reynolds-number effects, but it is the authors belief that the simple dynamics of the new model does not account for the complex effects for the stalling flows. The right figure shows the corresponding non-dimensional added mass. Analogous to the cases compared earlier, the analytical models underestimate the added mass quite dramatically for all stall modes. Again, it is evident from the figures that some dynamic features of stalling flows are not predicted correctly using the new model.

The last configuration for which the influence of reduced frequency is investigated, is $\alpha = 20^\circ$ and $\beta = 0^\circ$. The results for this case is shown in the lowest figures in figure 4.23. As the earlier comparisons have shown, the specification of separate force coefficients greatly improves the predicted level of the aerodynamic damping. The general trend in the experimental data is, as in the previous stalling cases, not predicted correctly using any of the analytical models.

The right figure shows the non-dimensional added mass, where it is noted that the predictions get worse using the separate force coefficients. The effect of the reduced frequency is, as for the previously investigated stalling cases, not predicted correctly.

Summarizing the investigations of the performance of the new dynamic stall model with regards to prediction of the non-dimensional aerodynamic damping and added mass, the following conclusions can be drawn.

- Good agreement between the new dynamic stall model and experimental results for angles of attack up to $\alpha = 8^\circ$.
- Not good agreement between the new dynamic stall model and experimental results for angles of attack above $\alpha = 8^\circ$.
- The prediction of the aerodynamic damping generally improves by use of separate force coefficients for each stall mode.
- The new stall model is missing important dynamics in the stalling case.

In order to investigate the dynamic behavior of the new stall model in depth, the rest of this section deals with comparison of force coefficient loops obtained with the new model, quasi-steady theory and experimental values.

A comparison of force coefficient hysteresis loops at $\alpha = 5^\circ$ and $f_{red} = 0.02$ are shown in figure 4.24. The direction of the motion, β , is varied. The first column of figures show the lift coefficient versus non-dimensional displacement parameter z/c . The second and third columns show the drag and moment coefficient loops, respectively. In order to indicate whether the force coefficient loops have the same direction, an opening is kept in the loops at identical times in the period of the three curves. This produces an easy way to determine if the direction of the quasi-steady, new dynamic model and experimental loops are the same.

Comparison of the lift coefficient loops in figure 4.24 shows that the dynamic behavior of the lift from new stall model matches the experimental results fairly good at this angle of attack. The small differences in the mean level of the dynamic experimental loops may be explained by the uncertainty in the adjustment of the angle of attack. The shown runs are measured several hours apart, adjusted from other angles of attack in between all the shown runs. Furthermore, the pressure-transducers were calibrated in between each of the shown measurements, which adds to the differences between the runs.

The middle column of the figure shows a comparison of the drag coefficient loops. In this case the agreement is quite good. It is seen that the loops predicted by the new model matches the experiments far better than the quasi-steady results at all shown directions of motion, β . It should be noted that all the values from the experiments are based on pressure measurements, and does therefore not include viscous forces. This is of no concern in this comparison, though, because this is the case for both the dynamic experimental results and the analytical results are pressure forces only.

The last column of figures shows a comparison of moment coefficient loops for the new stall model and the dynamic experimental results. The agreement between the loops is not especially good in any of the cases shown. The determination of the moments in the new stall model is based on an extension of the potential theory expressions, which in the case of low drag is practically identical to the potential theory results. These have the mean value zero because the theory is derived for airfoils of infinitesimal thickness. The mean slope of the experimental and new stall model hysteresis loops are in fairly good agreement, even though the actual shape of the loops differ considerably.

The reason for the difference in the shape of the curves may be caused by a variety of

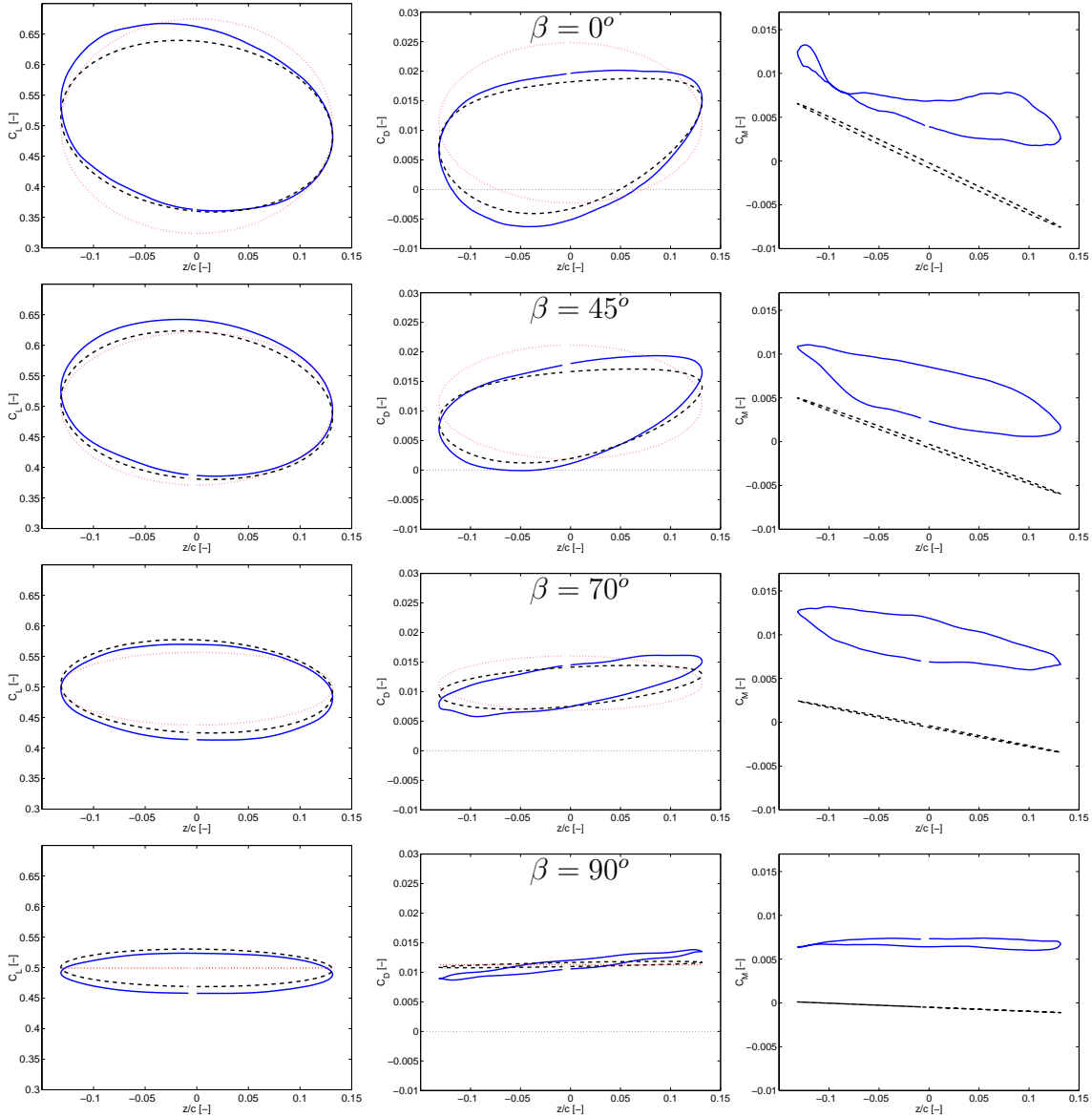


Figure 4.24: Comparison of experimental and analytical model force loops at $\alpha = 5^\circ$ and $f_{red} = 0.02$ at different directions of the movement, β . The left, middle and right column shows C_L , C_D and C_M , respectively. The solid curves are experimental results, whereas the dashed curves and the dotted curves are results from the new stall model and quasi-stationary theory, respectively.

effects, such as trip tape effects, measurement uncertainties, Reynolds number effects, profile thickness effects or other simplifications leading to the unsteady potential theory.

Figure 4.25 gives an insight into the effect of the angle of attack on the agreement between the experimental and predicted loops. In this figure, the force coefficient loops at $\beta = 0^\circ$ and $f_{red} = 0.03$ are shown at angles of attack ranging from $\alpha = 5^\circ$ to $\alpha = 20^\circ$.

The agreement between the predicted and measured lift and drag loops are fairly good up to incidences $\alpha = 8^\circ$. At $\alpha = 12^\circ$, there is a difference between the predicted and measured curves. This difference is attributed to the presence of stall. The analytical models are based on linearisation around a certain angle of attack. At the present experimental setup, the motion of the airfoil corresponds to a change of $\pm 2.8^\circ$ in the relative incidence. This could mean that the force coefficients and derivatives thereof in one point is not enough to describe what happens in the whole range of relative angle of attack.

The general agreement of the moment curves are comparable to the previously shown loops for incidences up to $\alpha = 8^\circ$. After that, considerable differences between the analytical and experimental curves exist. The differences between the curves in case of $\alpha = 12^\circ$ is attributed to the beginning of the stall and the nonlinearities following from that, as explained previously. In the theory section it was stated that the moment expressions were based on generalized potential theory results with an ad-hoc addition regarding the influence of the drag force on the moment. In the case of stalling flows, the drag increases, and with that the ad-hoc term becomes more important.

The comparison of the loops in case of $\alpha = 15^\circ$ does not make any sense, because the stall modes are different in the steady and unsteady experiments at this incidence. The steady experiments consists of the high and very high stall modes at $\alpha = 15^\circ$. The unsteady experiment at $\alpha = 15^\circ$ and $\beta = 0^\circ$ only consists of the low stall mode. The lowest figures, showing the force loops at the beginning of deep stall, $\alpha = 20^\circ$, shows better agreement of the experimental results and the results from the new stall model. The steady force coefficients and derivatives on which the results of the analytical models are based, are the steady low stall mode results. The dynamic loop of the moment curve is predicted fairly good, this may be a coincidence, because the general dynamic behavior of the new model is not good in the stalling cases. The results at $\alpha = 20^\circ$ suggests that the ad-hoc corrections to the generalized potential theory moment expressions gives moments in the right order of magnitude in deep stall.

To gain more insight into the specific behavior of the loops predicted by the new stall model in cases of multiple stall modes, figure 4.26 shows non-dimensional force loops for two cases at incidence $\alpha = 15^\circ$, where multiple stall modes occurs. The case shown in the left figures has $\beta = 70^\circ$ and $f_{red} = 0.03$, whereas the case shown in the right figures has $\beta = 135^\circ$ and $f_{red} = 0.02$.

It is seen in the left figures, that a comparison of the mean experimental loops (blue curves) with the loops predicted using the mean force coefficients from the static experiments compare very bad. As mentioned earlier, this is due to the presence of the multiple stall modes in the experiments. The dynamic experiments shown in the left figures show the occurrence of low and very high stall modes, whereas the static

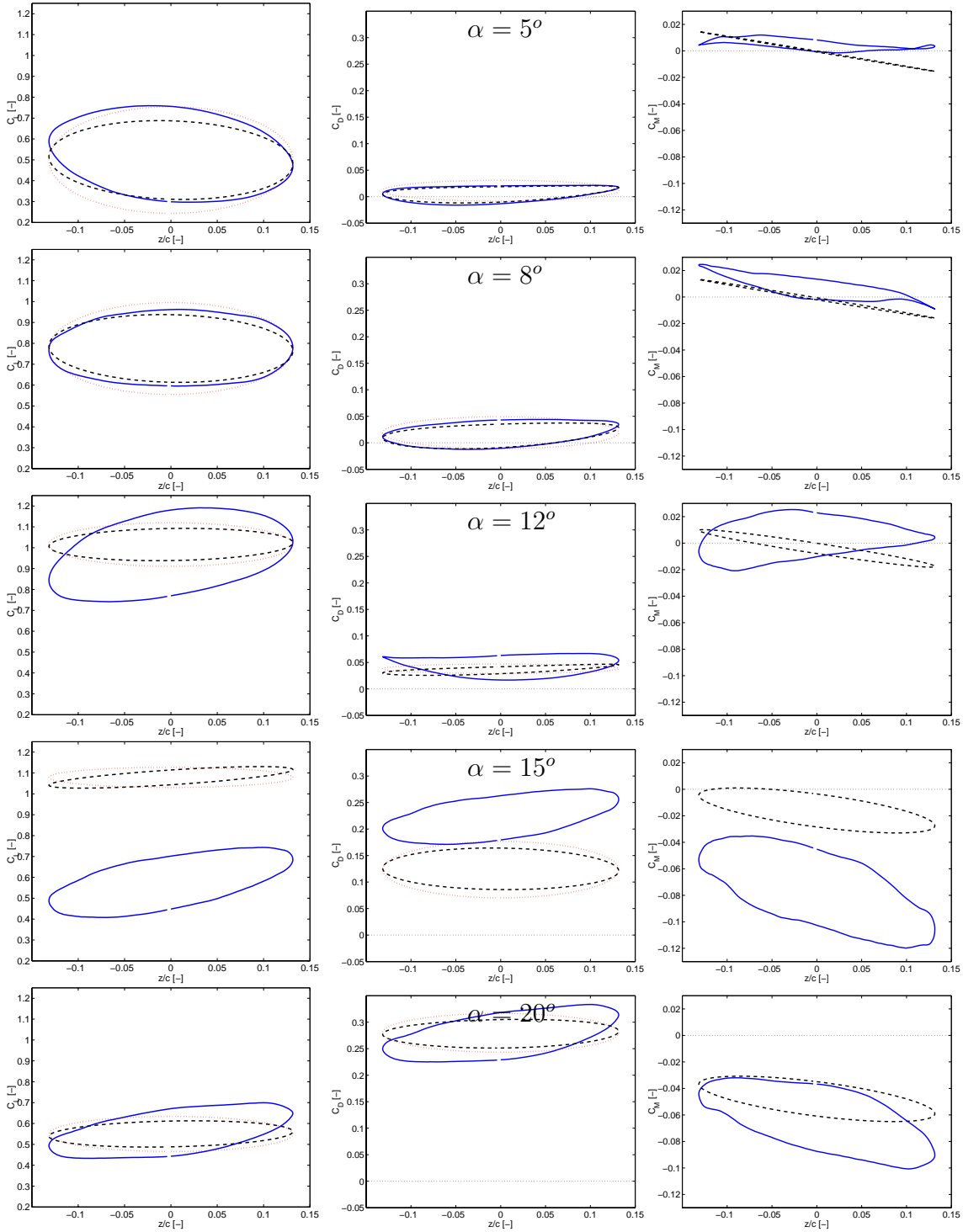


Figure 4.25: Comparison of experimental and analytical model force loops at $\beta = 0^\circ$ and $f_{red} = 0.03$ at different incidences, α . The left, middle and right column shows C_L , C_D and C_M , respectively. The solid curves are experimental results, the dashed curves and the dotted curves are results from the new stall model and quasi-stationary theory, respectively.

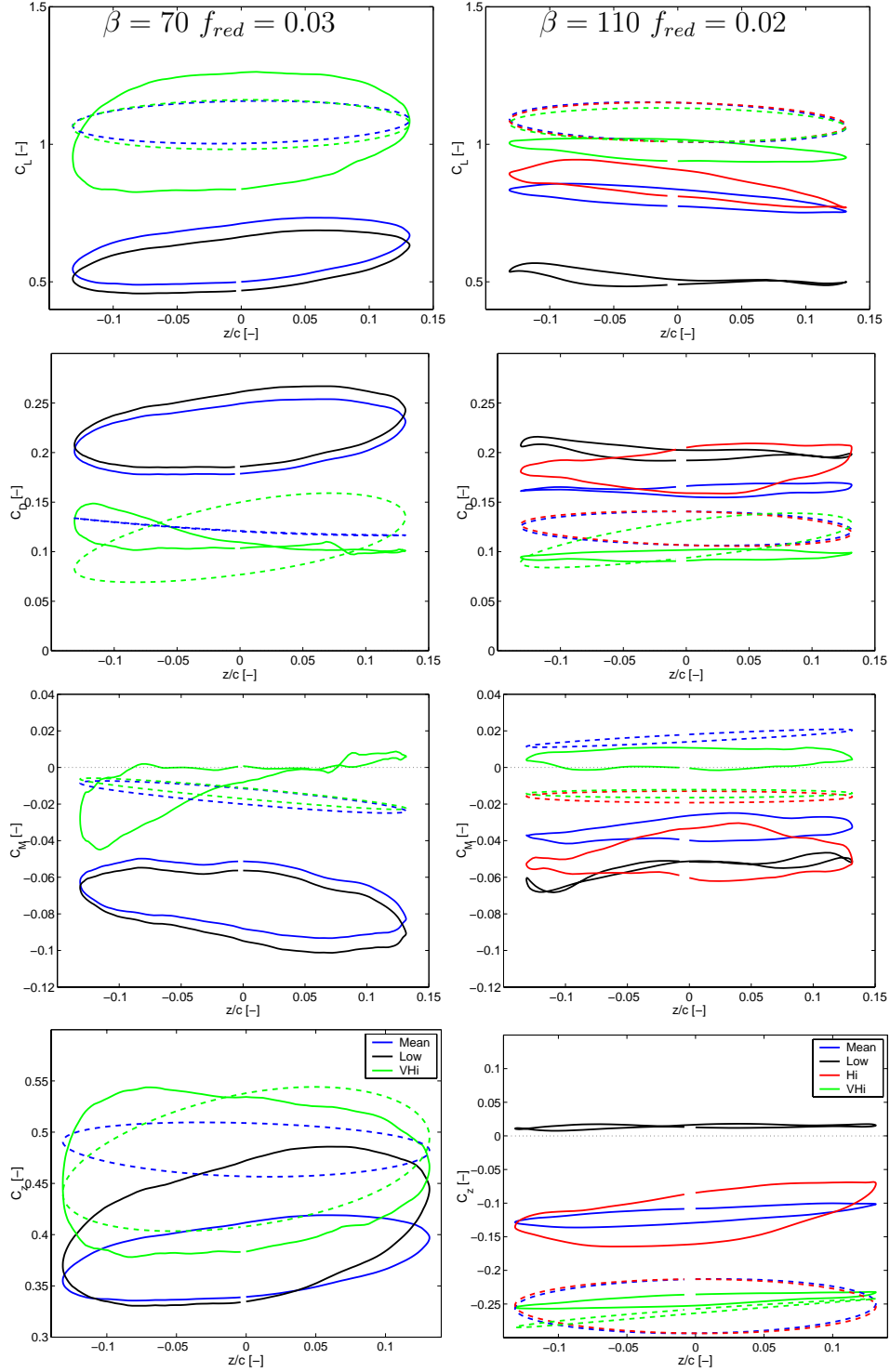


Figure 4.26: Comparison of experimental and new stall model force loops for experiments with multiple stall. The incidence is $\alpha = 15^\circ$ in both cases. Upper figures : C_L . Upper middle : C_D . Lower middle C_M . Lower : C_Z . The solid curves are experimental results, and the dashed curves are results from the new stall model. The mean loops are blue curves, whereas the black, red and green curves correspond to the low, high and very high stall modes, respectively. The figures to the left are for $\beta = 70^\circ$ and $f_{red} = 0.03$, whereas the figures shown to the right are for $\beta = 135^\circ$ and $f_{red} = 0.02$.

experiments consists of the high and very high stall modes. This causes the results to be very far apart in the two cases. Since the only stall mode in common in the results is the very high stall mode, only comparison of these results makes sense. The upper, upper middle and lower figures in figure 4.26 reveals that all mean levels of the very high stall mode force coefficients (green curves) are predicted in reasonable agreement with experimental results. It is noticeable that the mean level of the moment coefficient is predicted reasonably well, in spite of the crude assumptions under which the moment is calculated in the new model.

The dynamics of the predicted lift and drag loops does not agree well with the experimental results. These two wrongs more or less cancels each other out in the direction of movement, as seen in the loop of the force coefficient in the movement direction, C_Z , which agrees reasonable well with the experimental results. This should not be interpreted as an indication that the model works for this particular stall mode, but just as a lucky outcome to a somewhat random process. Effects like this may hide themselves in integral coefficients like aerodynamic mass and damping, which is why investigation of the finer levels of information is important.

The dynamic experimental results shown in the right figures has all three stall modes, whereas the steady counterpart has only two, namely the high and very high stall modes. As previously, this renders a comparison of the mean curves superfluous. Contrary to the previous results, the mean levels of the predicted and experimental results does not agree well in this case. The reason for this is not clear to the author. Common for all stalling cases is that the dynamics are not predicted well despite the specification of separate force coefficients and derivatives for each stall mode.

As a conclusion on the performance of the new dynamic stall model can be stated that it is not able to predict the magnitude or position of the minimum aerodynamic damping correctly, nor is it able to predict the effect of the reduced frequency for the stalling cases. This is attributed to the assumption of similarity between the dynamics in the attached and stalling cases, which clearly fail to describe the complex dynamics of stalling flows.

It was shown that the use of specific information about the force coefficients and derivatives thereof for the different stall modes improves the results of the model.

However, it was seen that the new model is a clear improvement over quasi-steady theory at the low angles of attack, where accurate prediction of the unsteady lift and drag loops are possible.

The general trend of the experimental moment curves were predicted correctly at low incidences, but very big differences between predicted and experimental results were observed in the lightly stalling and moderately stalling cases, $\alpha = 12^\circ$ and $\alpha = 15^\circ$. Comparison of the results at $\alpha = 20^\circ$, showed better agreement on the prediction of the moment coefficient.

4.4 Navier-Stokes Model

In this section, results from the Navier-Stokes computations are shown. The focus is on comparison with the steady and unsteady experimental data, but some results

shedding light on the details of the behavior of the Navier-Stokes computations are shown as well.

The computational grid employed for all Navier-Stokes computations in this work is an 17.5-chord radius o-grid, generated by means of the hyperbolic grid generator HypGrid2D [53]. The grid has 64 cells in the direction normal to the surface of the airfoil and 256 cells in the direction tangential to the airfoil surface. A grid sensitivity study leading to the choice of this grid can be found in appendix D.1, where also more details regarding the grid can be found. The computational grid is shown in figure 4.27.

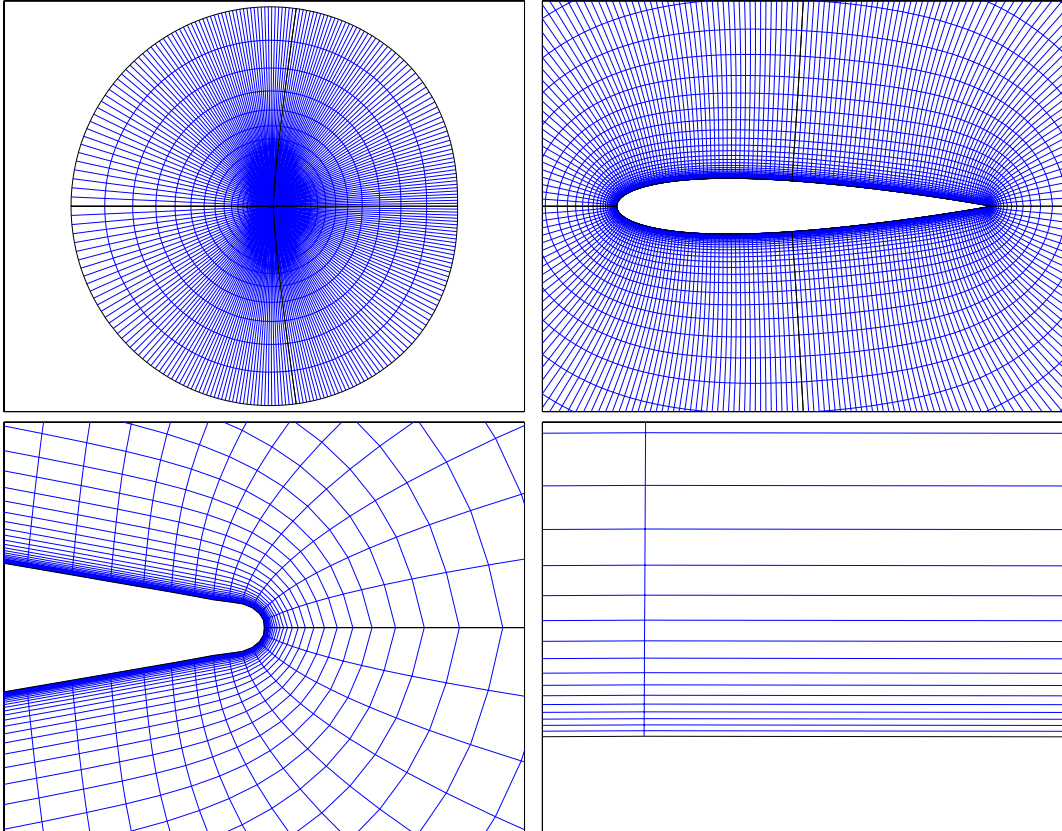


Figure 4.27: *Computational grid around NACA 0015 profile employed for the computations in the present work. The grid was generated by means of the hyperbolic grid-generator, HypGrid2D [53].*

The turbulence model used for all the computations was the $k - \omega$ SST model described in section 3.6.2. The non-dimensional time-step used in the computations were

$$\Delta\tilde{t} = \frac{\Delta t V}{c} = 2.0 \cdot 10^{-3}, \quad (4.41)$$

which ensured that the CFL⁶-number of the flow was below 1.3 in all computational cells for $Re = 555000$ at an angle of attack $\alpha = 5^\circ$. Except for two very small regions,

⁶Courant Friedrich Levy - number. The number of computational cells a fluid element passes during one time-step.

one at the suction peak and one at the trailing edge, the CFL-number was below 0.3 in the whole fluid domain, as shown in figure 4.28.



Figure 4.28: *CFL-number for the solution of the flow around the NACA 0015 airfoil at Reynolds number $Re = 555000$. The incidence is $\alpha = 5^\circ$.*

The presentation of the results obtained with the Navier-Stokes code is presented next. First the results describing the stationary NACA 0015 airfoil, followed by the results of the airfoil undergoing 1 DOF oscillatory translatory motion.

4.4.1 Stationary Airfoil

In order to determine the magnitude of the viscous forces, which are neglected in the experimental part of this work, an investigation were undertaken using the Navier-Stokes code.

Investigation of magnitude of viscous forces

Figure 4.29 show the lift and drag coefficient, and the isolated contributions from the viscosity alone. Note that the viscous drag gradually drops from $\alpha = 0^\circ$ to $\alpha = 20^\circ$ where it settles at an almost constant value. This is mainly due to the increase of the recirculating zone at the upper side of the airfoil. Furthermore, it is seen that the viscous forces contribute a very little part of the total forces apart from $\alpha = 0^\circ$. However, when projecting these forces onto the z -direction given by β , as defined in figure 4.30, we get

$$\text{Viscous Ratio} = \frac{F_V}{F_{\text{Tot}}} = \frac{C_{LV} \cos(\beta) + C_{DV} \sin(\beta)}{C_L \cos(\beta) + C_D \sin(\beta)} \quad (4.42)$$

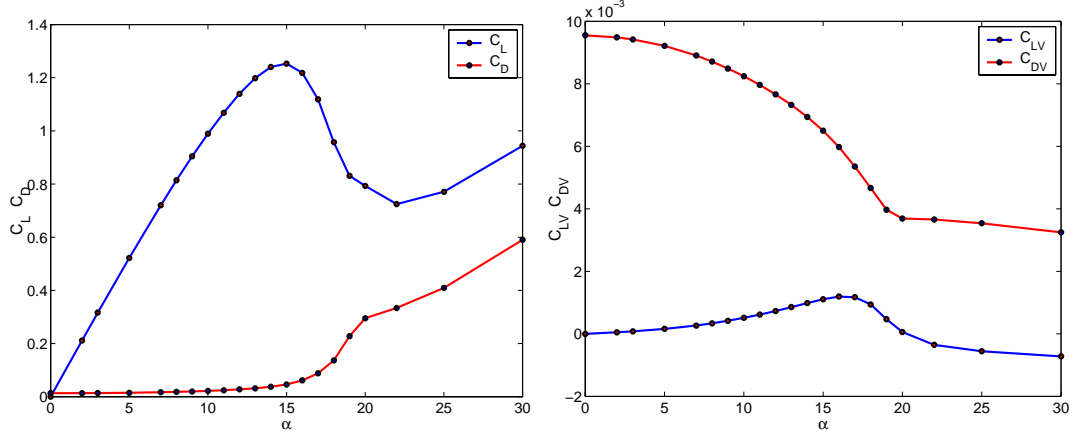


Figure 4.29: Total and viscous part of lift and drag coefficients. From RANS computations at Reynolds number $Re = 555000$.

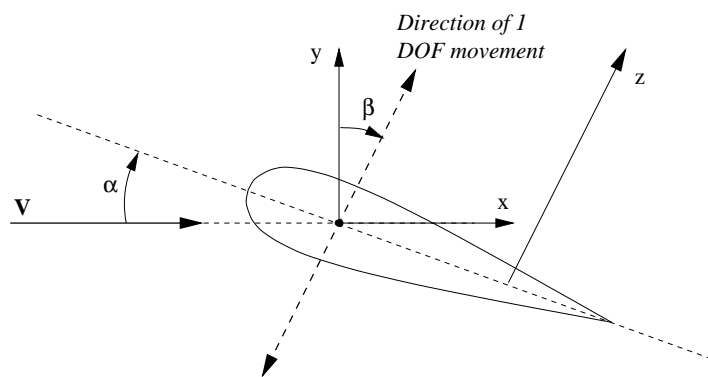


Figure 4.30: Definitions and positive directions of the angle of attack, α , the angle of movement, β , and the x and y axes. All quantities are defined with respect to the free stream velocity, V . The z -axis defines the positive direction for the motion of the profile.

It is seen that this expression goes to infinity for

$$\beta = \frac{\pi}{2} + \arctan \frac{C_D}{C_L} \quad (4.43)$$

if $C_L \neq 0$ and

$$\frac{C_D}{C_L} \neq \frac{C_{CV}}{C_{LV}}, \quad (4.44)$$

which practically always holds true. This is illustrated in figure 4.31, where the viscous force ratio is shown as a function of α and β . The points expressed by equation 4.43 corresponds to the direction normal to the force vector from the pressure. Note also in figure 4.31 that high ratios are found at $\alpha = 0^\circ$ due to the fact that the lift, which is practically exclusively pressure forces, in that case is zero. Apart from the areas close to $\alpha = 0^\circ$ and the curve given by equation 4.43, the viscous forces are negligible compared to the pressure forces.

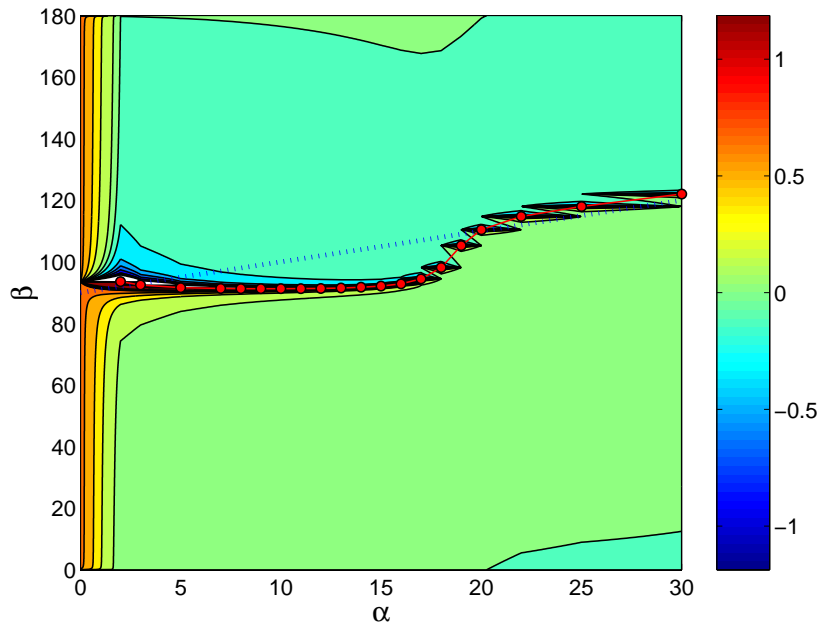


Figure 4.31: *Ratio of viscous to total forces. RANS data, $Re = 555000$. The dotted blue line outlines the chordwise direction, and the dotted red curve denote the direction where pressure forces vanish, given by equation 4.43.*

Even though it has been shown that the viscous forces dominate in certain directions in the stationary case, it should be of no practical influence in the unsteady experiments. This is so because the ratio of total to viscous force magnitudes is very big, as shown in figure 4.32, combined with the fact that the directions in which the forces act is varying due to the motion of the airfoil.

On the basis of these investigations, it is estimated that the error introduced by neglecting the viscous forces in the cases of 1 DOF translatory motion of the airfoil is of no consequence for the validity of the results from the unsteady experiments.

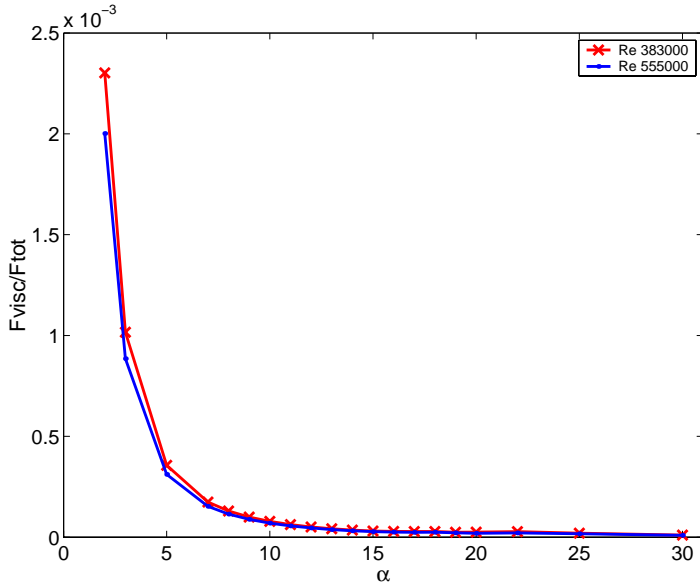


Figure 4.32: *Ratio of viscous to total force magnitudes versus angle of attack. Results from RANS computations.*

Comparison of Navier-Stokes computations with experimental data

A comparison of Navier-Stokes and experimental non-dimensional pressure coefficients are shown in figure 4.33 for the non-moving NACA 0015 airfoil. It is seen that the Navier-Stokes results are in fairly good agreement with the experimental results for incidences up to $\alpha = 8^\circ$. The effect of the trip tape is clearly seen on the suction side in the experimental results for angles of attack up to $\alpha = 12^\circ$. For incidences $\alpha = 10^\circ$ and $\alpha = 12^\circ$ the agreement is still generally fairly good, but a difference between the measured and predicted pressure coefficients is noted at the trailing edge, where the experimental values are slightly higher than the ones predicted by the RANS code. Big differences between the predicted and measured pressure coefficients are observed in the $\alpha = 15^\circ$ case. The multiple stall modes occurring in the experiments was not the case in the simulations. The specific C_P curves for the measured distinct stall modes are shown in the figures. It is seen, that the predicted pressure profile for the $\alpha = 15^\circ$ case looks most like the very high stall mode, but the levels predicted on both the pressure and suction side of the airfoil differs noticeably from the experimental values. In the $\alpha = 20^\circ$ and $\alpha = 25^\circ$ cases, the agreement between the curves are better, but still far from accurate. In the $\alpha = 20^\circ$ case, the Navier-Stokes predictions looks most like the low stall mode. The computations still show a minor suction peak for both $\alpha = 20^\circ$ and $\alpha = 25^\circ$ which is not seen in the experimental results. The results differ a little bit on the pressure side, where the experimental curves are slightly above the predicted ones. Disturbances appear on the pressures side of the experimental results due to the trip tape. Both the experimental and computed pressure coefficients has the features of deeply stalled airfoil flows.

It is the authors belief, that the explanation of the difference between the experimental and predicted values incidences $\alpha = 15^\circ$ and $\alpha = 20^\circ$ is caused by onset of stall at different incidences in the measured and computed results.

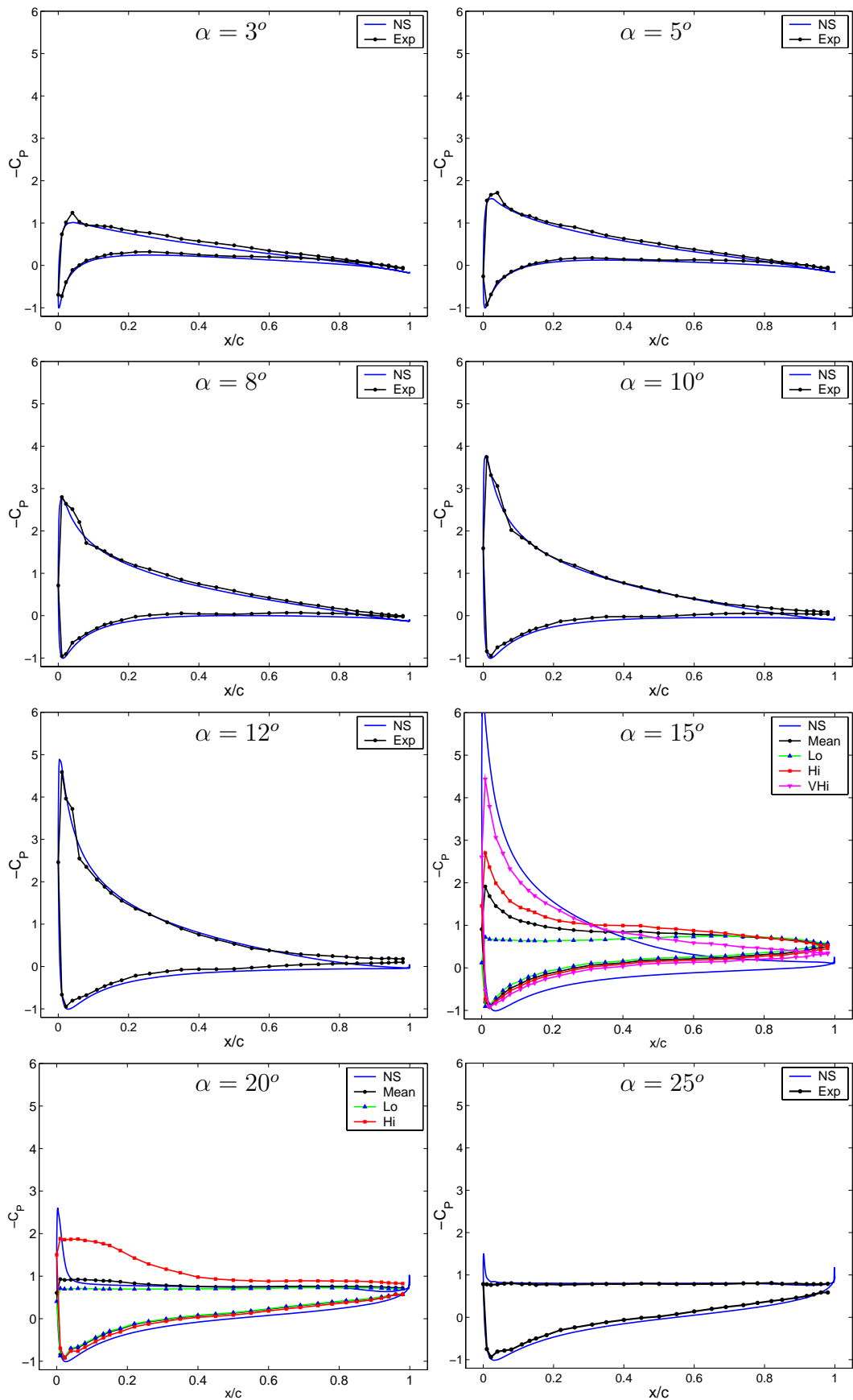


Figure 4.33: Comparison of the experimental non-dimensional pressure coefficients with RANS results for stationary airfoil. $Re = 555000$.

This is evident from figure 4.34 as well. This figure shows a comparison of the lift and

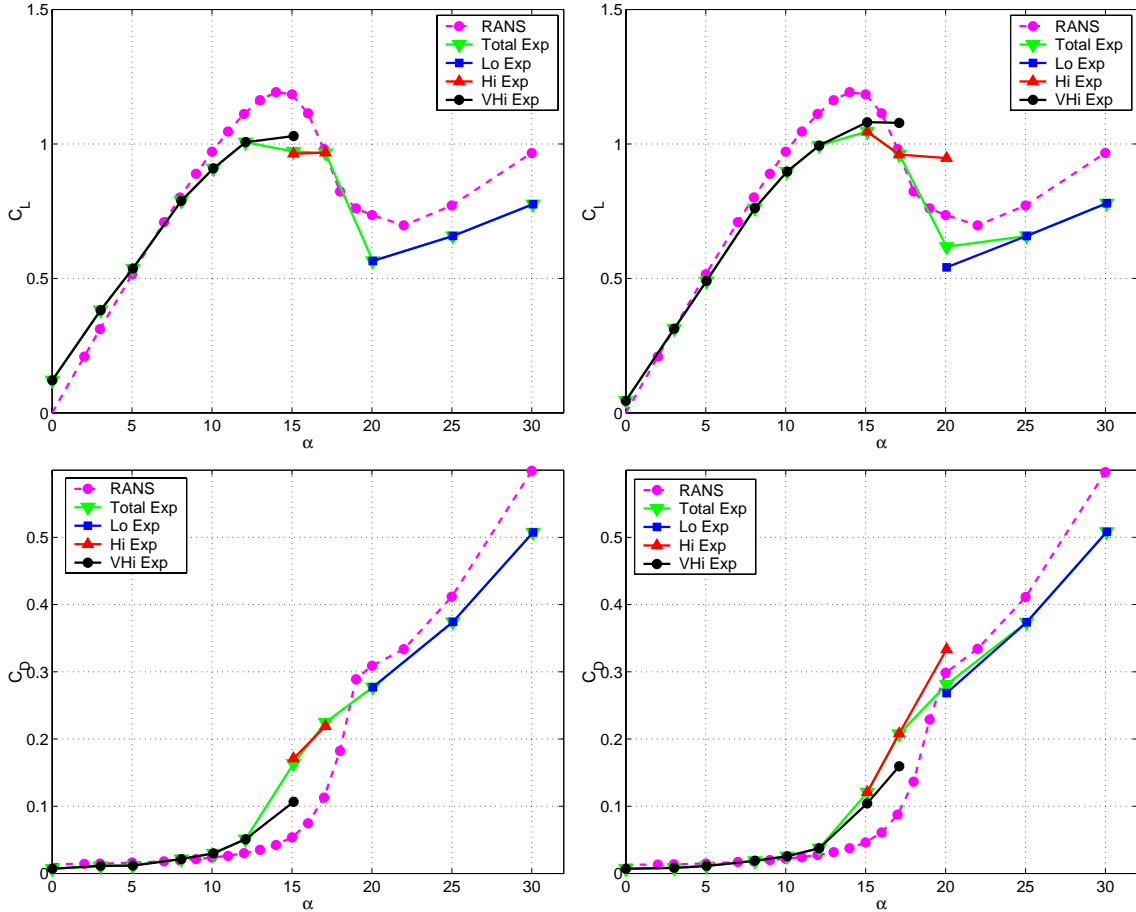


Figure 4.34: Steady C_L (upper) and C_D (lower) curves for $Re = 383000$ (left) and $Re = 555000$ (right). The green curves corresponds to the mean measured level, whereas the black, red and blue level corresponds to the Very High, High and Low levels, respectively.

drag coefficients for $Re = 383000$ and $Re = 555000$. From this figure it is seen that the maximum level of the predicted lift is somewhat higher than that of the experimental results.

It is known from previous studies that RANS solutions give higher values for the lift in the regions near maximum lift and in the deep stall cases than the more physically correct three dimensional DES computations. However, this alone may not explain all differences shown in the figures.

It is clear that very complex flow situations, such as multiple stall modes, are not predictable by standard 2D RANS computations. This alone complicates a comparison substantially in the regions where multiple stall modes occur. A determination of the location of the maximum lift in the experimental case is hard to do in these cases as well.

Another thing that strike the eye in the comparison of the lift is the apparent difference in the slope of the curves in the attached region. The slope of the lift curves in the RANS computations is higher than that of the experimental results. It is known

from for instance Selig et al. [46], that the slope of the C_L curves decrease when the Reynolds number is decreased. It is not known to the author how well this is reproducible with a 2D RANS code. The change in the slope between the $Re = 383000$ and $Re = 555000$ curves in the experimental results is not reflected in the RANS computations, but as explained in chapter 2, the uncertainty on the $Re = 383000$ data is lower than the uncertainty on the $Re = 555000$ data, making a conclusion harder to make on the basis of these results.

The turbulence model is another aspect that require special attention in this case. Usually the $k - \omega$ SST turbulence model is used at higher Reynolds numbers above, so the behavior of this specific model in this range of Reynolds numbers is not known to the author.

As mentioned in chapter 2, the tolerance on the shape of the airfoil has not been investigated, which leaves another unknown into this comparison, as does the effect of having all pressure holes in one span-wise coordinate. The flow is disturbed by the pressure taps, which means that the effect of having many pressure taps in one span-wise coordinate may have an effect on the measured pressure distribution.

One explanation to the high lift levels in the RANS computations could be that the relatively low turbulence kinetic energy level at the inlet of the domain decays before it has reached the airfoil, such that the airfoil effectively meets a laminar flow. This means that the flow within a distance from the stagnation point is effectively laminar, until the kinetic energy, and thereby the turbulent viscosity, has reached a level corresponding to the onset of turbulent flow.

Since a laminar suction peak is higher than a turbulent suction peak, this could cause the difference between the numerical and experimental lift curves.

To further investigate this, the friction coefficient $C_f = \mu/(\rho V \Delta y)$, is shown for $\alpha = 5^\circ$ in figure 4.35. The figure shows that a dip in the friction force occurs on both the

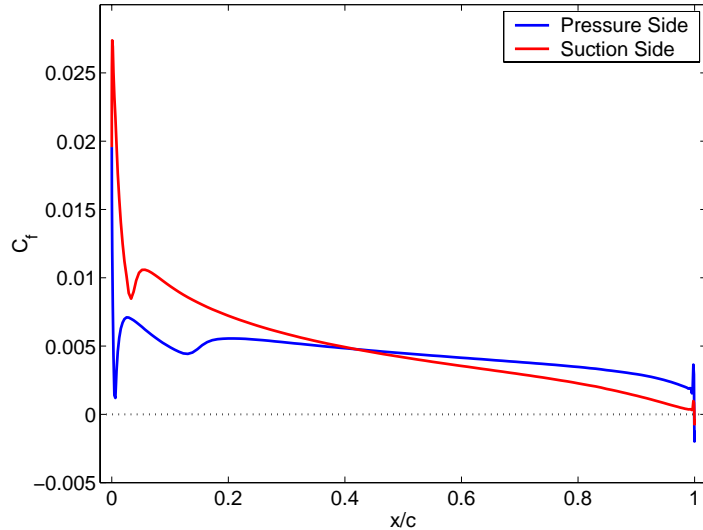


Figure 4.35: Friction coefficient, C_f , for the flow at an angle of attack, $\alpha = 5^\circ$, at Reynolds number $Re = 555000$.

pressure and suction sides of the airfoil, which corresponds to the friction coefficients

in transitional flows, as for example shown in [23]. This supports the explanation of the substantially higher lift curves due to practically laminar flow on the first part of the airfoil.

Comparison of the drag curves reveal that the predicted drag corresponds reasonably well with the experimentally obtained values for incidences up to $\alpha = 10^\circ$ despite the very coarse discretization of the pressure taps contributing to the force in the chordwise direction. For the low incidences the measured drag is lower than the RANS drag. However, the viscous drag should be added to the experimentally obtained values in order to get the true drag, which should be kept in mind when comparing the results.

The causes of the differences in the drag levels for incidences above $\alpha = 10^\circ$ are presumably the same as mentioned under the discussion of the lift above. The increase in the drag level from incidences $\alpha = 12^\circ$ in the experimental results corresponds to the behavior of the RANS results at incidences $\alpha = 15^\circ$. Again, this signifies that the onset of stall is not predicted correctly.

In order to evaluate the dynamics of the flow predicted with the RANS code, RMS⁷ values of the experimentally obtained lift and drag coefficients were compared with the corresponding values for the RANS simulations. The result is shown in figure 4.36, where it is noted that the dynamics of the RANS computations differs substantially from the experimental results. It should be noted, that the high RMS levels of the total (mean) experimental curve in the $Re = 555000$ case occurs due to the shift in the mean levels due to the multiple stall modes, and does not represent a physical rms value representing the oscillations in the values around one mean value.

From the figure it is seen that the RANS rms levels are zero up to $\alpha = 15^\circ$. This corresponds to fully stationary solutions to the flow. After this point the lift and drag levels oscillate harmonically with one clearly defined frequency. The experimental values display frequency content of a much wider spectrum, which could probably be predicted better using DES simulation [48].

The cause of the harmonic force output from the RANS code is caused by vortex shedding, as shown in figure 4.37.

4.4.2 Airfoil undergoing one DOF oscillatory translatory motion

In this section, a comparison of the results obtained with the Navier-Stokes code is compared with the corresponding experimentally obtained values. It is the aim to show both the cases where the results compare favorably and the cases where the results compare less favorably, to show the strengths and weaknesses of the 2D RANS code in the prediction of the aeroelastic response of an airfoil undergoing 1-DOF oscillatory translatory motion.

Prior to the comparison with experimental results, the behavior of the Navier-Stokes solutions at high angles of attack will be investigated.

⁷Root Mean Square: $\sqrt{\langle \cdot \rangle^2}$.

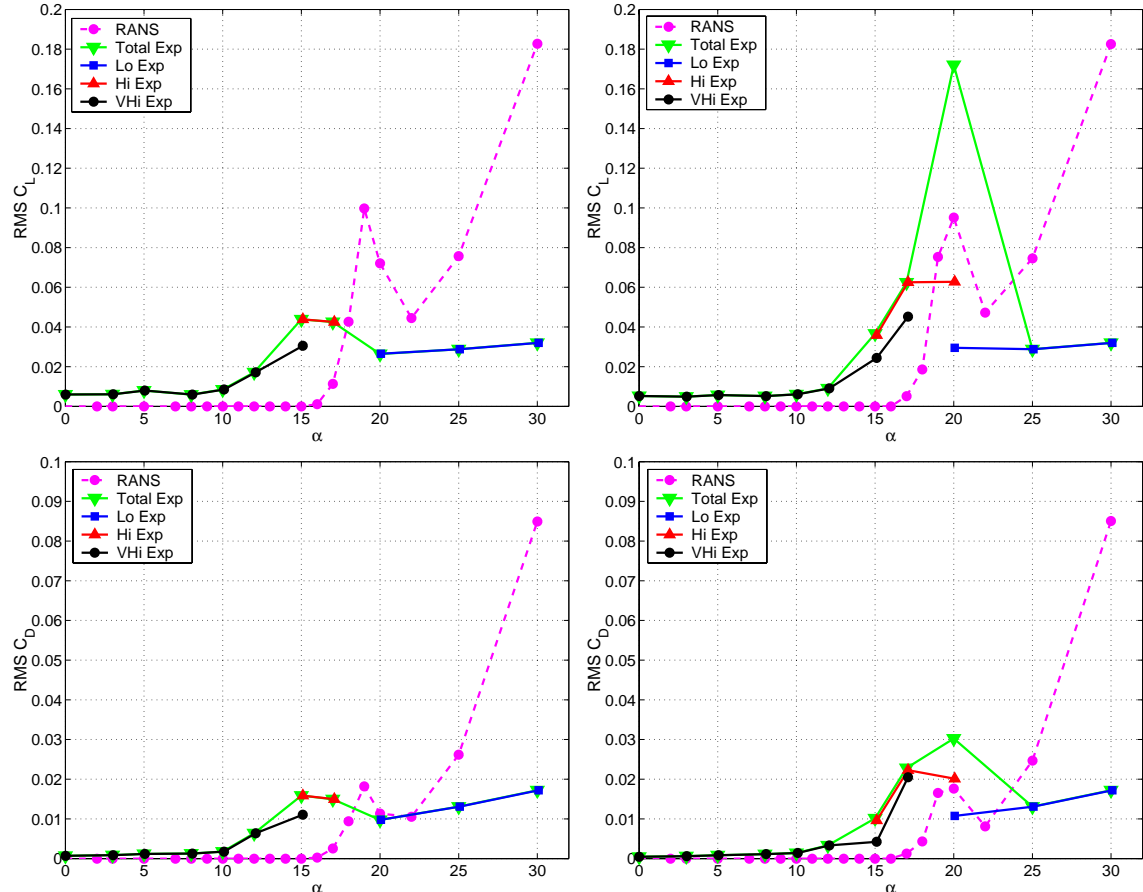


Figure 4.36: Root mean square values for non-moving airfoil. $Rms\ C_L$ (upper) and $rms\ C_D$ (lower) for $Re = 383000$ (left) and $Re = 555000$ (right). The green curves corresponds to the mean measured level, whereas the black, red and blue level corresponds to the Very High, High and Low levels, respectively.

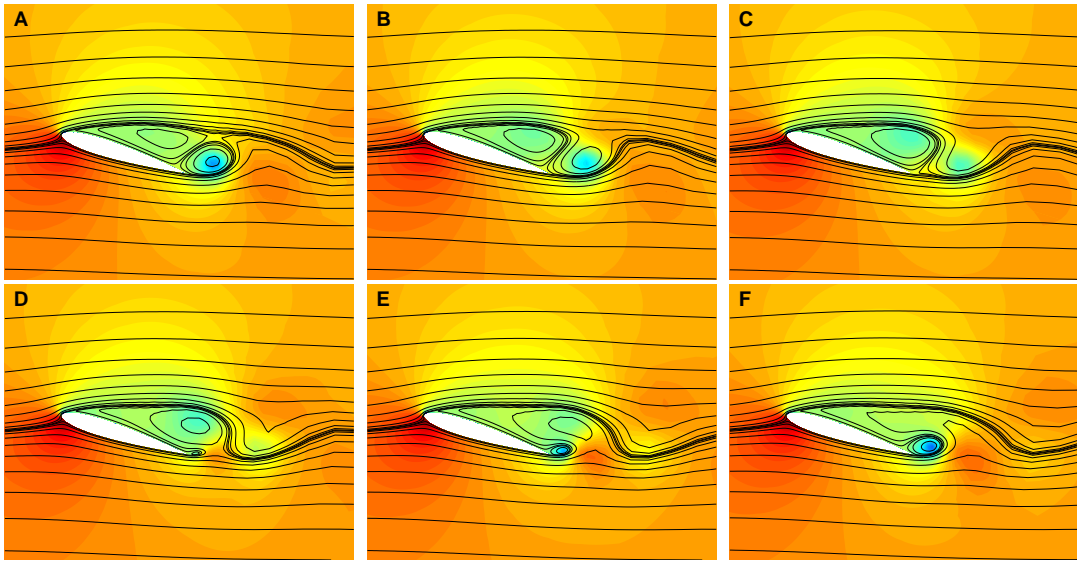


Figure 4.37: *Snapshots of stream lines and pressure from RANS computations are shown for a stationary NACA 0015 airfoil in stall. The snapshots are taken at equidistant times in the shedding cycle. The angle of attack is $\alpha = 20^\circ$, and the Reynolds number is $Re = 555000$. The red color corresponds to high pressure, whereas the blue color corresponds to low pressure.*

General behavior of the Navier-Stokes solutions

In order to explain some of the phenomena occurring in the Navier-Stokes solutions of oscillatory 1DOF translatory motion at high angles of attack, a selection of force loops at high incidences will be shown in detail to uncover the dynamics in the flows predicted by the Navier-Stokes code.

Figure 4.38 shows an example of the responses of three different configurations of incidences and direction of movement at the reduced frequency $f_{red} = 0.03$. The force coefficients are shown as functions of non-dimensional time, tV/c , and as functions of non-dimensional displacement position, z/c .

In the upper figure, where $\alpha = 15^\circ$ and $\beta = 0^\circ$, it is seen that the response is periodic. Another case of periodic response is seen in the middle figure, where $\alpha = 20^\circ$ and $\beta = 0^\circ$. In this case the periodic behavior is somewhat more complex. The reason for this will be investigated shortly. The last figure shown exhibits non-periodic behavior.

The behavior of the upper figures of 4.38, where $\alpha = 15^\circ$, $\beta = 0^\circ$ and $f_{red} = 0.03$, is examined in detail in figures 4.39-4.41. Figure 4.39 show the lift, drag and moment coefficients versus non-dimensional displacement, z/c , whereas figure 4.40 show the same quantities versus the relative angle of attack. This is done to relate the force loops to a familiar quantity. It should be noted that the obtained loops are not corresponding to the loops that would occur by a pitching oscillation, as described in section 4.2. The letters in figures 4.39-4.40 refer to the time-instances depicted in figure 4.41, which shows the snapshots of stream lines and pressure from the RANS computations.

The bump on the curves seen in figure 4.39 to the left of point A occurs because the

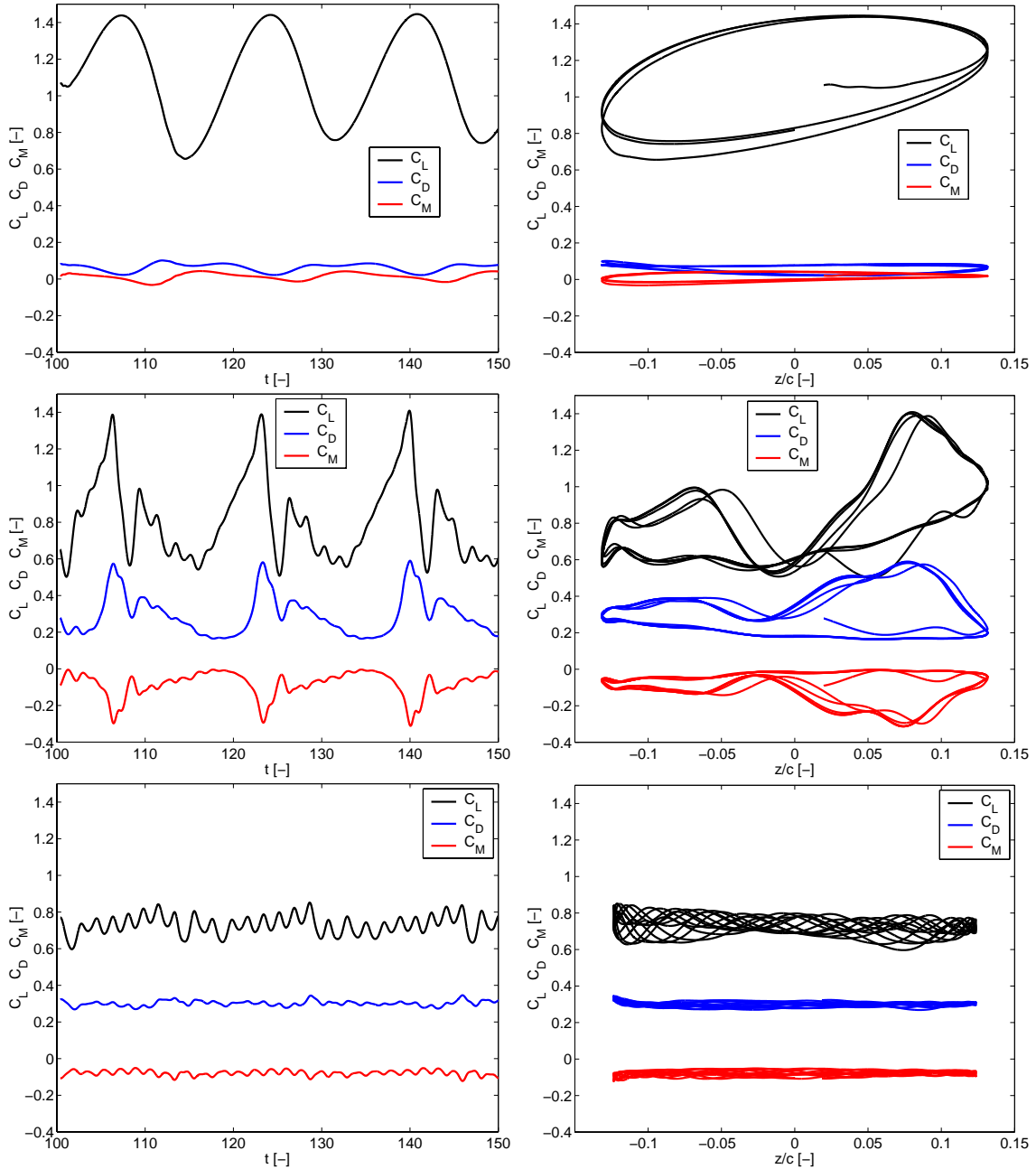


Figure 4.38: Periodic and non-periodic behavior. C_L , C_D and C_M versus time (left) and position z/c (right). Upper: $\alpha = 15^\circ$ $\beta = 0^\circ$. Middle: $\alpha = 20^\circ$ $\beta = 0^\circ$. Lower: $\alpha = 20^\circ$ $\beta = 90^\circ$. $f_{red} = 0.03$ in all shown figures.

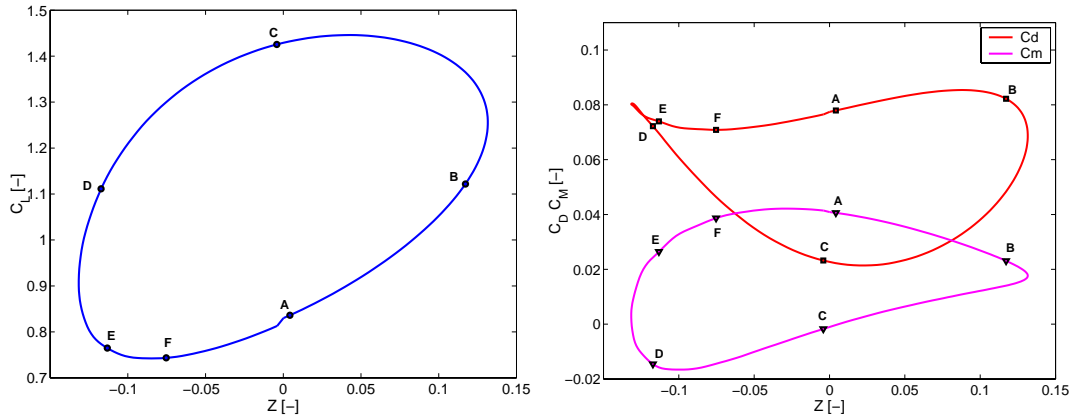


Figure 4.39: *Lift, drag and moment coefficients versus non-dimensional position parameter, z/c , obtained by RANS computations. The angle of attack is $\alpha = 15^\circ$, and the direction of the motion is perpendicular to the free stream direction, $\beta = 0^\circ$. The Reynolds number and reduced frequency is $Re = 383000$ and $f_{red} = 0.03$, respectively. The letters on the curves refer to the snapshots in figure 4.41*

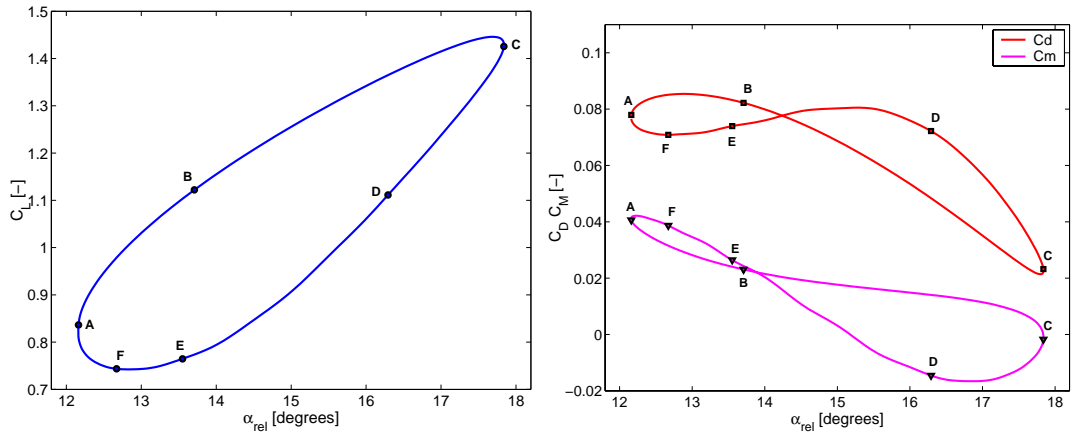


Figure 4.40: *Lift, drag and moment coefficients from figure 4.39 plotted against relative angle of attack. See figure 4.39 for details.*

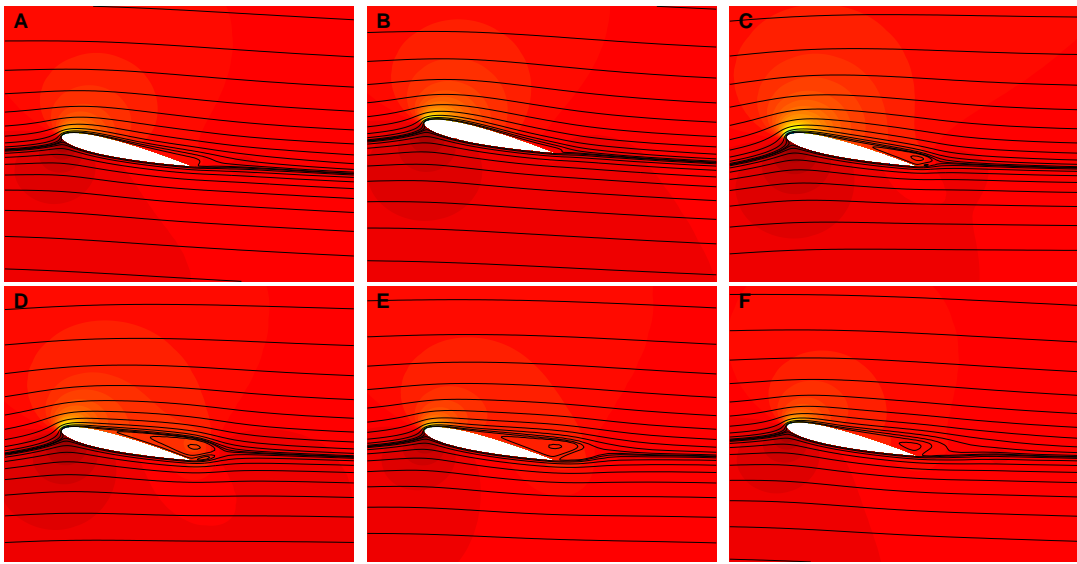


Figure 4.41: *Snapshots of stream lines and pressure from RANS computations are shown for NACA 0015 airfoil in light stall. The snapshots are taken at selected incidences with letters referring to figures 4.39-4.40. The angle of attack is $\alpha = 15^\circ$, and the direction of the motion is perpendicular to the free stream direction, $\beta = 0^\circ$. The Reynolds number and reduced frequency is $Re = 383000$ and $f_{red} = 0.03$, respectively. The dark red color corresponds to a high pressure, whereas the yellow color corresponds to low pressure.*

Navier-Stokes computations were not yet fully periodic for the loop shown in the figures.

It is seen in figure 4.41, that the size of the separated area increases on the downstroke of the airfoil, corresponding to snapshots B, C and D. No big difference in the size of the recirculating zone is seen from D to E despite the reduction in relative angle of attack. From E to B, the size of the recirculating zone is reduced again. It can be seen that there is a phase lag in the size of the recirculating zone with respect to the relative angle of attack.

Figures 4.39 and 4.40 show that the drag coefficient has a fairly constant value from snapshot D to B, whereas the drag coefficient is much lower at point C. The behavior of the drag coefficient loop can be explained by noting in the steady results obtained with the Navier-Stokes code, that the major part of the forces are in the lift direction in the region of incidences close to $\alpha = 15^\circ$. From standard potential theory we know that as a first approximation, the forces on a moving airfoil is perpendicular to the relative velocity seen by the airfoil. When this is adopted to the current case, it is seen that the total forces are shifted approximately 2.8° toward the incoming velocity at point C. This means that the force in the direction of the free stream flow is reduced. From point C to D this angle is reduced somewhat while the area of the recirculating zone is increased, leading to an increase in the drag force. This balance between the direction (and size) of the main forces and the drag forces from the stalling zone explains the shape of the drag loops.

According to the investigations of the dynamics of the flow for a steady airfoil, vortex shedding occurs for flows at angles of attack larger than or equal to $\alpha = 17^\circ$. The present results show that no vortex shedding occur even though the relative angle of attack exceeds this limit.

A combination of two effects may cause this. The first of these is the time-lag effect connected to the build-up of the boundary layer. If the angle of attack for an airfoil is suddenly changed from one value to another, the boundary layer has to adjust to the new angle of attack. This takes some time, hence the time-lag. If the time the airfoil is above the critical relative angle of attack is short enough, then the boundary layer will not have the time to adjust to the new conditions, and no vortex shedding will occur.

The second effect explaining why no vortex shedding occur at the investigated incidence is an analogy to pitching flows. According to Sørensen and Nygreen [50], an upstroke pitching-wise has a stabilizing effect on the growth of the separation bubble. If this can be transferred to the translating case in terms of the relative angle of attack, then this should limit the growth of the separation bubble up to point C.

Since the direction of the lift loop in figure 4.39 is counter-clockwise and the direction of the motion of the profile is in the lift direction, it is seen that the aerodynamic damping is negative. The slope of the steady C_L curve is negative for this incidence, which would lead to negative aerodynamic damping for this direction of the motion when analyzed by quasi-steady theory or the new dynamic stall model. From figure 4.40 it is seen that the maximum and minimum lift predicted by the Navier-Stokes computations lie close to the maximum and minimum of the relative incidence. The minimum force in the lift direction is found close to point F, which is before the minimum relative angle of attack is reached. The reason for this is the recirculating zone, which is almost gone in point C, thereby raising the lift.

As a side note it can be mentioned that the phase-lag of the size of the recirculating zone with respect to the relative angle of attack can be explained by the time-lag effect connected to the boundary layer.

A similar investigation of the force loops predicted in the case of $\alpha = 20^\circ$, $\beta = 0^\circ$ and $f_{red} = 0.03$, shown in the middle figures of figure 4.38, is given below.

Analogous to the figures in the previous investigation, figure 4.42 and 4.43 shows the force loops and snapshots corresponding to selected incidences in the oscillation cycle. Compared to the previous figures, the force loops in figure 4.42 are more complex. This, as we shall see, is connected to shedding of vortices from the leading and trailing edge of the airfoil. First the shape of the lift force loop will be connected to the dynamics of the vortex shedding.

It is seen from snapshots A,B and C, that there is vortex shedding at the trailing edge in this part of the oscillation cycle. Counter-clockwise vortices are shed from the trailing edge whereas clockwise vortices are shed from the separation bubble extending from the leading edge. The relative angle of attach has its minimum at point A. From point C to F, there is a build-up of a elongated separation bubble/vortex, which causes an increase in the lift because it represents an effective thickening of the airfoil. In point E, a small counter-clockwise vortex is formed at the trailing edge, which prevents the big clockwise vortex from being shed. This little vortex is then shed from

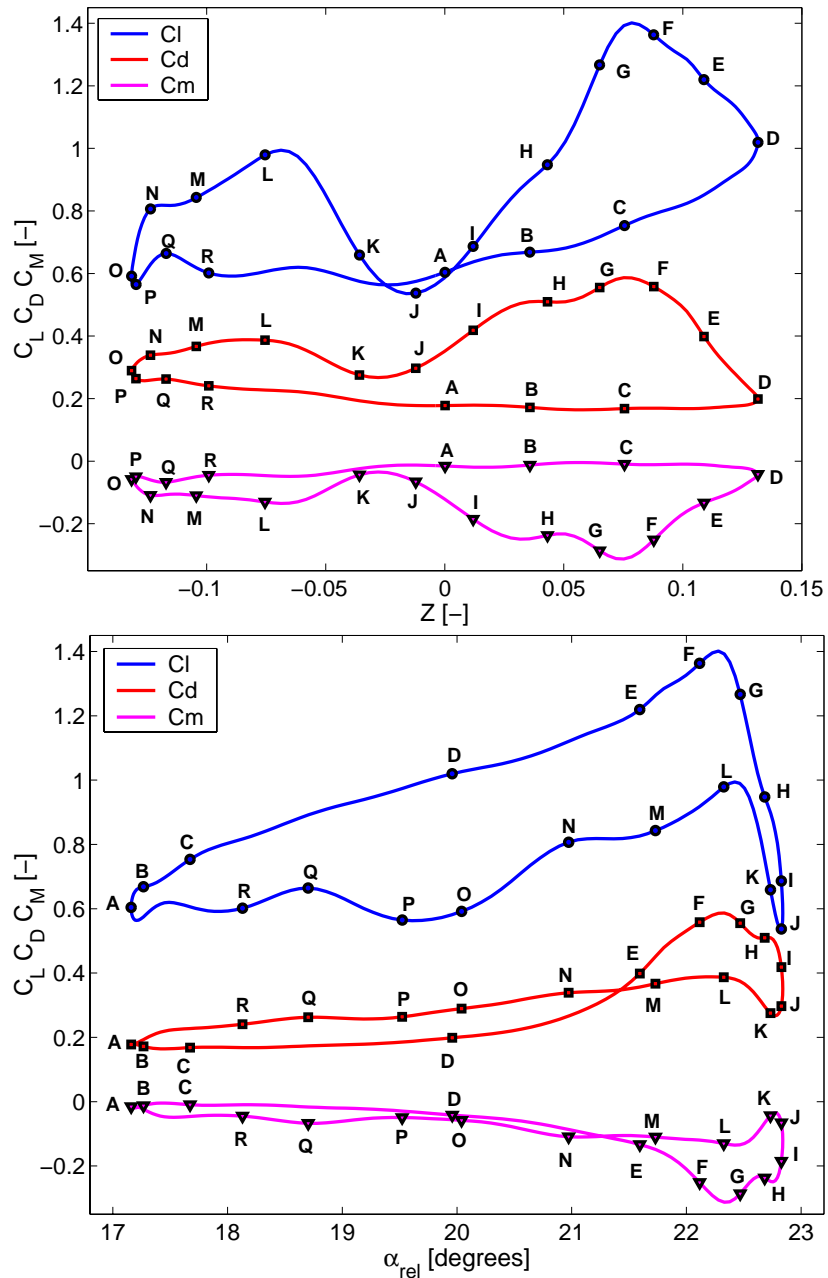


Figure 4.42: Lift, drag and moment coefficients versus non-dimensional position parameter, z/c and relative angle of attack. The results are obtained by RANS computations. The angle of attack is $\alpha = 20^\circ$, and the direction of the motion is perpendicular to the free stream direction, $\beta = 0^\circ$. The Reynolds number and reduced frequency is $Re = 383000$ and $f_{red} = 0.03$, respectively. The letters on the curves refer to the snapshots in figure 4.43

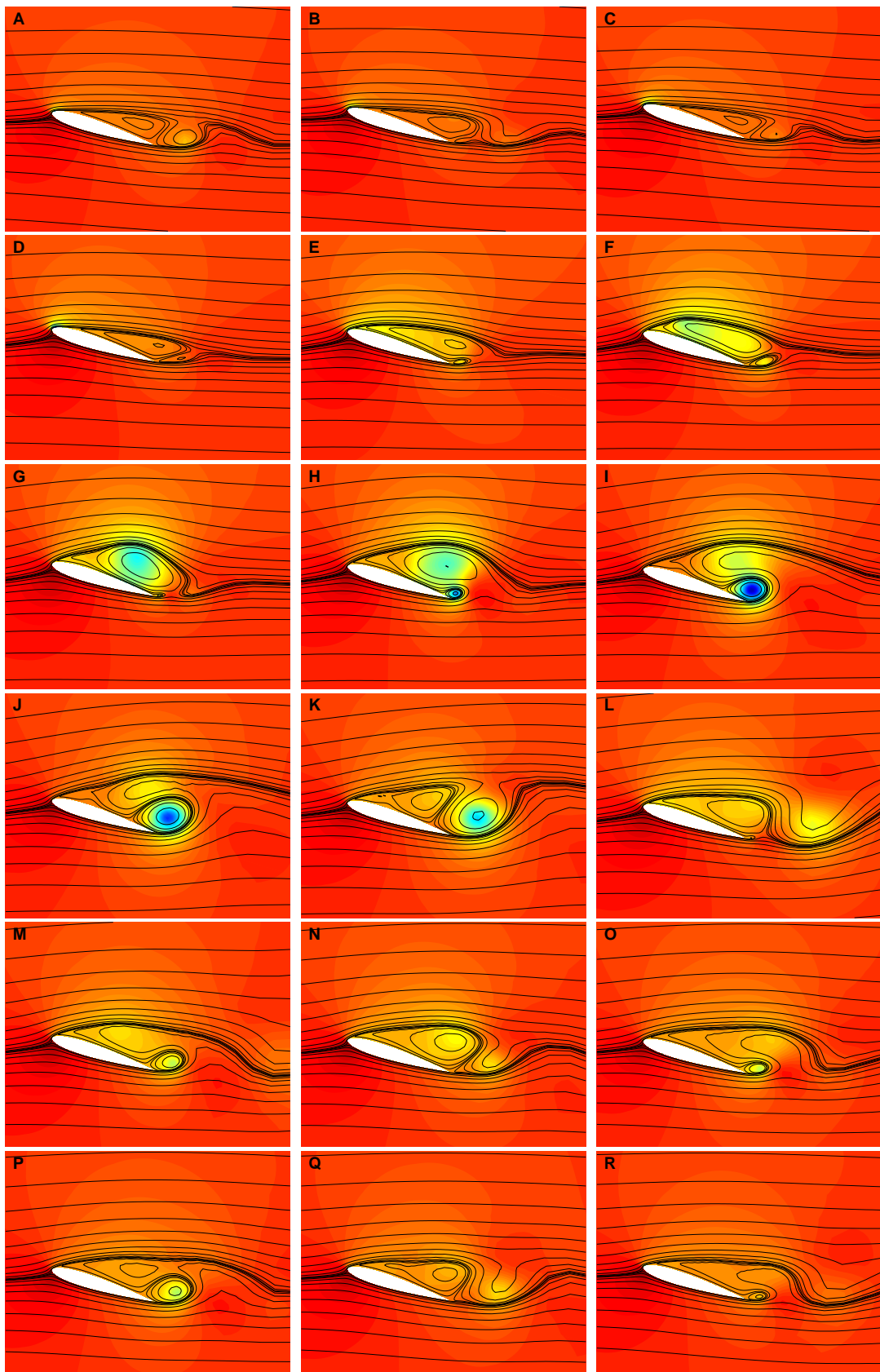


Figure 4.43: Snapshots of stream lines and pressure from RANS computations are shown for a moving NACA 0015 airfoil in stall. The letters are referring to figure 4.42. The angle of attack is $\alpha = 20^\circ$, and the direction of the motion is perpendicular to the free stream direction, $\beta = 0^\circ$. The Reynolds number and reduced frequency is $Re = 383000$ and $f_{red} = 0.03$, respectively. The red and blue color corresponds to high and low pressure, respectively.

the trailing edge in point F, causing the big vortex to be shed from G to J. When the big vortex is shed, the lift connected to the effective thickening of the airfoil disappear as well, causing the drop in the lift. As the big vortex is shed (G-J), the jump in velocity at the trailing edge is very big. This feeds a concentrated vortex at the trailing edge, which builds up from H to I, after which it is shed and convected from J to L. Analogous to the feeding of the counter-clockwise vortices by the clockwise vortices, the opposite is the case as well. The concentrated trailing edge vortex at snapshots H-J causes the build-up of a clockwise vortex which causes the local top in the lift in point L. From point L to point A only smaller bumps on the lift curve is seen. These bumps correspond to trailing edge vortex shedding similar to the one seen from point A to C. One period of the trailing edge vortex shedding occurs from point L to point N, one period from point N to point Q, and two periods from point Q to point A.

Shifting the focus to the behavior of the drag, it is seen that the value is fairly constant all the way from point O to point D. The explanation to this is identical to the one given in the $\alpha = 15^\circ$ case. The effects of stall and the effect from the change in the forces from the flow due to the change in the relative angle of the flow cancel out each other.

The maximum drag occurs the same time in the oscillation cycle as the maximum lift. Both maxima are caused by the big separation bubble/vortex.

Similar to the lift and drag force cases, the noticeably peaks in the quarter chord moment curve occur between point E and point M, where the relative angle of attack has its maximum. Analogous to the other forces, the dynamics in the vortex shedding causes the peaks and valleys. The minimum quarter chord moment occurs in the same time in the oscillation cycle as the maxima in the lift and drag forces. The reason for all these phenomena are the same. The big suction forces on the whole upper side of the airfoil causes the negative peak in the quarter chord moment.

After this investigation, it is now clear that the reason for the force response with higher frequency content than the motion of the airfoil, such as shown in the lower four graphs of figure 4.38, is vortex shedding during the oscillation cycle. The periodic response is a coupling of the vortex shedding on the motion of the airfoil during the oscillation cycle, whereas the vortex shedding for the non-periodic force loops is independent of the motion of the airfoil.

All peaks and dips in the force curves are seen to be governed by a complicated dynamic process, involving both clockwise and counterclockwise vortices, shed from the leading and trailing edge, respectively. If the motion of the airfoil is fast enough and the amplitude is big enough, then the vortex shedding will be locked into a periodic behavior. As shown in figure 4.38, the direction of the motion is a key element in locking the vortex shedding period onto the motion of the airfoil. This is probably due to the influence of the direction of motion on the relative angle of attack.

Comparison of Navier-Stokes computations with experimental data

In order to evaluate the overall behavior of the Navier-Stokes computations, figure 4.44 shows the non-dimensional aerodynamic damping (left) and non dimensional added

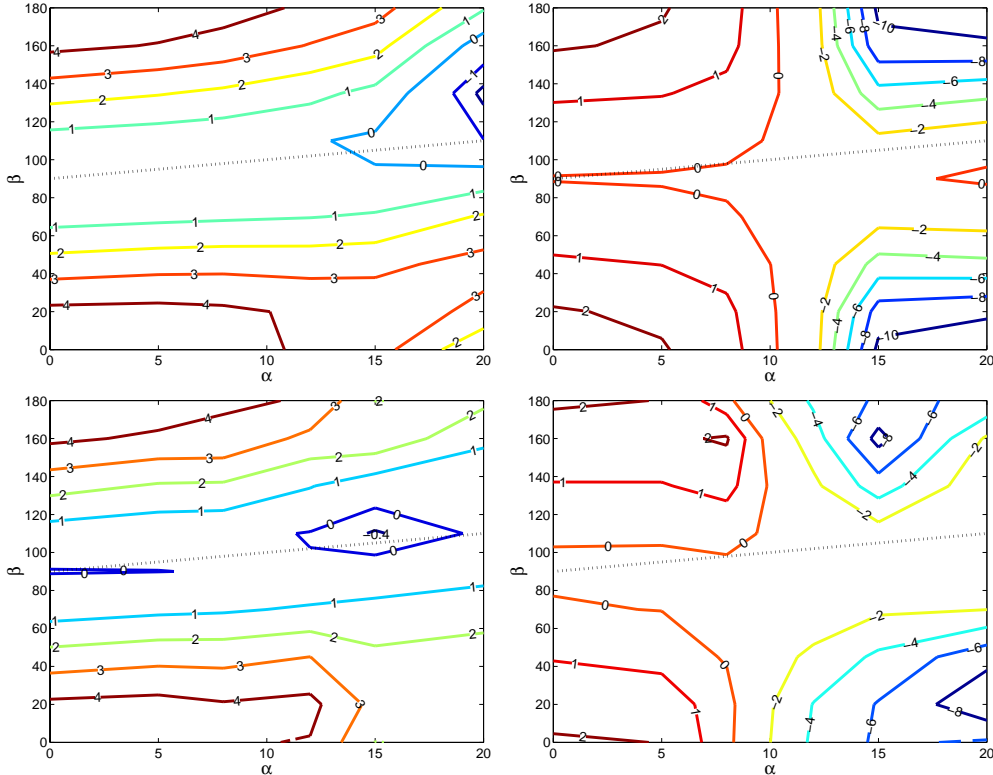


Figure 4.44: Non-dimensional aerodynamic damping (left) and non dimensional added mass (right) versus β and α for $f_{red} = 0.02$. Upper: RANS results. Lower: Experimental results.

mass (right) for the Navier-Stokes predictions (upper) and the experiments (lower). The reduced frequency is $f_{red} = 0.02$ and the Reynolds number is $Re = 555000$. The selection of incidences and directions of motion on which the contour plot is made is identical to the experimental test-matrix, namely $\alpha = 0^\circ, 5^\circ, 8^\circ, 12^\circ, 15^\circ, 20^\circ$ and $\beta = 0^\circ, 20^\circ, 45^\circ, 70^\circ, 90^\circ, 110^\circ, 135^\circ, 160^\circ$.

Comparison of the aerodynamic damping computed using the pressure forces only instead of the total forces showed that the effect of the viscous forces were indeed negligible, as indicated by the investigation of the magnitude and direction of the viscous forces from the non-moving airfoil.

Comparison of the aerodynamic damping from the Navier-Stokes computations and the experimentally obtained values show that the agreement is good for angles of attack up to $\alpha = 15^\circ$. The big difference shows at $\alpha = 20^\circ$, where the predicted damping is much more negative than the measured ones.

The non-dimensional aerodynamic added mass is shown in the right figures. Here it is seen that the predicted values are generally slightly further from the experimental values than in the case of the damping. The general shape of the predicted contour, however, corresponds well with the contour of the experimentally added mass up to

angles of attack $\alpha = 12^\circ$.

In order to investigate how the dynamics of the results from the Navier-Stokes code compares with the dynamics of the specific multiple stall modes, the aerodynamic damping and the aerodynamic mass obtained from the Navier-Stokes computations were compared to the experimental results in figure 4.45 for $\alpha = 15^\circ$ and $\alpha = 20^\circ$. It is seen

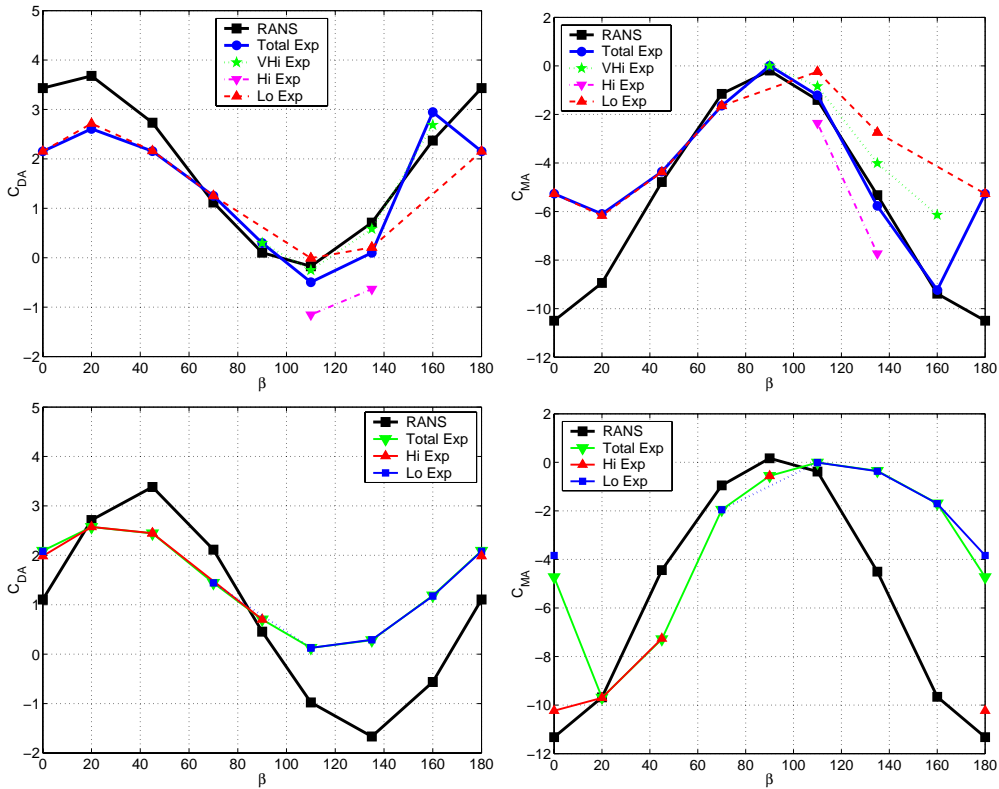


Figure 4.45: Comparison of Navier-Stokes and experimental results at incidences where multiple stall occurs. Non-dimensional aerodynamic damping (Left) and non-dimensional added mass (Right) versus movement direction, β . The reduced frequency is $f_{red} = 0.02$. Upper: $\alpha = 15^\circ$. Lower: $\alpha = 20^\circ$.

that the general shape of the aerodynamic damping computed with the Navier-Stokes code compares best with the very high stall mode. However, since this stall mode appears only in four points, it is hard to say whether this is a general feature or not. The aerodynamic damping is predicted much worse in the case of $\alpha = 20^\circ$ than it is for $\alpha = 15^\circ$.

In the case of the added mass, it is seen that this quantity is predicted quite poorly at $\alpha = 20^\circ$, and only slightly better at $\alpha = 15^\circ$. In this case the Navier-Stokes results does not match the added mass for any of the multiple stall modes.

The reason for the relatively bad predictions at $\alpha = 20^\circ$ may be linked to the occurrence of the complex vortex interaction described previously. If the complex vortex interaction is predicted wrong, then the whole force response is computed wrong as well. This issue will be addressed later.

In order to evaluate the performance of the Navier-Stokes code on a range of reduced frequencies, computations were carried out at reduced frequencies $f_{red} = 0.01$,

$f_{red} = 0.02$, $f_{red} = 0.03$ and $f_{red} = 0.04$ for four different combinations of angles of attack and directions of the movement. The results are shown in figure 4.46, where non-dimensional aerodynamic damping (left) and non-dimensional aerodynamic added mass (right) is shown as functions of the reduced frequency.

The upper figures show the integral dynamic quantities for $\alpha = 5^\circ$ and $\beta = 0^\circ$, whereas the upper middle figures show the results for $\alpha = 8^\circ$ and $\beta = 160^\circ$. Generally the aerodynamic damping for these low incidences are predicted well. In the $\alpha = 5^\circ$ case there is some deviation from the experimental results, but this is attributed to noise and measurement inaccuracy. The non-dimensional aerodynamic added mass, however, is not predicted quite as good as the non-dimensional damping. Apart from the higher sensitivity of the added mass with respect to phase lag, the added mass is probably more sensitive to all kinds of disturbances because it seems that there is no pattern in differences between the Navier-Stokes results and the experimental results. As mentioned previously, the experimental results were obtained at different Reynolds numbers, as shown in the table below

| | | | | | |
|-----------|----------|---------|---------|---------|---------|
| f_{red} | < 0.0225 | 0.024 | 0.031 | 0.035 | 0.041 |
| Re | 555.000 | 470.000 | 383.000 | 330.000 | 270.000 |

whereas the shown Navier-Stokes results are for one Reynolds-number $Re = 555000$. The lower middle and lower figures show the results for the $\alpha = 15^\circ$, $\beta = 135^\circ$ and $\alpha = 20^\circ$, $\beta = 0^\circ$ cases. From these figures it is seen that the general behavior of the damping and added mass is predicted fairly well in the $\alpha = 15^\circ$ case, whereas the agreement is not as good in the $\alpha = 20^\circ$ case. Furthermore, it is indicated in these data, that the data predicted with the Navier-Stokes code is not always closest to the very high stall mode results even though that was the case at $f_{red} = 0.02$, as shown in figure 4.45.

Further comparison of the dynamics of the Navier-Stokes computations with the experimental results are shown in figure 4.47, where the non-dimensional force coefficient hysteresis loops are compared at $\alpha = 5^\circ$ for different values of the direction of the motion, β . The Reynolds number is $Re = 555000$ and the reduced frequency is $f_{red} = 0.02$. The left, middle and right figures show the lift, drag and quarter-chord moment coefficient loops, respectively.

From the figure it is seen that the predictions of the dynamics of the lift and drag in general is very good at this angle of attack. The differences in the level of the lift coefficient is attributed to the general uncertainty when adjusting the angle of attack in the experiments, and to the slightly higher stationary lift coefficient at $\alpha = 5^\circ$. Comparison of the drag curves show that the predicted drag is always higher than the measured drag. The reason for this could be the viscous part of the force, which is not included in the experiments. As mentioned earlier, the discretization of the pressure taps with regards to determining the force in the chord-wise direction is very coarse, which adds to the uncertainty of the experimental drag. The cause of the difference in the slope of the drag curves for $\beta \geq 45^\circ$ is not clear to the author.

It is seen that the moment loops compare quite bad. Only the main features of the moment loops are predicted well. Even though there is trip tape on both sides of the airfoil, the disturbance is much more pronounced on the suction side of the profile. It

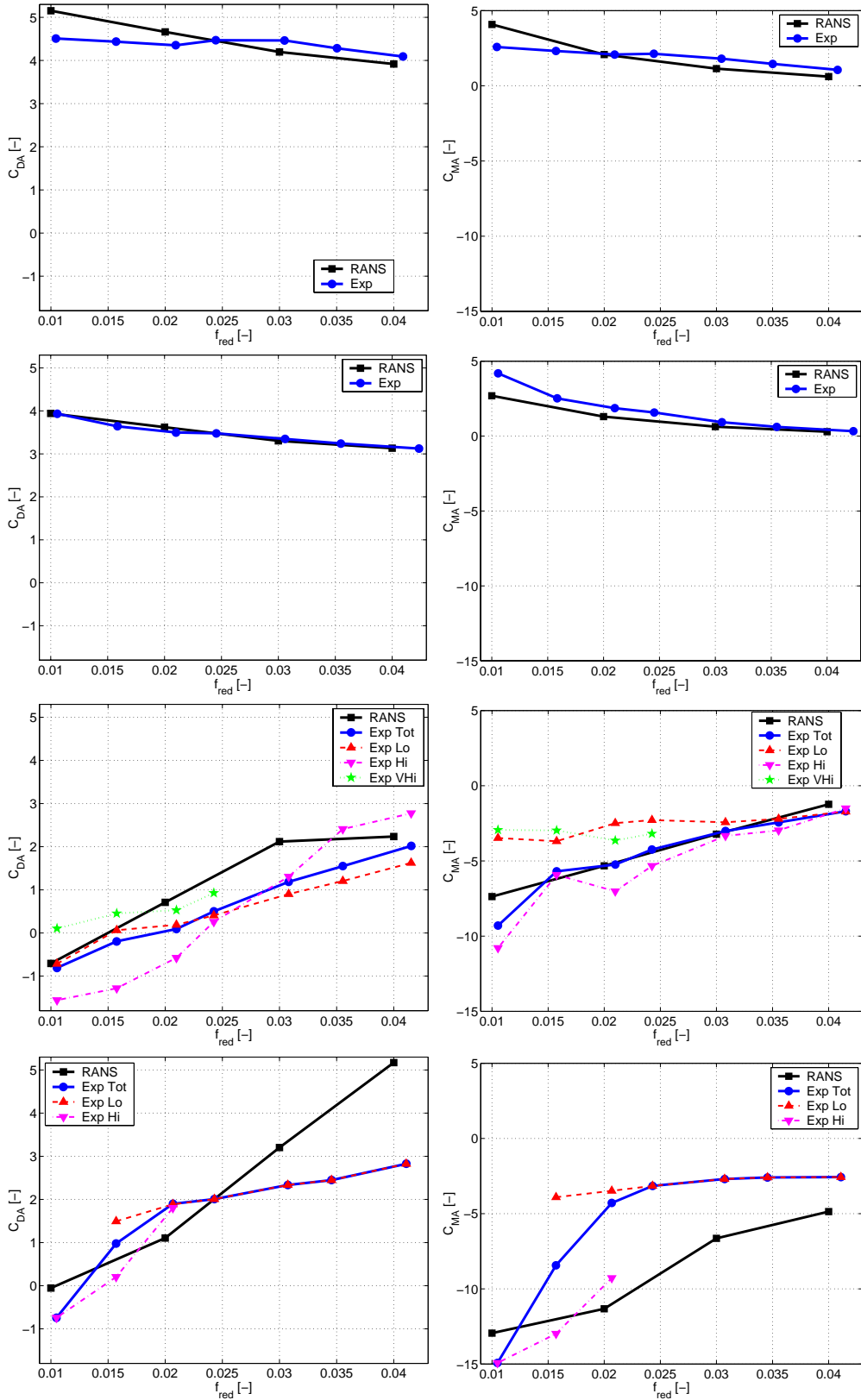


Figure 4.46: Comparison between Navier-Stokes and experimental results. Non dimensional aerodynamic damping (left) and Non dimensional added mass (right) versus reduced frequency. Upper: $\alpha = 5^\circ \beta = 0^\circ$. Upper middle: $\alpha = 8^\circ \beta = 160^\circ$. Lower middle: $\alpha = 15^\circ \beta = 135^\circ$. Lower: $\alpha = 20^\circ \beta = 0^\circ$

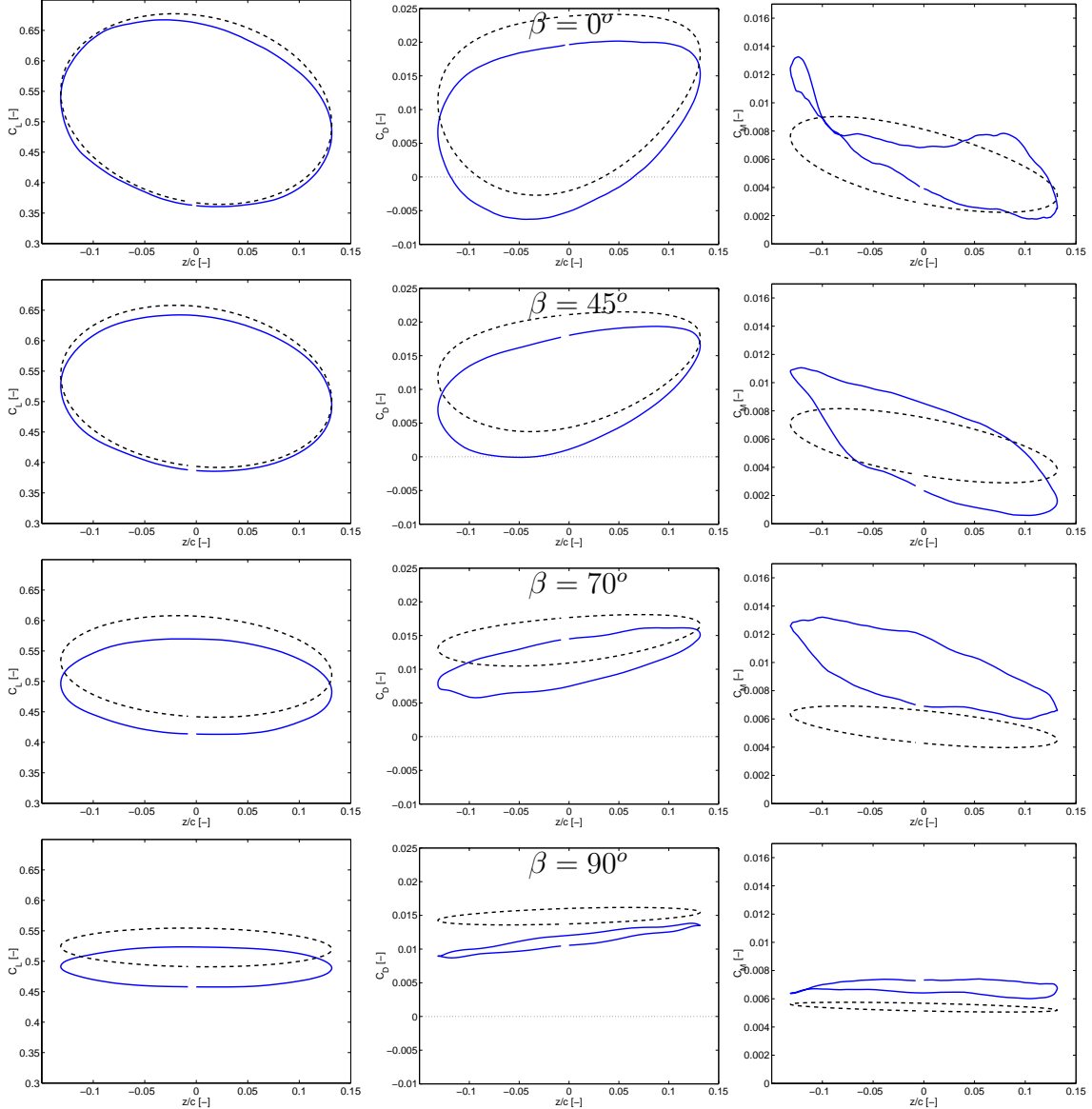


Figure 4.47: Comparison of Navier-Stokes and experimental force loops at $\alpha = 5^\circ$ and $f_{red} = 0.02$ at different directions of the movement, β . The left, middle and right column shows C_L , C_D and C_M , respectively. The solid curves are experimental results, whereas the dashed curves are Navier-Stokes computations.

is likely that the disturbance introduced by the trip tape affects the measured moment dynamically as well as the mean value.

Proceeding to comparison of the performance of the Navier-Stokes code for various angles of attack, figure 4.48 shows the hysteresis loops for motion perpendicular to the free-stream, $\beta = 0^\circ$, at incidences $\alpha = 5^\circ, 8^\circ, 12^\circ, 15^\circ$ and 20° . The Reynolds number and reduced frequency for these computations are $Re = 383000$ and $f_{red} = 0.03$, respectively.

It is seen that the predictions for incidences up to $\alpha = 8^\circ$ are in fairly good agreement with the experimental data. At angles of attack above this, the differences are quite big. For $\alpha = 12^\circ$ it is noted that all predicted force loops differ noticeably from the experimental ones. Both the mean values and the shape of the loops.

The explanation for the big difference in the loops at $\alpha = 12^\circ$ could be that the onset of stall occurs at different angles of attack in the experimental and numerical work. This was evident from the comparison of the static results as well. One interesting feature of the curves is that the general shape of the experimental loops at $\alpha = 12^\circ$, in particular the drag and moment loops, match the predicted ones at $\alpha = 15^\circ$. This roughly means that the dynamics of the measured flow at $\alpha = 12^\circ$ corresponds to the one predicted by the Navier-Stokes code at $\alpha = 15^\circ$.

In the case of $\alpha = 15^\circ$ the measured and predicted loops differ drastically. The only stall mode present in the experiments was the low stall mode, which was the one furthest from the predicted level at this incidence in the comparison of the static results.

The lowest figures showing the comparison of the loops in the $\alpha = 20^\circ$ case again shows a drastic difference between measured and predicted loops. The dips and peaks due to the vortex shedding in the predicted loops are not found in the experimental data. The shown experimental loops are computed as a mean of approximately 144 oscillation cycles, a process which can hide higher frequency oscillations if these are not periodic in the oscillation cycle. When viewing the instantaneous pressure coefficients in time, it was seen that pressure peaks corresponding to vortices was observed in cases where the low stall mode was present. However, the force response corresponding to these vortices were not as violent as the ones predicted by the Navier-Stokes code, and the location of these were not fixed with regards to the oscillation cycle, but seemed to appear more random.

The reason that the Navier-Stokes code predicts the strong effect from the large vortices, which leads to the drastic behavior of the forces, may be caused by a combination of three reasons. The two dimensional nature of the computations, the relatively coarse grid in the vicinity of the airfoil, and the low free stream turbulence. Two dimensional simulations generally generate larger structures in the flow than the three dimensional counterpart, and the structures generated in the flow are generally maintained longer. A part of the reason for this is that there is no possibility for breakdown of the vortices due to instabilities in the third direction.

The size of the vortices/eddies that can be resolved with a certain computational grid is connected to the size of the computational cells. If the radius of the vortice/eddy is smaller than the grid size, then it is not possible to resolve the basic features of it.

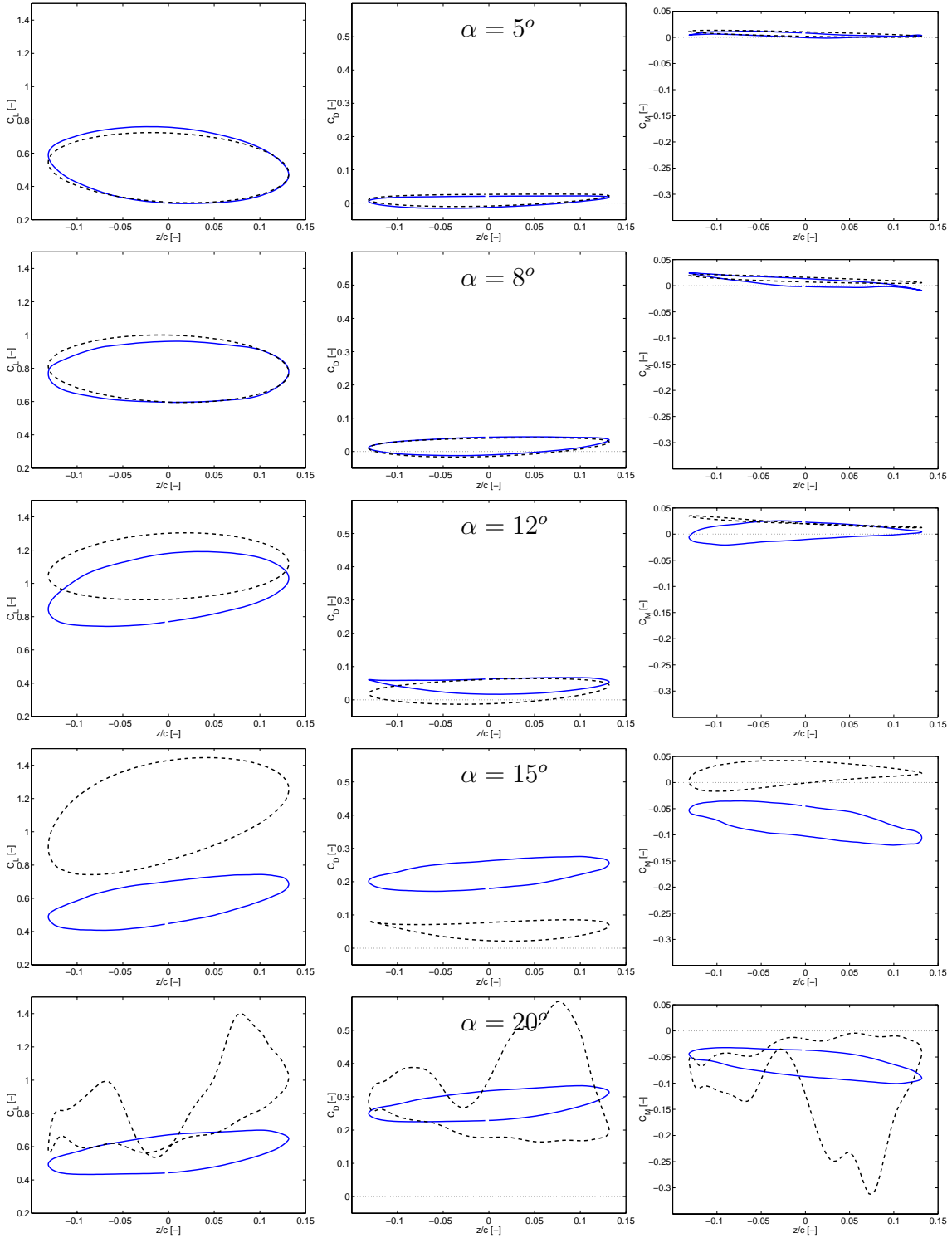


Figure 4.48: Comparison of Navier-Stokes and experimental force loops at $\beta = 0^\circ$ and $f_{red} = 0.03$ at different incidences, α . The left, middle and right column shows C_L , C_D and C_M , respectively. The solid curves are experimental results, whereas the dashed curves are Navier-Stokes computations.

This means that the size of the eddies that can be resolved with the computational grid increases with the distance from the airfoil.

It has been observed, that the $k - \omega$ SST turbulence model dissipates the free-stream turbulence set as inflow boundary condition before the flow is convected to the airfoil. This means that the flow meeting the airfoil in essence is laminar. This could have implications on the dynamics of the flow as well.

The last figure in the comparison between the experimental results and the results obtained with the Navier-Stokes code is a comparison of the force loops in two cases with $\alpha = 15^\circ$ where multiple stall modes occurred in the experiments. This is shown in figure 4.49. The case shown in the left figure has $\beta = 70^\circ$ and $f_{red} = 0.03$, whereas the case shown in the right figures has $\beta = 110^\circ$ and $f_{red} = 0.02$.

It is seen in the left figures, that the predicted lift, drag and moment values compare very bad with the low stall mode. The agreement between the very high stall mode and the numerical results are somewhat better, even though there is still considerable differences in both the mean values and the shape of the loops. It is seen in the lowermost figure, that most of the big differences between the specific loops are cancelled out in this direction of the movement, $\beta = 70^\circ$. The agreement between the predicted loop and the very high stall mode loop is very good. As pointed out in the case of the comparison with the analytical results, this is just a lucky case where two wrongs cancel each other out. In this case the too high lift level is compensated by the too low drag.

All three stall modes are present in the right figures. This is the case where $f_{red} = 0.02$ and $\beta = 135^\circ$. As in the previous case, the predicted loops compare best with the loops from the very high stall mode, but the agreement between the mean levels is still not good. As was the case in the comparison of the analytical models, this case compared much worse in the direction of the motion than the first multiple stall case. The shape of the predicted loop corresponds well with the shape of the very high stall mode loop, though.

The performance of the Navier-Stokes code can be summarized

- The agreement between force coefficients for stationary airfoil are reasonable good up to $\alpha = 12^\circ$.
- The Navier-Stokes code predicts onset of stall later than the experimental value
- Multiple stall modes are not captured with a basic set-up of the computational parameters.
- Quite big differences between experimental and numerical results for angles of attack above $\alpha = 12^\circ$.
- The lift and drag loops are predicted well for low angles of attack.
- The moment loops are predicted fairly well for low angles of attack. Some of the differences are attributed to uncertainties in the measurements.

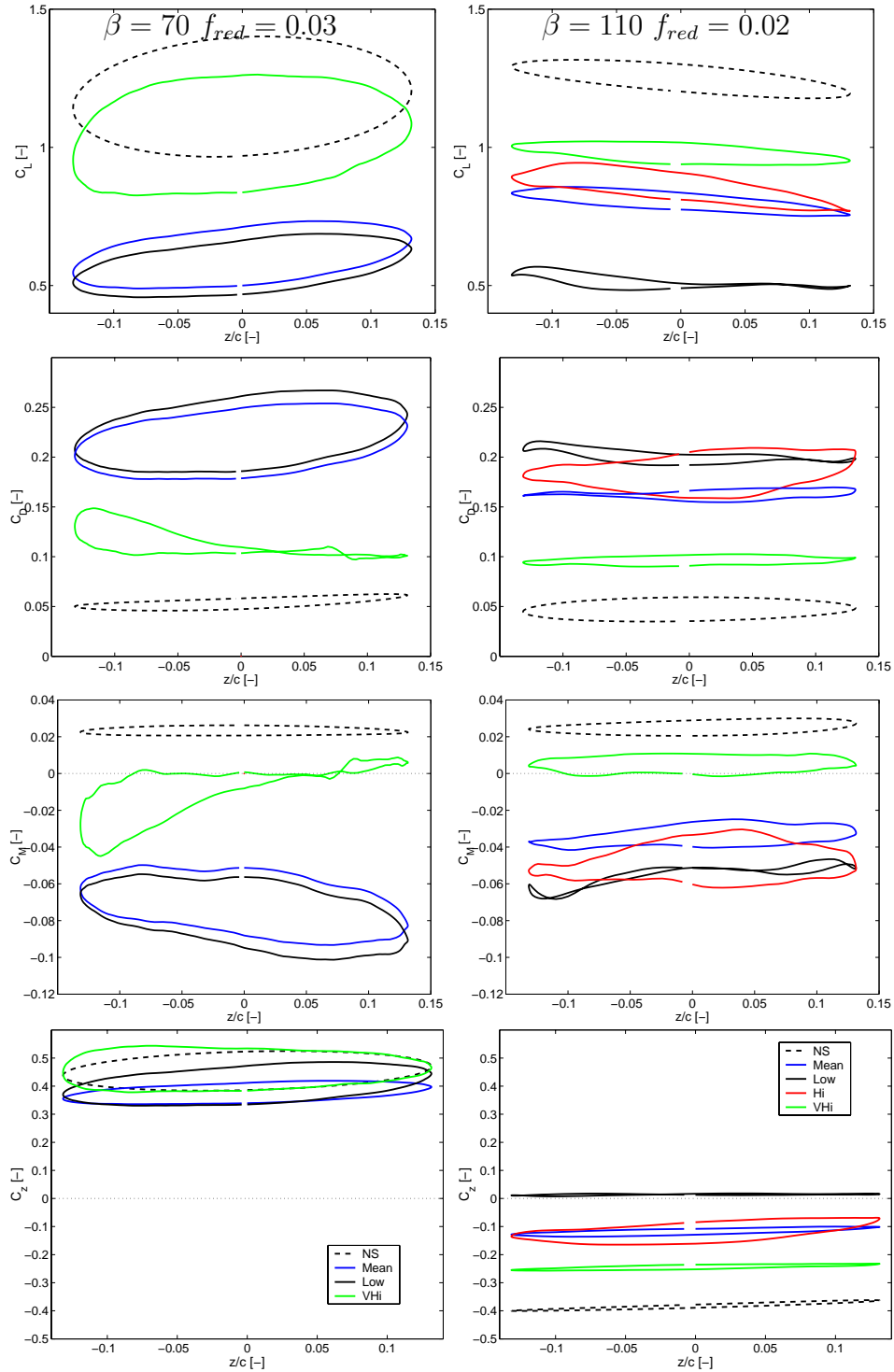


Figure 4.49: Comparison of Navier-Stokes and experimental force loops for experiments with multiple stall. The incidence is $\alpha = 15^\circ$. Upper : C_L . Upper middle : C_D . Lower middle C_M . Lower : C_Z . The solid curves are experimental results, whereas the dashed curves are Navier-Stokes computations.

- At $\alpha = 12^\circ$ significant differences in moment loops, but damping and mass loops are in fair agreement with the experiments.
- For $\alpha = 15^\circ$ and above, the agreement between the numerical and experimental loops is bad.
- At $\alpha = 20^\circ$. Violent peaks and dips predicted due to vortex shedding. This is not present in the experimental results.
- The aerodynamic damping is predicted well up to $\alpha = 15^\circ$.
- The features of the very high stall mode force loops compares best with the force loops obtained with the Navier-Stokes code.
- The general dependence of the aerodynamic damping and mass on reduced frequency is captured well.

Chapter 5

Conclusion

The work presented in this dissertation has focussed on investigation of the unsteady two-dimensional aerodynamic forces acting on a NACA 0015 airfoil undergoing harmonic translatory motions. The work falls in two categories.

Experimental and theoretical work.

The main part of the experimental work was devoted to measurement of the unsteady pressure on the NACA 0015 airfoil undergoing translatory motions, but measurements on a stationary airfoil was carried out as well.

The Reynolds number in the majority of the experiments was in the range from $Re = 383000$ to $Re = 555000$.

Up to three distinctively different stall modes was observed in the experimental work between maximum lift and the beginning of deep stall, $15^\circ \leq \alpha \leq 20^\circ$, for identical boundary conditions. The multiple stall modes occurred in both steady and unsteady experiments, where the duration of each mode varied from about one second to the entire time-span of the specific measurement, 60 seconds. The cause of the shift from one to another level was not found. Both the mean as well as the dynamic characteristics was found to differ from mode to mode.

The flow mechanisms leading to stall induced vibrations was studied from the results of the unsteady experiments, where the aerodynamic damping and added mass was measured as a function of angle of attack and angle of movement at two different reduced frequencies, $f_{red} = 0.02$ and $f_{red} = 0.03$. The maximum negative aerodynamic damping was in both cases found to exist in the stalled region of the airfoil, at 15° angle of attack, with a movement direction close to the chordwise direction.

The influence of amplitude and reduced frequency of the movement on the aerodynamic damping was investigated. The influence of the amplitude was found to be very weak, but the reduced frequency had a dramatic effect on the aerodynamic damping. The experimental results showed that aerodynamic damping decreased as the reduced frequency was reduced for the stalling flows at incidences $\alpha = 15^\circ$ and $\alpha = 20^\circ$.

It was found that the least damped stall mode at the low reduced frequencies was the lowest of the two high lift stall modes. This particular stall mode showed greater dependance of the reduced frequency than the other, and showed greater aerodynamic damping than the other stall modes at reduced frequencies above $f_{red} = 0.03$.

The result that slower oscillations are more prone to negative aerodynamic damping

for the stalling flows between $\alpha = 15^\circ$ and $\alpha = 20^\circ$ may have interesting implications. If this result is general, and not dependent on the type of the airfoil profile and Reynolds number, then this may have implications on the aeroelastic stability of wind turbines in the future. The trend in wind turbine design through the last decades has been toward bigger turbines, and thereby lower eigenfrequencies. The tip speed, on the other hand, has been kept fairly constant due to noise constraints. With increasing size of the wind turbines, the reduced frequency decrease, causing a decrease in the aerodynamic damping. If the sum of the structural and the aerodynamic damping is negative, then dynamic instabilities will occur, resulting in system failure, or, at best, a drastic reduction of the life-time of the turbine.

As a part of the theoretical part of the work carried out, a two-dimensional unsteady panel code was developed, in which the option to include the wind tunnel walls was implemented. This code was used for computing the effect of the imposition of the wind tunnel walls on the dynamic response of the airfoil. Based on the results from the code, dynamic tunnel corrections for the experimental work was derived. The results computed with a Navier-Stokes solver was in fair agreement with the dynamically corrected experimental results for attached flows, which indicated that the corrections works satisfactorily.

A different application for the unsteady panel code was the investigation of the difference between the aerodynamic response of a heaving and a pitching airfoil with identical relative angle of attack. It was shown that the lift was matched very well for pitching motion around the 75% chord point, but that the drag and moments were very different in the heaving and the pitching cases. The investigation is valid only for attached flows. However, since the mechanisms for attached flows, which are much lower in complexity than for stalling flows, showed that both drag and moment loops were predicted very different in the cases with identical relative angles of attack, it seems most likely that the response of the aerodynamic forces from airfoils in stall could be substantially different in the two cases as well.

Another part of the theoretical work concerned the development of a new heuristic stall model, which could be considered an ‘interpolation’ between Quasi-Stationary and Unsteady Potential theory. The model is identical to Unsteady Potential Theory when airfoil characteristics from steady potential theory is used as input to the model, and except from the terms arising from acceleration of a virtual mass, the new model is identical to Quasi-Stationary theory as $f_{red} \rightarrow 0$.

Overall conclusions from comparison with the experimental results are, that the new dynamic stall model is a clear improvement over quasi-steady theory in the attached region, but that the new model fails to reproduce the features of the moderately and deeply stalled flows significantly better than the quasi-steady results. This is attributed to the assumption of similarity between the dynamics in the attached and stalling cases, which clearly fail to describe the complex dynamics of stalling flows.

The most complex model for prediction of the flow used in this work is a Reynolds Averaged Navier-Stokes model. The eddy-viscosity was calculated by utilizing the two-

equation $k - \omega$ SST turbulence model of Menter. No transitional model were employed in the present work, meaning that a fully turbulent flow was assumed.

From the comparison with experimental data, it was seen that the Navier-Stokes code predicts onset of stall later than the experimental value.

Multiple stall modes were not captured with the Navier-Stokes code. The characteristics of the predicted stall type corresponded best with the very high stall mode, but substantial differences were present.

Comparison of the force loops from the Navier-Stokes results with the experimental results showed that the exact dynamics of the complex stalling flows were not predicted correctly.

The force loops generally showed reasonable agreement up to $\alpha = 12^\circ$. After this point, there was disagreement between the results. The agreement between the experimental and computed force loops in the $\alpha = 20^\circ$ case differs considerably. The computed loops show violent peaks and dips due to shedding of vortices. Such behavior was not seen in the experimental results.

Three reasons for this were suggested. Effects of two dimensional modelling, insufficient mesh resolution of the region near the airfoil where the vortices are shed, and the practically laminar flow the airfoil meets in the Navier-Stokes computations.

An investigation of the general dependence of the aerodynamic damping and added mass on the reduced frequency is captured well using the Navier-Stokes model. This suggests that dynamic corrections or engineering models based on results from Navier-Stokes computations are plausible even though the actual level of the computation compares bad with experiments.

Future Perspectives

A possible extension to the new stall model described in the present work would be to modify Theodorsens function $\mathbf{C}(k)$ to take into account the change in dynamics due to separation and stall. In this case the renormalization function corresponding to Theodorsens function would be of the form $\tilde{\mathbf{C}}(k, f_{stall})$, where $f_{stall} = f(\alpha)$ denotes the level of stall at the mean angle of attack.

An interesting perspective on the present data would be to quantify the differences in aerodynamic response between pitching and heaving motion of the airfoil by direct comparison of experimental results for which the flow is stalling.

In order to be able to use the dynamic data for validation of dynamic models, more accurate and closer spaced steady results are required.

With regards to the Navier-Stokes simulations, grid-independence studies in the stalling region would be of interest.

A straightforward extension to the Navier-Stokes investigations in this work would be to investigate the effect of specifying the transition points at the trip-tape locations, or to apply a transition model and investigate the natural transition points.

Further investigations using Navier-Stokes code could include three dimensional simulations and DES modelling.

Bibliography

- [1] I.A. Abbot and A.E.v. Doenhoff
Theory of Wing Sections.
Dover Publications, 1958.
- [2] C. Bak and P. Fuglsang
Modification of the NACA 63₂ – 415 Leading Edge for Better Aerodynamic Performance.
A Collection of the 2001 ASME Wind Energy Symposium Technical Papers Presented at the 39'th AIAA Aerospace Sciences Meeting and Exhibit, Reno, NV 11-14 January, 2001.
- [3] C. Bak, H.A. Madsen, P. Fuglsang and F. Rasmussen
Double Stall.
Risø-R-1043(EN), 1998.
- [4] C. Bak, H.A. Madsen, P. Fuglsang and F. Rasmussen
Observations and Hypothesis of Double Stall.
Wind Energy, 2, p.195-210, 1999.
- [5] F. Bertagnolio, M. Gaunaa, M.H. Hansen, N.N Sørensen and F. Rasmussen
Computation of Aerodynamic Damping for Wind Turbine Applications.
4th GRACM Congress on Computational Mechanics, GRACM 2002, Patras 27-29 June, 2002.
- [6] F. Bertagnolio, N. Sørensen, J. Johansen and P. Fuglsang
Wind Turbine Airfoil Catalogue.
Risø-R-1280(EN), 2001.
- [7] R.L. Bisplinghoff, H. Ashley and R.L. Halfman
Aeroelasticity.
Dover Publications, 1955.
- [8] G.J.W. van Bussel
The Use of the Asymptotic Acceleration Potential Method for Horizontal Axis Wind Turbine Rotor Aerodynamics.
Journal of Wind Engineering and Industrial Aerodynamics, 39, 1992.
- [9] P.K. Chaviaropoulos, N.N. Sørensen, M.O.L. Hansen, I.G. Nikolaou, K.A. Agge- lis, J. Johansen, M. Gaunaa, T. Hambraus, H. vGeyr, C. Hirsch, K. Shun, S.G.

- Voutsinas, G. Tzambiras, Y. Perivolaris and S.Z. Dyrmose
Viscous and Aeroelastic Effects on Wind Turbine Blades. The VISCEL project. Part II: Aeroelastic Stability Investigations.
 Submitted to Wind Energy, 2002.
- [10] G. Christiansen, E. Both and P.Ø. Sørensen
Mekanik.
 Laboratoriet for teknisk fysik, Technical University of Denmark. 1990.
- [11] J.A. Ekaterinaris, G.R. Srinivasan and W.J. McCroskey
Present capabilities of predicting two-dimensional dynamic stall.
 AGARD 75th fluid dynamics panel meeting and symposium on aerodynamics and aeronautics of rotorcraft. 1994.
- [12] R.W. Fox and A.T. McDonald
Introduction to Fluid Mechanics.
 McGraw-Hill, Third edition, 1985.
- [13] Y.C. Fung
An Introduction to the Theory of Aeroelasticity.
 Dover Publications, 1955.
- [14] R.A. McD Galbraith, M.W. Gracey and E. Leitch
Summary of Pressure Data for Thirteen Aerofoils on the University of Glasgow's Aerofoil Database.
 G.U. Aero Report 9221, University of Glasgow, 1992.
- [15] D.E. Gault
A Correlation of Low-Speed, Airfoil-Section Stalling Characteristics With Reynolds Number and Airfoil Geometry.
 NACA Technical Note 3963, 1957.
- [16] M. Gaunaa
Aeroelasticitet. (In Danish)
 Masters thesis, Department of Fluid Mechanics, Technical University of Denmark.
 1998.
- [17] M. Gaunaa
Aeroelastic Analysis of Airfoil Section.
 Proceedings of the European Wind Energy Conference, Nice, France, 1-5 March, 1999. p.164-167
- [18] M. Gaunaa
Experimental Investigation of Airfoil Subject to Harmonic Edge- and Flapwise Movement.
 Proceedings of the European Wind Energy Conference, Copenhagen, Denmark, 2-6 July, 2001. p.446-449

- [19] M. Gaunaa and J.N. Sørensen
Experimental Investigation of Airfoil Subject to Harmonic Translatory Motions.
AIAA-2002-0035, ASME Wind Energy Symposium, Reno, USA. 2002. p.133-140
- [20] E. Guilmeneau, J. Piquet and P. Queutey
Two-Dimensional Turbulent Viscous Flow Simulation Past Airfoils at Fixed Incidence.
Computers and Fluids, Vol 26,2, 1997.
- [21] M.O.L. Hansen
Aerodynamics of Wind Turbines; Rotors, Loads and Structure.
James and James Science Publishers Ltd., 2000.
- [22] J.L. Hess
Higher Order Numerical Solution of the Integral Equation for the Two-Dimensional Neumann Problem.
Computer Methods in Applied Mechanics and Engineering, (2), 1973.
- [23] J. Johansen
Unsteady Airfoil Flows with Application to Aeroelastic Stability.
Ph.D. Thesis, Risø-R-1116(EN), Risø National Laboratory. 1999.
- [24] J. Johansen and N.N Sørensen
Application of a Detached-Eddy Simulation Model on Airfoil Flows.
IEA Joint Action, Aerodynamics of Wind Turbines, 14th Symposium, Boulder, December, 2000. pp.1-9.
- [25] J. Johansen, N.N Sørensen, J.A. Michelsen and S. Schreck
Detached-Eddy Simulation of Flow Around the S809 Airfoil.
EWEC 2001, Copenhagen, 2-6 July, 2001. pp.414-417.
- [26] K.D. Jones, C.M. Dohring and M.F. Platzer
An Experimental and Computational Investigation of the Knoller-Betz Effect.
AIAA Journal, Vol. 36, No. 7, 1998, pp. 1240-1246.
- [27] J. Katz and A. Plotkin
Low-Speed Aerodynamics From Wing Theory to Panel Methods.
Mc-Graw Hill, Inc. 1991.
- [28] J.G. Leishmann
Dynamic Stall Experiments on the NACA 23012 Aerofoil.
Experiments in Fluids 9, 1990. pp. 49-58.
- [29] J.G. Leishman and T.S. Beddoes
A Semi-Empirical Model for Dynamic Stall.
J. of the American Helicopter Society. 1986.
- [30] W.J. McCroskey
Unsteady Airfoils.
Ann. Rev. Fluid Mech, 1982, pp. 285-311.

- [31] W.J. McCroskey, L.W. Carr and K.W. McAlister
Dynamic Stall Experiments on Oscillating Airfoils.
 AIAA Journal, Vol. 14, No. 1, 1976, pp. 57-63.
- [32] W.J. McCroskey and S.L. Pucci
Viscous-Inviscid Interaction on Oscillating Airfoils in Subsonic Flow.
 AIAA Journal, Vol. 20, No. 2, 1982, pp. 167-174.
- [33] G.B. McCullough and D.E. Gault
Examples of Three Representative Types of Airfoil-Section Stall at Low Speed.
 NACA Technical Note 2502. 1951.
- [34] F.R. Menter
Zonal Two Equation $k-\omega$ Turbulence Models for Aerodynamic Flows.
 24th Fluid Dynamics Conference
 AIAA 93-2906. 1993.
- [35] J.A. Michelsen
Basis3D - a platform for development of multiblock PDE solvers.
 Technical Report AFM 92-05, Department of Fluid Mechanics, Technical University of Denmark, 1992.
- [36] J.A. Michelsen
Block-Structured Multigrid Solution of 2D and 3D Elliptic PDE's.
 Technical Report AFM 94-06, Department of Fluid Mechanics, Technical University of Denmark, 1994.
- [37] T. Moeller
Blade Cracks Signal New Stress Problem.
 WindPower Monthly, May 1997.
- [38] L. Myllerup
Turbulence Models for Complex Flows.
 Ph.D. Thesis, Fluid Mechanics, Department of Mechanical Engineering, Technical University of Denmark. 2000.
- [39] H. Oshima and B.R. Ramaprian
Velocity Measurements over a Pitching Airfoil.
 AIAA Journal, Vol. 35, No. 1, 1997, pp. 119-126.
- [40] R.C. Pankhurst and D.W. Holder
Wind-Tunnel Technique.
 Sir Isaac Pitman and Sons, ltd., 1952.
- [41] J.T. Petersen, H.Aa. Madsen, A. Björck, P. Enevoldsen, S. Øye, H. Ganander, D. Winkelaar. *Prediction of Dynamic Loads and Induced Vibrations in Stall.* Risø report. Risø-R-1045(EN), Risø National Laboratory. 1998.

- [42] R.A. Piziali
2-D and 3-D Oscillating Wing Aerodynamics for a Range of Angles of Attack Including Stall.
NASA Technical Memorandum 4632/USAATCOM Technical Report 94-A-011, 1994.
- [43] W.H. Rae and A. Pope
Low-Speed Wind Tunnel Testing.
John Wiley and Sons, Inc., Second Edition, 1984.
- [44] C.M. Rhie
A Numerical Study of the Flow Past an Isolated Airfoil With Separation
Phd Thesis. University of London. 1985.
- [45] P.J. Roache
Quantification of Uncertainty in Computational Fluid Dynamics.
Annual Review in Fluid Mechanics, 29. 1997.
- [46] M.S. Selig, C.A. Lyon, P. Giguere, C.N. Ningham, and J.J. Guglielmo
Summary of Low-Speed Airfoil Data - Vol. 1.
SoarTech Publications, June 1995.
- [47] H. Stiesdal
Extreme Wind Loads on Stall Regulated Wind Turbines
In G. Elliot, editor. Proceedings of the 16th British Wind Energy Association Conference, pp.101-106, June 1994.
- [48] M. Strelets
Detached-Eddy Simulation of Massively Separated Flows
AIAA 2001-0879, 2001.
- [49] J.N. Sørensen and A. Myken
Unsteady Actuator Disc Model for Horizontal Axis Wind Turbine.
Journal of Wind Engineering and Industrial Aerodynamics, 39, 1992. pp. 139-149.
- [50] J.N. Sørensen and P.J. Nygreen
Unsteady Vorticity-Streamfunction Algorithm for External Flows.
Computers and Fluids, 30, pp.69-87, 2001.
- [51] N.N. Sørensen
General purpose flow solver applied to flow over hills.
Technical Report Risø-R-827(EN). Risø National Laboratory. 1995.
- [52] N.N. Sørensen and J.A. Michelsen
Aerodynamic Predictions for the Unsteady Aerodynamics Experiment Phase-II Rotor at the National Renewable Energy Laboratory.
AIAA Paper 2000-0037, 2000.
- [53] N.N. Sørensen
HypGrid2D a 2-D Mesh Generator.
Technical Report Risø-R-1035(EN). Risø National Laboratory. 1998.

- [54] N.N. Sørensen
k – ω Turbulence Models Implementation and Testing.
 Technical Report Risø-R-864(EN). Risø National Laboratory. 1995.
- [55] T. Theodorsen
General Theory of Aerodynamic Instability and the Mechanism of Flutter.
 NACA Report, No. 496, 1935.
- [56] K. Thomsen, J.T. Petersen, M.H. Hansen and E. Nim
Experimental Investigation of Aerodynamic Damping.
 Proceedings of the European Wind Energy Conference, Copenhagen, Denmark,
 2-6 July, 2001. pp. 573-576.
- [57] C.T Tran and D. Petot
Semi-Empirical Model for the Dynamic Stall of Airfoils in View of the Application of a Helicopter Blade in Forward Flight.
 6th European Rotorcraft and Powered-Lift Aircraft Forum, Bristol, UK, September 1980.
- [58] S.G. Voutsinas, M.A. Belessis and K.G. Rados
Investigation of the Yawed Operation of Wind Turbines by Means of a Vortex Particle Method.
 Aerodynamics and Aeroacoustics of Rotorcraft, AGARD-CP-552, 1994.
- [59] J.M. Walker, H.E. Helin and J. Strickland
An Experimental Investigation of an Airfoil Undergoing Large Amplitude Pitching Motions.
 AIAA Journal, Vol. 23, No. 8, 1985, pp. 1141-1142.
- [60] F.M. White
Viscous Fluid Flow.
 McGraw-Hill, 1991.
- [61] D. Wilcox
Reassessment of the Scale-Determining Equation for Advanced Turbulence Models.
 AIAA Journal 26(11), 1299-1310. 1988.
- [62] T.Y. Wu
Flow Through a Heavily Loaded Actuator Disc.
 Schifftechnik, 9. 1962. pp. 134-138.
- [63] S. Øye
Dynamic Stall Simulated as Time Lag of Separation.
 Proceedings of the Fourth IEA Symposium on the Aerodynamics of Wind Turbines, Rome, Nov. 20.-21. 1990.
- [64] S. Øye
FLEX4 Simulation of Wind Turbine Dynamics.
 Proceedings of the 28th IEA Meeting of Experts, State of the Art of Aeroelastic

Codes for Wind Turbine Calculations.
(Available through the IEA)

- [65] S. Øye
Instationary, Aerodynamic Forces on Two-Dimensional Airfoil. (In Danish)
AFM Notat 81-05, Department of Fluid Mechanics, Technical University of Denmark, 1981.

Nomenclature

Latin symbols

| | |
|----------------------|--|
| a | Acceleration |
| a | Speed of sound |
| a | Non-dimensional hinge-point parameter |
| A | Amplitude |
| \tilde{A} | Non-dimensional amplitude |
| A_{Tunnel} | Cross sectional area of wind tunnel test section |
| b | Half-chord |
| c | Length of airfoil chord |
| $\mathbf{C}(k)$ | Theodorsens function |
| C_D | Non dimensional drag coefficient |
| C_f | Non dimensional friction coefficient |
| C_L | Non dimensional lift coefficient |
| C_M | Non dimensional moment coefficient |
| C_P | Non dimensional pressure coefficient |
| D | Drag force |
| D_A | Aerodynamic damping |
| F_1, F_2, F_3, F_4 | Unsteady tunnel correction coefficients |
| F | Froude number |
| f_{red} | Reduced frequency |
| F_{Total} | Total forces |
| F_{Visc} | Viscous forces |
| g | Gravitational constant |
| h | Height of wind tunnel test section |
| k | Turbulent kinetic energy |
| k | Non-dimensional wavenumber |
| L | Lift force |
| m | Molar mass |
| M | Mach number |
| M | Moment |
| N | Normal force |
| \vec{n} | Unit vector |
| p | Pressure |
| R | Universal gas constant |
| Re | Reynolds number |

| | |
|---------------|--|
| s | Surface length parameter |
| S_v | Source terms |
| t | Time |
| \tilde{t} | Non-dimensional time |
| T | Temperature |
| T | Tangential force |
| U | Fluid velocity |
| U | Fluid velocity in X -direction |
| U_s | Fluid velocity component along path s |
| V | Free-stream velocity |
| V | Fluid velocity in Y -direction |
| x | Coordinate in direction of free-stream |
| y | Coordinate perpendicular to free-stream |
| $y_{0.0125c}$ | Upper-surface ordinat for airfoil at 1.25% chord |
| z | Coordinate in direction of motion |

Greek symbols

| | |
|-----------------|---|
| α | Angle of attack |
| α_{rel} | Relative angle of attack |
| α^+ | Non-dimensional pitch rate |
| β | Direction of 1DOF motion |
| β_{rel} | Direction of 1DOF motion relative to airfoil |
| γ | Vortex distribution |
| γ | Angle between relative and absolute velocity |
| Γ | Circulation |
| δ^* | Displacement thickness |
| ϵ | Total blocking coefficient |
| ϵ_{sb} | Solid body blocking parameter |
| ϵ_{wb} | Wake blocking parameter |
| ω | Specific dissipation rate of turbulent kinetic energy |
| ρ | Density |
| σ | Wind tunnel incidence correction constant |
| ψ | Velocity potential |
| σ | Source strength |
| η | Length parameter perpendicular to the chordwise direction |
| μ | Viscosity |
| μ_t | Turbulent viscosity |
| ξ | Length parameter in the chordwise direction |

Superscripts

| | |
|------|-------------------------------|
| D | Terms related to drag |
| L | Terms related to lift |
| VM | Terms related to virtual mass |

| | |
|----|--|
| QS | Quasi-stationary |
| * | Quantity corrected for unsteady tunnel effects |
| ' | Derivative with respect to angle of attack |

Subscripts

| | |
|------------|--|
| <i>fic</i> | Fictitious |
| <i>l</i> | Lower |
| Kutta | Kutta-direction |
| panel | Quantities in panel coordinate system |
| <i>pot</i> | Potential theory |
| <i>rel</i> | Relative |
| <i>sb</i> | Solid blocking |
| <i>T</i> | Tunnel |
| <i>T</i> | Translatory |
| <i>TE</i> | Trailing edge |
| <i>u</i> | Upper |
| <i>V</i> | Viscous |
| VM | Virtual mass |
| W | Wake |
| <i>x</i> | Chord-wise |
| <i>y</i> | Flap-wise |
| WWI | Wake-wake interaction (wake roll-up) |
| QS | Quasi-stationary |
| α | Aerodynamic quantities a angle α |
| η | Direction perpendicular to the chordwise direction |

Abbreviations

| | |
|------|---------------------------------|
| BEM | Blade Element Momentum |
| CFD | Computational Fluid Mechanics |
| DES | Detached Eddy Simulation |
| DOF | Degrees of Freedom |
| PIV | Particle Image Velocimetry |
| RANS | Reynolds Averaged Navier-Stokes |

Appendix A

Airfoil section and movement mechanism

Pictures showing the airfoil section, airfoil section setup and movement mechanism are shown in this section. Figures A.1 to A.3 show the airfoil and airfoil setup, whereas figures A.4 to A.7 show the movement mechanism.



Figure A.1: *The pressure transducers were located inside the airfoil test section to minimize the length of the tubes connecting the pressure taps to the transducers. The orientation of the transducers were such that the fictitious forces from the motion of the airfoil had identical effect on all transducers, thus cancelling out in the computation of lift, drag and moment. Note the hollow rectangular aluminum beam at the quarter-chord, which provides the stiffness to the model .*

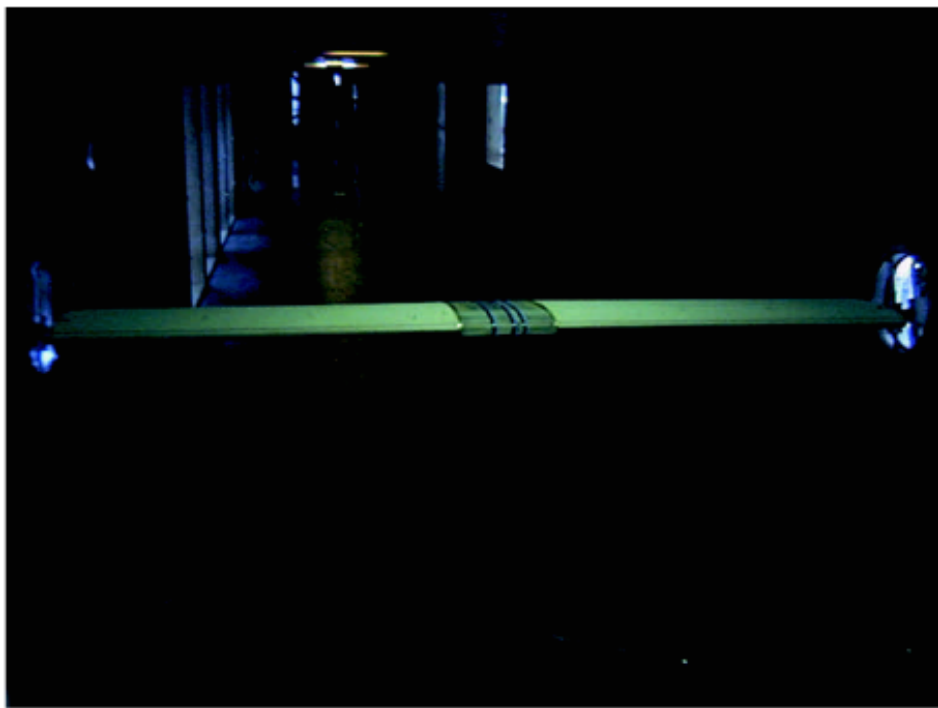


Figure A.2: *The airfoil test section spans the entire width of the wind tunnel to minimize three-dimensional effects. The test measuring section is located in center span. All connections from and to the pressure transducers were led through the hollow rectangular aluminum beam to one side of the airfoil, such that the airflow was disturbed minimally at the center measuring span.*



Figure A.3: *The angle of attack was measured using a inclinometer attached to a piece of wood machined to fit on top of the airfoil profile.*



Figure A.4: One servo, shown in the upper part of the left figure, drives the 1DOF movement mechanisms on both sides using a shaft on top of the wind tunnel. This ensures that the phase-difference between the motion on the two sides of the tunnel is kept very low.



Figure A.5: *Movement mechanism for the 1DOF translatory motion shown at four different stages of the rotational cycle. Left figures: View from inside of the wind tunnel. Right figures: View from the outside of the tunnel.*



Figure A.6: *The direction of the 1DOF motion, β , is set by rotating the ring on which the guiding rods are attached. Left: Inside view. Right: Outside view.*



Figure A.7: *A plexiglass cover encloses the movement mechanism to prevent air from leaking into the tunnel during operation of the wind tunnel. Outside tunnel view.*

Appendix B

Expressions for Unsteady Potential Forces for Oscillatory Motion

An important subcase of the general unsteady motion of the airfoil described in section 3.2.3 is oscillation of the profile with angular frequency of the motion ω . Introducing complex notation, the motion of the airfoil can be expressed as

$$x = x_1 e^{i\omega t} \quad (B.1)$$

$$y = y_1 e^{i\omega t} \quad (B.2)$$

$$\alpha = \alpha_0 + \alpha_1 \quad (B.3)$$

$$\alpha_1 = \alpha'_1 e^{i\omega t} \quad (B.4)$$

The amplitude and phase of the motion is given by the modulus and argument of the complex amplitudes, x_1 , y_1 and α'_1 . The physical position of the airfoil is given by the real part of the complex quantities.

Assuming that the amplitudes x_1 , y_1 and α'_1 are small, the expressions for the forces on the profile can be linearized. This leads us to the assumption that the total bound circulation on the profile will be of the form

$$\Gamma = \Gamma_0 + \Gamma_1 e^{i\omega t} \quad (B.5)$$

Due to Kelvin's Theorem, the strength of the vorticity shed in the wake will have the form

$$\gamma = \gamma_0 + \gamma_1 \quad (B.6)$$

where γ_0 corresponds to the starting vortex of the flow

$$\gamma_0 = 0 \quad \text{for } 1 < \xi < \infty - \Delta l \quad (B.7)$$

$$\gamma_0 = \gamma'_0 \quad \text{for } \infty - \Delta l < \xi < \infty, \quad (B.8)$$

such that

$$\int_{\infty - \Delta l}^{\infty} \gamma'_0 d\xi = \Gamma_0.$$

The vorticity belonging to the oscillation of the airfoil, γ_1 , is given by

$$\gamma_1 = \gamma'_1 e^{i\omega(t-b\xi/V)} = \gamma'_1 e^{i\omega t} e^{-k\xi} \quad (\text{B.9})$$

for $\xi >= 1$. In equation B.9, the variable k is defined as

$$k = \frac{\omega b}{V} = 2\pi f_{\text{red}}. \quad (\text{B.10})$$

Note that it is assumed that $V >> \dot{x}$ in order for the real part of γ_1 in equation B.9 to be a harmonic function of ξ .

Consider the motion of the profile, equations B.1-B.4, to consist of two parts, one of which gives the bound circulation Γ_0 , and the other which gives the other part of the total circulation in equation B.5, $\Gamma_1 e^{i\omega t}$. Corresponding to these, the vortex-sheets in the wake of these motions are denoted by γ_0 and γ_1 , respectively. The corresponding value of the vortex'-normal force

$$N_\Gamma = N_{\text{QS}} + N_W = N_{\text{QS}} \cdot C \quad (\text{B.11})$$

for the starting-vortex' motion, N_{Γ_0} , is evaluated by integrating the total bound vorticity from equation 3.10

$$\Gamma = b \int_{-1}^1 \gamma d\xi = b\pi(A_0 + 0.5A_1) \quad (\text{B.12})$$

From equations B.7 and B.8 we get that

$$\int_1^\infty \frac{\gamma_0}{\sqrt{\xi^2 - 1}} d\xi = 0 \quad (\text{B.13})$$

$$\int_1^\infty \left(\frac{\xi}{\sqrt{\xi^2 - 1}} - 1 \right) \gamma_0 d\xi = 0 \quad (\text{B.14})$$

By evaluating equation B.12 with equations 3.17, 3.18, B.13 and B.14 the following expression arises

$$\Gamma = (V - \dot{x})\alpha - \dot{y} - b(a - 0.5)\dot{\alpha} = \text{constant} \quad (\text{B.15})$$

Inserting the expressions for the oscillating motion, B.1-B.4, into this yields

$$(V - \dot{x})\alpha - \dot{y} - b(a - 0.5)\dot{\alpha} = V\alpha_0 = \text{constant} \quad (\text{B.16})$$

Which after insertion into equation B.11, and using the results in equations 3.30 and 3.31 yields for the normal force corresponding to the Γ_0 term

$$N_{\Gamma_0} = 2\pi\rho b(V - \dot{x})V\alpha_0 \quad (\text{B.17})$$

Since $N_\Gamma = N_{\Gamma_0} + N_{\Gamma_1}$ we must have that

$$\begin{aligned} N_{\Gamma_1} = N_\Gamma - N_{\Gamma_0} &= 2\pi\rho b(V - \dot{x}) [V\alpha_1 - \dot{x}\alpha_0 - \dot{y} - b(a - 0.5)\dot{\alpha}] \\ &\quad + \rho b(V - \dot{x}) \int_1^\infty \frac{\gamma_1}{\sqrt{\xi^2 - 1}} d\xi \end{aligned} \quad (\text{B.18})$$

Analogous to the introduction of Theodorsen's function, \mathbf{C} , earlier, the oscillatory part of the normal force can be rewritten as

$$N_{\Gamma_1} = 2\pi\rho b(V - \dot{x}) [V\alpha_1 - \dot{x}\alpha_0 - \dot{y} - b(a - 0.5)\dot{\alpha}] \cdot \mathbf{C} \quad (\text{B.19})$$

In this case \mathbf{C} is expressed by

$$\mathbf{C} = \frac{\int_1^\infty \frac{\xi}{\sqrt{\xi^2-1}} \gamma_1 \, d\xi}{\int_1^\infty \sqrt{\frac{\xi+1}{\xi-1}} \gamma_1 \, d\xi} \quad (\text{B.20})$$

inserting γ_1 from equation B.9 yields the final expression for \mathbf{C} in the oscillatory case

$$\mathbf{C} = \frac{\int_1^\infty \frac{\xi}{\sqrt{\xi^2-1}} e^{-ik\xi} \, d\xi}{\int_1^\infty \sqrt{\frac{\xi+1}{\xi-1}} e^{-ik\xi} \, d\xi} \quad (\text{B.21})$$

Note that Theodorsen's function, \mathbf{C} , in the oscillatory case is a function of reduced frequency, or k , alone. The total normal force in the oscillatory case is found by adding N_{Γ_0} , equation B.17, and N_{Γ_1} , equation B.18, with the virtual mass term N_{VM} , equation 3.32. Using equation 3.51 the final form of the lift force in the oscillatory case is obtained

$$\begin{aligned} L = & 2\pi\rho b(V - \dot{x}) \{ V\alpha_0 + [V\alpha_1 - \dot{x}\alpha_0 - \dot{y} - b(a - 0.5)\dot{\alpha}] \cdot \mathbf{C}(k) \} \\ & + \pi\rho b^2 [(V - \dot{x})\dot{\alpha} - \ddot{x}\alpha - \ddot{y} - ab\ddot{\alpha}] \end{aligned} \quad (\text{B.22})$$

Note the (obvious) similarity with equation 3.55.

Since the normal forces from the bound vorticity and the wake influence acts in the quarter-chord point, the oscillatory moment is given by

$$\begin{aligned} M = & (a + 0.5)2\pi\rho b^2(V - \dot{x}) \{ V\alpha_0 + (V\alpha_1 - \dot{x}\alpha_0 - \dot{y} - b(a - 0.5)\dot{\alpha}) \cdot \mathbf{C}(k) \} \\ & - 0.5\pi\rho b^3(V - \dot{x})\dot{\alpha} + \pi\rho b^3a [(V - \dot{x})\dot{\alpha} - \ddot{x}\alpha - \ddot{y} - ab\ddot{\alpha}] - 1/8\pi\rho b^4\ddot{\alpha} \end{aligned} \quad (\text{B.23})$$

The oscillatory drag is found by computing the tangential force as in equation 3.49 and using equation 3.52 for the projection of the forces to obtain

$$\begin{aligned} D = & 2\pi\rho b \{ V\alpha_0 + (V\alpha_1 - \dot{x}\alpha_0 - \dot{y} - b(a - 0.5)\dot{\alpha}) \cdot \mathbf{C}(k) \} \\ & \cdot \{ [\dot{y} + b(a + 1/2)\dot{\alpha}] + [V\alpha_1 - \dot{x}\alpha_0 - \dot{y} - b(a - 0.5)\dot{\alpha}] (1 - \mathbf{C}(k)) \} \\ & - 0.5\pi\rho b^3\dot{\alpha}^2 + \pi\rho b^2 [(V - \dot{x})\dot{\alpha} - \ddot{x}\alpha - \ddot{y} - ab\ddot{\alpha}] \alpha \end{aligned} \quad (\text{B.24})$$

Appendix C

Numerical Panel Code Validation

In order to validate and investigate the accuracy of the developed potential panel code, analytical solutions were used as reference case. The investigation of the accuracy includes determination of the errors associated with the discretization of both space and time.

The analytical solutions chosen as test-cases in the present case are in case of steady flow the solution of the pressure distribution on a Van Den Vooren airfoil, and the lift and drag coefficient on a symmetrical Joukowski airfoil.

For validation of the unsteady version of the code, two analytical solutions of unsteady phenomena using infinitely thin profiles, were chosen. The first of these is the impulsively started flow over an airfoil at an angle of attack, and the other is an oscillating airfoil, as described in section 3.2.

C.1 Van de Vooren airfoil

A mapping capable of transforming a circle to a symmetrical airfoil with finite trailing edge was proposed by van de Vooren and de Jong. A van de Vooren airfoil of thickness ratio 0.15 and trailing edge angle $\tau = 12.5^\circ$ is shown in figure C.1.



Figure C.1: 15 % thick Van de Vooren airfoil with a trailing angle $\tau = 12.5^\circ$.

Analytical functions expressing the velocities on the surface of the airfoil can be found in for example Katz et. al. [27]. From these the surface pressure can be computed using Bernoulli's equation, equation 3.9. Figure C.2 shows analytically and numerically obtained negative dimensionless pressure coefficients. It is seen that the agreement between the analytical expression and the panel code solution is excellent. Note that the difficulties associated with constant strength doublets at the thin trailing edge, as shown in figure 3.10, are avoided using the present approach.

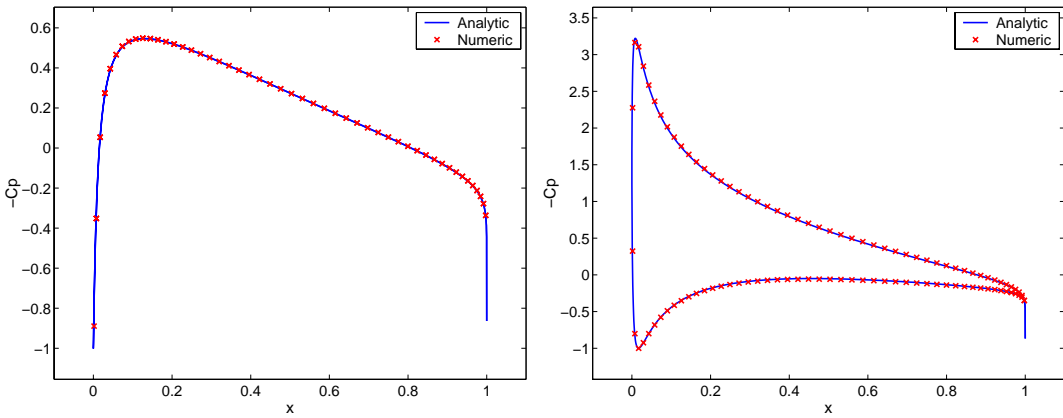


Figure C.2: $-C_p$ versus x for Van de Vooren airfoil. Analytic to panel code comparison. Left : $\alpha = 0^\circ$. Right : $\alpha = 8^\circ$.

C.2 Joukowski airfoil

It is possible to compute the exact, analytical, solutions to a number of airfoils using conformal mapping. One of the existing solutions is based on the Joukowski transformation, which maps a series of airfoil profiles, known as Joukowski profiles, to a circle. It can be shown [27], that the analytical value for the lift coefficient for a symmetrical Joukowski airfoil is

$$C_L = 2\pi(1 + \epsilon) \sin(\alpha). \quad (\text{C.1})$$

The thickness parameter, ϵ , is related to the thickness ratio, such that the thickness ratio is approximately equal to 1.299ϵ [27]. Figure C.3 shows a symmetrical Joukowski

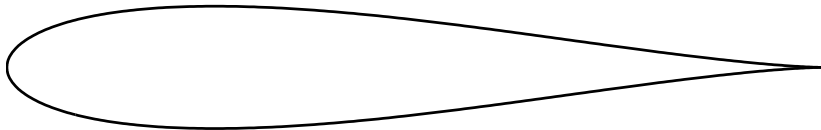


Figure C.3: 15 % thick Joukowski airfoil. Notice the cusped trailing edge.

airfoil with a thickness ratio of 0.15.

Note that the trailing edge of the Joukowski airfoil is cusped, which is known to present some numerical difficulties for panel code solutions. In the equations used to express the profile shape, the exact value for the thickness parameter is computed for use in the validation. The derivation of analytic expressions can be found in [27]. Figure C.4 shows the comparison between analytically and numerically obtained characteristics of a 15% thick Joukowski airfoil. The upper figures show the numerically obtained values for C_L and C_D versus number of panels in the discretization of the airfoil. As expected the difference between the numerical and analytical results decrease with the number of panels used. For 100 panels, the difference in lift coefficient is 0.007, corresponding to 1.1%. According to d'Alembert's Paradox, the drag from a potential flow should be zero. The value obtained from the panel code was $C_D = 0.002$ using 100 panels. The lower figure shows lift coefficient, C_L , versus angle of attack, α . The numerically

obtained values of the lift coefficient lies 1.0% to 1.1% above the analytical results for all angles of attack. On the basis of these results it was concluded, that the steady

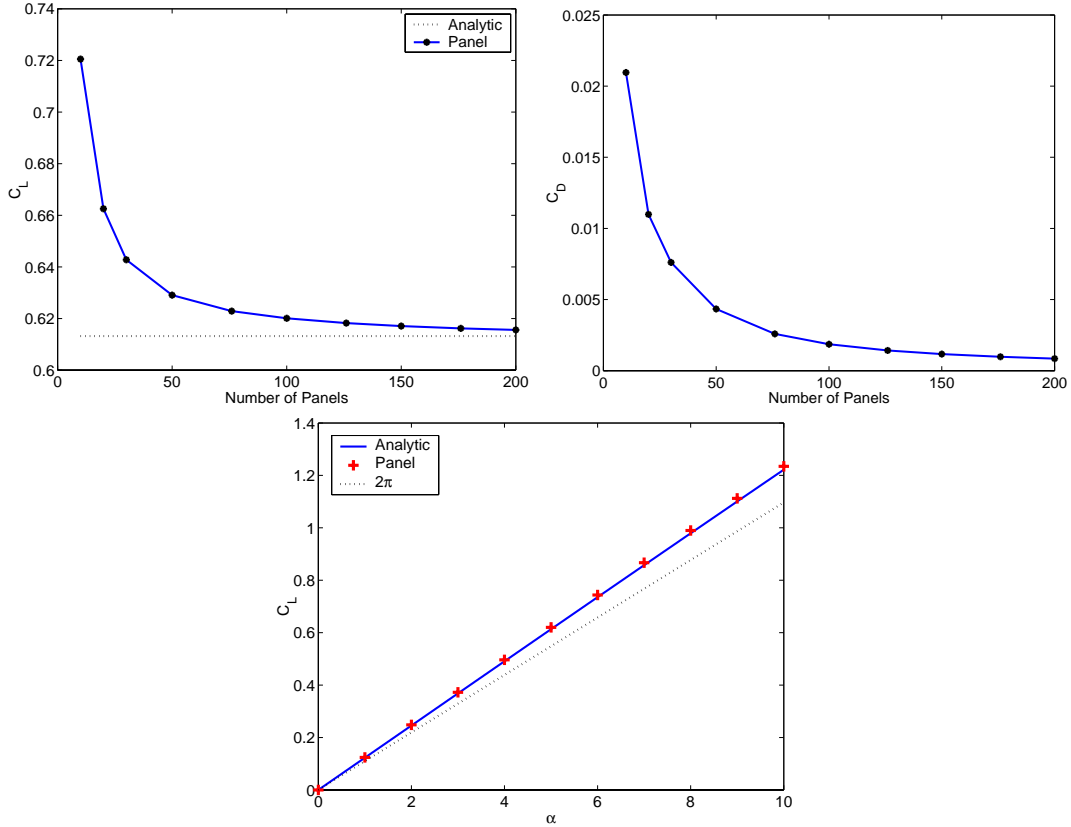


Figure C.4: Comparison between analytically and numerically obtained characteristics of a 15% thick Joukowski airfoil. Upper figures: C_L (left) and C_D (right) versus number of panels in the discretization for $\alpha = 5^\circ$. Lower figure: C_L versus α for a discretization using 100 panels.

version of the panel code was functional, and that a discretization of airfoils using 100 panels gives results with satisfactory accuracy.

C.3 Impulsive Motion, the Wagner function

The solution of the lift history of a impulsively started incompressible inviscid flow over an infinitely thin airfoil at an angle of attack were solved by Wagner in 1925.

The development of the lift in time for this case can be characterized by a function, Φ , such that

$$C_L = 2\pi\alpha\Phi(\tilde{t}) = C_{L\text{steady}}\Phi(\tilde{t}). \quad (\text{C.2})$$

Wagners function, Φ , is a function of non-dimensional time, \tilde{t} , only. The non-dimensional time is given by

$$\tilde{t} = \frac{tU}{c}. \quad (\text{C.3})$$

According to Fung [13] the exact form of Wagner's function can be expressed in terms of Bessel functions of first and second order

$$\Phi(\tilde{t}) = 1 - \int_0^{\infty} \{(K_0(x) - K_1(x))^2 + \pi^2(I_O(x) + I_1(x))^2\}^{-1} e^{-2x\tilde{t}} x^{-2} dx. \quad (\text{C.4})$$

Since this expression is not expressible in terms of well known (analytical) functions, the following approximate representations are used [13]:

$$\Phi_1(\tilde{t}) = 1 - 0.165e^{-0.0910\tilde{t}} - 0.335e^{-0.600\tilde{t}} \quad (\text{C.5})$$

$$\Phi_2(\tilde{t}) = 1 - 0.165e^{-0.082\tilde{t}} - 0.335e^{-0.64\tilde{t}} \quad (\text{C.6})$$

Fung [13] states that the expression in equation C.6 gives a slightly better approximation than equation C.5 for $\tilde{t} < 1.1$. Due to this, a function consisting of equations C.5 and C.6 multiplied by weight functions is used as reference in the validations to follow. The combined approximate expression for Wagner's function reads

$$\begin{aligned} \Phi(\tilde{t}) &= \Phi_1(\tilde{t})w(\tilde{t}) + \Phi_2(\tilde{t})(1 - w(\tilde{t})) \\ w(\tilde{t}) &= 0 \text{ if } \tilde{t} \leq 1.3 \\ w(\tilde{t}) &= \frac{\tilde{t} - 1.3}{2} \text{ if } 1.3 < \tilde{t} < 3.3 \\ w(\tilde{t}) &= 1 \text{ if } \tilde{t} \geq 3.3 \end{aligned} \quad (\text{C.7})$$

In figure C.5, numerically obtained values equivalent to Wagner's function for 15% profile thickness is shown with the approximate representation, equation C.7. The numerical expressions were obtained using 100 panels on a NACA 0015 airfoil, using time steps between $\Delta\tilde{t} = 0.02$ and $\Delta\tilde{t} = 0.2$.

It is observed that the panel code solutions approaches a value lower than the analytical value as the time step is refined. In order to investigate this, the right figure shows the same graphs for NACA 00-airfoils of thicknesses in the range from 1% to 15% using $\Delta\tilde{t} = 0.05$. It is noted that the curves get closer to the analytical curve as the thickness ratio of the airfoils is reduced. The curve labelled as an airfoil of 0% thickness is a computation employing the lumped vortex approach, corresponding to an infinitely thin airfoil.

From the results shown in the right graph it was concluded that the rather big difference between the results in the case of the 15% thick airfoil is attributed to the difference in thickness. Wagners solution assumes a infinitely thin airfoil, and the results in the left graph is for a 15% thick airfoil.

The slight differences between the analytical and numerical results for the thin airfoils in the right graph is explained by the more detailed modelling of the wake in the numerical case. Wagner's function is derived under the assumption that the angle of attack is so small that the profile and the wake lies on one straight line. This is not the case in the panel code simulations, where $\alpha = 5^\circ$, and full wake roll-up is computed. From the right figure it was concluded that a non-dimensional time-step of $\Delta\tilde{t} = 0.05$ is sufficient for the computations on this work.

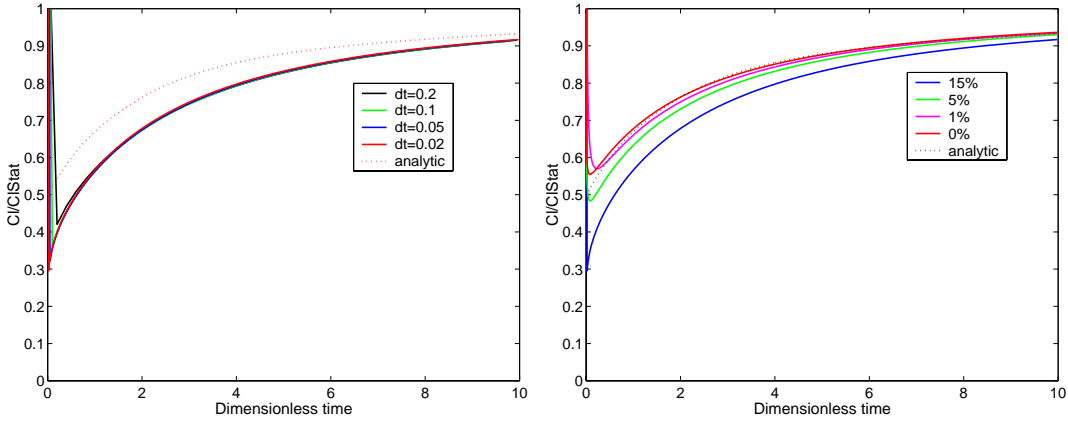


Figure C.5: Comparison of analytically and numerically obtained values of Wagners function. The left figure shows $C_L/C_{L,\text{static}}$ versus non-dimensional time, \tilde{t} , for a NACA 0015 airfoil using non-dimensional time-steps, $\Delta\tilde{t}$, in the range from 0.02 to 0.2. The right figure shows $C_L/C_{L,\text{Steady}}$ versus \tilde{t} , for NACA 00-airfoils of varying thickness using a dimensionless time-step $\Delta\tilde{t} = 0.05$.

C.4 Oscillating airfoil

In order to validate the unsteady panel code with an airfoil in oscillatory motion, the results from computations on symmetrical NACA profiles with thickness ratios in the range of 0.01 to 0.15 were compared to the analytic expressions from section 3.2. From figure C.6 it is seen that there is excellent agreement between the analytical and

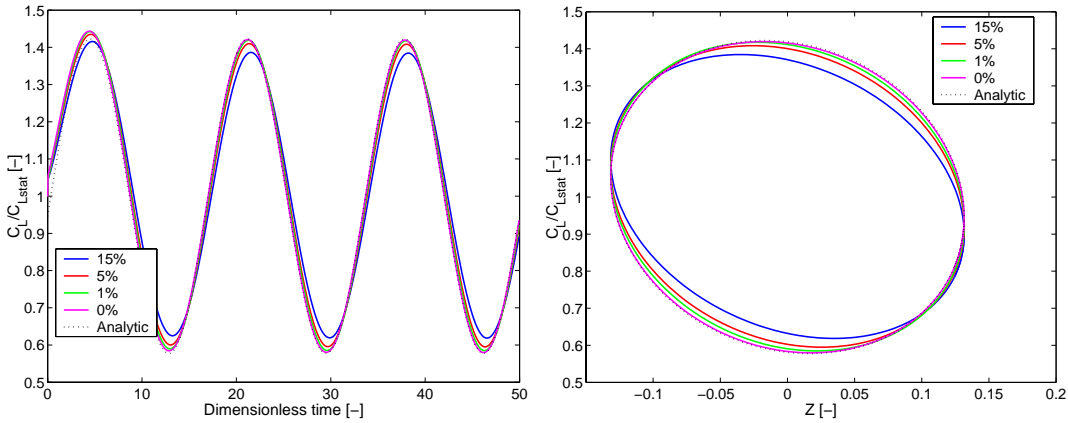


Figure C.6: Comparison of symmetrical NACA profiles with thickness ratios in the range of 0.01 to 0.15 with analytic solutions to airfoil in heaving motion, $\beta = 0^\circ$. $C_L/C_{L,\text{Steady}}$ versus non dimensional time (left) and heave coordinate, z (right). The airfoil is at $\alpha = 5^\circ$ incidence, and the reduced frequency of the motion is $f_{\text{red}} = 0.03$.

numerical results for the very thin profiles. This shows that the crude assumptions made in the analytical derivation regarding the geometry of the wake has no big effect at the small angles of attack where the requirement of fully attached flow is met. Furthermore it is seen that the effect of the profile thickness is a reduction of the relative amplitude of C_L , as well as a slight phase-shift.

C.5 Tunnel validation

The effect of tunnel walls is shown in figure C.7, where the non dimensional lift and moment is shown as a function of tunnel wall spacing. As expected, the asymptotic value in the case $h/c \rightarrow \infty$ is the free lift as computed by the unbounded potential

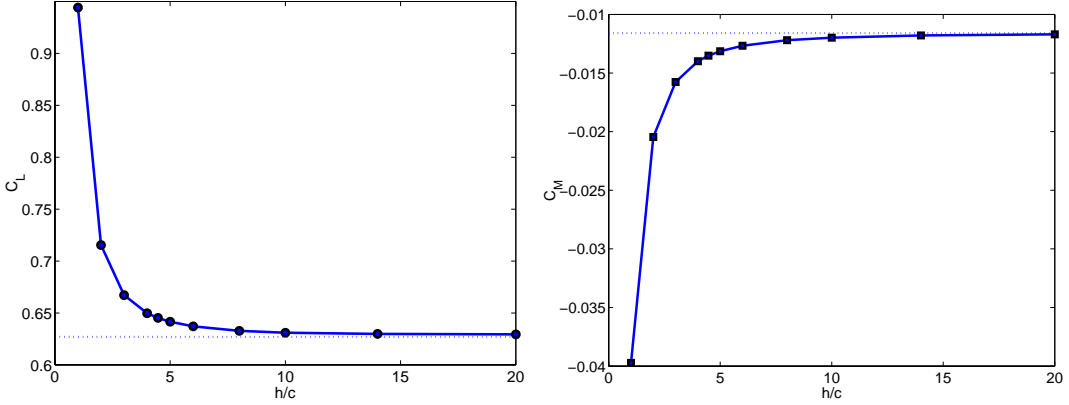


Figure C.7: Influence of tunnel wall spacing for a NACA 0015 airfoil at $\alpha = 5^\circ$, using 100 panels on the airfoil and 50 panels on each of the panel walls. Left: Lift coefficient versus height to chord ratio. Right: Moment coefficient versus height to chord ratio.

code. It is observed that the absolute value of the lift and the moment increases as the tunnel height is decreased.

The result of further validation of the tunnel wall implementation is shown in figure C.8, where normal and tangential velocities are plotted as functions of x-coordinate

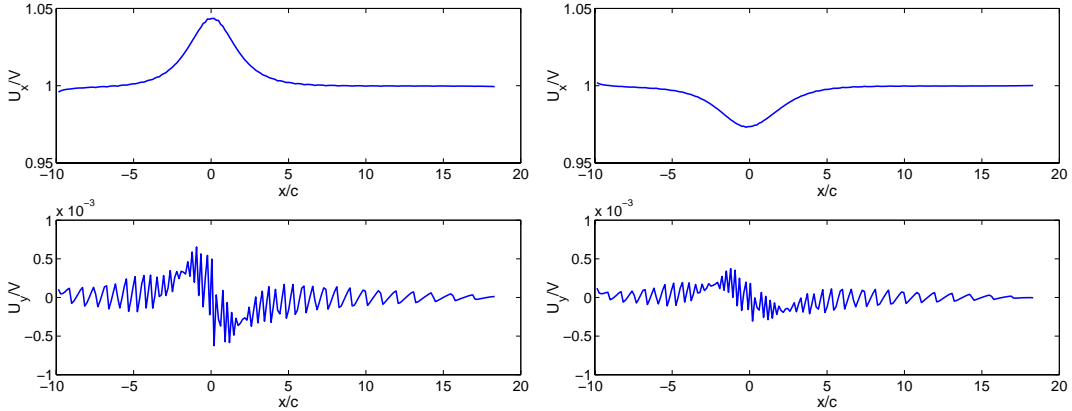


Figure C.8: Normal (lower) and tangential (upper) velocities versus x-coordinate a distance $\Delta l/c = 0.022$ from the upper (left) and lower (right) tunnel walls. The airfoil is located at $x = 0$. $h/c = 4.47$.

close to the upper and lower tunnel walls. It is seen that the velocities normal to the tunnel walls are well below 0.1% of the free stream velocity. The 'wiggles' on the normal velocities are due to the discontinuities in source strength between the panels. The tangential velocities are smooth, and close to the free-stream velocity far from the airfoil. The tangential velocity on the upper wall is increased in the region near the

airfoil while the tangential velocity on the lower wall is decreased in the region near the airfoil. This is due to the circulation of the airfoil. It is seen that the increase on the upper wall is larger than the decrease on the lower wall. This is the blocking effect of the airfoil in the tunnel.

The method used in the unsteady panel computations is analog to the steady case, no need for further validation of the tunnel implementation were needed.

In order to determine an appropriate discretization of the tunnel walls, an investigation of the tunnel panel size was undertaken. The left graph in figure C.9 shows the lift

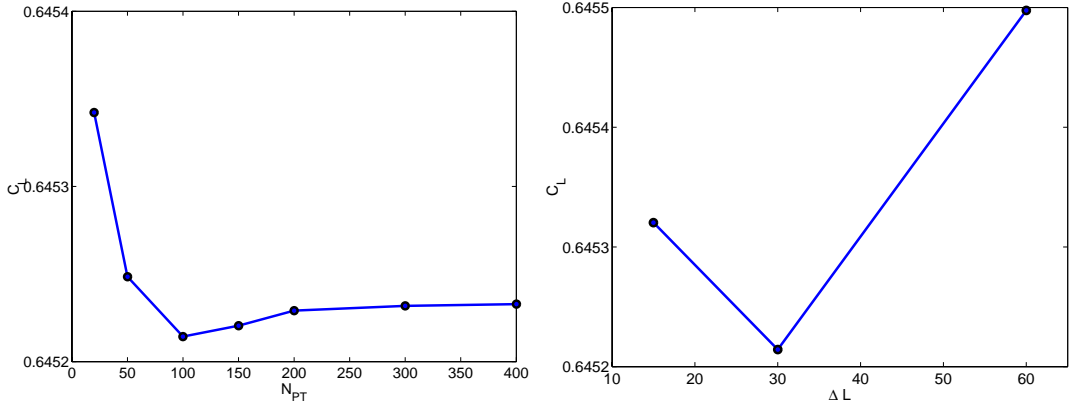


Figure C.9: *Investigation of tunnel wall discretization. Left: Influence of number of panels on tunnel walls of fixed length. The tunnel extends from 10 chord-lengths upstream of the airfoil to 20 chord-lengths downstream of the airfoil. Right: Influence of tunnel length of fixed panel density. The ratio of the tunnel height to chord-length is \$h/c = 4.47\$.*

coefficient as function of the number of panels for a fixed tunnel length. The variation in \$C_L\$ for numbers of panels higher than or equal to 50 is less than 0.03%. The right figure shows the influence of the length of the tunnel walls, using identical panel densities. Here the influence is very small too for the investigated total lengths. The variation in \$C_L\$ for total tunnel lengths between 15 and 60 chord-lengths is less than 0.05%.

From the above investigations it was concluded that a discretization of the tunnel walls using 100 tunnel panels in total was sufficiently accurate. The total tunnel length used in all tunnel computations in this work was set to \$\Delta L = 30\$. 10 chord-lengths upstream and 20 chord-lengths downstream. The reason for going further in the downstream direction than in the upstream is the unsteady wake, making the need for more tunnel in that direction to capture correctly the coupled tunnel-wake interaction, and its influence on the airfoil.

The length of the tunnel panels at the airfoil was determined according to

$$L_{panel} = 0.4 \frac{x_{Out} - x_{In}}{N_{Panels}}. \quad (\text{C.8})$$

The spatial distribution of the tunnel wall panel lengths were determined by a third-order polynomium, such that the specified panel length at the airfoil was the shortest of all the panels, while prescribing the tunnel inlet and outlet positions.

The discretization and size of the tunnel walls used for all tunnel computations in this work are shown in figure C.10.

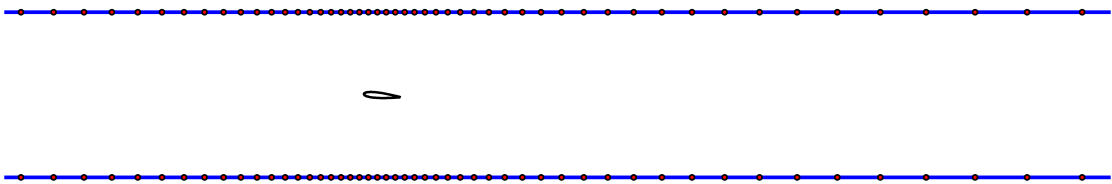


Figure C.10: *Discretization of the tunnel walls using 2×50 constant strength source panels extending 10 chord-lengths upstream and 20 chord-lengths downstream.*

Appendix D

RANS grid sensitivity study and code validation

D.1 Grid sensitivity study

In order to determine the error committed when using a specific computational grid, a grid sensitivity study is presented in this appendix. The first part concerns the influence of the radius of the grid, and the last part concerns the discretization of the grid.

D.1.1 Grid radius

The influence of the distance from the airfoil to the outer boundary of the computational domain was estimated using relations from potential theory to link the lift coefficient to a velocity disturbance at a radius r , far from the airfoil.

$$C_L = \frac{2\Gamma}{cV} \quad (\text{D.1})$$

$$V_\Theta = \frac{\Gamma}{2\pi r} \quad (\text{D.2})$$

Equation D.1 relates the lift coefficient to the circulation of the bound vorticity on the airfoil, whereas equation D.2 expresses the induced tangential velocity from a point vortex at the distance r from the vortex. Combining equations D.1 and D.2, yields for the disturbance from the circulation of the airfoil

$$\frac{V_\Theta}{V} = \frac{C_L c}{4\pi r} \quad (\text{D.3})$$

This corresponds to the angle

$$\alpha' = \arctan \left(\frac{V_\Theta}{V} \right) \quad (\text{D.4})$$

upstream of the airfoil.

At the inlet of a RANS computation, the velocity is specified. Therefore the disturbance on the inflow velocity from a grid of radius r can be quantified using equations D.3 and

D.4.

Figure D.1 shows V_Θ/V and α' as function of non dimensional grid radius r/c for $C_L = 1$. As a compromise between accuracy and computing costs, we employ grid

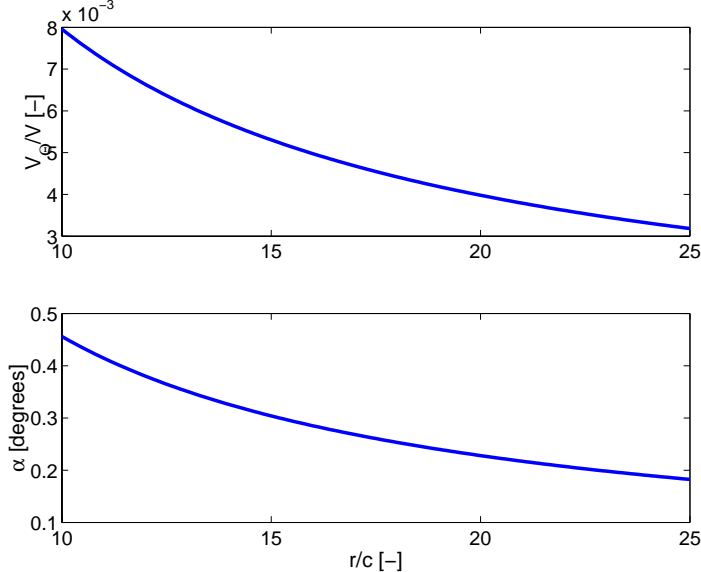


Figure D.1: *Effect of grid radius on disturbance of inlet velocity compared to an infinite grid. Upper figure: V_Θ/V versus r/c . Lower figure: α' versus r/c . In both figures a unit lift coefficient is used. $C_L = 1$.*

radius 17.5 throughout. This radius of the computational grid corresponds to a relative disturbance of the velocity $V_\Theta/V = 0.0045$ for $C_L = 1$. The corresponding change in the angle of attack of the flow is $\alpha' = 0.26^\circ$, upstream of the airfoil.

D.1.2 Grid discretization

The computational grids around the NACA 0015 airfoil used in this work were generated using the hyperbolic grid generator HypGrid2D, developed by Sørensen [53]. The topology used for the grids is the O-grid configuration. The O-grid configuration avoids the problem of specifying where the wake is, making it a more general grid. This is a strength when dealing with moving grids, since the wake of the airfoil in this case is not in the same relative position at all times. Moreover, the cells in the wake are not as stretched as in a C-grid.

In order to quantify the error associated with the discretization of the fluid domain, three computational grids were used to estimate the exact value of the lift coefficient as suggested by Roache [45]. The three grids employed for the grid sensitivity studies were of approximately the same outer radius, $r = 17.5$. The grids were constructed to have a distance to the first gridline away from the surface corresponding to $y^+ = 1.0$ in order to satisfactorily resolve the laminar sublayer. The value of y^+ for these grids more than meets the requirements from the $k - \omega$ SST turbulence model, which is $y^+ < 3.0$ [34]. With these requirements, the height of the innermost computational cell was approximately $2 \cdot 10^{-5}$ chord-lengths. The following three grids were used as a basis for computing the exact value of the lift coefficient.

- **Grid A** 384×192 grid points. (tangential \times normal direction)
- **Grid B** 256×128 grid points.
- **Grid C** 192×128 grid points.

Transient computations were carried out using grids A, B and C at incidence $\alpha = 5^\circ$ using the $k - \omega$ SST turbulence model.

According to Roache [45], Richardson extrapolation can be used to determine the exact value of a given quantity, f . The discrete solutions are assumed to have a series representation in the grid spacing, h , of

$$f = f_{\text{exact}} + g_1 h + g_2 h^2 + \text{HOT}. \quad (\text{D.5})$$

The functions g_1 and g_2 are defined in the continuum, and does not depend on the discretization. The term labelled HOT is the higher order terms. From solutions using three different discretizations, the exact value, f_{exact} , can be determined. Using the above method on the present case, the exact value of the lift coefficient, C_L , was estimated using the cell width on the surface as the dependant grid spacing.

$$C_{L,\text{exact}} = 0.5157 \quad (\text{D.6})$$

In order to save computational costs, a fourth computational grid was generated

- **Grid D** 256×64 grid points.

Grid D has fewer grid points in the normal direction than the other grids, but due to the high resolution in the direction around the airfoil, the computational accuracy match grid C even though fewer computational points are used. Comparison of the lift using grid D,

$$C_{L,\text{gridD}} = 0.5221, \quad (\text{D.7})$$

with the estimated exact value show that the error committed when using grid D is $\Delta C_L = 0.0064$, corresponding to 1.25%.

As a compromise between accuracy and computational cost, grid D was employed for all RANS computations in this work. Figure D.2 shows grid D.

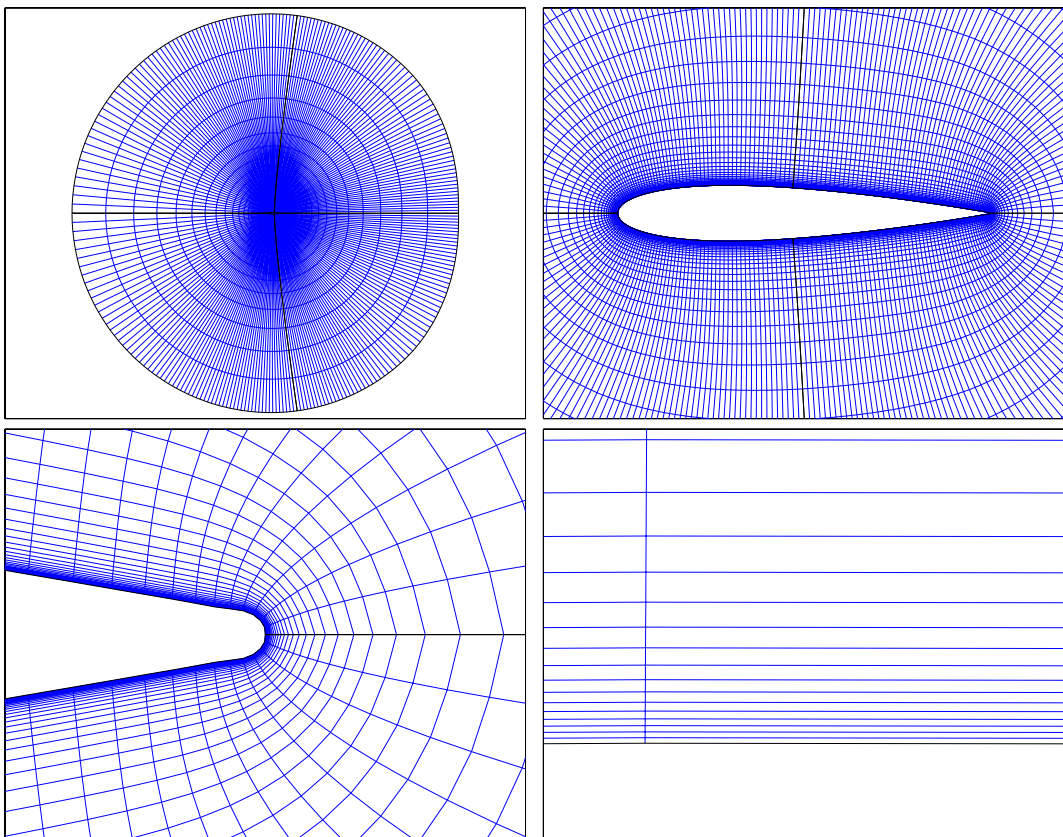


Figure D.2: *The computational O-grid (D) around NACA 0015 profile employed for the computations in the present work. 256×64 grid points. Grid radius is 17.5 chord-lengths.*

D.2 Moving grid validation

Since the basic elements of the code employed for the RANS computations carried out in the present work is thoroughly tested and validated previously, for example in [51] and [54] by Sørensen, only validation of the new implementations were needed.

Validation of the implementation of the moving grid method described in section 3.6 is undertaken by running computations on an empty rectangular grid undergoing oscillatory motion in the direction perpendicular to the motion of the free-stream. The grid is shown in figure D.3. The result of such a computation should give the specified inlet velocity in the whole domain when subtracting the velocity field from the motion of the computational grid. The grid is undergoing harmonic oscillation per-

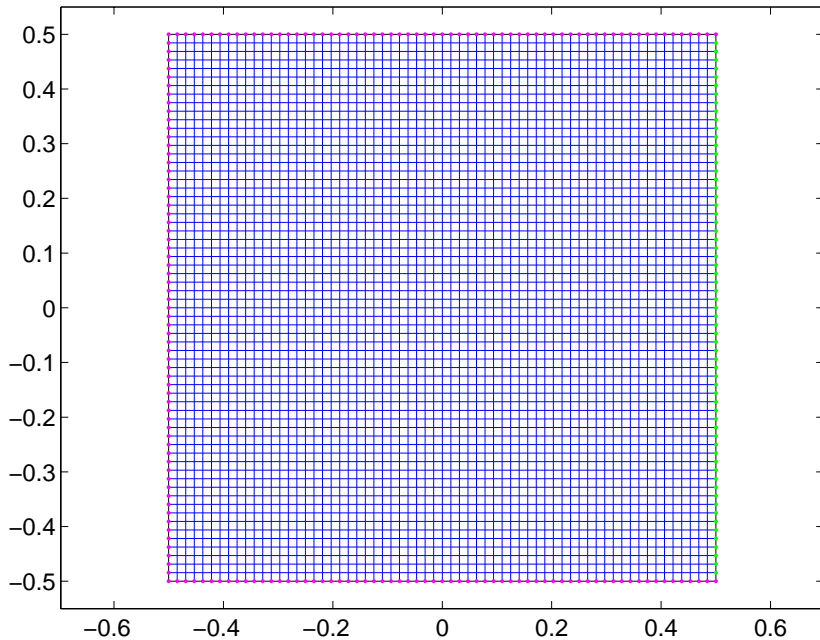


Figure D.3: *Quadratic grid used for validation of the moving grid method. The grid-size is 64, and the side-length of the quadratic grid is 1. The leftmost, upper and lower edges of the domain have inlet condition (magenta), whereas the rightmost edge has an outlet boundary condition (green). All other points are internal points in the domain.*

pendicular to the incoming flow with an amplitude equal to 80% of the side length of the grid. The period of the oscillatory motion equals the time for the flow to move from through the computational domain. This gives a maximum flow velocity in the y-direction, $V_{y,max}/V_x = 0.8\pi = 2.51$ in the relative frame of reference, corresponding to a maximum relative flow angle

$$\alpha_{\text{rel}} = \arctan(0.8\pi/1) = 68.3^\circ$$

with respect to the horizontal grid lines.

For the computations, the following values were used

- Flow quantities: $V = 1$, $\rho = 1$ and $\mu = 1$
- Movement parameters: $A = 0.8$ and $T = 1$

- Time step: $\Delta t = 0.78125 \cdot 10^{-3}$

The parameters corresponds to 1280 time steps per oscillation period, and a maximum CFL value 0.126.

The flow-fields were investigated after 2 and 2.5 periods of the motion, at $y = 0$ and $\dot{y}/V_x = \pm 2.51$.

It was observed that the disturbance on the velocity in the direction of and perpendicular to the free-stream was

$$\begin{aligned} V_x &< 3 \cdot 10^{-6} \\ V_y &< 1 \cdot 10^{-4}. \end{aligned}$$

From this it is seen that the disturbances added to the flow from the motion of the grid is negligible, which validates the moving grid implementation.